

ABSTRACT

BROWN, CHRISTOPHER JOHN. Impact of Environmental Conditions on the Contact Physics of Gold Contact RF Microelectromechanical Systems (MEMS) Switches. (Under the direction of Professor Jacqueline Krim.)

RF MEMS switch technology is poised to create a new generation of devices capable of vastly outperforming current mechanical and semiconductor switching technology. Despite the efforts of top industrial, academic, and government labs, commercialization of RF MEMS switches has lagged expectations. This dissertation focuses on issues associated with switch contact physics.

Understanding the failure mechanisms for metal contact switches is a complex challenge. There is strong interplay between variables such as mechanical creep, deformation, contact heating, contact asperity size, real contact area, and current flow leading to the eventual failure of the switch. Stiction failures moreover are highly sensitive to ambient conditions and absorbed film layers at the switch contact.

The experiments in this thesis seek to isolate individual failure mechanisms and tie them to the physics driving that behavior through correlation of experimental data and theoretical modeling. Four experiments in controlled environments were performed: 1) the impact of cryogenic temperatures on RF MEMS contacts, 2) a correlation between experimental data and theoretical modeling for gold asperity creep at room and cryogenic temperatures, 3) a power law relationship between contact resistance and time dependent creep, and 4) the pressure dependence of switch closure.

Cryogenic temperatures were used to isolate contaminant film effects. Contaminant films were found to have less mobility at 77 K, and contact resistance measurements showed that the film could be reduced on the contact surface through mechanical cycling and high temperatures at the gold asperities. It was also noted at cryogenic temperatures that the choice of atmosphere was important. A nitrogen atmosphere at liquid nitrogen temperature produced variable contact resistance as the condensed liquid boiled off the switch contacts.

Data was correlated with a single asperity creep model to show that change in contact resistance as a function of time is related to the creep of gold asperities at the contact interface. The change in contact resistance over time can be described by a power law relation derived from the single asperity creep model that takes into account the surface topography, material characteristics, and contributions from additional sources such as adsorbed film layers. Additionally, it was shown that the creep mechanism was temperature dependent and that creep was significantly decreased at cryogenic temperatures.

A drop in pressure as a result from cryogenic temperatures was observed to create switch bounce at closure. This was explored in a set of room temperature experiments which established the onset of bounce at 60 Torr. The results were and correlated to the damping coefficient and the ratio of the damping force to the electrostatic force of actuation.

This work contributes to the field of contact physics and MEMS switch technology by firmly establishing the role of creep in contact mechanics and quantifying its time and temperature dependent impact on contact resistance.

Impact of Environmental Conditions on the Contact Physics of Gold Contact
RF Microelectromechanical Systems (MEMS) Switches

by
Christopher John Brown

A dissertation submitted to the Graduate Faculty of
North Carolina State University
in partial fulfillment of the
requirements for the Degree of
Doctor of Philosophy

Physics

Raleigh, North Carolina

2008

APPROVED BY:

Dr. Thomas P. Pearl

Dr. Angus I. Kingon

Dr. Lubos Mitas

Dr. Jacqueline Krim
Chair of Advisory Committee

DEDICATION

In dedication –

To my mother who taught me about perseverance and never accepted anything less than the best from me.

Most importantly to my wife who held down the fort while I plowed through these last five years and has signed on for another two while I go to Harvard Business School.

In memory of my friend Ralph who stayed up with me into the wee hours of the morning while I endured endless torture at the hands of Griffiths, Jackson, and Sakurai. And to Atlas who has taken over for him.

BIOGRAPHY

Chris Brown earned the B.S. in Physics in 1999 from the College of Charleston in Charleston, SC. Afterward he was employed as an Optical Measurements Engineer with Corning, Inc. at the world largest fiber optic manufacturing facility in Wilmington, NC. While at Corning Chris served as the Subject Matter Expert for PMD (polarization mode dispersion), coating geometry, and fiber curl. Chris led several teams in the improvement of PMD measurement capability at the facility. This included jointly developing several novel PMD measurement techniques including a POTDR (polarization optical time domain reflectometer) for indentifying fiber at risk of significant optical transmission defects and a JME (Jones matrix eigenanalysis) measurement method for long-length, ultra-low PMD optical fiber. Chris also developed a set of measurement standards often referred to as the “Golden Fibers” which are still used at Corning as a benchmark standard for PMD measurement. Despite leaving the company in 2003, his work and technical developments continued to strengthen Corning’s overall product health and profitability by solving a major functional quality issue with the division’s highest margin products.

In 2003 Chris entered NCSU’s physics program. He has worked for four years in the Nanotribology Lab under the direction of Dr. Jacqueline Krim. His research has focused on the environmental impacts on the contact physics of RF MEMS devices. He will earn a doctorate in physics in the summer of 2008.

While working in the lab, Chris took classes in NCSU’s Jenkins Graduate School of Management. Through an opportunity arising from an entrepreneurship class, Chris and three other students started a textile dye company, ChormaFix, based on a patented dye developed in the university’s Textiles College. Chris currently serves as the CEO for ChromaFix and is advancing the company toward product launch and expansion.

In the fall of 2008 Chris will attend Harvard Business School as part of the MBA class of 2010. In the future he plans to work in venture capital or corporate venture where he can use his business and science background to evaluate and invest in high growth potential companies with innovative, high-tech intellectual property.

ACKNOWLEDGEMENTS

Even though a large amount of time is spent toiling in the lab alone and achieving the doctoral level is great personal achievement, science is a team effort. The list of those that deserve thanks is long, and I cannot thank them all here. However, I would like to note the following people and groups who helped me advance my professional career.

First off, Dr. Krim, not only because she writes the paychecks, but because she put up with me and heard the sentence, “I have no working switches” more times than she cared to. I am especially thankful for her understanding and flexibility as I tried to balance my lab work with running a company.

To the MURI RF MEMS team. Dr. Angus Kingon who provided oversight of the group and helped pull together all the loose ends that eventually became a part of this thesis. To Dr. Zikry and Dr. Omid Rezvani who provided the theoretical modeling basis for my experimental creep measurements. To Dr. Don Brenner and Dr. Doug Irving for their insight into contact mechanics and assistance in making sense of the data I had taken. To Matt Walker who worked with me in the trenches in the lab and the newly minted Dr. Zhenyin Yang who provided me many an opportunity to argue about data. Special thanks to Keeley Stevens who prepared my data and graphs for inclusion in the thesis.

Thanks to all my fellow members of the Nanotribology Lab for their help in the everyday stuff from finding tools to building circuits. Special thanks to Adam Hook and Dr. Matt Highland who helped me learn circuits, build my equipment, and learn LabView.

This work was supported by AFOSR MURI Grant No. FA9550-04-1-0381 entitled “Multifunctional Extreme Environment Surfaces: Nanotribology for Air and Space” and DARPA S&T Fundamentals Program, “Center for RF MEMS Reliability and Design Fundamentals,” Grant No. HR0011-06-1-0051.

TABLE OF CONTENTS

LIST OF TABLES	x
LIST OF FIGURES	xi
CHAPTER 1: Introduction to RF MEMS	1
1.1 RF MEMS and Nanotechnology.....	2
1.2 RF MEMS switch types	3
1.3 RF MEMS applications.....	5
1.4 Metal contacting RF MEMS failure modes	6
1.4.1 Contact wear.....	6
1.4.2 Stiction.....	7
1.4.3 Arcing and field induced material transfer	7
1.4.4 Adsorbed film layers	8
1.4.5 Creep.....	8
1.5 Aims of dissertation	9
1.6 References	11
CHAPTER 2: RF MEMS Contact Physics Literature Review	15
2.1 Overview	16
2.2 Contact physics – contact materials and surface conditions	16
2.2.1 Contact materials	16
2.2.2 Contact models	19
2.2.3 Constriction resistance.....	22
2.3 Impact of operational parameters	25
2.3.1 Contact load	25
2.3.2 Current	28
2.4 Adsorbed film effects.....	29
2.4.1 Origin.....	30
2.4.2 Physical properties.....	31
2.4.3 Temperature dependence	34

2.4.4 Removal techniques.....	35
2.4.5 Contact physics modeling with adsorbed films.....	36
2.5 Environmental impacts.....	37
2.5.1 Temperature	37
2.5.2 Atmosphere	38
2.5.3 Pressure	38
2.6 Thesis material.....	39
2.7 References	40
CHAPTER 3: Experimental Details	53
3.1 Experimental apparatus.....	54
3.1.1 Vacuum test chamber	54
3.1.2 Wiring configuration	59
3.1.3 Device cooling and temperature measurement	60
3.2 RF MEMS test devices.....	62
3.2.1 wiSpry RF MEMS switch.....	62
3.2.2 NEU RF MEMS switch	64
3.2.3 RFMD RF MEMS switch.....	65
3.3 Data taking procedures.....	67
3.3.1 Device handling and storage.....	68
3.3.2 Electronics.....	69
3.3.3 Pre-test procedures	71
3.4 Chapter organization.....	73
3.5 References	74
CHAPTER 4: The Impact of High and Low Pressure on Switch Contact.....	76
4.1 Introduction	77
4.2 Fluid physics and damping fundamentals	78
4.3 Damping coefficient and quality factor.....	80
4.4 Switch bounce.....	81
4.5 Switching time	87

4.6 Conclusion.....	89
4.7 References	90
CHAPTER 5: Cryogenic Performance of Gold RF MEMS Switch Contacts.....	93
5.1 Abstract	94
5.2 Introduction	94
5.3 Contact theory.....	95
5.4 Device	97
5.5 Experimental setup.....	99
5.6 Experimental results.....	101
5.6.1 Gas dependence.....	101
5.6.2 Time dependence.....	103
5.7 Analysis.....	105
5.7.1 Comparison to temperature dependence.....	107
5.7.2 Comparison to time and temperature dependence	107
5.8 Summary	111
5.9 References	112
CHAPTER 6: Surface Roughness, Asperity Contact, and Gold RF MEMS Switch Behavior.....	116
6.1 Abstract	117
6.2 Introduction	117
6.3 Contact mechanics and topography	119
6.4 Physics of contact resistance and surface roughness	121
6.5 RF MEMS fabrication and experimental setup.....	124
6.6 Contact models	125
6.7 Results and discussion.....	130
6.8 Conclusions	139
6.9 Acknowledgements.....	140
6.10 References	140

CHAPTER 7: The Role of Creep in the Time-Dependent Resistance of Ohmic Gold Contacts in RF-MEMS Devices	145
7.1 Abstract	146
7.2 Introduction	146
7.3 Analysis of experimental and calculated resistance data	147
7.4 Analytic single asperity model	152
7.5 Summary	156
7.6 Acknowledgements	157
7.7 References	157
CHAPTER 8: Additional Contact Resistance Measurements	159
8.1 RF MEMS contact resistance temperature dependence	160
8.2 Thermometer calibration	163
8.3 Additional contact resistance versus time data	165
8.4 Contact heating	168
8.5 Contact resistance as a function of switch cycles	172
8.6 References	173
CHAPTER 9: Temperature Dependence of Asperity Contact and Contact Resistance in Gold RF MEMS Switches	174
9.1 Abstract	175
9.2 Introduction	175
9.3 Experimental device and apparatus	177
9.4 Experimental results and analysis	180
9.4.1 Temperature-dependent creep	180
9.4.2 Asperity heating	184
9.5 Modeling predictions	186
9.6 Conclusions	193
9.7 Acknowledgements	195
9.8 References	195
CHAPTER 10: Summary and Future Work	198

10.2 Suggested future work.....	201
10.3 References	203
APPENDIX.....	204
A.1 Cycle testing	205
A.2 Wiring diagrams.....	207
A.3 References	211

LIST OF TABLES

Table 1.1 – Comparison of electrostatic switch performance	2
Table 2.1 – Material dependent contact resistance and adhesion force.....	17
Table 4.1 – Knudsen number and damping coefficient values.	86
Table 6.1 – Roughness parameters.	126
Table 6.2 – Electromechanical properties of Gold.	126
Table 7.1 – Resulting parameters from the fit of (7.2) to the prior experimental and modeling data.....	151
Table 9.1 – Electromechanical properties of Gold.	189
Table A.1 – Impact of operating and environmental conditions on cycle lifetime.	207
Table A.2 – Ceramic pin, switch bond pad, and function corresponding to wirebond diagram for wiSpry RF MEMS switch.....	209

LIST OF FIGURES

Figure 1.1 – Raytheon capacitive RF MEMS switch (a) top view and (b) schematic cross-section view.	4
Figure 1.2 – Metal contacting series switch types; a) fixed broadside, b) fixed-fixed broadside, and c) inline RF MEMS switches.	4
Figure 2.1 – Contact resistance versus cycle number for pure gold and Au-Ni alloys under high current, hot-switching condition.	18
Figure 2.2 – Volume pixel, or voxel, surface area model used by Dickrell <i>et al.</i> to directly calculate surface area from the measured surface topography of a MEMS device.	21
Figure 2.3 – Schematic of the contact asperities and the real contact area established when two rough surfaces touch.	23
Figure 2.4 – Illustration of (a) diffusive electron transport, or Maxwell resistance, and (b) ballistic electron transport, or Sharvin resistance.	23
Figure 2.5 – Contact resistance as a function of contact load.	26
Figure 2.6 – Nanowire formation on MEMS switch contact surface.	29
Figure 2.7 – Increase in contact resistance after a critical concentration of 100 vpm (=ppm volume) of dodecane is added to the atmosphere around a MEMS switch.	30
Figure 2.8 – Force and contact resistance profile for approach and withdrawal of Tungsten tip from a gold surface.	31
Figure 2.9 – Proposed mechanism for adsorbed film removal and re-growth.	33
Figure 2.10 – Comparison of contact resistance for room temperature and externally heated contacts.	34
Figure 2.11 – Auger spectra of a freshly cleaned Au wafer.	35
Figure 3.1 – Schematic of experimental apparatus.	54
Figure 3.2 – (a) Vacuum chamber for testing wiSpry RF MEMS switch with dewar (dewar height is 48 inches). (b) End-on picture of environmental sample chamber	56
Figure 3.3 - (a) Environmental sample chamber for testing NEU, Sandia, and RFMD RF MEMS switches.	57
Figure 3.4 – (a) Schematic planar view of wiSpry RF MEMS switch. (b) wiSpry RF MEMS die with four SPDT switch sets.	63

Figure 3.5 – Northeastern University (NEU) RF MEMS switch.....	65
Figure 3.6 – NEU switch die.....	65
Figure 3.7 – RFMD RF MEMS switch	67
Figure 3.8 – RFMD switch hermetically sealed in a WLP	67
Figure 4.1 – Electrostatic Force F_e , Damping Force F_d , and ratio for an NEU switch at an actuation voltage of 74 V.	82
Figure 4.2 – Schematic representation of instrumentation used to measure switch bounce and close time.	82
Figure 4.3 – Switch bounce and settling time for a wiSpry RF MEMS switch at 750, 60, and 40 Torr.	84
Figure 4.4 – Switch bounce and settling time for a RFMD RF MEMS switch at 750 Torr.....	85
Figure 4.5 – Switch bounce (solid lines) and single step actuation for NEU RF MEMS switch at three actuation voltages.	85
Figure 4.6 – Switching time at 750 Torr for a wiSpry RF MEMS switch	88
Figure 4.7 – Switching time for a wiSpry RF MEMS switch at 750, 60, and 40 Torr.....	88
Figure 5.1 – Side view of RF MEMS switch cantilever.....	98
Figure 5.2 – Experimental setup.	99
Figure 5.3 – Rapid cooldown of the device by boiling off liquid nitrogen directly on the vacuum system induces large fluctuations in contact resistance.	101
Figure 5.4 – Contact resistance fluctuations are seen just after switch closure for a nitrogen atmosphere at liquid nitrogen temperatures, but not for a helium atmosphere.....	102
Figure 5.5 – Contact resistance decreases over time while a switch is left in the actuated position at room temperature and at 77 Kelvin.	104
Figure 5.6 – According to the asperity-heating model, a contact voltage chosen between the two curves will generate a contact temperature high enough to disassociate the adsorbed films on the contacts but low enough to keep gold asperities from softening.	109
Figure 6.1 – (a) Side view of RF MEMS switch.....	122

Figure 6.2 – Three-dimensional fractal surface topographies generated using a Weierstrass-Mandelbrot function.....	127
Figure 6.3 – (a) Schematic front view of a cross section of the actual asperity geometry with smooth surface (S1), and its equivalent geometry with an irregular surface (S2) that is obtained by connecting the sampling points. (b) The Asperity geometry that is assumed as stacked layers with uniform cross sectional areas along the thickness direction. (c) A schematic top view of a cross section of actual asperity, and its equivalent geometry that is obtained by connecting the corresponding sampling points.	129
Figure 6.4 – Ratio of the real contact area to the apparent area over a 48-hour time span for the two surface roughness models.	130
Figure 6.5 – Number of the contact spots over a 48-hour time span for the two surface roughness models.	131
Figure 6.6 – The lower and upper limits of the contact resistance over a 48-hour time span for the two surface roughness models.	133
Figure 6.7 – Normalized Contact resistance over a 90-minute time span.	134
Figure 6.8 – Average contact spot resistance of the two surface roughness models over a 48-hour time span.	135
Figure 6.9 – Maximum resistivity at the contact spots for the two surface roughness models over a 48-hour time span.	136
Figure 6.10 – Top-view snap shots of the contact evolution for Model 2.....	137
Figure 6.11 – Contour of current magnitude for a voltage drop of 1 mV.	138
Figure 7.1 – Resistances across gold-gold contacts as a function of time.....	150
Figure 7.2 – Illustration of the conical geometry used in the single asperity model.....	153
Figure 7.3 – Curves I, II and III from Fig 7.1 for the first 10 seconds.....	156
Figure 8.1 – Contact resistance as a function of temperature for a wiSpry RF MEMS switch.	161
Figure 8.2 – Contact resistance versus temperature from 293 to 363 K	163
Figure 8.3 – Thermometer calibration data.....	164
Figure 8.4 – Contact resistance versus time for 1500 minutes showing multiple drops in resistance.	166
Figure 8.5 – Upwardly trending contact resistance versus time.	166

Figure 8.6 – Contact resistance versus time for 2900 minutes showing multiple increases in resistance.....	167
Figure 8.7 – Onset of asperity contact heating as a function of contact voltage.....	169
Figure 8.8 – Initial Onset of asperity contact heating between 50 mV and 60 mV.	170
Figure 8.9 – Transition point from heating dominated to real contact area creation dominated contact resistance measurement for a RF MEMS switch at room temperature.	171
Figure 8.10 – Contact resistance as a function of switch cycles for a wiSpry RF MEMS switch.	172
Figure 9.1 – Northeastern University (NEU) RF MEMS switch.....	177
Figure 9.2 – Side view of RF MEMS switch cantilever.....	178
Figure 9.3 – Schematic of experimental setup.....	179
Figure 9.4 – Contact resistance verses time at 293 K, 77.4 K, and 5.6 K for the NEU switch.....	182
Figure 9.5 – Contact resistance verses time at 293 K and 77.4 K for the wiSpry switch.....	182
Figure 9.6 – Contact resistance versus time data from a NEU RF MEMS switch and the power law fit.	183
Figure 9.7 – Contact resistance versus time data from a wiSpry RF MEMS switch and the power law fit.	183
Figure 9.8 – Contact resistance versus time as a function of applied current for the NEU switch at 5.6 K.....	185
Figure 9.9 – Contact resistance versus switch voltage for the NEU switch at 5.6 K.....	186
Figure 9.10 – Surface roughness simulation from AFM measurements of roughness of the top contact surface in a RF MEMS switch.	187
Figure 9.11 – Contact resistance verses time for the simulated surface roughness (a) at 293 K, (b) at 77.4 K, and 5.6 K.	190
Figure 9.12 – Real contact area percentage with respect to apparent contact area verses time for the simulated surface roughness at 293 K, 77.4 K, and 5.6 K.	191
Figure 9.13 – Top view of the real contact area for the simulated surface roughness after 60 minutes (a) 293 K (b) 77.4 K and (c) 5.6 K.	191

Figure 9.14 – Contact resistance versus switch voltage for the simulated surface roughness at 5.6K..... 193

Figure A.1 – Wirebonding diagram for wiSpry RF MEMS switch to 40 pin ceramic package..... 210

CHAPTER 1

Introduction to RF MEMS

1.1 RF MEMS and Nanotechnology

In 1959, Feynman gave a lecture at the American Physical Society entitled, *There's Plenty at the Bottom*, in which he considered the ramifications of being able to manipulate individual atoms and the tools needed to do so. Feynman noted that as the tools needed to manipulate the atoms became smaller the relative strength of forces would shift. Mass to surface area ratios would drive forces normally neglected on the macro scale, such as Van der Waals attraction, to become more important while the effects of gravity waned. This scaling of forces is still a prevalent issue in the reliability of MEMS. While his miniaturization idea was not new, his speech did lend credence to the emerging micro and nanotechnology trends.

With the advent of anisotropic Si etching in the late 1960's and early 1970's, Feynman's tools took the form of microelectromechanical systems, or MEMS, which were first introduced in the 1970's. The first RF MEMS switch was introduced in 1991 by Dr. Larry Larson at Hughes Research Lab. The switch was specifically designed for microwave applications^{2,3}. The switch's ability to perform well up to 50 GHz was a significant leap forward over solid-state and mechanical switches (Table 1.1). While the first RF MEMS switch was far from perfect, the devices were attractive on many levels to government

Table 1.1 – Comparison of electrostatic switch performance (Ref. [1], Table 1.2).

Parameter	RF MEMS	PIN	FET
Actuation Voltage (V)	20-80	3-5	3-5
Current (mA)	0	3-20	0
Power consumption ^a (mW)	0.05-0.1	5-100	0.05-0.1
Switching time	1-200 μ s	1-100 ns	1-100 ns
C _{up} (series) (fF)	1-6	40-80	70-140
R _s (Series) (Ω)	0.5-2	2-4	4-6
Cutoff frequency (THz)	20-80	1-4	0.5-2
Isolation (1-10 GHz)	Very high	High	Medium
Isolation (10-40 GHz)	Very high	Medium	Low
Isolation (60-100 GHz)	High	Medium	None
Loss (1-100 GHz) (dB)	0.05-0.2	0.3-1.2	0.4-2.5
Power handling (W)	< 1	< 10	< 10

^a Includes voltage up-converter or drive circuitry

agencies and companies looking to enhance their own RF systems.

This first RF switch was followed by a number of other designs that mostly emanated from defense-oriented companies funded by DARPA and the Air Force in an effort to improve radar and communications systems ⁴. All hope to create a new generation of devices capable of vastly outperforming the current mechanical and semiconductor switching technology; thus laying the foundation for current and future communication systems with enormous potential. Despite the efforts of all the industrial, academic, and government labs, commercialization of RF MEMS switches has lagged market expectations for three decades (particularly so between 2000 and 2003) ⁵. The main reason for this is that a number of design hurdles need to be overcome, especially those dealing with the tribological issues at the switch contacts, before the devices are robust enough to be commercially marketed.

1.2 RF MEMS switch types

RF switches are categorized as either capacitive switches or metal-metal contact switches. Both are comprised of two parts. The electrical section makes contact with the signal transfer lines and modulates the on/off states of the signal. The actuation section moves the electrical section in and out of contact with the transmission lines. Actuation can be lateral or vertical. Actuation forces are generated by several methods, but the most prevalent is electrostatic actuation, where the potential difference between two charged plates produces mechanical movement. Most switches are fabricated using surface micromachining and are compatible with post-CMOS, SiGe, and GaAs integration.

The first commercially practical capacitive switch was designed to operate in a shunt configuration where the switch is placed between the signal line and ground (Fig. 1.1) ^{6,7}. These switches are often referred to as fixed-fixed as both ends of the metal contacting membrane are attached to anchors on the substrate and grounded. For these switches the RF signal is continuously on and is allowed to pass when the switch membrane is in the open state. In the closed state, contact is made between the metal membrane and the dielectric material on the lower actuation electrode. This forms a low impedance path to ground for the

RF signal, and the signal off state is achieved. The RF signal range for capacitive RF MEMS switches is 6GHz to 120 GHz.

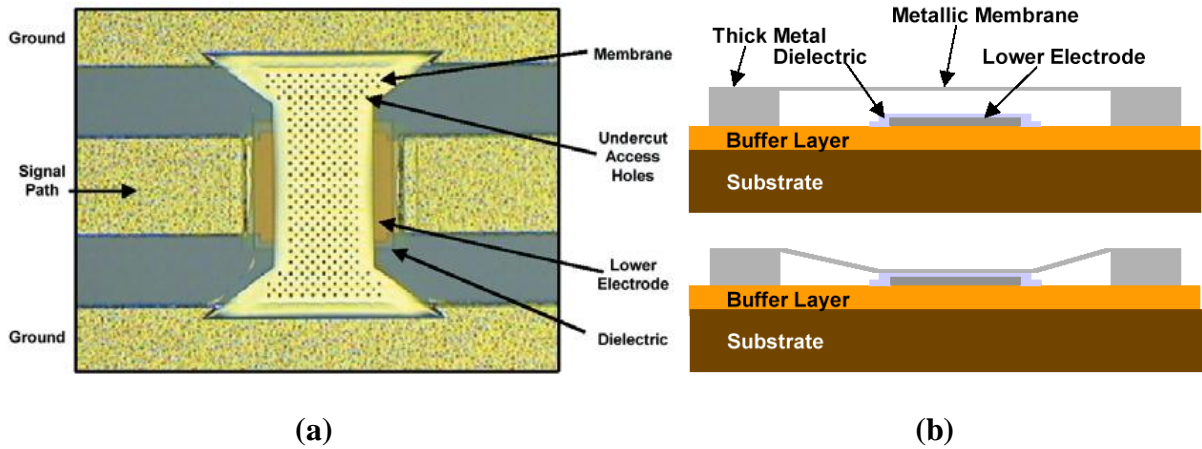


Figure 1.1 – Raytheon capacitive RF MEMS switch (a) top view and (b) schematic cross-section view. In (b) the upper schematic represents the on state and the lower schematic represents the off state. The membrane in (a) and (b) is 120 μm wide by 280 μm . (Ref. [8], Fig. 5)

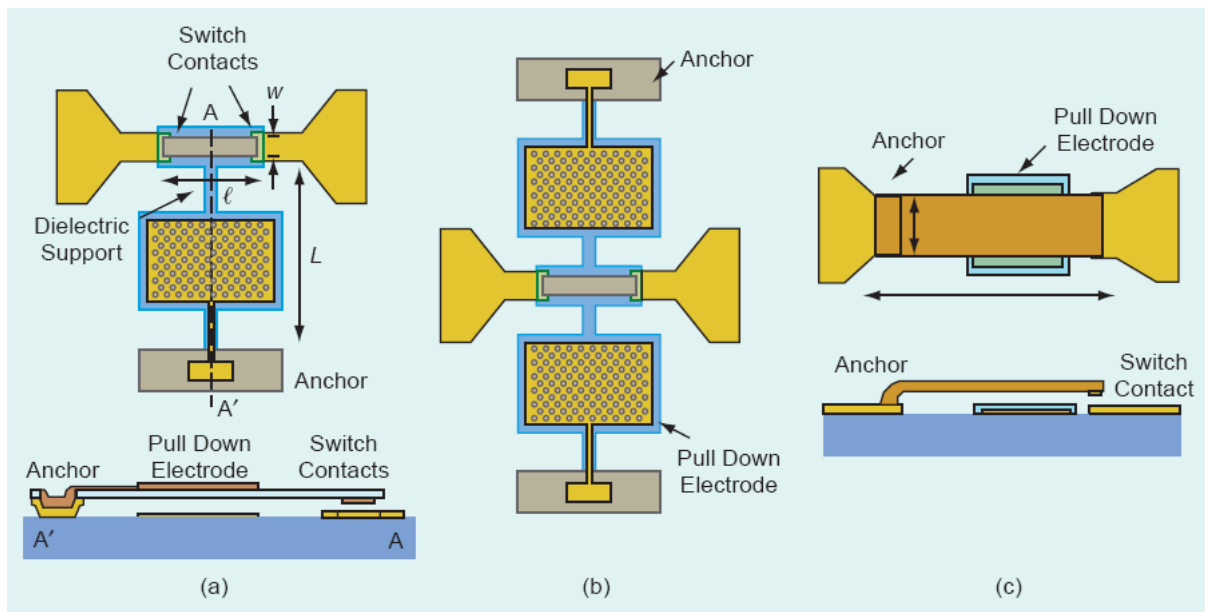


Figure 1.2 – Metal contacting series switch types; a) fixed broadside, b) fixed-fixed broadside, and c) in-line RF MEMS switches. Cantilever length L is generally on the order of 100 μm . (Ref. [9], Fig. 2)

Metal-metal contacting switches are used as series switches (Fig. 1.2). The switch is placed between two transmission lines, and the open and closed states of the switch are used to complete the signal path. Metal contacting switches are generally engineered in two configurations: broadside series and inline series. In the broadside series the switch actuates perpendicular to the transmission line (Fig. 1.2 (a) and (b)). In the closed state, the metal contacting portion of the broadside switch provides the signal path completing the circuit. The non-contact portion of the beam is used for switch actuation and can be configured as a singled fixed end cantilever or a fixed-fixed cantilever. For inline switches the actuation is in the same plane as the transmission line. The signal enters at the anchor or fixed end, travels the length of the cantilever beam and exits to the transmission line through the contacts at the end of the cantilever beam. The signal range for metal contacting series switches is DC to 60 GHz.

The work contained in this thesis uses actuated broadside metal contacting switches provided by wiSpry and inline metal contacting switches provided by RFMD and Northeastern University. All three experimentally used switches are electrostatic actuation designs.

1.3 RF MEMS applications

RF MEMS switches have great upside potential for use in low and medium power applications as replacements for current switching technology and the potential to create highly flexible RF systems. RF MEMS switches are already shipping to or poised to grow into five distinct applications types ¹⁰:

- High value applications – satellites, military tactical radio, military phased array
- Test equipment – RF instrumentation, automated test equipment (ATE)
- Telecom infrastructure – base stations, microwave communications
- Mass applications – mobile phones, consumer electronics, and IT
- Automotive – anti-collision radar, roof antenna

1.4 Metal contacting RF MEMS failure modes

Commercialization of metal contacting RF MEMS switches has been slowed by a number of operational shortcomings limiting their reliability and lifetime. Wear, stiction, arcing, creep, adhesion, nanowire formation, and adsorbed film layers all lead to premature switch failure.

1.4.1 Contact wear

Wear and stiction are the two most prevalent failure modes in MEMS switches. The wear rate, or transfer of material from one contact to another, is highly dependent on the switching mode, cold or hot switching, and the switch's power handling capability. In the case of cold switching, when the dc current or RF signal is applied only after the switch is closed and removed before the switch opens, mechanical wear dominates. Contact damage, pitting, and hardening occur to the metal as the same site is repeatedly hit during cycling ¹¹. Over time the contact area is reduced, causing an increase in resistance. The contact load, which ranges from 10s of μN up to 1 mN, but is typically on the order of $100\mu\text{N}$, is not large enough to create large scale changes in contact area, which would result in large changes in contact resistance.

Reduced contact area constricts current flow and becomes a significant problem under high power conditions (10-100 mW). The current densities and the resultant contact voltage drop across the asperity produce temperatures high enough to soften or melt gold contact asperities, thus making changes to the contact surface topography. Softening or melting gold asperities leads to additional failures such as switch shorting from nanowire formation, and welding, where the switch remains permanently closed ^{12,13,14}. While softening can occur under high current condition in cold-switching applications, the wear associated with softening/melting is most severe under hot switching conditions. During hot switching, the DC signal is continuously on, even during the opening and closing of the switch. As the switch contacts and the lower transmission line pull apart, a voltage transient produces metal arcing at the contact site with temperatures high enough to melt gold asperities ^{15,16}. Significant material transfer can occur during these events ¹⁷.

1.4.2 Stiction

Stiction failures arise when the surface interaction energy at a contact points is greater than the restoring forces used to bring the switch into the equilibrium/open position. Stiction results in RF MEMS switches that stick in the closed position and are unable to open. The adhesive force can come from the capillary force of condensed water at the contact surface or from the molecular van der Waals force ¹⁸.

Capillary forces and humidity have driven many device manufacturers to hermetically package devices and fill the package with an inert gas like nitrogen or argon ¹⁹. Within the scientific community, carefully controlled MEMS reliability testing is done in nitrogen environments or low vacuum. Van der Waals forces arise from the interaction between two clean gold surfaces. Once enough clean surface area is in contact, cold weld adhesion can occur even at low current, low load conditions. At high current conditions, adhesion failures will generally result from hot-welding. Additionally, stiction events can create mechanical wear through material transfer in cases where the surface adhesion is very high ²⁰.

1.4.3 Arcing and field induced material transfer

Transient arc phenomena, or metal phase arcing, has been linked to premature switch failure under hot switching conditions ²¹. Surface roughness and submicron spacing between the signal contact makes arcing possible, even below the transient voltage level required by Paschen's law ²². As the contacts pull apart, current is restricted to rapidly decreasing contact area, causing an increase in contact resistance and temperature at the point of constriction. Local temperatures at the point of constriction can reach the metal boiling point (3080 K for gold). Modeling has shown that even with no current present, switch opening draws nanowires a few atoms thick between the upper and lower contacts ²³. During hot switching, the contact voltage drop across the nanowire is beyond the 0.97 volts required to boil the gold, and the metal bridge is evaporated. Evaporated metal follows the field emission of electrons from the cathode and deposited on the anode. Surface contaminants in the local area are pyrolyzed, creating a nonconductive film over the gold surface ²⁴.

Recent work by Z. Yang at NCSU, reveals that field evaporation, may be the real cause of contact degradation, and not metal phase arc, as most hot-switched MEMS switches are operated in non-arc test conditions ²⁵. Experimental results showed gold contact material transfer followed the direction of the electrical field when open circuit voltages and current loads were well below the minimum arc voltages and minimum arc currents needed for arcing. Field evaporation as the material transfer mechanism was further supported when the directionality of transfer reversed itself with a corresponding change in the field direction. Material transfer directionality is eliminated with an AC field in place of a DC field.

1.4.4 Adsorbed film layers

Adsorbed film layers on the gold contact surface raise the contact resistance and play a critical role in premature switch failure. However, its role in switch failure is not well understood, nor has it been extensively studied. The composition of the film will vary depending on the switch contact material. In the case of metal contacting RF MEMS switches, gold is the contact material of choice, and while it does not oxidize, it still adsorbs hydrocarbons and water to its surface in ambient air conditions. At low current and low contact loads, adsorbed films create an unstable, insulating layer between the gold contacts resulting in unusually high contact resistance, sometimes several orders of magnitude greater than the predicted values. One of the most prevalent failure modes among RF MEMS switches is a sudden, large increase in contact resistance. Large jumps in contact resistance are seen early during hot switching, but may not appear until millions of cold-switching cycles have occurred ^{26,27}.

1.4.5 Creep

Mechanical creep is a significant reliability issue for RF MEMS switches, especially in high power applications ^{28,29}. Creep occurs at two critical regions on the switch, the cantilever beam and the switch contacts. Under high loads or high temperatures, stress in the cantilever can create warping or curvature which moves the cantilever out of plane. This in turn changes the contact force applied to the switch contacts in the closed state and also the

geometry with which the switch contacts attached to the cantilever beam make contact with the lower signal electrodes. Changes in contact force and geometry at the switch contacts will have a significant effect on the contact resistance. In the most severe cases, creep can cause enough cantilever beam deflection that the switch contacts are unable to make contact no matter how much contact force is applied through electrostatic actuation.

Creep at the switch contacts is also a significant issue. The gold asperities composing the switch contacts surface tend to blunt with time or cycling. While blunting can increase contacting surface and lower the contact resistance, the contact material can also become strain hardened, which increases contact resistance. In the cases of prolonged closure, application of high contact loads, or application of high contact voltages creep can generate enough contact area to create an adhesion failure through van der Waals interaction (if the contact area is free of adsorbed films).

1.5 Aims of dissertation

It is clear that RF MEMS switch failure mechanisms are not well understood. After a brief survey of literature, it becomes apparent the failure mechanisms are very convoluted. Many RF MEMS switch failures can now be traced back to tribological factors. The performance and reliability of RF MEMS switches are directly related to the switch contact interface and its degradation over time. A number of physical phenomena, such as plastic deformation, creep, joule heating, nanowire formation, arcing, and adsorbed films at the contact surface combine to create a convoluted set of failure mechanisms. Overcoming these barriers is difficult because the physics underlying these mechanisms is not always well understood or easily applied to MEMS devices. Until the failure mechanisms can be separated and the physics for each understood, RF MEMS devices may continue to fall short of market expectations.

The focus of this thesis is to detangle the physics of contacting RF MEMS switch failure mechanisms and derive the physics associated with how each mechanism contributes to premature failure of the device. By understanding the failure modes, a new set of design rules can be implemented which increase the robustness of RF MEMS switches.

This thesis focuses on carefully manipulating environmental (temperature, atmosphere, pressure) and operational conditions (current, contact voltage, contact force) to isolate each failure mechanism and matching experimental data with theoretical understanding to produce a detailed understanding of metal contacting RF MEMS physics. The following subjects are covered as part of this thesis:

- *RF MEMS Closure Physics* – Cantilever beam physics as related to atmospheric pressure is relatively untouched by literature, but has a significant effect on device performance. Pressure can have both adverse and positive impacts on the contact physics. In particular pressure dependent switch bounce is explored.
- *Cycling Effects on Contact Physics* – Number of cycles to failure is the metric of choice in literature to quantify device reliability, however little is known about the failure mode associated with adsorbed film layers and prolonged cold switch cycling. A comparison of contact resistance in the cold and hot switched regimes
- *Atmospheric Effects on Contact Physics* – Literature has shown that atmospheric conditions can have a significant impact on device longevity. The atmospheric work in this section correlates atmospheric conditions to the short term effects on contact physics and contact resistance of a RF MEMS switch.
- *Temperature Effects on Contact Physics* – Nearly all literature on temperature dependence in MEMS switches focuses on contact mechanics. A series of work was presented by Jensen *et al.* describing contact physics for temperatures ranging from room temperature to 400 K. The work presented in this thesis section is a complementary set of temperature data ranging from 5.6 K to room temperature.
- *Time Dependence of Contact Physics* – Time dependent contact resistance data can be found in a number of experimental publications, but the underlying impact of this phenomenon is not explored in depth. Contact physics of creep and adsorbed film presence are correlated to time and temperature dependent contact resistance.

1.6 References

- ¹ G. M. Rebeiz, RF MEMS Theory, design, and technology, New Jersey: John Wiley & Sons, Inc. 2003, pp. 5.
- ² G. M. Rebeiz, RF MEMS Theory, design, and technology, New Jersey: John Wiley & Sons, Inc. 2003
- ³ L. E. Larson *et al*, “Micromachined microwave actuator (MIMAC) technology-a new tuning approach for microwave integrated circuits,” *Microwave and Millimeter-Wave Monolithic Circuits Symposium Digest. (Boston, MA)* pp 27-30.
- ⁴ http://www.memsinvestorjournal.com/2006/10/rf_mems_a_brief.html
- ⁵ <http://electronicdesign.com/Articles/ArticleID/15220/15220.html>
- ⁶ C.L. Goldsmith, J. Randall, S. Eshelman, T.H. Lin, D. Denniston, S. Chen, and B. Norvell, “Characteristics of micromachined switches at microwave frequencies,” IEEE Int. Microwave Symp. Dig., pp. 1141-1144, June 1996.
- ⁷ C.L. Goldsmith, Z. Yao, S. Eshelman, and D. Denniston, “Performance of low-loss RF MEMS capacitive switches,” IEEE Microwave Guided Wave Lett., vol. 8, pp. 269-271, Aug. 1998.
- ⁸ J.J. Yao, “RF MEMS from a device perspective,” *J. Micromech. Microeng.*, vol. 10, pp.R9–R38, 2000.
- ⁹ G. M. Rebeiz and J. Muldavin, “RF MEMS Switches and Switch Circuits,” IEEE Microwave Magazine, pp. 59-71, December 2001.
- ¹⁰ http://www.i-micronews.com/upload/Rapports/rf_brochure.pdf
- ¹¹ G. M. Rebeiz, RF MEMS Theory, design, and technology, New Jersey: John Wiley

& Sons, Inc. 2003

¹² Jensen, B.D.; Zhongde Wang; Chow, L.; Saitou, K.; Kurabayashi, K.; Volakis, J.L., "Integrated electrothermal modeling of RF MEMS switches for improved power handling capability," *Wireless Communication Technology, 2003. IEEE Topical Conference on* , vol., no., pp. 10-11, 15-17 Oct. 2003

¹³ L Almeida, R Ramadoss, R Jackson, K Ishikawa and Q Yu, "Study of the electrical contact resistance of multi-contact MEMS relays fabricated using the MetalMUMPs process," *J. Micromech. Microeng.* 16 (2006) 1189–1194

¹⁴ Hyouk Kwon; Dong-June Choi; Jae-Hyoung Park; Hee-Chul Lee; Yong-Hee Park; Yong-Dae Kim; Hyo-Jin Nam; Young-Chang Joo; Jong-Uk Bu, "Contact materials and reliability for high power RF-MEMS switches," *Micro Electro Mechanical Systems, 2007. MEMS. IEEE 20th International Conference on* , vol., no., pp.231-234, 21-25 Jan. 2007

¹⁵ Dickrell, D.J., III; Dugger, M.T., "The effects of surface contamination on resistance degradation of hot-switched low-force MEMS electrical contacts," *Electrical Contacts, 2005. Proceedings of the Fifty-First IEEE Holm Conference on*, pp. 255-258, 26-28 Sept. 2005

¹⁶ Dickrell, D.J.; Dugger, M.T., "Electrical Contact Resistance Degradation of a Hot-Switched Simulated Metal MEMS Contact," *Components and Packaging Technologies, IEEE Transactions*, vol.30, no.1, pp.75-80, March 2007.

¹⁷ Z. Yang, "Contact Material Optimization and Contact Physics in Metal-contact Microelectromechanical Systems (MEMS) Switches," Ph.D. dissertation, North Carolina State University, 2008.

-
- ¹⁸ van Spengen, W.M.; Puers, R.; De Wolf, I., "The prediction of stiction failures in MEMS," *Device and Materials Reliability, IEEE Transactions on* , vol.3, no.4, pp. 167-172, Dec. 2003
- ¹⁹ Margomenos, A.; Katehi, L.P.B., "Fabrication and accelerated hermeticity testing of an on-wafer package for RF MEMS," *Microwave Theory and Techniques, IEEE Transactions on* , vol.52, no.6, pp. 1626-1636, June 2004
- ²⁰ G. G. Adams and M. Nosonovshy, "Contact modeling – forces," *Tribology International*, 33: pp. 431-442 (2000).
- ²¹ E. J. J. Kruglick and K. S. J. Pister, "Lateral MEMS microcontact consideration," *J. Microelectromechanical Syst.* vol. 8, pp. 264-271, 1999.
- ²² P. G. Slade and E. D. Taylor, "Electrical breakdown in atmospheric air between closely spaced (0.2 μ m–40 μ m) electrical contacts," *IEEE Trans. Compon. Packag. Technol.*, vol. 25, no. 3, pp. 245–250, Sep. 2002.
- ²³ Private communication with W. Crill, D. Irving, and D. Brenner.
- ²⁴ Dickrell, D.J.; Dugger, M.T., "Electrical Contact Resistance Degradation of a Hot-Switched Simulated Metal MEMS Contact," *Components and Packaging Technologies, IEEE Transactions*, vol.30, no.1, pp.75-80, March 2007.
- ²⁵ Z. Yang, "Contact Material Optimization and Contact Physics in Metal-contact Microelectromechanical Systems (MEMS) Switches," Ph.D. dissertation, North Carolina State University, 2008.
- ²⁶ Z. Yang, "Contact Material Optimization and Contact Physics in Metal-contact Microelectromechanical Systems (MEMS) Switches," Ph.D. dissertation, North Carolina State

University, 2008.

²⁷ Dickrell, D.J.; Dugger, M.T., "Electrical Contact Resistance Degradation of a Hot-Switched Simulated Metal MEMS Contact," *Components and Packaging Technologies, IEEE Transactions*, vol.30, no.1, pp.75-80, March 2007.

²⁸ R. Modlinski, A. Witvrouw, P. Ratchev, R. Puers, J.M.J. den Toonder, and I. De Wolf, "Creep characterization of Al alloy thin films for use in MEMS applications," *Microelectronic Engineering*, **76**, pp.272-278, 2004.

²⁹ G. Gregori and D.R. Clarke, "Mechanical creep as life-limiting factor of radio frequency microswitches," *Appl. Phys. Lett.*, **87**, 2005

CHAPTER 2

RF MEMS Contact Physics Literature Review

2.1 Overview

Since the first viable RF MEMS switch was introduced in 1991 a large and growing body of literature has focused on their reliability ¹. Initial publications focused on switch design and robustness, as measured by number of cycles to failure. It was soon evident that switch reliability was far short of market demands of 10^{13} cycles before failure. At present, the longest lasting switches fall short of 10^{10} cycles. Recognizing that a more fundamental understanding was required, researchers moved toward a focus on failure modes. More recent publications focus on surface physics with concentrations on contact materials, surface morphology, operational parameters (current, contact load), and adsorbed film layers. However, the physics of switch failure is still not well understood, and environmental effects for the most part have not been explored.

This chapter presents the findings of key publications studying RF MEMS switch failure modes. The widely varying behavior seen in the literature is difficult to explain because the results presented are often a combination of multiple failure mechanisms. The reader should be cognizant as he/she progresses through the chapter that although the findings are presented in topical sections, the underlying physics overlaps these sections. The goal of this thesis is not to report on a failure mechanism of an RF MEMS switch, but to isolate it, measure its characteristic behavior, and tie it to the physics driving that behavior through correlation of experimental data and theoretical modeling. This is achieved by carefully regulating the switch's operating environment, something that receives secondary consideration in most publications.

2.2 Contact physics – contact materials and surface conditions

2.2.1 Contact materials

Contact material plays a critical role in switch performance. Its selection needs to take into account many factors including contact resistance, stiction behavior, wear rates, contact force, required lifetime, and switch operational environment and packaging ². Typically gold is chosen for the contact material. Gold has a number of advantageous

properties that make it a desirable choice: (1) low resistivity, superior conductivity, (2) easily deposited, (3) easily deformed, (4) noble natured, (5) compatible with MMICs (Monolithic Microwave Integrated Circuits), and (6) a high melting point ^{3,4,5}.

Gold may be an obvious choice for RF MEMS switch fabrication, but it also creates limitations in switch performance. While gold is noble in nature and does not oxidize, layers of hydrocarbons are known to form on its surface. The adsorbed film layers increase contact resistance. The ability to easily deform gold leads to several failure mechanisms, such as creep in the cantilever and at the contacts. Under heavy contact loads, asperity deformation can create adhesion failures. Lateral movement during contact will wear gold contacts, or transfer material to harder surfaces.

To overcome the adhesion and wear issues with gold, researchers have turned to alternative metals and gold alloys for contact materials. These include aluminum (Al), doped polysilicon, palladium (Pd), platinum (Pt), nickel (Ni), gold-nickel alloys, and rhodium (Rh) ⁶. Harder metals will alleviate the stiction and wear issues, but often come at the price of higher contact resistance.

Schimkat studied contact resistance as a function of contact force for AuNi (5%) and Rh to determine their viability as possible replacements for Au contacts ⁷. His experiment used half-sphere simulated contacts pressed together with forces up to 10mN. Contact forces were recorded for the amount of load required to make stable contact resistance, F_{min} , and the force required to overcome contact adhesion and break electrical contact, F_{adh} . Results showed that AuNi(5%) and Rh required less force to break contact than Au, indicating that adhesion was lower (Table 2.1). However, the force required to make stable contact resistance was also greater for AuNi(5%) and Rh than that of Au. Additionally, the contact resistance of the harder metals was significantly higher than gold.

Table 2.1 – Material dependent contact resistance and adhesion force.

Parameter	Au	AuNi (5%)	Rh	unit
F_{min}	< 0.1	0.3	0.6	mN
R (F_{min})	< 30	< 100	< 1000	m Ω
F_{adh}	2.7	0.3	< 0.1	mN

Couto *et al.* studied contact resistances and lifetimes for bi-metallic, binary, tertiary gold alloys ^{8,9}. The study compared pure gold to AuPt, AuPd, AuAg, and AuPtCu. Bi-metallic and binary alloys resulted in a cycle lifetime increase over gold of 3.3 and 2.6 times, respectively. The tertiary alloys increased lifetime by 6.5 times over that of pure gold contacts. In all cases the substantial lifetime increases were achieved at the expense of contact resistance. The initial contact resistance for sputtered gold was 0.2 Ω , while the alloys ranged from 1.2 to 1.8 Ω .

Z. Yang *et al.* performed an in depth comparison of pure gold and gold-nickel alloy contacts ¹¹. A test facility was designed where the cantilever from a wiSpry RF MEMS switch was glued to an AFM tip carrier and actuated against lower electrodes. Lower electrode composition ranged from pure Au to an AuNi (20%) alloy. The contacts were hot-switched until an abrupt, large jump in contact resistance indicated failure. The data provided a correlation between material properties (micro-hardness, resistivity, surface topology, and surface microstructure) and contact performance. As with previous alloy

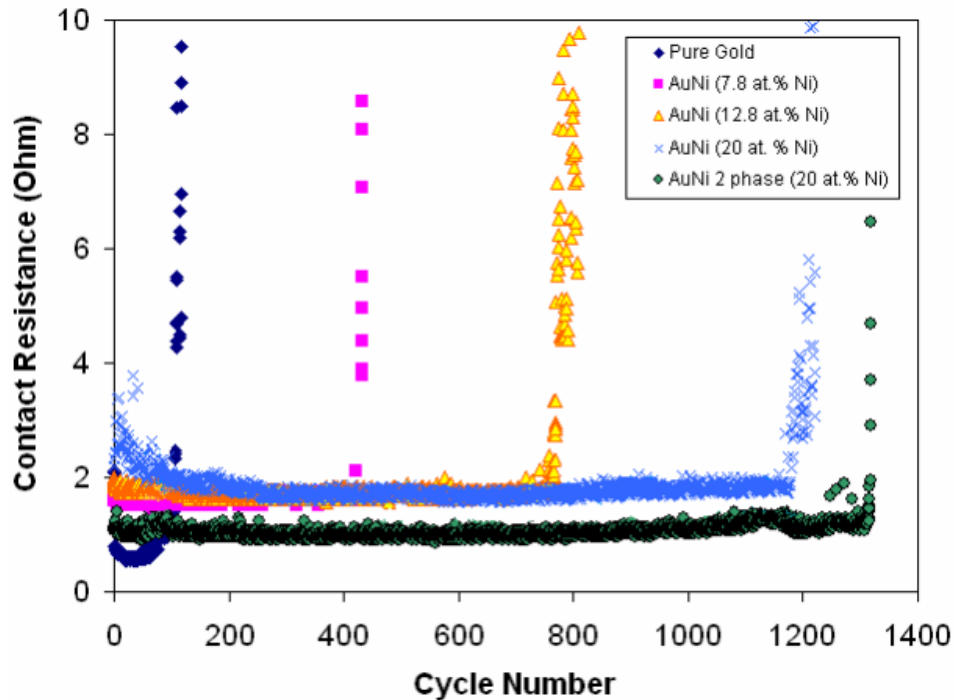


Figure 2.1 – Contact resistance versus cycle number for pure gold and Au-Ni alloys under high current, hot-switching condition. (Ref. [10], Ch. 5, Fig. 11)

studies, increased switch reliability was linked with increased contact hardness (Fig. 2.1). The data also showed that surface roughness, in addition to material hardness, must be maintained below a critical level to avoid increased contact resistance. A two-phase Au-Ni alloy (previously not covered by other contact material investigations) significantly improved contact performance, and the presence of Ni_2O_3 oxide correlated with increased switch lifetime. Experimental results indicate that both material surface properties and material volume must be a consideration in switch contact optimization.

2.2.2 Contact models

Surface roughness and asperity behavior are critical factors that affect contact behavior at scales ranging from the nano to the micro in microelectromechanical, electronic, and photonic devices. Large surface to volume ratios in MEMS devices underscore that it is essential to understand how asperities behave in contact devices. The complex physical interactions between thermo-mechanical deformation, current flow, and heating at the contact, have made it extremely difficult to obtain accurate predictions of contact behavior.

Various analytical and numerical methods have been employed to study the contact physics of ideally smooth surfaces¹². Hertzian contact theory was one of the first methods to calculate the contact area between two interacting bodies¹³. The model assumed completely elastic contact and neglected surface roughness effects. Despite neglecting the importance of surface area, Hertzian contact is still used because of its simplicity.

Holm followed with a completely plastic model where stresses at the local contact sites may be much higher than the overall stress, allowing for plastic deformation¹⁴. The fully plastic approach resolves contact area through the use of material hardness and normal load at the contacts. Contact geometry does not play a part in the contact area calculation. The Holm theory is widely accepted, but like Hertzian contact, it does not take full account of the surface topography.

Since surface topographies are critical in MEMS devices, some probabilistic models have been proposed to account for asperity height variations¹⁵. Greenwood and Williamson's (GW) 1966 theory on contact proposed a statistically-based asperity contact

model. It assumed that all contacts were spherical with the same radius of curvature, there was no interaction between asperities, and the heights of the asperities were normally distributed. Contact area and the supported load are computed by knowing the material composition, height distribution, and size of surface asperities.

Several refinements to the GW model have worked to remove the limiting assumption by incorporating anisotropically, or non-normally, distributed asperities and changing the asperity shape from spherical to paraboloidal ^{16,17}. Subsequent studies McCool and Bush showed only a small deviation from the original GW model, confirming that its use as a multi-asperity approach to contact area computation was a good approximation so long as the asperity height distribution is valid for the micro-contact it is modeling.

While the Hertz model and GW model cover elastic and plastic contact modeling, there are instances where some contact area is plastically deformed but is encapsulated by elastically deformed material. In these cases, the Chang, Etison, and Bogy (CEB) model may be used ¹⁸. The CEB model was applied to multi-asperity rough surface modeling by Majumder *et al* ¹⁹.

The Hertzian, GW, and CEB models have provided the basis for contact modeling for the past twenty years, however for MEMS applications, the assumption that the mathematics of the statistically-based contact models correlates well with the actual topography of the contact surface can be a weak one. In cases where a large contact force is applied, allowing a large number of asperities to come into contact, the GW model is still valid. At lower contact loads, fewer asperities are forced into contact, and the good correlation between the mathematical distribution functions and the actual surface topography diverges. In the case of low force applications, as with most RF MEMS switches, an alternative surface area calculation is needed.

The most feasible approach to providing the correct topography for contact modeling is through using directly acquired three-dimensional surface data from surface microscopy. The topographical data can be provided through stylus profilometry, optical profilometry, or atomic force microscopy (AFM). Each provides the surface height data required to compute the parameters needed for surface modeling or to directly compute the surface area. Dickrell

et al. used measured device surface topography to directly calculate the interfacial contact area²⁰. The switch surface is divided into an array of volume pixels, or voxels. Each voxel is given a height above the reference plane computed from measured surface heights (Fig. 2.2). Two contact surfaces, both modeled with this treatment are brought together and a contact area prediction is made. The voxel surface model allows for prediction in contact area shape, which was previously not attainable with other statistically base models.

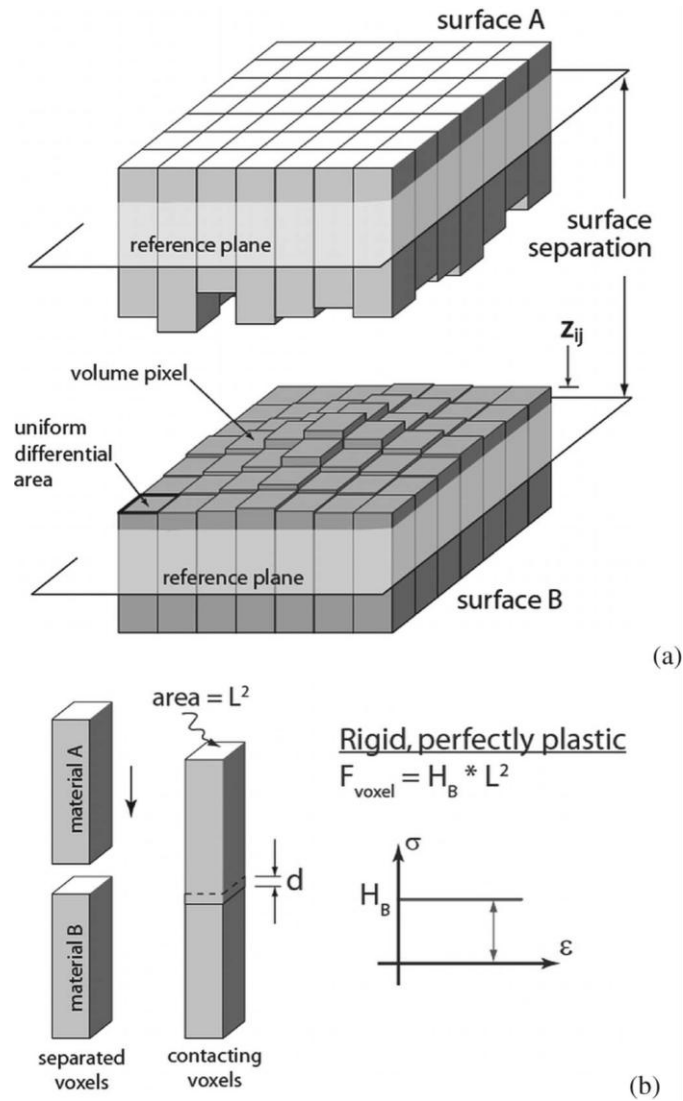


Figure 2.2 – Volume pixel, or voxel, surface area model used by Dickrell *et al.* to directly calculate surface area from the measured surface topography of a MEMS device. (Ref. [20], Fig. 2)

Rezvanian *et al.* used AFM roughness data from a wiSpry RF MEMS switch to build an accurate surface representation for contact area modeling through fractal geometry²¹. The random and multiscale nature of the surface roughness can be described by fractal geometry. The use of fractals to represent the surface roughness for contact analyses of MEMS devices has been used to relate contact parameters, such as the real area of contact, contact pressure, and contact resistance^{22,23,24,25,26,27}. Following the asperity-based model of Greenwood and Williamson, the asperities are dealt with individually; however, the deformation behavior of a contact asperity is influenced by other contact asperities, in that the share of the total applied load for each individual contact asperity will be determined by the set of all asperities that are in contact. Rezvanian *et al.*'s model predicted thermomechanical asperity deformations of contacting surfaces as a function of time.

Regardless of the contact model used, the end result is the same: to determine the real contact area. The real contact area is an integral part of the models used to calculate constriction resistance for micro-contacts. Validated modeling methods can provide MEMS switch designers with insights on how the interrelated effects of the contact resistance, the surface roughness of the contact surfaces, and the contact pressure evolve. With a firm understanding of contact physics in hand, guidelines can be formulated and incorporated in the design and fabrication process to effectively size critical components and forces to provide stable contact resistance for significantly improved device durability and performance.

2.2.3 Constriction resistance

When two rough surfaces are brought in contact, the contact is made at a finite number of points where asperities on both sides touch (Fig. 2.3). Electrical current is restricted to flowing through these contacting asperities. The electrical resistance felt by the electrons moving through the spatially restricted areas is called constriction resistance. The amount of resistance is determined by the way electrons are transported through the asperities.

There are three electron transport mechanisms that occur on the switch contact scale: diffusive transport, ballistic transport, and quasi-ballistic transport. The type of transport is determined by the mean free path of electrons in the contact material, λ , and the asperity contact radius, a (Fig. 2.4). In the case of RF MEMS switch contacts, asperity dimensions are on the order of the mean free path of electrons in gold, which is approximately 38 nm²⁹. Diffusive transport occurs when the electron mean free path is much smaller than the asperity radius ($\lambda \ll a$). Ballistic transport occurs when the electron mean free path is much greater than the asperity radius ($\lambda \gg a$). Quasi-ballistic transport occurs when the electron mean free

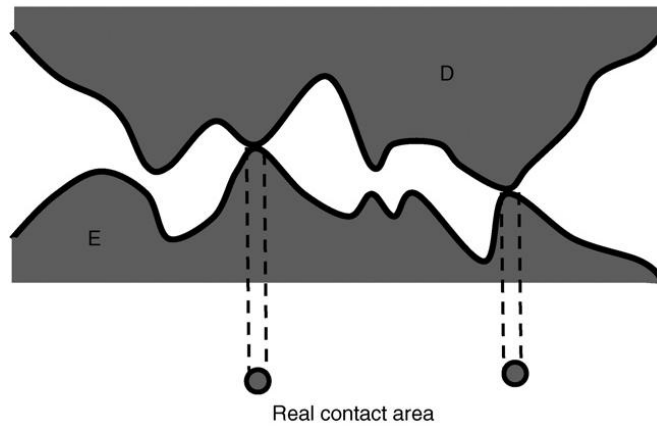


Figure 2.3 – Schematic of the contact asperities and the real contact area established when two rough surfaces touch.

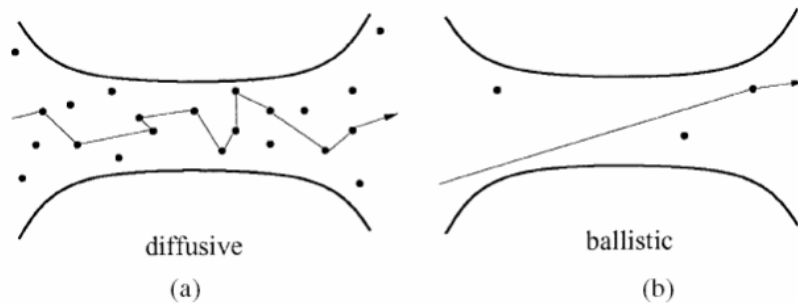


Figure 2.4 – Illustration of (a) diffusive electron transport, or Maxwell resistance, and (b) ballistic electron transport, or Sharvin resistance. (Ref. [28], Fig. 13)

path and asperity radius are nearly equivalent ($\lambda \sim a$).

The constriction resistance, R_C , of an asperity with radius a is ^{30,31}:

$$R_C = f\left(\frac{\lambda}{a}\right)R_M + R_S = \frac{1+0.83(\lambda/a)}{1+1.33(\lambda/a)} \frac{\rho}{2a} + \frac{4\rho\lambda}{3\pi a^2}, \quad (2.1)$$

where ρ is the electrical resistivity and λ is the electron mean free path. R_M is the Maxwell resistance (diffusive electron transport) due to lattice scattering and R_S is the Sharvin resistance (ballistic electron transport) due to boundary scattering. The Maxwell term is representative of the resistance found when the contact spot size is much greater than the mean free path of the electrons. The Sharvin term contributes to the overall contact resistance when the contact spot size is much smaller than the mean free path and the electrons are ballistically projected through the asperities without any scattering. The scaling factor $f(\lambda/a)$, or Knudsen number, accounts for the transition between resistance regimes. It has a maximum value of 1 as $a \gg \lambda$ and a minimum value of 0.624 as $a \ll \lambda$.

The constriction resistance can range between an upper and lower limit depending on how the real contact area is represented. The lower limit assumes that multiple asperities are in contact and that the contact spots do not interact. They can be represented as a number of parallel resistance points. The lower constriction resistance limit, R_L , can be approximated as:

$$\frac{1}{R_L} = \sum_{i=1}^N \frac{1}{R_{Ci}}, \quad (2.2)$$

where N is the number of asperities in contact, and R_{Ci} is the constriction resistance of the i^{th} contact spot. The upper limit for the constriction resistance is set by approximating the area of all individual asperity contacts with a single large asperity of equal area. The radius of the single asperity is a_{eff} and the upper limit, R_U , is:

$$R_U = f\left(\frac{\lambda}{a}\right) \frac{\rho}{2a_{\text{eff}}} + \frac{4\rho\lambda}{3\pi a_{\text{eff}}^2}. \quad (2.3)$$

The constriction resistance value from (2.1) is an integral part of the asperity-heating model, which relates the contact voltage, V_c , to the contact spot temperature, T_c . The contact spot temperature can be stated as:

$$T_c = \sqrt{\frac{f(\lambda/a)R_M}{4LR_c} V_c^2 + T_o^2}, \quad (2.4)$$

where $L = 2.45 \times 10^{-8} \text{ W}\cdot\Omega/\text{K}^2$ is the Lorentz constant and T_o is the ambient temperature³². It is important to note that the asperity-heating model accounts for the size of the contact spots and the increased boundary scattering contributions due to the small spot size. Additionally it eliminates an overestimation of contact spot temperature by assuming only the Maxwell term leads to contact heating with no contribution from the boundary scattering term³³.

A note of caution should be interjected at this point. Constriction resistance is often interchangeably used with the term contact resistance, but these values are distinctly different. Constriction resistance is the resistance at the point of contact due to the small contacting area between asperities. Contact resistance can include resistance contributions from a number of additional sources such as adsorbed films on the contact surfaces, device transmission lines, wirebonds connecting the device with packaging, and wires and connections in the test apparatus. A literature search will reveal that most experiments measure contact resistance and erroneously equate it to constriction resistance, and in nearly every case the contact resistance is orders of magnitude greater than the constriction resistance. Contact resistance will approach constriction resistance values in cases where four point probe techniques are used near the point of contact and high contact load and currents are used to remove adsorbed film layers from the contacts to create pure ohmic (metal to metal) contact. A setup like this was used by Z. Yang, and measured contact resistance values were on the order of the predicted constriction resistance values³⁴.

2.3 Impact of operational parameters

2.3.1 Contact load

Contact load, or contact force, is the force applied on the asperities when the switch is actuated to the closed position. Most MEMS switching devices are low contact force and have contact loads of 80 to 300 μN . In cases where the contact force is not known it can be

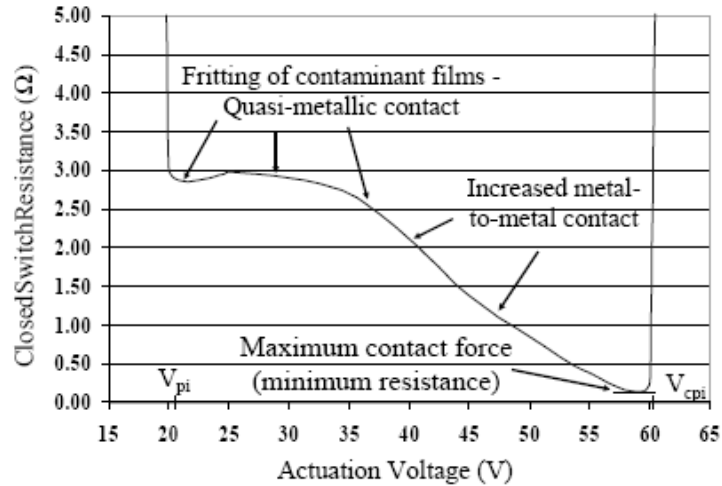


Figure 2.5 – Contact resistance as a function of contact load. First contact is made at V_{pi} , and resistance drops as adsorbed films and surface contaminants are removed. At V_{cpi} the cantilever collapses and contact is broken. (Ref. [35], Fig. 8)

inferred by the amount of actuation voltage, or the voltage needed to bring the switch into the closed position. The amount of voltage needed to make first contact at the switch contacts is referred to as the pull-in voltage. As more actuation is applied beyond the pull-in voltage, more contact force is applied to the switch contacts.

Contact load has a significant effect on the constriction and contact resistances [36,37,38,39,40,41,42,43,44,45](#). At first contact, the contact resistance is high and unstable ([Fig. 2.5](#)). The application of additional contact force will lower the contact resistance through creation of more contact area as the load deforms the contact asperities. Electrons traveling through the constriction must also quantum mechanically tunnel through adsorbed film layers between the asperities. Increasing contact load decreases the adsorbed film thickness and lowers the contact resistance [46,47](#). Continuing to apply additional contact force once stable contact resistance is achieved will not appreciably change the contact resistance. Applying too much contact load will cause the cantilever to buckle and switch contact to be lost.

Large contact loads can be detrimental to the switch cantilever and contacts. Large loads will create creep in both the cantilever and the contacts. Cantilever creep results in irreversible distortion of the cantilever beam. The distortion changes the contact geometry,

which will affect the contact load and area. Non-normal, or non-perpendicular, contact will result in additional wear to the contact area. In extreme cases, cantilever beam warping will cause the two parallel plates used for actuation, one attached to the cantilever beam and one directly underneath, to come into contact. This shorts the switch into a closed position, rendering it inoperable, unless mechanically opened by a probe. At high actuation voltages, the amount of current drawn through the circuit when the actuation plates touch is enough to evaporate the gold transmission lines in the circuit.

In the case of the switch contacts, increased contact load will increase the likelihood of a stiction failure as asperity deformation and creep increase the total contact area. The force of adhesion grows with the amount of contact area. This problem is compounded by the use of high currents, which accelerates the deformation process. Once the adhesion force at the contacts is greater than the restoring force of the cantilever beam, the switch will weld shut. The only means of opening the switch is mechanically with a probe.

Application of the contact load also plays a role in switch reliability^{48,49}. The adhesive force resisting switch separation is directly related to the maximum contact force. The force of impact at closure can be several times greater than the static force applied while the switch is closed. If the contact force produces elastic deformation, then the unloading will be elastic, and the adhesion force will be constant. However, plastic deformation is common in MEMS switch contacts, especially at the force levels present at contact closure. If plastic deformation occurs during loading, the unloading will have two possible separation modes, ductile or brittle. The adhesion force for plastic deformation is dependent on the maximum contact force. Therefore, higher contact forces lead to higher adhesion forces, increasing the likelihood of a stiction failure. Additionally, ductile separation occurs below the interface rather than at it, increasing the probability of material transfer.

Decreasing the adhesion force of the switch contacts can be solved by several methods. Increasing contact material hardness results in less plastic deformation during loading and smaller adhesion forces during unloading. An alternative solution is to decrease the force with which the contacts strike the drain, or lower electrodes. This is achieved by tailoring an actuation pulse that slows the cantilever tip as it approaches contact or by

increasing the viscous damping of the switch. Increasing cantilever cross-section area, decreasing the gap between the cantilever and substrate, or increasing the ambient pressure increases damping^{50,51}.

2.3.2 Current

Metal contacting switches have a large and complex set of failure mechanisms driven by the current level. Low current (1 mW) failures include pitting and hardening of the contact surface and buildup of adsorbed films and contaminants in the contact region.

The impact of current at medium- to high-power levels is not well understood⁵². Increasing the current by 10 mA will increase temperature at the contacts 10-30°C, and increasing the current by 200-500 mA will increase the temperature at the contacts by hundreds of degrees. At high-power (>100 mW) a positive feedback mechanism occurs. Increasing the temperature at the contact will result in increased contact resistance and in turn greater power dissipation at the contact site. The increased power dissipation increases the local temperature, but also causes the contact area to increase, resulting in lower contact resistance. The lower contact resistance in turn lowers the power dissipation. Over time the contact tends to maintain temperature and exhibit stable thermal behavior. At the high-power levels switch failure is a result of increased temperature at the contacts and high current densities, which lead to material transfer.

Patton and Zabinski performed extensive testing with simulated micro-contacts focusing on the effects of current on switch reliability and found asperity creep, slightly higher contact resistance, switching induced adhesion, and switch bouncing were prevalent at low current⁵³. At high current, asperity melting, near zero adhesion, poor durability, and switch shorting from nanowire formation were seen (Fig. 2.6). Z. Yang's work at high currents found that field emission could be the cause of material transfer⁵⁴.

Failures at medium-power (10-100 mW) are more difficult to explain. Experimental results for low contact force switches show that the number of cycles before failure decreased with a 30-100 mA increase in current. The small increase in current results in a small increase in asperity temperature, but nothing like the temperatures that cause failure and

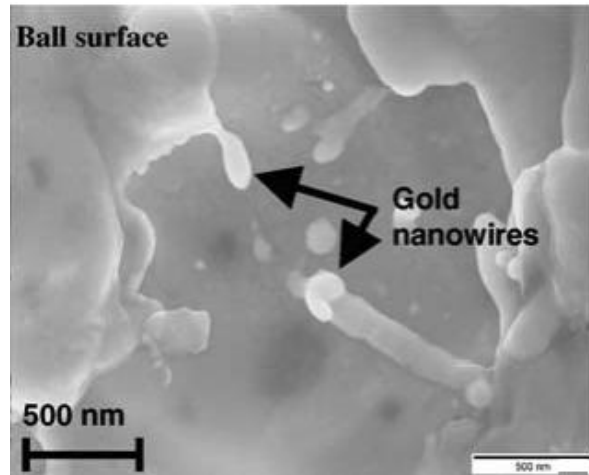


Figure 2.6 – Nanowire formation on MEMS switch contact surface. Patton and Zabinsky have shown that nanowire formation at high temperatures roughens the surface and decreases surface adhesion. (Ref. [55], Fig. 13)

material transfer at high-power. Rebeiz suspects the failures could be due to two mechanisms, either increased current density in the asperities or the actual contact area is much smaller than estimated, leading to high temperatures.

2.4 Adsorbed film effects

Citing adsorbed film effects in MEMS contact research as a reason for elevated contact resistance is ubiquitous. The resistance added by adsorbed films is orders of magnitude higher than the constriction resistance, and therefore dominates the contact resistance measurement⁵⁶. The adsorbed films have been estimated to range in thickness from 10 to 40 Angstroms^{57,58,59}. They have been observed to increase the contact resistance for contacting metals other than gold, including ruthenium, rhodium, and platinum⁶⁰. Adsorbed films are particularly problematic for MEMS switches because the contact loads and electrical currents used in normal operation are ineffective in removing them⁶¹.

2.4.1 Origin

While the effects of adsorbed film layers and contaminants are often cited in the literature, they are rarely studied. Adsorbed films are proposed to originate from several sources, including adsorption of organic molecules to the contact surface when exposed to atmosphere, residue from the cleaning and etching process, and pyrolyzed organic materials during arcing events ^{62,63,64}.

Koidl *et al.* performed an in-depth study to quantify the critical concentration of organic vapor needed to increase the contact resistance of a simulated MEMS switch with Ag, Au, and Pd contacts ⁶⁶. The switches were tested in a controlled atmosphere where the concentration of organic vapor was increased until the contact resistance increased (Fig. 2.7). The study found that a higher concentration of aliphatic, or linear, carbon chains was required to increase contact resistance when compared to vapors composed of aromatic rings. Additionally, shorter carbon chains, such as pentane, required a higher concentration of vapor to increase the contact resistance when compared to longer chains. The carbon type and chain lengths affected all contact materials. Terminating active groups such as amino, aldehyde, and ester groups were found to only affect gold contact materials. Amino groups

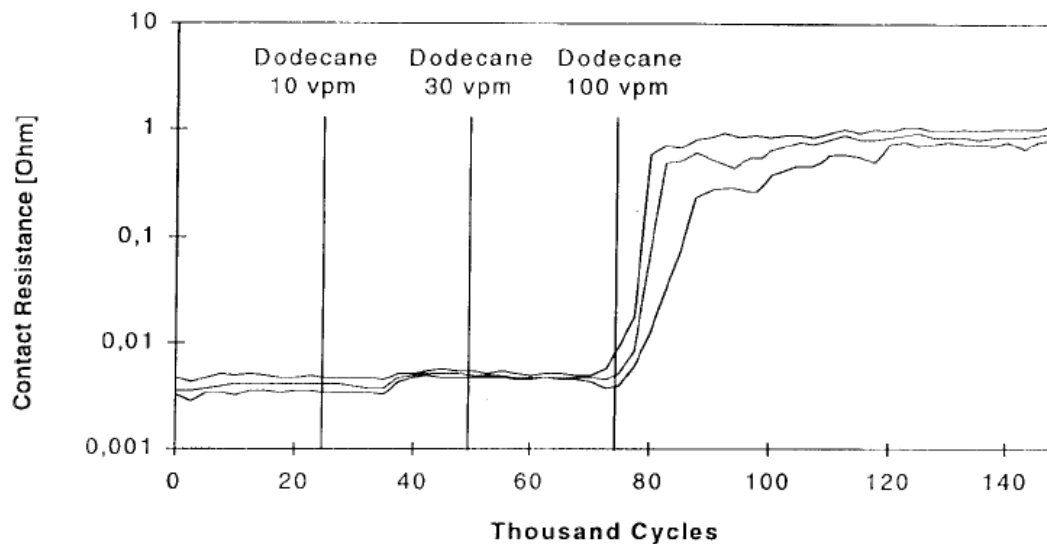


Figure 2.7 – Increase in contact resistance after a critical concentration of 100 vpm (=ppm volume) of dodecane is added to the atmosphere around a MEMS switch. (Ref. [65], Fig. 4)

increased the vapor concentration needed to change the contact resistance while ester groups decreased the vapor concentration required for the change. Aldehyde groups lowered the critical concentration for Pd. Humidity was found to increase the vapor concentration needed to increase the contact resistance. Gas adsorption from the atmosphere to the contact surface is further evidenced by an increase in contact resistance as a function of dwell time ⁶⁷.

2.4.2 Physical properties

Tringe *et al.* explicitly studied the adsorbed surface layers while using an IFM scanning force-probe technique to examine single asperity contact ⁶⁹. Attractive and repulsive forces were measured as an electrochemically-sharpened parabolic tungsten tip sputtered with 50 nm of gold was brought into contact with an electroplated gold surface. The maximum contact load was 36 μN with currents of 0.01, 0.1, and 1 mA. Data taken in nitrogen and air showed attractive forces on the tip during the approach, indicating a 5 nm

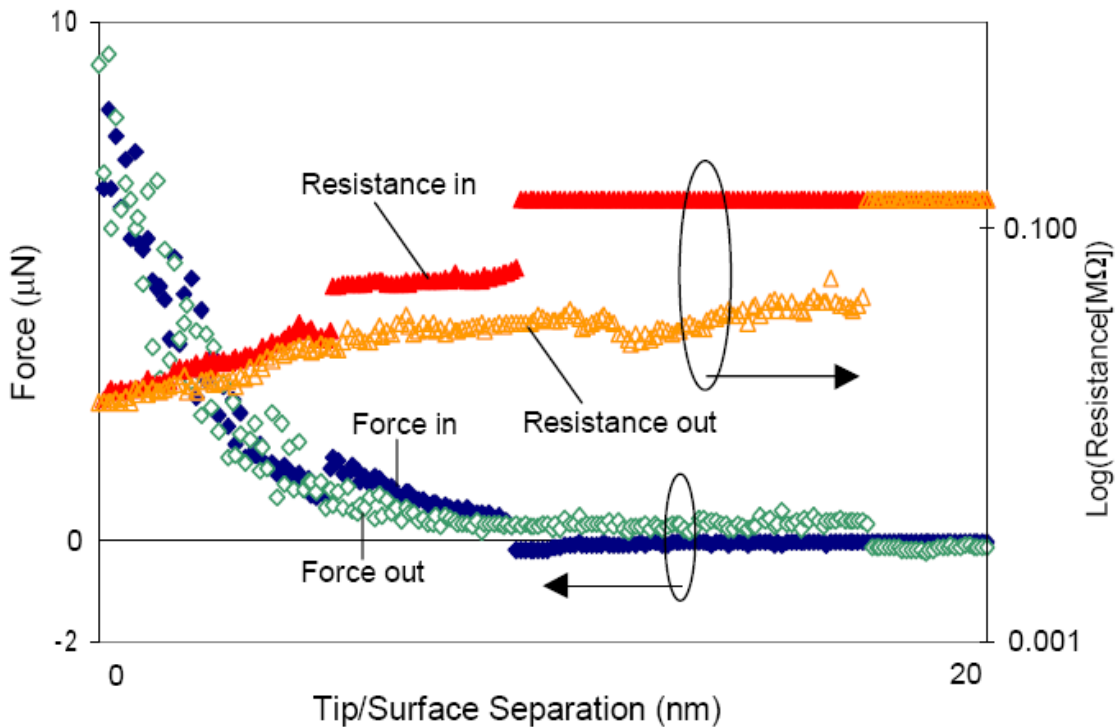


Figure 2.8 – Force and contact resistance profile for approach and withdrawal of Tungsten tip from a gold surface. 40 μA continues to flow between the tip and the adsorbed film even after the tip is more than 15 nm beyond the point of initial contact. (Ref. [68], Fig. 8)

thick water-hydrocarbon layer was deformed before contact was made. The contact resistance was 10 k Ω or greater and continued after the tip was retracted past the point of initial contact with the surface (Fig. 2.8). When repeated after ozone treatment, the contact resistance was 9-10 Ω , and the same attractive force and contact resistance during tip withdrawal was present. In a UHV environment, the resistance dropped below the measurement capability, and penetration through an adsorbed film was not recorded.

Tringe also noted the composition and persistence of the adsorbed film layer. X-ray photoelectron spectroscopy (XPS) and time-of-flight secondary ion mass spectrometry (TOF-SIMS) were taken of the gold contact surface before and after exposure to ozone. XPS revealed oxygen, nitrogen, carbon, and trace amounts of sulfur before ozone treatment. After ozone treatment, the same peaks appeared in the XPS spectra, but there were slight differences in the chemistry. The post-ozone film layer appeared to be more conductive, but the composition and thickness were not greatly changed. Weber *et al.* experienced the same problems with maintaining clean contact surface even after etching with hydrochloric and nitric acid solutions ⁷⁰. The sample was exposed to air for only a short period of time post-etching, yet the data showed evidence of an adsorbed film.

At light contact loads, like those encountered in MEMS switches, the adsorbed film layer creates instability in the contact resistance measurement. Tringe found at low contact loads the change in contact resistance with applied force did not uniformly match model predictions. The variability of contact resistance in this regime is due to the adsorbed film's inhomogeneity and compliant nature. Variances in its topography and chemical composition will affect contact resistance. Data showed that the layer retains its electrical conductivity even as it is deformed by tip approach and withdrawal. Walker recorded a similar response for a gold plated AFM tip contacting a gold MEMS switch contact ⁷¹. Tringe also noted that the initial contact resistances and the distance to which the adsorbed films followed the withdrawing tip varied by location on the contact surface indicating that film thickness was not consistent over the entire area and that it evolved with each contact event.

At low current (< 10 mA) adsorbed films create contact resistance variability during cycling. Majumder *et al.* recorded initially high contact resistance that decreased with

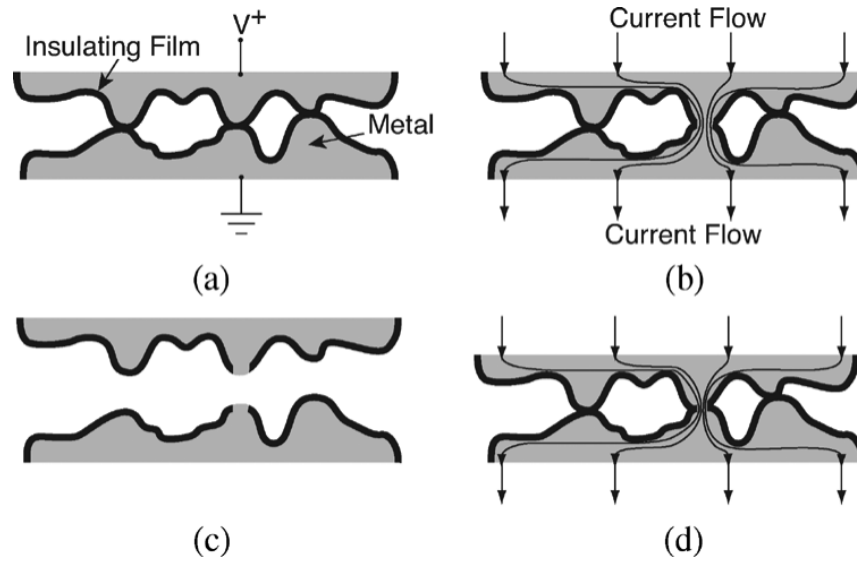


Figure 2.9 – Proposed mechanism for adsorbed film removal and re-growth. In (a) an adsorbed film separates two switch contacts but (b) is removed by pressure and heat at the asperity from current flow. The bare spot remains after the switch opens (c), but the film is pinched into the adsorbed film free area on the next closure (d). (Ref. [75], Fig. 12)

cycling with 4 mA applied. After 10^7 cold-switched cycles, one of the most prevalent MEMS switch failure modes occurred; the contact resistance steadily increased with cycling until it was beyond acceptable limits ⁷². Jensen *et al.* reported an increase from 1 Ω to 1000 Ω over the course of 300 cold-cycles at 48 μN of contact load and 1 mA of current ⁷³. Increased resistance with cycling is most prevalent in cold-switching applications, but has been reported in a hot-switching application as well ⁷⁴.

The increase in contact resistance with cycling is not well understood. In each reported instance the researchers have pointed to adsorbed films or other contaminants as the likely cause. Jensen *et al.* proposed a mechanism for the reappearance of high resistance after large numbers of cycles (Fig. 2.9). It is proposed that as surfaces meet, the pressure of contact and heat at the asperity interface clear the adsorbed film and create ohmic, or metal-on-metal, contact. The exposed, film-free contact area remains after the switch opens. The reappearance of the adsorbed film may be due to the randomness of switch closure. Asperities where the adsorbed film has been removed may not align exactly on subsequent

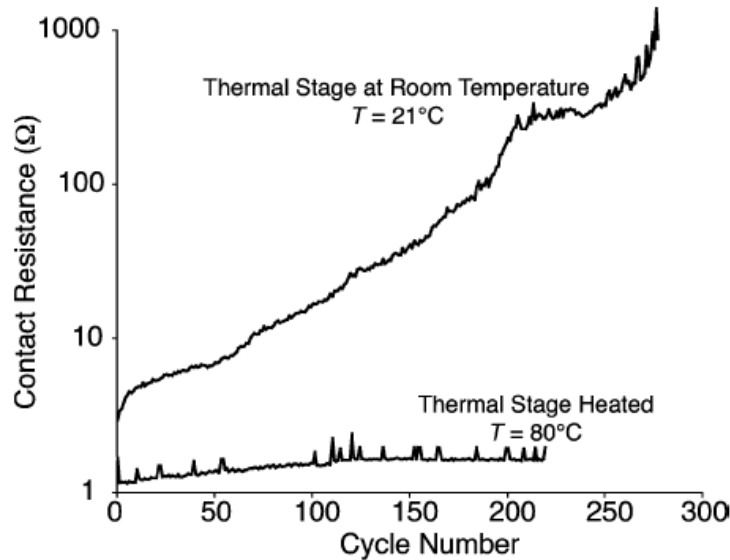


Figure 2.10 – Comparison of contact resistance for room temperature and externally heated contacts. (Ref. [76], Fig. 10)

closures. The misalignment presses the adsorbed film into ohmic contact area and promotes re-growth. The contact resistance increases with time as more adsorbed film is pushed back into the contact area.

2.4.3 Temperature dependence

Jensen *et al.* showed temperature dependence in film behavior from room temperature up to 100°C. Data showed that when the contact voltage was increased to 0.5 V (allowing the voltage drop across the contacts to increase, while maintaining a 1 mA current), contact resistance remained nearly constant during cycling for both cold and hot switching. To demonstrate that elevated temperature at the contacts caused the effect, the input voltage was lowered to 10 mV with a 1 mA current, and the switch was externally heated to 80°C. Contact resistance, as a function of cycles, remained constant for the externally heated contacts. The contact resistance for room temperature contacts increased hundreds of times over 200 cycles (Fig. 2.10). Jensen proposes that contact heating may be used to avoid the cycle induced contact resistance failures. One study lightly explored gold metal micro-

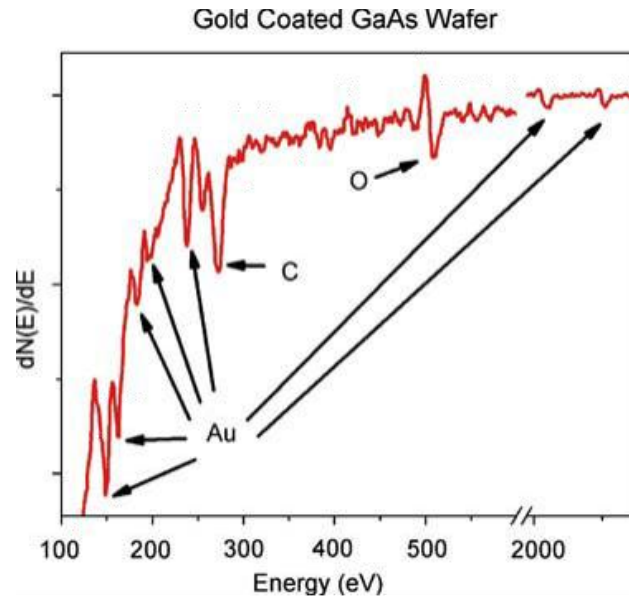


Figure 2.11 – Auger spectra of a freshly cleaned Au wafer. Data indicates that carbon and oxygen species still cover the surface. (Ref. [78], Fig. 7)

contacts at cryogenic temperatures and found no temperature dependence for contact resistance over the range of 2 to 50 K ⁷⁷. The work contained in this thesis is the first extensive study of cryogenic effects on metal contacting MEMS switches.

2.4.4 Removal techniques

Adsorbed films are very persistent and are still present even after cleaning the surface. The Auger spectrum of gold wafer after ultrasonic cleaning in hexane, acetone, and methanol for five minutes each is shown in Fig. 2.11 ⁷⁹. Only a few methods have been devised to completely remove or lessen the effects of adsorbed films. Vacuum conditions are used to help alleviate stiction and remove the adsorbed film. Jensen *et al.* used mTorr level vacuum to remove water from the contact area, but this is not enough to remove adsorbed film layers. Tringe *et al.* successfully used a combination of UHV and ozone treatment to remove adsorbed films. Walker at NCSU has constructed a vacuum system with in-situ oxygen plasma cleaning capability. Oxygen plasma is capable of removing contaminants in non-line of sight areas including under overhangs like cantilever beams. A commonly used

technique adsorbed film removal is fritting^{80,81,82,83,84}. Fritting uses cycling, large contact forces, high currents, or a combination thereof to pierce the adsorbed film layer or contamination layer and achieve ohmic contact. After the fritting and removal of the oxide layer, testing is performed at the normal current levels and contact forces. Fritting has the advantage that it can be performed in-situ, while under UHV or cryogenic conditions, without exposing the switch to atmospheric conditions and recontamination.

While adsorbed film layers lead to contact asperity heating and eventual failure, the complete removal of the film leads to adhesion failure. Tringe *et al.* noted that under UHV conditions as the tungsten tip was retracted from the contact substrate, gold necking occurred. Gold wires pulled from the contact surface to the tungsten tip out to a displacement of 28 nm before fracturing and severing the electrical connection. A single gold asperity can generate ~40 μN of attractive force under UHV conditions. Since most cantilevers have a restoring force on the order of a few hundred μN , only a few asperities would have to touch for adhesion to overcome the restoring force. The data clearly shows that the adsorbed film layer on gold surface acts as a conductive pathway and as a surface passivator.

2.4.5 Contact physics modeling with adsorbed films

Holm introduced one of the earliest electrical contact resistance (ECR) models to include adsorbed film effects⁸⁵. The contact resistance constituents were constriction resistance, R_C , and film resistance R_F ,

$$R = R_C + R_F = \frac{\rho}{2a} + \frac{\rho_F d}{\pi a^2}, \quad (2.5)$$

where ρ is the contact material resistivity, a is the contact radius, ρ_F is the film resistivity, and d is the film thickness. This is an oversimplification, but it did make several things very evident about the impact of adsorbed films on contact resistance. As a increases, the film resistance and contact resistance decrease. The film thickness and its resistivity (directly related to its chemical composition) play key roles in the film resistance.

Several iterations to the ECR have been introduced which have used fractal geometry to represent surface topography, elastic-plastic asperity deformation, and the inclusion of thin

insulation films ⁸⁶. However each of these had a shortcoming in their ability to accurately describe the surface topography, the physical behavior of the micro-contacts, or the properties of the insulating film. Kogut and Komvopoulos introduced a new ECR based on fractal geometry for surface topography representation and elastic, elastic-plastic, and fully plastic asperity deformation. A quantum mechanical approach is taken for the insulating film since it is possible for current to flow through via the tunnel effect.

Results from the latest ECR show that constriction resistance plays a reduced role in the overall contact resistance. The tunnel effect dominates the contact resistance. The ECR decreases with increases in contact load, current flow, and fractal dimension D (higher D at a fixed G indicates smoother surface). The ECR also decreases with decreases in fractal roughness G (lower G indicates smoother surface), film thickness, and energy barrier height (lower barrier means lower electrical resistivity of adsorbed film).

2.5 Environmental impacts

A relatively small amount of work has been done relating the switch contact physics to environmental conditions. Early literature focuses heavily on number of cycles to failure as a gauge of robustness. While the number of cycles is certainly an indicator of the switch's performance capability, the number of cycles loses meaning if the operational and environmental conditions are not stated alongside the cycle data. Patton and Zabinski provide a thorough examination of literature in which results are published but key factors such as the surface characterization, current, contact load, switching mode, atmospheric conditions, etc. are not mentioned, thus leaving little basis for independent comparison to be performed ⁸⁷.

2.5.1 Temperature

Prior to this thesis and connected publications, Jensen *et al.*'s work stood as the only published study of temperature dependent contact resistance for metal contacting MEMS switches. It is highly evident from their work that temperature plays an important role in the contact physics of RF MEMS switches.

A small amount of work has been published on temperature effects for capacitive MEMS switches. Actuation voltage increases for capacitive MEMS switches at lower temperatures. Differences in thermal expansion coefficients between the metal and the substrate at cryogenic temperatures create residual stress in the actuators, which must be overcome by greater actuation voltage to make contact ^{88,89,90}. The increased actuation voltage resulted in charge build-up in the dielectric layer, a common failure mode for capacitive MEMS switches ⁹¹. At elevated temperature, the spring constant and restoring force of the contact membrane decreased, leaving the switch prone to charge-induced stiction failure ⁹². Temperature induced stress is not a problem for the single fixed end, or cantilever type beams, studied in this thesis.

2.5.2 Atmosphere

There is no evidence to indicate that inert atmospheric conditions will change the contact physics of MEMS devices. Studies show that nitrogen does not decrease the initial contact resistance when compared to air; tunneling effects still dominate the contact resistance ^{93,94,95}. Majumder *et al.* showed that the number of hot-switched cycles was the same for air and nitrogen atmospheres ⁹⁶. The industry standard is to package MEMS switches in inert gases to abate stiction failures from humidity ⁹⁷.

To date the only comprehensive study on atmospheric effects to the contact physics of MEMS switches is by Koidl *et al.* ⁹⁸. This study only covered the effects of organic vapors on micro-switch contacts. No in-depth research has been conducted on the relationship between atmosphere and failure mechanisms.

2.5.3 Pressure

Pressure effects were peripherally covered in the modeling and simulations of metal contacting MEMS switches during closure ⁹⁹. The physics and mechanics of cantilever beam closure were studied in depth. The simulation took into account switch geometry, a non-linear spring model used to model the interaction between the contact tip and drain, electrostatic actuation, and two-dimensional non-uniform squeeze damping effect. Ambient

gas was assumed to act as an ideal and isothermal fluid that could be modeled using the Reynolds squeeze-film equation. The simulation led to a number of findings useful for decreasing the force of impact at closure. This included tailoring actuation voltages and utilizing squeeze-film damping to slow the speed of the cantilever during closure. One possible mechanism for increasing the squeeze-film damping is to increase the pressure of the ambient gas. The experimental portion of the study was performed at standard pressure and none of the pressure dependent mechanisms were tested.

To date no comprehensive study has been published on the effect of pressure on contact mechanics and beam physics.

2.6 Thesis material

The theory and experimentation presented in this thesis focus on isolating and characterizing failure modes of gold contact RF MEMS switches at low contact force and low current. It is designed to be a companion to the research performed by Z. Yang at NCSU, which focused on failure mechanisms of pure gold and gold alloys at high contact force and high current¹⁰⁰. The temperature related research contained in this thesis is a cold temperature extension of the high temperature contact resistance and creep work performed by Jensen *et al*¹⁰¹.

In this thesis a few specific subjects are covered addressing the contact physics of RF MEMS gold contacting switches:

1. ***Failure mechanism isolation*** – Isolation is achieved by carefully controlling the switching environment to ensure that only one mechanism is active. Temperature is used to isolate the material properties of gold and observe the physical characteristics of adsorbed films. Current and voltage drop across the contacts are adjusted while temperature is held constant at 5.6 K to study creep and current effects on clean gold surfaces. Adsorbed film presence, mobility, and re-growth are characterized at 5.6 K and at 77 K. Temperature dependent effects are presented in Chapters 5 and 9 of the thesis.
2. ***Convergence of theory and experimentation*** – To this point much of the modeling

has been statistically based and provides an inaccurate interpretation of the actual surface topography at low contact loads. Additionally, the literature review showed that the theory and experimentation have not agreed except at very high loads and current. This is because of a flaw in methodology, in which modeled constriction resistance is incorrectly compared to contact resistance.

The theoretical work presented in the thesis uses fractal geometry to accurately represent the surface topography and changes to it at low contact forces. A power law relation for changes in contact resistance as function of time is presented which properly segregates the constriction and adsorbed film components of contact resistance. The revised theory is compared to experimental data. Chapters 6, 7, and 9 present correlated data and modeling for creep at both room temperature and cryogenic temperatures.

3. ***Environmental impacts*** – Environmental conditions were not regularly reported in existing MEMS switch literature and have not been a focus of an in-depth contact physics study. In this thesis, data is presented and tied to existing theory for the effects of temperature, atmosphere, and pressure on RF MEMS contact physics. Chapters 5 and 9 present data and modeling for cryogenic temperatures. Chapter 4 provides an analysis of pressure effects on contact physics.

2.7 References

¹ L. E. Larson *et al*, “Micromachined microwave actuator (MIMAC) technology-a new tuning approach for microwave integrated circuits,” *Microwave and Millimeter-Wave Monolithic Circuits Symposium Digest. (Boston, MA)* pp 27-30.

² J. Yao, “RF MEMS from a device perspective.” *J. Micromech. Microeng.*, **10** (2000) R9–R38.

-
- ³ S.T. Patton and J.S. Zabinski, “ Fundamental studies of Au contacts in MEMS RF switches,” *Tribology Letters*, Vol. 18, No. 2, pp. 215-230, February 2005.
- ⁴ I. Schiele, J. Huber, B. Hillerich and F. Kozlowski, “Surface-micromachined electrostatic microrelay,” *Sens. Actuat. A*, **66**, pp. 345, 1998.
- ⁵ G. M. Rebeiz, RF MEMS Theory, design, and technology, New Jersey: John Wiley & Sons, Inc. 2003.
- ⁶ S.T. Patton and J.S. Zabinski, “ Fundamental studies of Au contacts in MEMS RF switches,” *Tribology Letters*, Vol. 18, No. 2, pp. 215-230, February 2005.
- ⁷ J. Schimkat, "Contact materials for microrelays," *Micro Electro Mechanical Systems, 1998. MEMS 98. Proceedings., The Eleventh Annual International Workshop on* , vol., no., pp.190-194, 25-29 Jan 1998.
- ⁸ R.A. Coutu, P.E. Kladitis, K.D. Leedy and R.L. Crane, “ Selecting metal alloy electric contact materials for MEMS switches,” *J. Micromech. Microeng.* vol.14, pp. 1157-1164, 2004.
- ⁹ R.A. Coutu, J.R. Reid, R.Cortez, R.E. Strawser and P.E. Kladitis, “Microswitches with sputtered Au, AuPd, Au-on-AuPt, and AuPtCu alloy electric contacts,” *IEEE Trans. Comp. Packag. Tech.*, vol. 29, pp. 341-349, 2006.
- ¹⁰ Z. Yang, “Contact Material Optimization and Contact Physics in Metal-contact Microelectromechanical Systems (MEMS) Switches,” Ph.D. dissertation, North Carolina State University, 2008.
- ¹¹ Z. Yang, D. Lichtenwalner, A. Morris, S. Menzel, C. Nauenheim, A. Gruverman, J. Krim

and A. I. Kingon, "A new test facility for efficient evaluation of MEMS contact materials," accepted July 2007 for publication in *J. Micromech. Microeng.*

¹² K.L. Johnson, *Contact Mechanics*, Cambridge: Cambridge University Press (1985).

¹³ K.L. Johnson, *Contact Mechanics*, Cambridge University Press, London, 1998.

¹⁴ R. Holm, *Electric Contacts: Theory and Applications*, Berlin, Germany: Springer, 1969.

¹⁵ J.A. Greenwood and J.B.P. Williamson, "Contact of nominally flat surfaces," *Proc. R. Soc. London A*, 295, pp. 257-263, 1966.

¹⁶ A.W. Bush, R.D. Gibson, and T.R. Thomas, "The Elastic Contact of a Rough Surface," *Wear*, **35**, pp. 87-111, 1975.

¹⁷ J.I. McCool, "Comparison of Models for the Contact of Rough Surfaces," *Wear*, **107**, pp. 37-60, 1986.

¹⁸ W. Chang, I. Etsion and D. Bogy, "An elastic-plastic model for the contact of rough surfaces," *ASME J. Tribol.*, **109**, pp. 257-263, 1987.

¹⁹ S. Majumder, N.E. McGruer, G.G. Adams, P.M. Zavracky, R.H. Morrison, and J. Krim, "Study of contacts in an electrostatically actuated microswitch," *Sensors and Actuators A*, vol.93, no.1, pp. 19-26, 2001.

²⁰ D.J. Dickrell, M.T. Dugger, M.A. Hamilton, and W.G. Sawyer, "Direct Contact-Area Computation for MEMS Using Real Topographic Surface Data," *J. Microelectromech. Syst.*, vol.16, no.5, pp.1263-1268, Oct. 2007

²¹ O. Rezvanian, M.A. Zikry, C. Brown and J. Krim, "Surface roughness, asperity contact and gold RF MEMS switch behavior," *J. Micromech. Microeng.* **17**, pp. 2006-2015, 2007.

-
- ²² K. Komvopoulos and N. Ye, “Three-dimensional contact analysis of elastic-plastic layered media with fractal surface topographies,” *J. Tribol.*, **123**, pp. 632–40, 2001.
- ²³ S. Majumder, N.E. McGruer, G.G. Adams, P.M. Zavracky, R.H. Morrison, and J. Krim, “Study of contacts in an electrostatically actuated microswitch,” *Sensors Actuators A*, **93**, pp. 19–26, 2001.
- ²⁴ D. Blackmore and J.G. Zhou, “Fractal analysis of height distributions of anisotropic rough surfaces,” *Fractals*, **6**, pp. 43–58, 1998.
- ²⁵ M. Ciavarella, G. Demelio, J.R. Barber, and Y.H. Jang, “Linear elastic contact of Weierstrass profile,” *Proc. R. Soc. London A*, **456**, pp. 387–405, 2000.
- ²⁶ A. Majumder and B. Bhushan, “Fractal model of elastic-plastic contact between rough surfaces,” *J. Tribol.*, **113**, pp. 1–11, 1991.
- ²⁷ W. Yan and K. Komvopoulos, “Contact analysis of elastic-plastic fractal surfaces,” *J. Appl. Phys.*, **84**, pp. 3617–24, 1998.
- ²⁸ N. Agraït, “Quantum properties of atomic sized conductors,” *Phys. Rep.*, vol. 377, pp. 81–279, 2003.
- ²⁹ N. Ashcroft, N. Mermin, and D. Mermin, *Solid State Physics*, 1st ed. New York: Holt, Rinehart and Winston, 1976.
- ³⁰ G. Wexler, “The size effect and non-local Boltzmann transport equation in orifice and disk geometry,” *Proceedings of the Physics Society*, vol. 89, pp. 927–941, 1966.
- ³¹ B. Nikolic and P.B. Allen, “Electron transport through a circular constriction,” *Physical Review B*, vol. 60, pp. 3963–3969, 1999.

-
- ³² B. Jensen, L. Chow, K. Huang, K. Saitou, J. Volakis and K. Kurabayashi, "Effect of nanoscale heating on electrical transport in RF MEMS switch contacts," *J. Microelectromech. Syst.*, vol. 14, no. 5, pp. 935-946, 2005.
- ³³ L. Weber, M. Lehr and E. Gmelin, "Investigation of the transport properties of gold point contacts," *Physica B: Condensed Matter*, vol. 217, pp. 181-192, 1996.
- ³⁴ Z. Yang, "Contact Material Optimization and Contact Physics in Metal-contact Microelectromechanical Systems (MEMS) Switches," Ph.D. dissertation, North Carolina State University, 2008.
- ³⁵ R.A. Coutu, P.E. Kladitis, L.A. Starman, and J.R. Reid, "A comparison of micro-switch analytic, finite element, and experimental results," *Sensors and Actuators A*, vol.115, pp. 252–258, 2004.
- ³⁶ I. Schiele, J. Huber, B. Hillerich and F. Kozlowski, "Surface micromachined electrostatic microrelay," *Sensors and Actuators A*, **66**, pp. 345-354, 1998.
- ³⁷ J. A. Wright, Y.-C. Tai, and G. Lilienthal, "A magnetostatic MEMS switch for DC brushless motor commutation," in *Proc. Solid-State Sensor and Actuator Workshop 1998*, Hilton Head Island, SC, pp. 304–307, 1998.
- ³⁸ D. Hyman and M. Mehregany, "Contact physics of gold microcontacts for MEMS switches," *Components and Packaging Technologies, IEEE Transactions on [see also Components, Packaging and Manufacturing Technology, Part A: Packaging Technologies, IEEE Transactions on]*, vol.22, no.3, pp.357-364, Sep 1999.
- ³⁹ J. Tringe, W. Wilson and J. Houston, "Conduction properties of microscopic gold contact

surfaces,” *Proc. SPIE 4558*, pp. 151-158, 2001.

⁴⁰ S. Majumder, N.E. McGruer, G.G. Adams, A. Zavracky, P. Zavracky, P. Morrison and J. Krim, “Study of contacts in an electrostatically actuated microswitch,” *Proc. 44th IEEE Holm Con. on Electrical Contacts*, pp. 127-132, 1998.

⁴¹ S. Patton and J. Zabinski, “Fundamental studies of Au contacts in MEMS RF switches,” *Tribology Letters*, vol. 18, no. 2, pp. 215-230, 2004.

⁴² R. Chan, R. Lesnick, D. Becher and M. Feng, “Low actuation voltage RF MEMS shunt switch with cold switching lifetime of seven billion cycles,” *J. of MEMS* 12(5), pp. 713-719, 2003.

⁴³ D. Becher, R. Chan, M. Hattendorf and M. Feng, “Reliability study of low-voltage RF MEMS switches,” *Proc. GaAs MANTECH Conf. 03e*, April 2002.

⁴⁴ S. D. Lee, B. Jun, S. D. Kim and K. Mizuno, “An RF-MEMS switch with low actuation voltage and high reliability,” *J. Microelectromech. Syst.*, vol. 15, no. 6, pp. 1605-1611, 2006.

⁴⁵ C. H. Chu, W. P. Shih, S. Y. Chung, et al., “A low actuation voltage electrostatic actuator for RF MEMS switch applications,” *J. Micromech. Microeng.*, vol. 17, no. 8, pp. 1649-1656, 2007.

⁴⁶ L. Kogut and K. Komvopoulos, “Analytical current-voltage relationships for electron tunneling across rough interfaces,” *J. App. Phys.*, vol.97, no. 1, pp. 1-5, 2004.

⁴⁷ L. Kogut and K. Komvopoulos, “Electrical contact resistance theory for conductive rough surfaces separated by a thin insulating film,” *J. App. Phys.*, vol. 95, no. 2, pp. 576-585, 2005.

-
- ⁴⁸ N.E. McGruer, G.G. Adams, L. Chen, Z.J. Guo, and Y. Du, “Mechanical, Thermal and Material Influences on Ohmic-Contact-Type MEMS Switch Operation,” *Micro Electro Mechanical Systems, 2006. MEMS 2006 Istanbul. 19th IEEE International Conference on* , pp.230-233, 2006.
- ⁴⁹ G. M. Rebeiz, RF MEMS Theory, design, and technology, New Jersey: John Wiley & Sons, Inc. 2003.
- ⁵⁰ J.E. Massad, H. Sumali, D.S. Epp, C.W. Dyck, "Modeling, simulation, and testing of the mechanical dynamics of an RF MEMS switch," *MEMS, NANO and Smart Systems, 2005. Proceedings. 2005 International Conference on*, pp. 237-240, 24-27 July 2005.
- ⁵¹ Z.J. Guo, N.E. McGruer and G.G. Adams, “Modeling, simulation and measurement of the dynamic performance of an ohmic contact, electrostatically actuated RF MEMS switch,” *J. Micromech. Microeng.*, vol. 17, pp. 1899–1909, 2007.
- ⁵² G. M. Rebeiz, RF MEMS Theory, design, and technology, New Jersey: John Wiley & Sons, Inc. 2003.
- ⁵³ S.T. Patton and J.S. Zabinski, “Fundamental studies of Au contacts in MEMS RF switches,” *Tribology Letters*, Vol. 18, No. 2, pp. 215-230, February 2005.
- ⁵⁴ Z. Yang, “Contact Material Optimization and Contact Physics in Metal-contact Microelectromechanical Systems (MEMS) Switches,” Ph.D. dissertation, North Carolina State University, 2008.
- ⁵⁵ S.T. Patton and J.S. Zabinski, “Fundamental studies of Au contacts in MEMS RF switches,” *Tribology Letters*, Vol. 18, No. 2, pp. 215-230, February 2005.

-
- ⁵⁶ L. Kogut and K. Komvopoulos, "Analytical current-voltage relationships for electron tunneling across rough interfaces," *J. Applied Physics*, vol. 97, no. 1, 2005.
- ⁵⁷ K. Hansen, S.K. Nielsen, M. Brandbyge, E. Lægsgaard, I. Stensgaard and F. Besenbacher, "Current-voltage curves of gold quantum point contacts revisited," *Applied Physics Letter*, vol.77, no.5, pp. 708-710, 2000.
- ⁵⁸ D. Hyman and M. Mehregany "Contact physics of gold microncontacts for MEMS switches", *Components and Packaging Technologies, IEEE Transactions on*, vol.22, p. 357, 1999.
- ⁵⁹ J. Tringe, W. Wilson and J. Houston, "Conduction properties of microscopic gold contact surfaces," *Proc. SPIE 4558*, pp. 151-158, 2001.
- ⁶⁰ N.E. McGruer, G.G. Adams, L. Chen, Z.J. Guo, and Y. Du, "Mechanical, Thermal and Material Influences on Ohmic-Contact-Type MEMS Switch Operation," *Micro Electro Mechanical Systems, 2006. MEMS 2006 Istanbul. 19th IEEE International Conference on* , pp.230-233, 2006.
- ⁶¹ C.N. Neufeld and C.N. Rieder, "Electrical Characteristics of Various Contact Contaminations," *Trans. Comp. Pack. Manufact. Technol. A*, vol. 18, pp. 369-374, 1995.
- ⁶² C.N. Neufeld and C.N. Rieder, "Carbon Contamination of Contacts Due to Organic Vapors," *Trans. Comp. Pack. Manufact. Technol. A*, vol. 18, pp. 399-404, 1995.
- ⁶³ D.J. Dickrell, III and M.T. Dugger, "Electrical Contact Resistance Degradation of a Hot-Switched Simulated Metal MEMS Contact," *Components and Packaging Technologies, IEEE Transactions on [see also Components, Packaging and Manufacturing Technology*,

Part A: Packaging Technologies, IEEE Transactions on], vol.30, no.1, pp.75-80, March 2007.

⁶⁴ H.P. Koidl, W.F. Rieder, Q.R. Salzmann, "Contact compatibility of organic vapors and their physical/chemical properties," *Electrical Contacts, 1997., Proceedings of the Forty-Third IEEE Holm Conference on*, pp.328-332, 20-22 Oct 1997.

⁶⁵ H.P. Koidl, W.F. Rieder, Q.R. Salzmann, "Influence of Physical/Chemical Characteristics of Organic Vapors and Gas Mixtures on their Contact Compatibility," *Components and Packaging Technologies, IEEE Transactions on*, vol.22, no.3, pp. 439-445, 1999.

⁶⁶ H.P. Koidl, W.F. Rieder, Q.R. Salzmann, "Influence of Physical/Chemical Characteristics of Organic Vapors and Gas Mixtures on their Contact Compatibility," *Components and Packaging Technologies, IEEE Transactions on*, vol.22, no.3, pp. 439-445, 1999.

⁶⁷ B. D. Jensen, L. L.-W. Chow, K. Huang, K. Saitou, J. L. Volakis and K. Kurabayashi, "Effect of nanoscale heating on electrical transport in RF MEMS switch contacts," *J. Microelectromechanical Systems*, vol.14, no.5, pp.435-946, 2005.

⁶⁸ J. Tringe, W. Wilson and J. Houston, "Conduction properties of microscopic gold contact surfaces," *Proc. SPIE 4558*, pp. 151-158, 2001.

⁶⁹ J.W. Tringe, T.A. Uhlman, A.C. Oliver and J.E. Houston, "A single asperity study of Au/Au electrical contacts," *J. Applied Physics*, vol.93, no.8, pp. 4661-4669, 2003.

⁷⁰ L. Weber, M. Lehr, and E. Gmelin, "Investigation of the transport properties of gold point contacts," *Physica B*, vol.217, pp.181-192, 1996.

⁷¹ M. Walker, unpublished work at North Carolina State University.

-
- ⁷² S. Majumder, N.E. McGruer, G.G. Adams, P.M. Zavracky, R.H. Morrison, and J. Krim, “Study of contacts in an electrostatically actuated microswitch,” *Sensors Actuators A*, vol.93, pp. 19–26, 2001.
- ⁷³ B. D. Jensen, L. L.-W. Chow, K. Huang, K. Saitou, J. L. Volakis and K. Kurabayashi, “Effect of nanoscale heating on electrical transport in RF MEMS switch contacts,” *J. Microelectromechanical Systems*, vol.14, no.5, pp.435-946, 2005.
- ⁷⁴ R.A. Coutu, J.R. Reid, R.Cortez, R.E. Strawser and P.E. Kladitis, “Microswitches with sputtered Au, AuPd, Au-on-AuPt, and AuPtCu alloy electric contacts,” *IEEE Trans. Comp. Packag. Tech.*, vol. 29, pp. 341-349, 2006.
- ⁷⁵ B. D. Jensen, L. L.-W. Chow, K. Huang, K. Saitou, J. L. Volakis and K. Kurabayashi, “Effect of nanoscale heating on electrical transport in RF MEMS switch contacts,” *J. Microelectromechanical Systems*, vol.14, no.5, pp.435-946, 2005.
- ⁷⁶ B. D. Jensen, L. L.-W. Chow, K. Huang, K. Saitou, J. L. Volakis and K. Kurabayashi, “Effect of nanoscale heating on electrical transport in RF MEMS switch contacts,” *J. Microelectromechanical Systems*, vol.14, no.5, pp.435-946, 2005.
- ⁷⁷ L. Weber, M. Lehr and E. Gmelin, “Investigation of the transport properties of gold point contacts,” *Physica B: Condensed Matter*, vol. 217, pp. 181-192, 1996.
- ⁷⁸ S.T. Patton and J.S. Zabinski, “Fundamental studies of Au contacts in MEMS RF switches,” *Tribology Letters*, Vol. 18, No. 2, pp. 215-230, February 2005.
- ⁷⁹ S.T. Patton and J.S. Zabinski, “Fundamental studies of Au contacts in MEMS RF switches,” *Tribology Letters*, Vol. 18, No. 2, pp. 215-230, February 2005.

-
- ⁸⁰ B. D. Jensen, L. L.-W. Chow, K. Huang, K. Saitou, J. L. Volakis and K. Kurabayashi, "Effect of nanoscale heating on electrical transport in RF MEMS switch contacts," *J. Microelectromechanical Systems*, vol.14, no.5, pp.435-946, 2005.
- ⁸¹ R.A. Coutu, P.E. Kladitis, L.A. Starman, and J.R. Reid, "A comparison of micro-switch analytic, finite element, and experimental results," *Sensors and Actuators A*, vol.115, pp. 252–258, 2004.
- ⁸² K. Kataoka, T. Itoh, and T. Suga, "Characterization of fritting phenomena on Al electrode for low contact force probe card," *IEEE Trans. Comp. Packag. Tech.*, vol. 26, pp. 382-387, 2004.
- ⁸³ T. Itoh, T. Suga, G. Engelmann, J. Wolf, O. Ehrmann, and H. Reichl, "Characteristics of fritting contacts utilized for micromachined wafer probe cards," *Review of Scientific Instruments*, vol.71, no.5, pp. 2224-2227, 2000.
- ⁸⁴ R. Holm, *Electric Contact Handbook*, Springer-Verlag: Berlin, 1958.
- ⁸⁵ R. Holm, *Electrical Contacts*, 4th ed. (Springer, New York, 1967).
- ⁸⁶ L. Kogut and K. Komvopoulos, "Electrical contact resistance theory for conductive rough surfaces separated by a thin insulating film," *J. Applied Physics*, vol.95, no.2, pp. 576-585, 2004.
- ⁸⁷ S.T. Patton and J.S. Zabinski, "Fundamental studies of Au contacts in MEMS RF switches," *Tribology Letters*, Vol. 18, No. 2, pp. 215-230, February 2005.
- ⁸⁸ H.T. Su et al., "Investigating the Performance of RF MEMS Switches," *ICSE2006 Proc.*, *Kuala Lumpur, Malaysia*, pp. 263-266, 2006.

-
- ⁸⁹ H.T. Su et al., "Performance of RF MEMS switches at low temperatures," *Electronic Letters*, vol. 42, no.21, 2006.
- ⁹⁰ P. Rantakari and T. Vähä-Heikkilä, "Characterization of CMOS Compatible RF MEMS Switch at Cryogenic Temperatures," *Transducers & Eurosensors 2007, 14th Int. Conf. on Solid-state Sensors, Actuators and Microsystems*, pp. 639-642, 2007.
- ⁹¹ Y. Zhy and H.D. Espinosa, "Effect of temperature on capacitive RF MEMS switch performance – a coupled-field analysis," *J. Micromech. Microeng.*, vol.14, pp. 1270-1279, 2004.
- ⁹² X. Yuan, Z. Peng, J.C.M. Hwang, D. Forehand, and C.L. Goldsmith, "Temperature acceleration of dielectric charging in RF MEMS capacitive switches," *IEEE MTT-S Int. Microwave Symp. Digest*, pp. 47-50, 2006.
- ⁹³ J. Tringe, W. Wilson and J. Houston, "Conduction properties of microscopic gold contact surfaces," *Proc. SPIE 4558*, pp. 151-158, 2001.
- ⁹⁴ J.W. Tringe, T.A. Uhlman, A.C. Oliver and J.E. Houston, "A single asperity study of Au/Au electrical contacts," *J. Applied Physics*, vol.93, no.8, pp. 4661-4669, 2003.
- ⁹⁵ A. Tonck, F. Houze, L. Boyer, J.L. Loubet and J.M. Georges, "Electrical and mechanical contact between rough gold surfaces in air," *J. Phys.: Cond. Matt.*, vol.3, pp. 5195-5201, 1991.
- ⁹⁶ S. Majumder, N.E. McGruer, and P.M. Zavracky, "Electrostatically actuated micromechanical switches," *J. Vac. Sci. Technol. A*, vol.15, no.3, pp. 1246-1249, 1997.

-
- ⁹⁷ G.M. Rebeiz and J.B. Muldavin, "RF MEMS switches and switch circuits," *Microwave Magazine, IEEE* , vol.2, no.4, pp.59-71, Dec 2001.
- ⁹⁸ H.P. Koidl, W.F. Rieder, Q.R. Salzmann, "Influence of Physical/Chemical Characteristics of Organic Vapors and Gas Mixtures on their Contact Compatibility," *Components and Packaging Technologies, IEEE Transactions on*, vol.22, no.3, pp. 439-445, 1999.
- ⁹⁹ Z.J. Guo, N.E. McGruer and G.G. Adams, "Modeling, simulation and measurement of the dynamic performance of an ohmic contact, electrostatically actuated RF MEMS switch," *J. Micromech. Microeng.*, vol. 17, pp. 1899–1909, 2007.
- ¹⁰⁰ Z. Yang, "Contact Material Optimization and Contact Physics in Metal-contact Microelectromechanical Systems (MEMS) Switches," Ph.D. dissertation, North Carolina State University, 2008.
- ¹⁰¹ B. D. Jensen, L. L.-W. Chow, K. Huang, K. Saitou, J. L. Volakis and K. Kurabayashi, "Effect of nanoscale heating on electrical transport in RF MEMS switch contacts," *J. Microelectromechanical Systems*, vol.14, no.5, pp.435-946, 2005.

CHAPTER 3

Experimental Details

3.1 Experimental apparatus

3.1.1 Vacuum test chamber

The devices used in this study were tested in two custom vacuum chambers built from UHV compatible components. The first test chamber is specifically designed and wired for testing the wiSpry RF MEMS switches. The test chamber consists of three sections: four-way cross, extension arm, and sample chamber (Fig. 3.1). Each section is attached with conflat (CF) flanges to maintain vacuum. The four-way cross is fitted at the top with a right angle valve, where the chamber is connected to the vacuum pump via a quick connect flange. The right angle valve is placed such that CF flange opposite the handwheel actuator is connected to the test chamber. This allows high pressure from the side port to build up behind the poppet and create a firm seal at the Viton poppet seal in addition to the mechanical force applied by the handwheel.

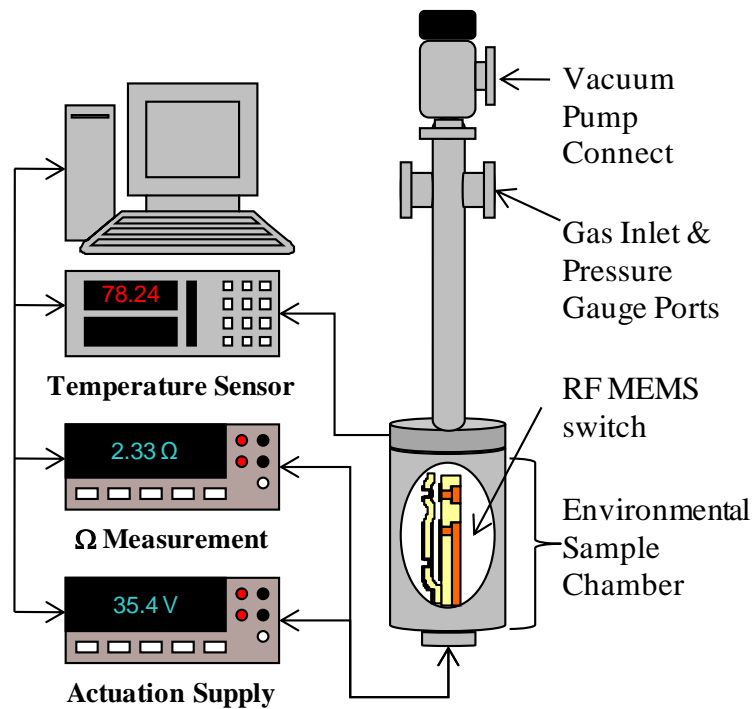


Figure 3.1 – Schematic of experimental apparatus.

A pressure gauge and a gas shut-off valve are used at the other two connections on the four-way cross. The pressure gauge is a 947 convection enhanced pirani gauge capable of reading from 10^{-3} to 1200 Torr. In instances where lower pressures readings were required, the testing chamber was attached to and pumped down through another chamber that had an ion gauge. The final four-way cross position was fitted with a Nupro gas shut-off valve welded into a pass-through CF flange and capped with a CF flange blank. The blank can be removed and an ion gauge inserted in its place for low-pressure measurements. The gas shut-off valve is fitted with Swage-lock fittings that connect to compressed helium and nitrogen sources to backfill the test chamber.

Connecting the four-way cross and the test chamber is a 28-inch extension arm. The arm is made of thin steel tubing welded at the ends to a 2.75-inch CF flange connecting to the four-way cross and a 3-3/8-inch CF flange connecting to the test chamber. Thin steel tubing is required to rapidly cool the test chamber. Less liquid helium or nitrogen is needed to cool the thin steel. The extension arm length maximizes the test chamber's depth inside of the cryostat

The first test chamber is comprised of a thin steel tub with a 3-3/8 inch CF flange at the top allowing access to the test device and a 2.75-inch CF flange attached to a 20-pin UHV compatible electrical feedthrough (Fig. 3.2). The tube length not including the electrical feedthrough is 10 inches. RF MEMS switches were mounted in ceramic gold sidebrazed packages and placed in a 40-pin ZIF (zero insertion force) socket. The ZIF socket is mounted on the canister centerline near the 3-3/8-inch CF flange opening and is held in place by two steel posts tig welded to the inside of the canister. With the ZIF socket ceramic packages can be easily and quickly swapped out, and the chance of damaging the package leads is decreased.

A second test chamber was designed with more flexibility, allowing switches from Northeastern University (NEU), RFMD, and Sandia to be tested (Fig. 3.3). The apparatus used the same four-way cross setup previously described for the wiSpry test chamber, a shorter extension arm (26 inches) with 2.75-inch CR flanges at both ends, and MEMS

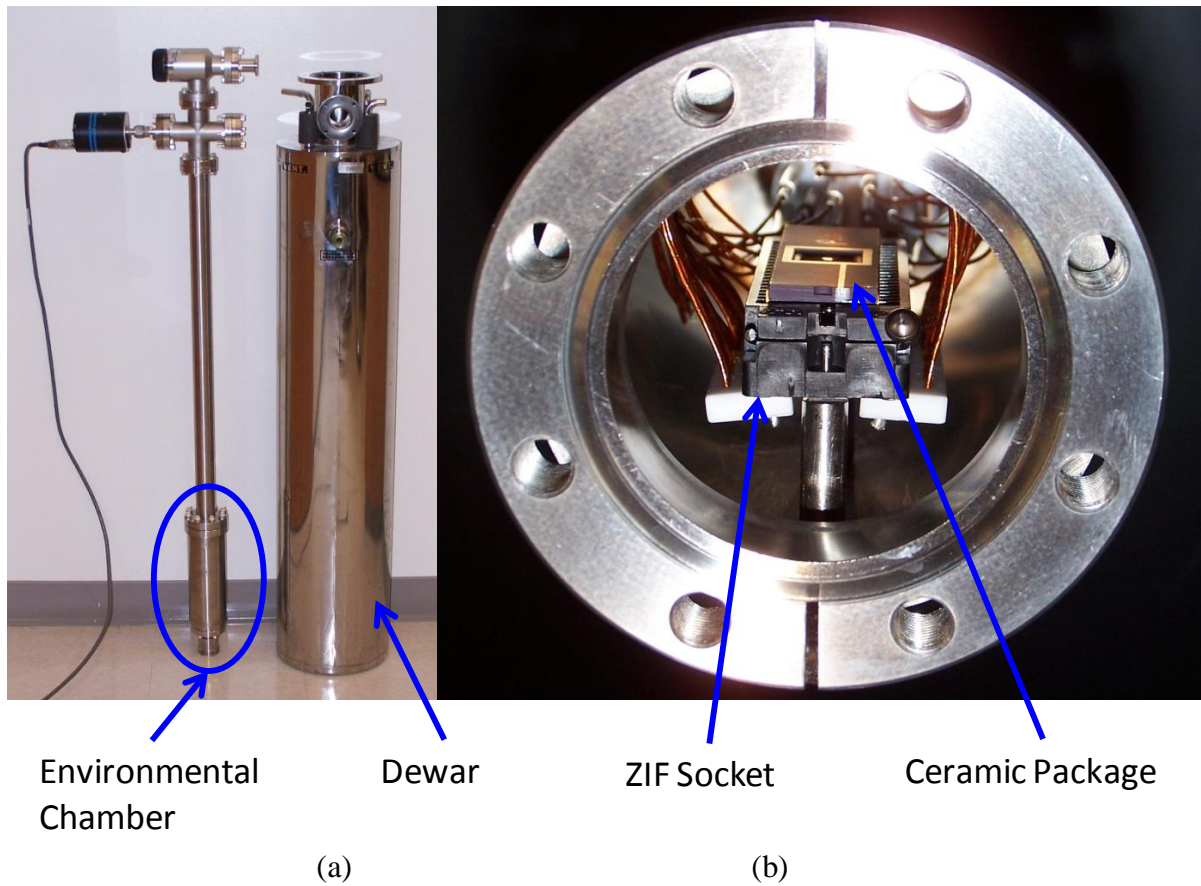


Figure 3.2 – (a) Vacuum chamber for testing wiSpry RF MEMS switch with dewar (dewar height is 48 inches). (b) End-on picture of environmental sample chamber (width is 3-3/8 inches). The device is mounted in the center cavity of the ceramic package.

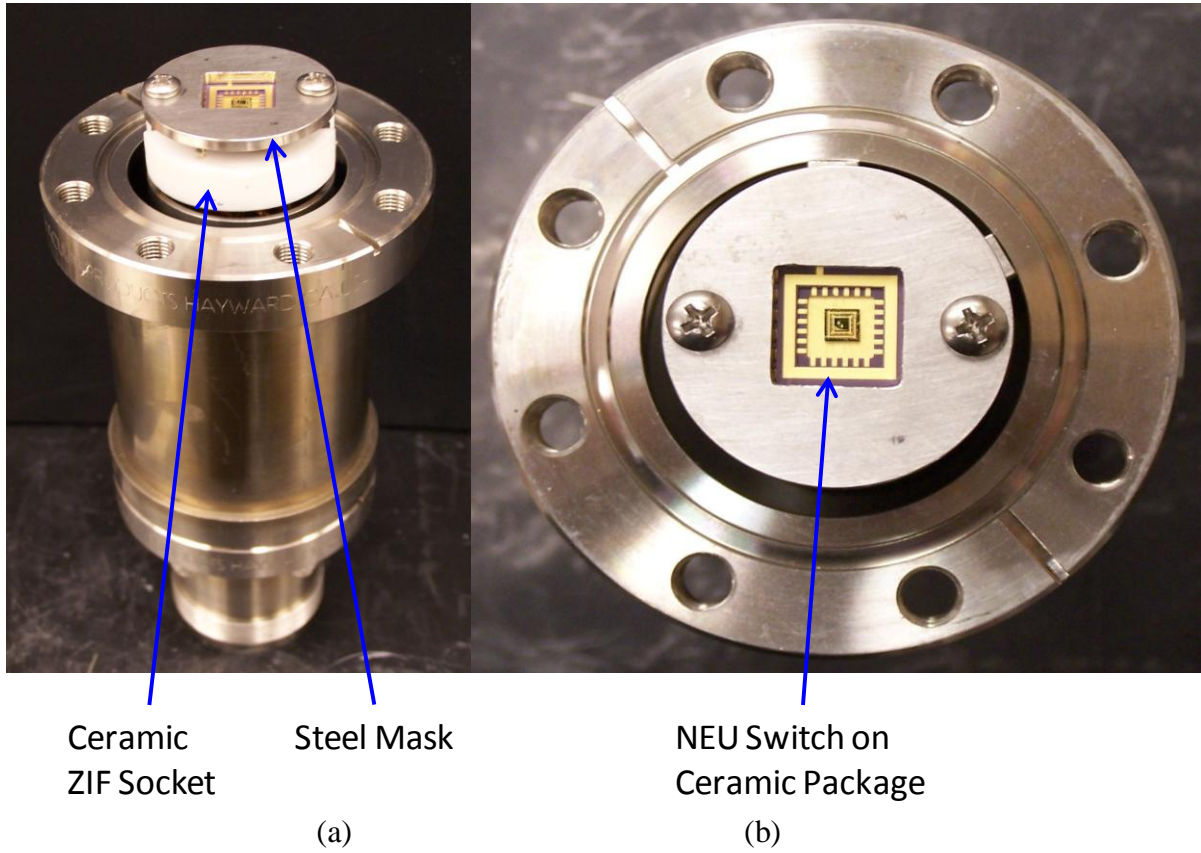


Figure 3.3 - (a) Environmental sample chamber for testing NEU, Sandia, and RFMD RF MEMS switches. The chamber height is 7.5 inches including ceramic ZIF socket and mask. (b) End-on picture of environmental sample chamber (width is 3-3/8 inches).

switches mounted on ceramic gold sidebrazed packages. Electrical connections were made through a 20-pin electrical feedthrough.

The main difference between the first test chamber and the second is the design of the sample chamber. The second chamber is smaller in both length and diameter than the first, making it easier to cool. The 40-pin ZIF socket was replaced with a 24-pin cylindrical ceramic sample holder fitted with spring-loaded gold pin sockets countersunk below the ceramic's surface. The sample holder sits on a thin steel cylinder insert sleeve. The thin steel sleeve and ceramic sockets are just slightly smaller than the inside diameter of the CF flange, allowing them to slide in and out of the test chamber. When inside the sample chamber, the sleeve is seated firmly on the copper seal between the sample chamber's lower CF flange and the electrical feedthrough CF flange. The sleeve walls have vent openings and the ceramic package is slightly raised above the top of sleeve to prevent slow flow rates and trapped air during pumping.

The ceramic package holding the switch is held against the spring-loaded pin sockets and ceramic sample holder by a steel mask. The steel mask has the same diameter as the sample holder and steel sleeve and has a cavity in the center to expose the switch and wirebonds. The mask is held in place by two bolts that are tightened as needed to maintain the electrical connection between the package and spring-loaded pins. The bolts are fed into two tapped posts welded to the steel sleeve. The posts are tapped through their length ensuring no air will be trapped in the threads when the system is under vacuum. The sleeve, posts, and mask are designed to maximize thermal contact between the sample chamber and the ceramic package.

Unlike the ZIF socket, which is mounted inside of the chamber vertically along the centerline axis, the second configuration mounts the package horizontally above the sample chamber opening. The exposed socket offers the same quick and easy sample replacement found with the ZIF socket, but is constructed with vacuum compatible materials (ceramic versus plastic). A conical reducer is used to provide clearance for the ceramic sample holder and steel mask between the sample chamber and the extension arm.

Pressure in the 10^{-7} Torr range is achieved using a TMP 361 turbomolecular pump backed with an EcoDry M15 rotary piston pump ^{1,2}. It takes approximately 12 hours of pumping to achieve high vacuum with the configurations described above. High vacuum was chosen to balance the likelihood of stiction failure events. Below the mTorr range most of the water is removed from the chamber and humidity induced stiction events are reduced. At UHV, the surfaces are too clean, and the switches cold-welds on first contact. An adhesion failure at first closure was recorded during this experimentation for a switch operated at 10^{-10} Torr. Despite only pumping to high vacuum, the apparatus was designed for UHV to accommodate the low pressure associated with testing at liquid helium temperature.

3.1.2 Wiring configuration

The RF MEMS switch die are mounted on ceramic gold sidebrazed packages. The die is seated in a 0.250 square cavity and is electrically connected to the package via 1 mil gold wirebonds. Wirebonding was performed by a commercial company who used conductive epoxy to bond the die to the package. Later, in an effort to remove any materials that might cause the formation of adsorbed film layers or stiction failures, the devices were wirebonded at NEU with no epoxy, using only the strength of the wirebonds to hold the die in place on the package. Initially there was concern that the wirebonds lacked the strength to anchor the die to package using only wirebonds, but to date only three bonds of the several hundred made have fractured.

Internal wiring is composed of standard braided copper vacuum wire. Wire ends terminating at the electrical feedthrough are silver soldered to crimp connectors that slide over the feedthrough pins. The opposite terminating end is soldered to pin sockets. In the case of the wiSpry sample chamber, the pin sockets attach to the ZIF socket. In the second chamber, the wires terminate with spring-loaded gold pin sockets, which make direct connection with the ceramic package carrying the MEMS die.

External wiring configurations are specific to the device being measured and can be found in the Appendix. Constantan wiring is used for the external wiring on the apparatus.

Constantan wire maintains nearly the same resistance over a wide temperature range. This ensures that fluctuations in the measured contact resistance were not from thermal fluctuations in the wires. Externally strung wires were taped against the outer walls of the apparatus and are directly exposed to liquid helium and liquid nitrogen to stop heat conduction along their length that can cause sample warming. The ends connecting with the electrical feedthrough were soldered into place, while the opposite ends were fed into to d-sub connectors. The d-sub connectors are mated with complimentary d-sub connectors with static ends terminating at the electronics used to operate the switch and measure the contact resistance. This ensures that the wiring configuration is consistent and limits mistakes made by measuring the incorrect electrical lead. More importantly it limits damage to the switch that may occur by connecting high voltage actuation leads across the switch contacts. In instances where wiring mistakes have been made, the switch has been irreversibly damaged. This has included shorting the switch into the closed position, evaporating the gate voltage line, and extreme degradation of the switch contacts.

3.1.3 Device cooling and temperature measurement

A three-chamber Cryofab cryostat is used to cool the apparatus to liquid helium (LHe) and liquid nitrogen (LN₂) temperatures. During data collection the innermost chamber, where the vacuum test chamber is inserted, is filled with either LHe or LN₂. The intermediate chamber is filled with LN₂. Sample chamber temperatures of ~100 K can be achieved by filling the intermediate chamber with LN₂ while leaving the inner chamber empty. The outermost chamber is an evacuated shell that insulates the inner chambers from ambient temperatures. The top of the cryostat is fitted with a specially fabricated cap that seals the innermost chamber from ambient conditions. The four-way cross rests on the top of the cap and the extension arm passes through the center of cap. A firm seal, but not vacuum tight, is formed between the cap and extension arm. Nearly all of the extension arm and the sample chamber are sealed below the cap inside of the innermost cryostat chamber. The cap has an access port for filling the cryostat with LN₂ and LHe.

LN₂ and LHe temperatures are achieved by filling the innermost chamber of the cryostat. LN₂ is poured into the cryostat chamber through the access port on the cap. Due to the large mass of the sample chamber and transfer arm and the heat conducted by the four-way cross outside of the nitrogen bath, it takes approximately one hour for the sample chamber to reach an equilibrium temperature of 78 K.

Additional steps are required for cooling the sample chamber before immersion in LHe. LHe will evaporate if applied directly to the sample chamber, even if the chamber has been pre-cooled to 100 K. Prior to immersion in LHe, the sample chamber is placed in a LN₂ bath for an hour, and then placed into the cryostat just prior to the addition of LHe. Both ends of the transfer rod used to move LHe from its dewar into the cryostat are also placed in the LN₂ bath. To move LHe into the cryostat, the transfer rod is lowered into the LHe dewar and into the access port on the cryostat cap. The LHe dewar is sealed and gas backpressure forces LHe into the cryostat. Raising and lowering the transfer arm into and out of the LHe dewar changes the flow rate of LHe into the cryostat. Due to the large mass of the sample chamber, LHe must be released into the cryostat chamber at a slow, controlled rate or it will evaporate. This process may take up to an hour. While the large mass of the sample chamber makes it more difficult to cool, once it reaches 5.6 K it will remain there for over 24 hours.

Two thermometers are used for measurement, a silicon diode and a platinum resistance (PT-100). The temperature is read and recorded with a LakeShore Model 330 Autotuning Temperature controller. The thermometers are mounted on the outside of the sample chamber at the same level as the device. The thermometer wiring is composed of constantan wire in a four-wire sense configuration.

External temperature measurements are used in place to internal temperature measurements to reserve electrical feedthrough slots for data collection. A comparison of two platinum resistance thermometers, one mounted internally on the ceramic package and the other externally, shows that the internal temperature lags behind the external temperature as the system is warmed (Fig. 8.3). However, the internal and external temperature readings are accurate at static temperatures.

3.2 RF MEMS test devices

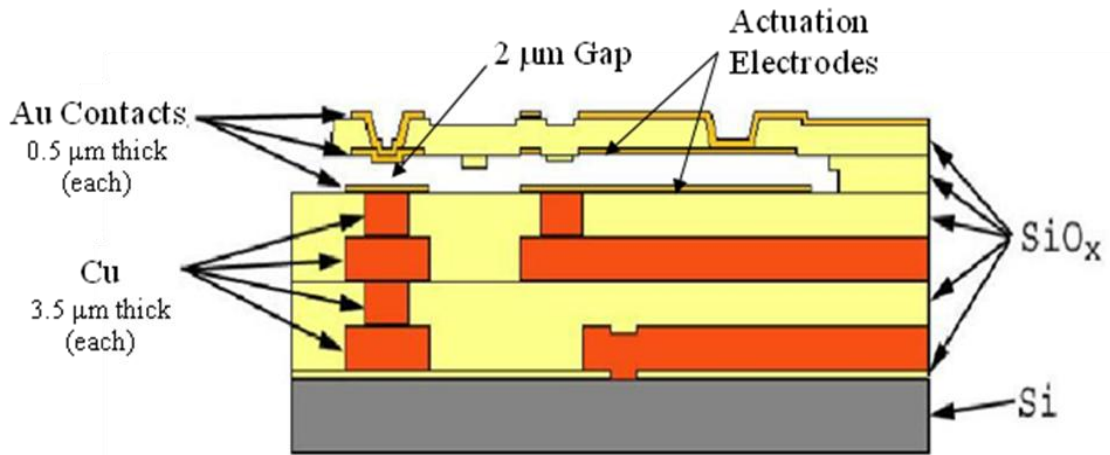
Data was recorded on three different RF MEMS devices provided by wiSpry, NEU, and RFMD. All three switches are metal contacting MEMS switches with gold contacts. Temperature and creep experimentation was performed on the wiSpry and NEU switches. Pressure and atmospheric experimentation was performed on the wiSpry and RFMD devices. Switch characteristics and differences in contacting mechanics and geometries are enumerated below.

3.2.1 *wiSpry RF MEMS switch*

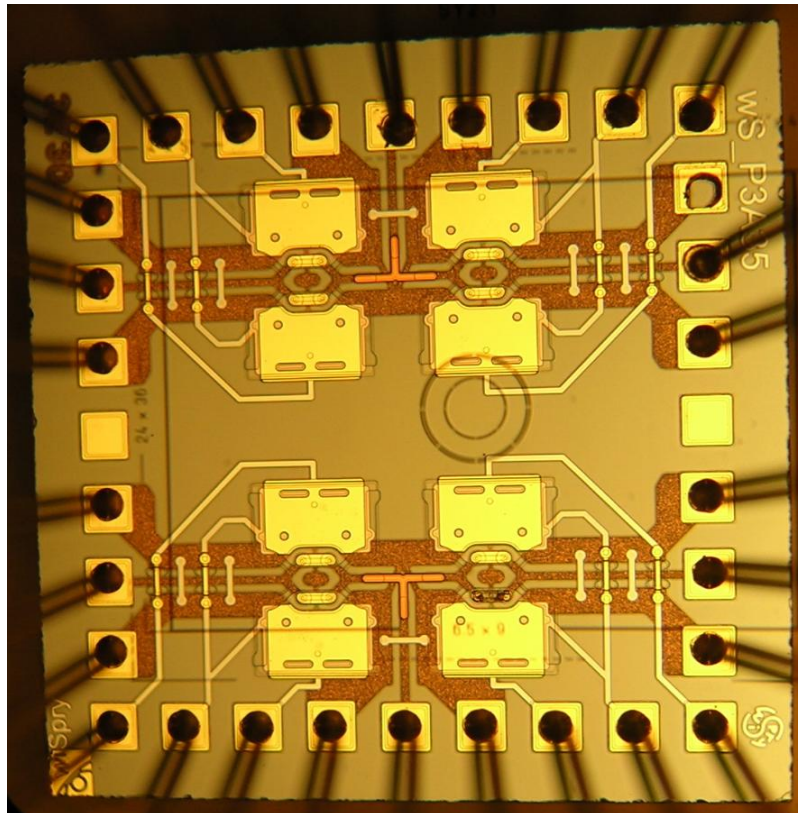
The wiSpry switch is a broadside metal contacting switch (Fig. 3.4). The transmission line is fabricated with a gap that is bridged by the contacts while the switch is in the closed state. The non-contact portion of the beam is used for switch actuation. In the case of the wiSpry switch, the cantilever is a single fixed end beam composed of SiO_x with gold embedded to form the actuation electrode. The contacts are at the end of the beam. The cantilever beam is 135.5 μm in length and 251 μm in width. Actuation requires 30–40 V and a current of ~3–5 μA.

The switch has two contacts in series that are separated by 55 μm and are 2 μm above the drain, or transmission line. The contacts are 5 μm in diameter. Contact resistance measurement taken in a helium gas environment at room temperature ranged from 0.7–6 Ω, with most devices in the 1.5–2.0 Ω range.

Fabrication of the die includes four sets of switches in a single pole double throw (SPDT) configuration. 32 bond pads are placed around the perimeter and are used to provide signal to and from the switch and actuate it. Each die contains four pairs of SPDT switches. Two SPDT switches share a common input signal pad but each SPDT has its own output signal pad. Each SPDT is actuated using three bond pads. SPDT switches can be wired so that both switches actuate at the same time, or one side at a time depending on the configuration of hot and ground leads applied to the bond pads. Wirebonding and pin-out schematics are contained in the Appendix.



(a)



(b)

Figure 3.4 – (a) Schematic planar view of wiSpry RF MEMS switch. (b) wiSpry RF MEMS die with four SPDT switch sets ³.

3.2.2 NEU RF MEMS switch

The NEU switch is an inline metal contacting switch (Fig. 3.5). The transmission signal enters at the anchor or fixed end, travels the length of the cantilever beam and exits to the transmission line (drain) through the contacts at the end of the cantilever beam. Because the signal must travel through the cantilever beam and the beam must be stiff enough to overcome the force of adhesion at the contacts, the cantilever is fabricated using a thick layer of electroplated gold ($\sim 9 \mu\text{m}$). The cantilever is $75 \mu\text{m}$ long by $30 \mu\text{m}$ wide⁴. The pull-down electrode is $15 \times 25 \mu\text{m}^2$ and separated from the cantilever by $0.6\text{--}1.2 \mu\text{m}$. The short, thick design results in a stiff structure and requires $60\text{--}80 \text{ V}$ and a current of $\sim 6\text{--}10 \mu\text{A}$ to actuate into the closed position.

The switch has two contacts separated from the transmission line by $0.4\text{--}0.6 \mu\text{m}$ above the drain. The contact area is $\sim 5 \mu\text{m}^2$. Contact resistance is $2\text{--}3 \Omega$ at $100 \mu\text{N}$ of contact force.

Fabrication of the switch die includes 32 switches around the perimeter and another ring of 16 with four point probe configurations set inside of those (Fig. 3.6). The switches from Fig. 3.5 used for experimentation are along the perimeter of the die. They are operated using three bond pads. These bond pads are wirebonded to the gold sidebrazed ceramic package (bond diagrams and pin-outs contained in the Appendix). All switches share a common signal bond pad. The remaining two bond pads are device specific. The first bond pad is the gate used for actuation. Unlike the wiSpry configuration where a ground is provided for the lower actuation electrode, only one bond pad is needed to actuate the NEU switch. The second unique pad is the drain, or signal out.

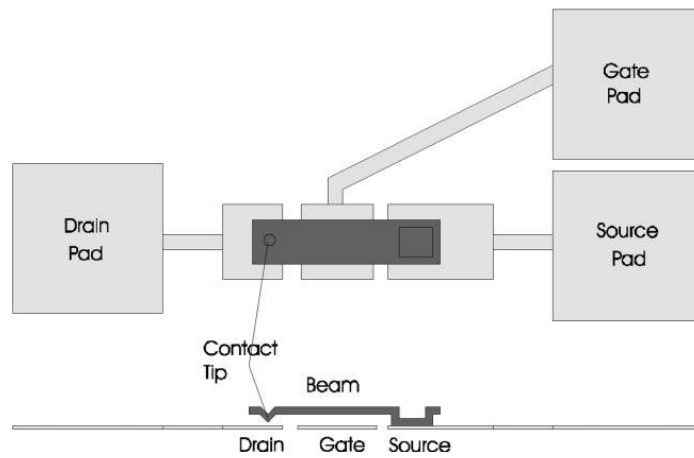
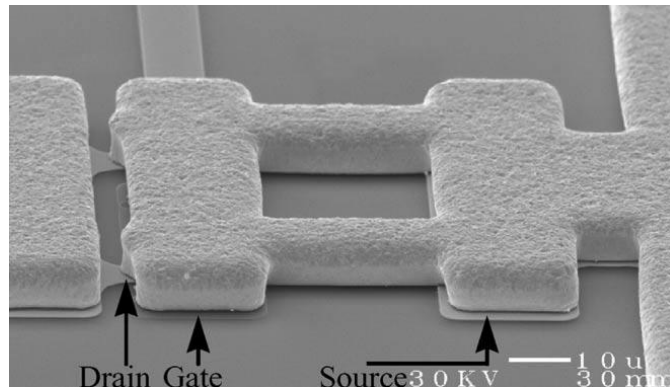


Figure 3.5 – Northeastern University (NEU) RF MEMS switch. (Ref. [5], Figs. 1&2)

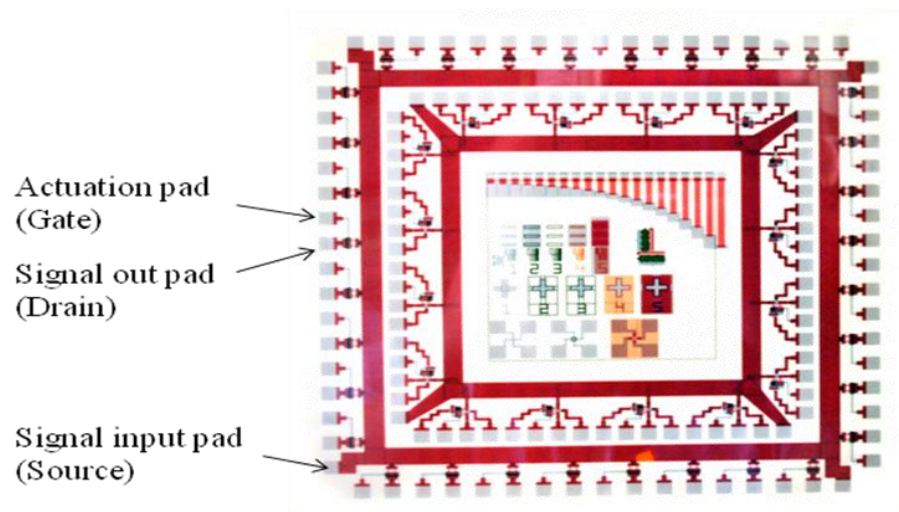


Figure 3.6 – NEU switch die ⁶.

3.2.3 RFMD RF MEMS switch

The RFMD switch is an inline metal contacting switch (Fig. 3.7). Like the NEU switch, the cantilever is constructed of thick gold layer which allows the transmission signal to travel through the length of the beam and maintains the stiffness required to break contact. The pull-in voltage is less than 100 V with beam collapse and shorting at 150 V. The close time is approximately 5 μ s. The contact resistance is approximately 1 Ω . The switch is designed to meet the power handling (> 2 W) and frequency requirements of cellular communications systems and has been proven to 1×10^8 cycles.

For commercial applications the switch is sealed under vacuum conditions in a WLP (wafer level package, Fig. 3.8). The vacuum environment creates very little gas damping and greatly increases the quality factor, Q . As a result the switch bounces numerous times under single step square wave actuation voltages. RFMD has devised a two step actuation scheme that reduces switch bouncing in the WLP. The switches used for bounce testing in this thesis were not hermetically sealed and were tested in normal atmospheric conditions.

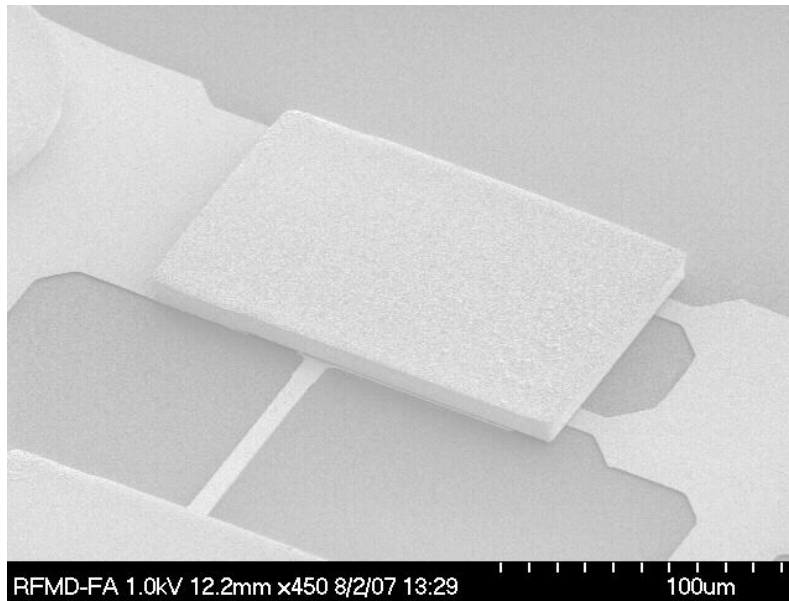


Figure 3.7 – RFMD RF MEMS switch ⁷.

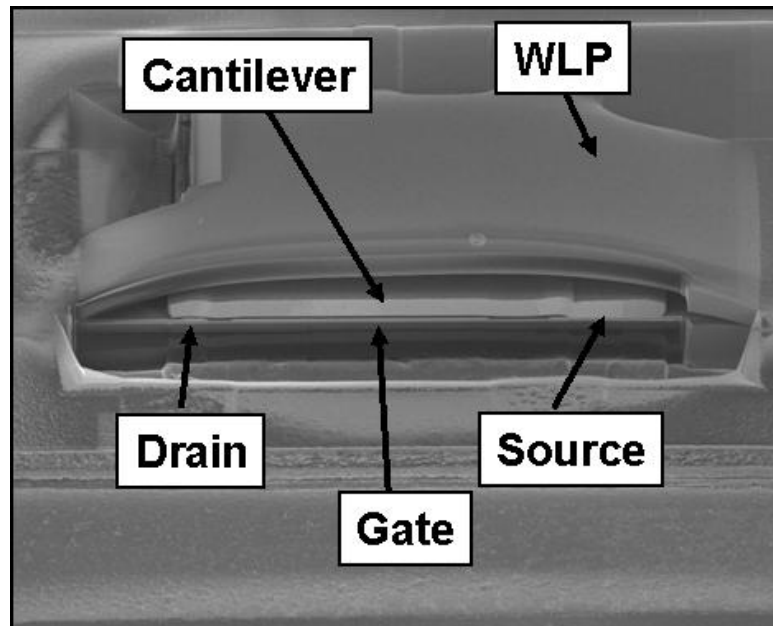


Figure 3.8 – RFMD switch hermetically sealed in a WLP ⁸.

3.3 Data taking procedures

3.3.1 Device handling and storage

MEMS devices are highly susceptible to damage and contamination from their storage environment. A set of procedures were enacted to lessen the number of failures due to release, handling, and storage of MEMS switches. These procedures were initiated due to a large number of switches (> 80%) that were unusable for experimentation. The most common pre-experimentation failures were switches stuck at the contacts, shorted switches, and switches unable to actuate. Many switches also had abnormally high contact resistances (> 10 Ω) on first closure, and a large portion had physical damage to the die.

A large portion of the observed physical damage occurred during the release procedure. Die must be kept separate from each other during the etching and rinsing steps. In an attempt to speed the release process, ten die were placed in the same etching and rinse solutions without physical separation from each other. During the rinse step, eight of the ten die stuck together, rubbing the exposed switch structures against the die above it. Visual examination of these die showed widespread damage, including deep surface gouges, malformed switch structures, and switches torn from the die. Contact testing of the intact switches revealed that more than 90% were inoperable, mostly from being stuck in the closed position.

Additionally the release process should be performed before wirebonding. In an attempt to provide clean contact surfaces, a die was wirebonded and then released while on the package, with the intent of immediately placing the released device in the vacuum chamber. The harsh etching chemicals used during the release process caused the gold wirebond pads on the ceramic package to delaminate. More than 50% of the wirebonds broke free of the ceramic package.

Currently, the procedure is to release and wirebond the switches in the laboratory; however, at the time of experimentation, the devices were released either by the switch supplier or in the laboratory and sent to a commercial wirebonding service. Post-release the NEU switches are tested with a probe station to check for switch failures and to determine

pull-in voltage for working switches. Over 40% of the switches operated with the probe station were not operable once wirebonded to the ceramic package. There is no available data to determine if the large number of inoperable switches was impacted by shipping the devices or from the wirebonding procedure itself.

Post-wirebonding the switches are stored in gel-pak boxes in a nitrogen glovebox. Storing in the nitrogen glovebox controls relative humidity levels between 10-40%. Too low humidity promotes a build-up of electrostatic fields and too high promotes stiction failures. Prior to experimentation the switches were cleaned via oxygen plasma for 15 minutes in a MARCH Asher O₂ plasma cleaner (300 W, 600 mTorr, 75 sccm flow). The only exception to the storage and plasma cleaning procedures was for the wiSpry switches before the impacts of switch cleanliness and failure mechanisms were understood.

Beyond release and storage, additional steps were taken to limit failures from electrostatic discharge (ESD). The voltage released from person to device during an ESD event can easily destroy a switch. Switches are always handled while wearing an ESD wrist strap and any work done with the switches in ambient conditions is performed on an anti-static tablemat with an ion fan (Eliminator Jr. high output ion fan) blowing across the switch. Additionally, the vacuum chamber is always grounded during experimentation and while transferring the package in and out of the sample chamber.

3.3.2 Electronics

Before and during data taking the experimental apparatus is connected to a number of instruments used to determine the switch's operational state, actuate the switch, and record data. Switch actuation is controlled with a Keithley 2400 Sourcemeter ⁹. It can deliver actuation voltages up to 210 V while limiting the current to a user defined level. For Actuation voltages ranged from 30 V for wiSpry switches to 70 V for NEU switches (at room temperature), and the current compliance was set at 10 μ A. The current compliance is set to prevent damage to do the switch, but a penalty is paid in the slew rate from 0 V to the desired output. A rise time of 400 μ s was recorded for 55 V. This is a comparatively long time given the NEU switch time is 1–2 μ s. Putting the Keithley 2400 in fast mode cuts the rise

time to 250 μ s at 55 V. In fast mode the desired voltage is delivered more quickly, but with less precision. An alternative hardware configuration utilized a waveform function generator, which has nanosecond rise times, with a signal amplifier (TEGAM) to obtain faster switching speeds. All experimentation described in this thesis used a Keithley 2400 for actuation.

The actuation wiring configuration is switch dependent. The wiSpry switch has three bond pads for switch actuation. To actuate both switches in the SPDT at the same time (as the switch was designed for) the two hot leads are tied together and connected to the high side output from the Keithley 2400, and the ground actuation bond pad is connected to the low side of the Keithley 2400. It is possible to actuate one side of the SPDT pair by tying the hot lead for the unactuated switch and the actuation ground to the low side of the Keithley 2400. The high side is attached to the bond pad corresponding to the switch to be actuated.

In the case of the NEU and RFMD switches only one bond pad is used to actuate the switch. The high side of the Keithley 2400 is connected to the gate bond pad. The low side of the Keithley 2400 is connected to the ground lug on the back of the instrument.

A second Keithley 2400 measures contact resistance. The resistance measurement is made by supplying current and reading voltage or vice-versa. Initial experiments on the wiSpry switches supplied current, usually 100 μ A or 1 mA, while limiting the voltage to 0.5 V. Current was kept low to prevent damage to the contacts. However, with a firmer grasp on the contact physics, it became apparent that the voltage drop across the asperities drove heating effects and changes in contact resistance. Thus, subsequent experiments were reconfigured to deliver a constant voltage and read the current (limited to 50 mA). Four-point measurements were made for all contact resistance measurements.

Temperature is measured via a Lakeshore Model 330 Autotuning Temperature Controller with a platinum resistance (PT-100) and a silicon diode thermometer. The platinum resistance thermometer uses the preset Curve 03 (DIN Curve 43760) on the LakeShore to measure temperature. The silicon diode thermometer uses a user defined soft-calibration curve generated for this apparatus/thermometer combination by making voltage/temperature measurements at room temperature, in a LN₂ bath, and in a LHe bath¹⁰. Temperature data in this thesis is recorded from the silicon diode thermometer because it

provides the most accurate reading over a wide range of temperatures and is calibrated specifically for this apparatus.

3.3.3 Pre-test procedures

Before placing the die into the vacuum chamber, every switch is visually inspected under a microscope. Broken wirebonds, large debris on the die, scratches, and other abnormalities are recorded. This provides a physical record of preexisting conditions that may have led to switch failure. The visual inspection is followed by an electrical inspection to check for nonfunctioning switches. This is a double check of the switch condition taken pre or post-wirebonding and is performed because switches have changed their operational disposition between testing post-release and insertion into the vacuum system (i.e. previously nonfunctional switches become operational).

The electrical check is made with the Keithley 2400s. 1 mA of current (0.1 V compliance) is applied to the transmission line with no actuation voltage applied. Switches stuck at the contacts will register a contact resistance value. Potentially operational switches will reach voltage compliance as the Keithley 2400 attempts to supply an infinite amount of voltage in reaction to the infinite resistance of the open switch circuit. A secondary check is made to see if the switch is fully operational by applying actuation voltage and then applying the DC signal to see if the switch is closed (the DC signal should be removed before opening the switch to avoid hot-switching). The Keithley 2400 supplying actuation voltage should be checked to see if current compliance has been reached. Current compliance on the actuating Keithley 2400 indicates that the switch has shorted (i.e. the two actuation electrodes have come into contact).

Operational switches are tested for the voltage needed to make contact, or pull-in voltage. This is done using a hot-switching setup with a very low voltage compliance set on the DC signal power supply. Actuation voltage is ramped in small steps until stable contact resistance is achieved. The actuation voltage is then lowered until the switch opens. The actuation voltage required to break contact is about 60% of the voltage required to make contact. This procedure should be repeated if the sample is cooled to lower temperatures to

determine the effects of temperature on cantilever stiffness and the amount of voltage required to properly test the switch contact resistance.

Pre-test cycling is built in as an option on all LabView programs written for these experiments. The pretest cycling allows for a user-defined number of cold cycles, usually 200, to be applied directly before an experimental run initiates. The cycling is not meant to be like the “Schaltreinigung” procedure (50 V, 50 mA, for 40 cycles in an N₂ atmosphere) used by Schimkat to produce clean metallic surface prior to contact resistance measurements¹¹. The cold cycling is utilized to roughen the surface and remove any changes to the surface topography from previous tests.

Additionally, null runs are taken to determine the contact resistance contribution from the experimental apparatus and the switch transmission lines. For this experiment a four-point resistance measurement is taken at the electrical feedthrough. Therefore the measured contact resistance includes the resistance from the vacuum wire, sockets, ceramic package, and wirebonds in addition to resistance from the device’s transmission lines and the constriction resistance. Two null runs are taken. The first uses a ceramic package where two leads have been wirebonded together. A contact resistance measurement is taken for the system across a temperature range from 5.6 K to 293 K and is used as a baseline for the apparatus’ contribution to the measured contact resistance at a given temperature.

The second null run is designed to account for the resistance from everything but the constriction resistance. To achieve this, a switch is subjected to a procedure much like the Schaltreinigung procedure, where it is hot-switched at high voltage, but is left in the closed position with the voltage applied after the cycling. After 15 minutes of closure with the voltage applied, the voltage is removed, but the switch is left in the closed state where it will weld shut as it cools. The end result is a fused switch with large contact area. A contact resistance measurement is taken for the fused switch across a temperature range from 5.6 K to 293 K and is used as a baseline for the apparatus and device contributions to the measured contact resistance at a given temperature.

3.4 Chapter organization

In the following chapters data and theory will be presented on the environmental effects on switch contact physics and creep in gold contact RF MEMS switches:

Chapter 4 covers the impact of high and low pressure on switch contact. It forms the preliminary basis for understanding how the switch operates under normal conditions and the observed changes in operation when the pressure is reduced. Results are reported for switch bounce and switch close time as a function of pressure. Bounce data and switch geometries are correlated to the fluid mechanics governing switch actuation.

Chapter 5 covers the impact of cryogenic temperatures on the contact physics of gold micro-contacts. Results are reported for changes in contact resistance at 293 K and 77 K. The effects of rapid cooldown on contact resistance are reported as well as contact resistance variability for switches operating in nitrogen atmosphere at liquid nitrogen temperature. Results are shown that indicate the presence of an adsorbed film with temperature dependent properties. The results are correlated to existing single asperity contact physics equations and the asperity heating model.

Chapter 6 uses experimental measurements of contact resistance as a function of time and modeling predictions to characterize the electro-mechanical response of gold micro-contacts. Experimental data show that the contact resistance is time dependent. The data is correlated to a single asperity model that uses a fractal representation of the surface topography. The recorded changes in contact resistance are shown to evolve as a function of time due to changes in real contact area, then numbers of asperities in contact, and the temperature and resistivity profiles at the contact points.

Chapter 7 correlates the measured and calculated time-dependent contact resistance reported in Chapter 6 to a power law relation derived from the single asperity creep model. Theoretical data is shown to have an exact fit with the power law. The experimental data is also well described by the power law when an additional term accounting for contributions from other switch components and adsorbed films on the contacts is included. Power law parameters are correlated to switch characteristics such as contact materials and surface roughness.

Chapter 8 covers contact resistance measurements as a function of dynamic temperature change, time, contact voltage, and cycle number. Results are reported the temperature dependence of contact resistance ranging from 77 K up to 293 K and are correlated to data reported by Jensen *et al.* over a temperature range of 293 K to 393 K. Additionally, time dependent contact resistance is reported for extended closures on the order of days. The onset and effects of contact heating are reported for a fused switch at room temperature. Contact resistance as function of cycles is reported for a wiSpry switch out to 10^6 cycles.

Chapter 9 covers the temperature dependence of the creep mechanism. Results are reported for time dependent contact resistance at 293, 77 and 5.6 K for two different RF MEMS switches. The switches are shown to follow the power law described in Chapter 7 at room temperature; however, at cryogenic temperatures the power law does not accurately describe the time dependent contact resistance. Data show the creep mechanism is significantly decreased at cryogenic temperatures. The single asperity creep model in Chapter 6 is modified to account for changes in temperature and shows that the increase in real contact area as a function of time is reduced at 77 K. At 5.6 K experimental data and modeling show that contact heating dominates the contact resistance measurement.

Chapter 10 summarizes the experimental and modeling results reported in the thesis, and suggestions for future work are provided.

3.5 References

¹ See Kurt J. Lesker catalogue,

http://lesker.com/newweb/Vacuum_Pumps/turbopump_leybold_tmp_1.cfm

² See Kurt J. Lesker catalogue,

http://lesker.com/newweb/Vacuum_Pumps/rotarydrypistonpump_leybold_ecodry_1.cfm

³ Provided by Art Morris of wiSpry, Inc.

⁴ J. Guo, N.E. McGruer, and G.G. Adams, "Modeling, simulation and measurement of the dynamic performance of an ohmic contact, electrostatically actuated RF MEMS switch," *J. Micromech. Microeng.*, vol.17, pp. 1899-1909, 2007.

⁵ S. Majumder, N.E. McGruer, G.G. Adams, P.M. Zavracky, R.H. Morrison, and J. Krim, "Study of contacts in an electrostatically actuated microswitch," *Sensors and Actuators A*, vol.93, pp. 19-26, 2001.

⁶ Provided by N.E. McGruer of Northeastern University.

⁷ Provided J. Hammond of RFMD.

⁸ J. Costa, T. Ivanov, J. Hammond, J. Gering, E. Glass, J. Jorgenson, D. Denning, D. Kerr, J. Reed, S. Crist, T. Mercier, S. Kim, P. Gorisse, "Integrated MEMS switch technology on SOI-CMOS," 2008 Solid State Sensor, Actuator and Microsystems Workshop (Hilton Head 2008), Hilton Head Island, South Carolina, June 1-5, 2008.

⁹ See Keithley 2400 user's manual, www.keithley.com/data?asset=888

¹⁰ See LakeShore 330 user's manual,
http://www.lakeshore.com/pdf_files/Obsolete/330_Manual.pdf

¹¹ Schimkat, J., "Contact materials for microrelays," *Micro Electro Mechanical Systems, 1998. MEMS 98. Proceedings., The Eleventh Annual International Workshop on*, pp.190-194, 25-29 Jan 1998.

CHAPTER 4

The Impact of High and Low Pressure on Switch Contact

4.1 Introduction

The environmental operating conditions can have a substantial impact on the contact physics of RF MEMS switches. Typically device failure mechanisms and their impact on the contact physics are tested by varying the operational parameters such as actuation voltage, contact force, contact voltage, and current. However each of these varies as the operating environment changes. For example, temperature affects the material properties such as resistivity and heating at the asperity level, which in turn have a substantial impact on the measured contact resistance. The actuation voltage required to achieve optimum contact force also shifts with temperature. The force with which the switch contacts strike the lower electrodes is governed by design characteristics, temperature, and pressure. How the switch makes contact and stays in contact affects the switch contact surface topography and the contact resistance.

Since the impact of operational parameters is relative to the environment, it is important to understand how switch dynamics, or how the switch operates, vary when subjected to a change in environment. In order to form baseline knowledge of switch dynamics a series of experiments were conducted across a range of pressures (Chapter 4) and temperatures (Chapter 5). These results provide a basis for understanding how environmentally induced changes to switch dynamics contribute change the contact physics and how those changes can be harnessed to isolate failure mechanisms.

Ambient pressure strongly affects damping in MEMS devices. The damping has considerable impact on the device's performance and longevity. MEMS devices are designed to operate in specific damping conditions. For example microaccelerometers use high damping to reduce the influence of external disturbances and resonant sensors use low damping to achieve high sensitivity and resolution. Damping is especially prevalent in RF MEMS switches, both cantilever and fixed-fixed designs ¹. Therefore, it is essential to understand damping and its effect on beam physics to optimize device performance.

A large body of literature exists exploring cantilever beam mechanics and simulations for MEMS switches. Guo *et al.* and Younis *et al.* both provide excellent coverage of previous beam physics and damping simulations as well as offer new variations on the beam

mechanics as a function of physical parameters such as device dimensions and pull-in voltages ^{2,3}. Very few papers focus on the environmental component of damping. Newell measured the variation in the quality factor, Q , with respect to air pressure for resonators with various length-to-thickness ratios ⁴. Gupta and Senturia measured the pull-in time of a fixed-fixed beam as function of pressure ⁵. This section of the thesis focuses on the pressure dependence of damping in RF MEMS switches.

4.2 Fluid physics and damping fundamentals

The equation of motion for a MEMS switch beam is given by d'Alembert's principle as ⁶:

$$m \frac{d^2 x}{dt^2} + b \frac{dx}{dt} + kx = f_{ext} \quad (4.1)$$

where m is the mass of the cantilever, x is the cantilever displacement, b is the damping coefficient, k is the spring constant, and f_{ext} is the external force. The second and third terms of the equation are of particular interest as these arise from pressure dependent switch dynamics.

There are several energy dissipation mechanisms in MEMS cantilevers; however, this chapter focuses on viscous damping. Most of the damping in MEMS structures is from squeeze film damping ⁷. During actuation, as the beam approaches the substrate, gas molecules undergo collisions as they are pushed from underneath of the cantilever. The gas pushed out from under the cantilever creates a damping force (second term in (4.1)) and the compressed air in the gap creates a spring force resisting closure (third term in (4.1)). These forces are derived from fluid mechanics physics.

Squeeze-film damping is modeled using the Reynolds equation derived from the Navier-Stokes equations. The Reynolds equation relates time-dependent pressure, viscosity of the fluid (gas), and the distance between the cantilever and substrate. The underlying assumption is that the gas in the gap can be considered as a continuum. The gas flow can be divided into four regimes, with each regime correlated to a range of values for the Knudsen number:

$$K_n = \frac{\lambda}{g} \quad (4.2)$$

where λ is the mean free path, or distance a gas molecule travels between collisions, and g is the gap distance between the cantilever and the substrate.

The mean free path is pressure dependent and for a pressure P_a is:

$$\lambda_a = \frac{P_0}{P_a} \lambda_0 \quad (4.3)$$

where λ_0 is the mean free path at pressure P_0 . The mean free path for most gasses is 0.07-0.09 μm at standard temperature and pressure (STP), but at low pressure (mTorr or less) the mean free path can be greater than the gap in most MEMS switches.

The Knudsen number is a measure of the viscosity of the gas under the cantilever. A small value means that there are many collisions and that the gas is viscous. However, in the case of large K_n as is the case with most MEMS switches, particle-wall interactions become important. In this regime the flow resistance, or viscosity (μ), is reduced and a slip effect must be taken into account for the reduced number of collisions gas molecules undergo before escaping the gap. The viscosity for ideal and quasi-ideal gases (air, nitrogen) is:

$$\mu = 1.2566 \times 10^{-6} \sqrt{T} \left(1 + \frac{\beta}{T}\right)^{-1} \text{ kg/m}\cdot\text{s} \quad (4.4)$$

where $\beta = 110.33 \text{ K}$ and T is temperature in Kelvin. At STP, the viscosity of an ideal gas is $1.845 \times 10^{-5} \text{ kg/m}\cdot\text{s}$ (or $\text{Pa}\cdot\text{s}$). Note that by (4.3) and (4.3), the viscosity is directly dependent on pressure, thus impacting the damping. The viscosity in (4.5) is valid for an ideal gas at STP, however as pressure decreases and the Knudsen number increases, the flow is no longer viscous and must be described by the effective viscosity coefficient:

$$\mu_e = \frac{\mu}{1 + 9.638 K_n^{1.159}} \quad (4.5)$$

The effective viscosity is accurate to within $\pm 5\%$ for Knudsen numbers between 0 and 880.

A final fluid physics parameter associated with damping is the nondimensional squeeze number:

$$\sigma = \frac{12\mu_e \omega^2}{P_a g^2} \quad (4.6)$$

where ω is the mechanical frequency and ω is the characteristic length (the shorter of the length or width of the cantilever). The squeeze number is directly related to the pressure as well. A high squeeze number ($\sigma > 3$) indicates that the gas is trapped under the cantilever by its own viscosity and is compressed. The compressed air acts as a spring, resisting the closure. A low squeeze number indicates that the gas escapes without compression.

4.3 Damping coefficient and quality factor

A linearized form of the compressible Reynolds gas-film equation is used to derive the damping coefficient for rectangular parallel-plate cantilevers. The damping coefficient is:

$$b = \frac{3}{2\pi} \frac{\mu A^2}{g_0^3} \quad (4.7)$$

where A is the cross-section area of the cantilever, g_0 is the gap distance, and the pressure dependence is captured in the viscosity term μ . The damping force is dissipative and can have a significant effect on the switch beam physics.

The damping force changes as a function of cantilever position and speed. It reaches a maximum just before the switch contacts meet the lower electrodes. At this point the switch is traveling at maximum speed while the gap distance is reaching a minimum. Additionally, changing the design of the switch will change the damping coefficient. The wiSpry switch uses a large cantilever area, A , to increase damping, whereas the NEU and RFMD switches use decreased gap distances. Increasing the damping increases the time to closure but also decreases the number and amplitude of bounces. Close time and bouncing as related to pressure will be discussed later in the chapter.

The damping coefficient and pressure directly affect the beam's quality factor, which can be written expressly for a cantilever as:

$$Q_{cant} = \frac{k}{\omega_0 b} = \frac{\sqrt{E\rho} t^2}{\mu (wt)^2} g_0^3 \quad (4.8)$$

where the numerator of the fraction contains the physical cantilever properties of modulus E , density ρ , and thickness t .

The pressure dependence of the Q factor is captured in the viscosity term μ . At low pressures air damping is negligible, $\mu \cong 0$. Most of the damping is internal, arising from interactions between the different materials in the cantilever and dissipation in the beam root. Metal-based beams like the NEU and RFMD switches have a Q of 30 to 150 in vacuum. Polysilicon beams, like the wiSpry cantilever, can have Q values ranging from 500 to 5,000 in vacuum.

4.4 Switch bounce

Switches have been experimentally observed to bounce several times before making permanent contact with the drain ^{8,9,10,11}. The bouncing occurs due to stored energy in the cantilever and deformed contact material. Bouncing increases the effective closing time and leads to stiction failures. The high impact force, which is dissipated in the subsequent bounces, may induce local hardening and pitting of contact materials and can lead to material transfer and contact welding.

Squeeze-film damping plays an important role in switch bounce. Guo *et al.* found that the damping force was as much as 13.5% of the electrostatic force used to pull the switch into contact (Fig. 4.1) ¹². They further showed that as the switch closed, the squeeze-film damping force resisted closing, and then resisted the cantilever as it bounced upward after first contact. Additional measurements showed that as more actuation voltage was applied (i.e. the downward speed of the cantilever increased), the squeeze-film force increased, resulting in lower impact forces. The increase in actuation voltage decreased close time, but it also increased the magnitude and number of bounces. Guo *et al.* modeled bouncing at high pressures and found that the magnitude and number of bounces, as well as the settling time was substantially decreased with a pressure to 10 atm. To date, no published results include switch bounce as a function of ambient pressure.

The study contained in this chapter explores switch bounce as a function of ambient pressure. wiSpry RF MEMS switches were placed in the first vacuum chamber described in

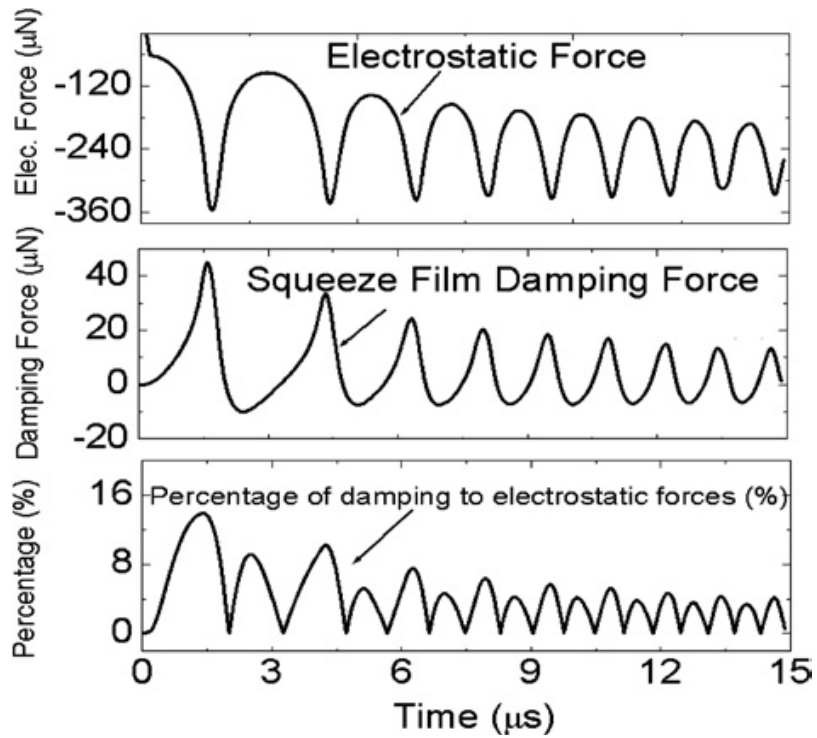


Figure 4.1 – Electrostatic Force F_e , Damping Force F_d , and ratio $\langle F_e/F_d \rangle$ for an NEU switch at an actuation voltage of 74 V. At maximum F_e is 13.5% of F_d . (Ref. [12], Fig. 6)

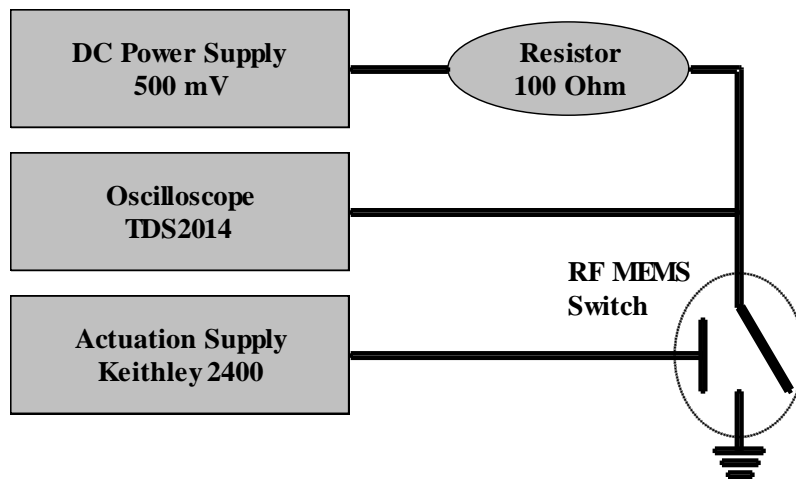


Figure 4.2 – Schematic representation of instrumentation used to measure switch bounce and close time.

Chapter 3. The chamber was evacuated of air and then backfilled with gaseous nitrogen. The pressure was lowered in 10 Torr increments from 760 Torr down to 1 mTorr. At each pressure the switch closure was recorded with a Tektronix TDS2014 oscilloscope that measured the voltage across the switch. The actuation voltage was sourced from a Keithley 2400 source-meter, and the contact voltage was sourced from an unregulated dc power supply. The actuation is a single step voltage from 0V to the voltage required for stable contact resistance measurements. The oscilloscope shows the open and closed state of the switch. When the switch is in the closed state, the reading shows 500mV applied to the contacts. In the open state, the oscilloscope reads 0V. The measurement circuit is show in [Fig. 4.2](#).

Switch closure results for a wiSpry switch at 750, 60, and 40 Torr are shown in [Fig. 4.3](#). The three traces have been normalized to make $t = 0$ the point of first contact on the closure. The wiSpry switch's large cantilever provides a substantial damping force that prevents switch bouncing from normal atmospheric pressure down to 60 Torr. A 20 Torr decrease in pressures results in a significantly longer settling time. [Figures 4.4 and 4.5](#) show switch closure for a RFMD and NEU RF MEMS switches respectively. The directionality of the oscilloscope measurement has been reversed to accentuate the switch bounce. Both the RFMD and also the NEU switch (the same used by Guo *et al.*) bounce at normal atmospheric pressure.

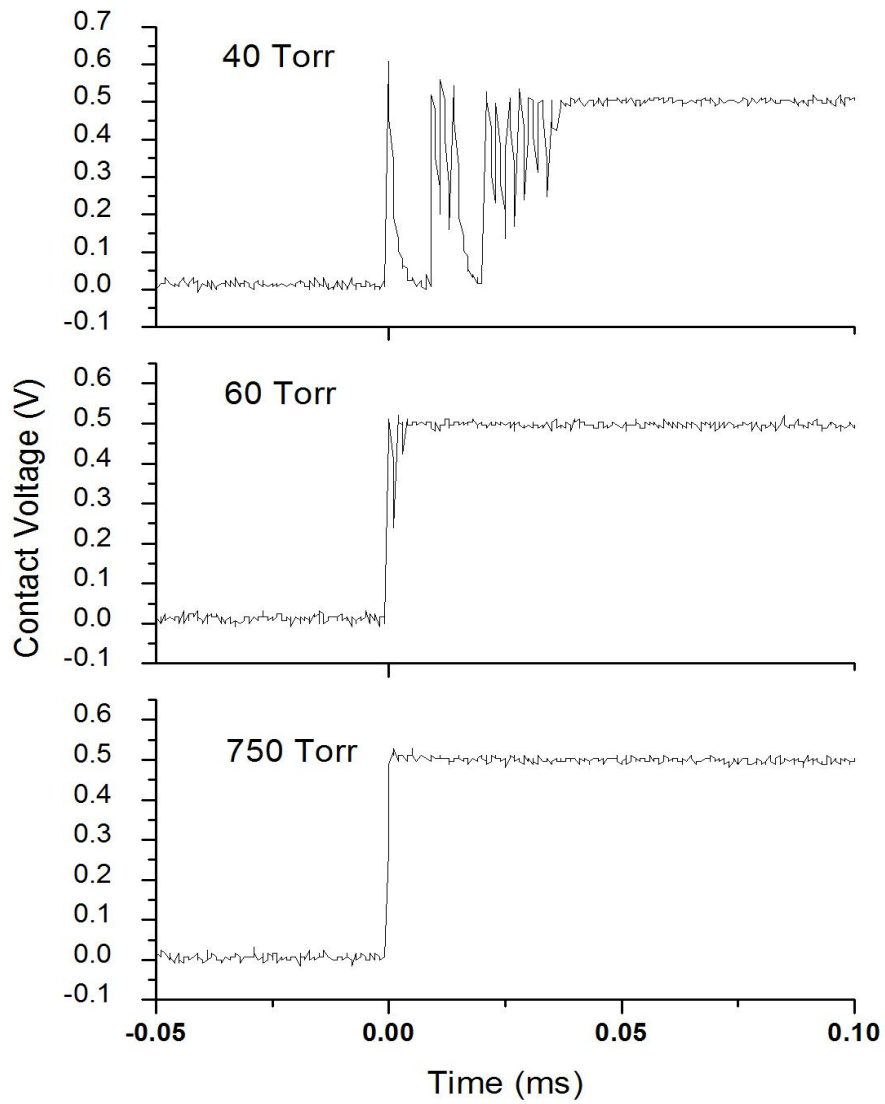


Figure 4.3 – Switch bounce and settling time for a wiSpry RF MEMS switch at 750, 60, and 40 Torr.

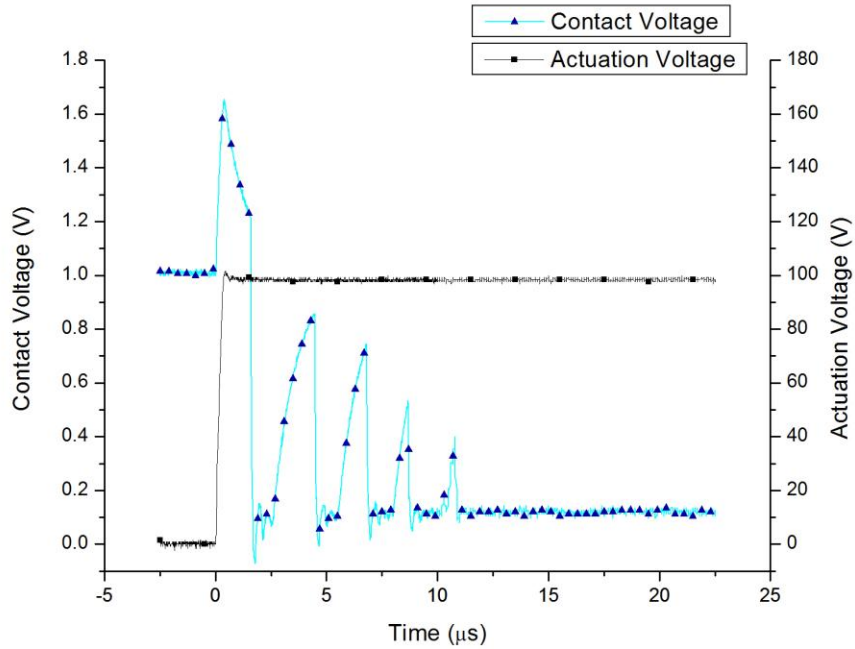


Figure 4.4 – Switch bounce and settling time for a RFMD RF MEMS switch at 750 Torr.

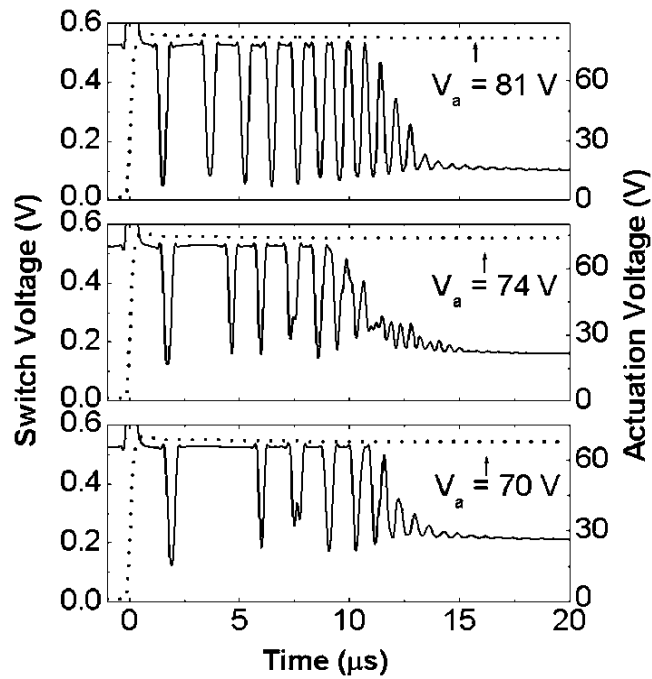


Figure 4.5 – Switch bounce (solid lines) and single step actuation for NEU RF MEMS switch at three actuation voltages. The number and magnitude of bounces is larger for higher actuation voltage, but the settling time is decreased. (Ref. [12], Fig. 11)

Exploring the Knudsen number and damping coefficient for the switches quantifies differences in switch dynamics due to pressure (Table 4.1). At STP the wiSpry switch has a Knudsen number of 5.3×10^{-2} , while at 1 mTorr it has a value of 4.1×10^4 . Reducing the pressure increases the mean free path of the gas and increases the Knudsen number, indicating fewer collisions between the gas molecules in the gap (i.e. lower viscosity) and less resistance to the cantilever upon closing. The damping coefficient at 1 mTorr, using μ_e in place of μ to account for the large Knudsen number and low pressure, is 1.2×10^{-9} . Compared to the downward force used to close the switch, the damping is negligible. This results in switch bouncing that will continue until the energy stored in the cantilever is dissipated.

The NEU and RFMD switches still bounce at atmospheric pressure despite having large Knudsen numbers and damping coefficients. This is driven mostly by the switch’s design. The NEU and RFMD switches both have significantly less cantilever cross-section area than the wiSpry switches. The decrease in cantilever cross-section area decreases the damping coefficient. In the case of the NEU switch, this results in a damping coefficient of 4.3×10^{-4} kg/s, which is nearly an order of magnitude less than that of the wiSpry switch. The gap distance also plays a role in the bouncing. The NEU switch’s gap distance is approximately five times smaller than wiSpry’s. This mitigates some of the bouncing induced by the smaller cantilever area. At normal atmospheric pressure a smaller gap distance results in a higher viscosity and a larger Knudsen number. Additionally, the

Table 4.1 – Knudsen number and damping coefficient values.

Parameter	wiSpry	NEU	RFMD	Units
Knudsen # @ 760 Torr	5.3×10^{-2}	2.0×10^{-1}	8.0×10^{-2}	
Damping Coeff. @ 760 Torr	2.6×10^{-3}	4.3×10^{-4}	9.0×10^{-4}	kg/s
Knudsen # @ 1 mTorr	4.1×10^4	1.5×10^5	6.1×10^4	
Damping Coeff. @ 1 mTorr	1.2×10^{-9}	4.4×10^{-11}	4.1×10^{-10}	kg/s

damping coefficient has a strong dependence on the gap distance. Small decreases in the gap distance can significantly increase the damping.

The damping force must be significant with respect to the electrostatic force pulling the switch into the closed position to mitigate bouncing. It is apparent from a comparison of results from the wiSpry switch in this thesis and the NEU switch in Guo *et al.* that at atmospheric pressure the damping force must be greater than 13.5% of the actuation force in order to mitigate bouncing at closure¹³. Future bounce experimentation will quantify the damping force relative to the electrostatic force for the wiSpry switch and determine the threshold ratio between the forces required to mitigate switch bounce.

4.5 Switching time

Switching time, or the time it takes for a switch to close after the actuation voltage is applied, is strongly dependent on the applied actuation voltage. An increase in actuation voltage results in a decrease in switching time and a decrease in settling time¹⁴. Using the same configuration in Fig. 4.2, the switching time was measured for a wiSpry switch. Results for 48.8 V, the minimum pull-in voltage, and 55.0 V, the voltage needed to sustain stable contact resistance, are found in Fig. 4.6. The data clearly shows a substantial difference in the switching time. It should be noted that the time to switch closure is substantially longer than other reported switching times because of the slow slew rate of the Keithley 2400 as it delivers the actuation voltage. Normal switching times for the wiSpry switch are on the order of 100 μ s. The large delta in switching time between the two actuation voltages is driven by the slow cantilever speed at the lower actuation voltage. At 48.8 V the cantilever velocity is at its slowest. Application of less actuation voltage would result in the switch not making contact.

Pressure is also a factor in switching time, however it has not been experimentally reported in the literature. As previous discussed, a decrease in pressure will decrease the damping force. The decreased damping force results in reduced switching time. Switching time for a wiSpry RF MEMS switch actuated at 55.0 V in 750 Torr, and 60 Torr is recorded in Fig. 4.7.

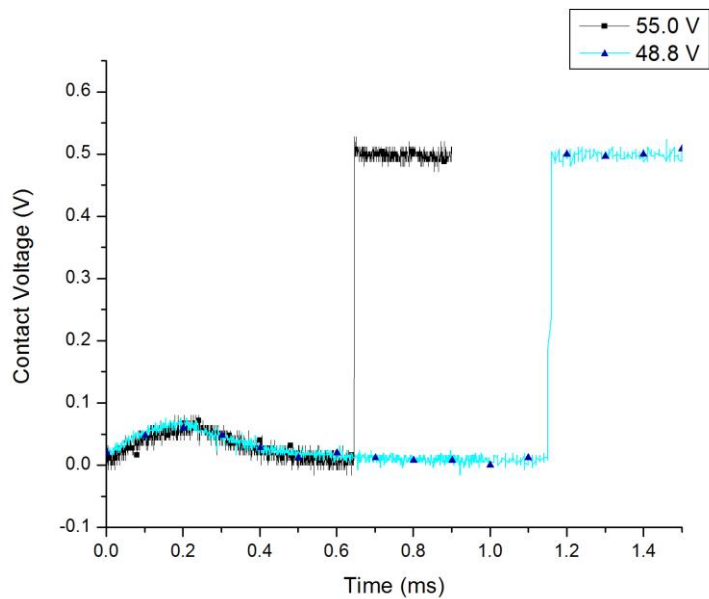


Figure 4.6 – Switching time at 750 Torr for a wiSpry RF MEMS switch at the pull-in voltage of 48.8 V and the actuation voltage needed to reach stable contact resistance, 55.0 V.

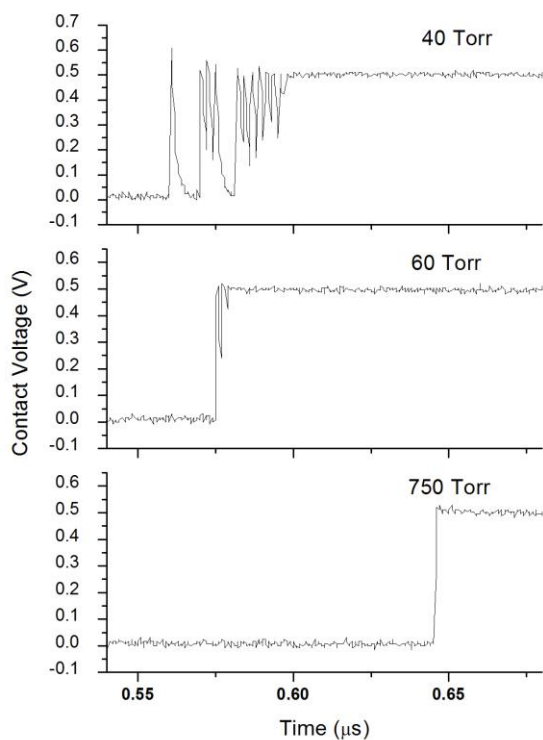


Figure 4.7 – Switching time for a wiSpry RF MEMS switch at 750, 60, and 40 Torr.

While increasing the voltage or decreasing the pressure achieves the same result, they do so in mechanistically different ways. Lowering the pressure lowers the viscosity, which has the effect of significantly reducing the damping force and spring force terms in (4.1). The decreased switching time is offset by increased bouncing and a longer settling time as the energy dissipates in the cantilever. Increasing the actuation voltage increases the damping and spring force terms in (4.1). A higher actuation voltage increases the downward speed of the cantilever, which increases the damping term. Additionally, the increased cantilever speed at higher pressures where viscosity is high, traps more gas underneath of beam. This gas is compressed and acts to resist the closure and the subsequent bounce. The end result is a faster switching time with less bouncing and a shorter settling time. However, this is offset by the increased striking force on initial contact, which can lead to stiction failures.

4.6 Conclusion

Through application of beam physics and fluid mechanics, the impact of pressure on switch bounce and switching time is derived and matched to experimental data. Pairing these results with literature referenced in Chapter 2, pressure is seen to have a significant effect on the contact physics and plays a significant role in several failure modes.

Low pressure results in several changes in the switch dynamics including decreased viscosity, damping force, and spring force. The switching time is reduced, but below a threshold ratio of damping force to electrostatic force, switch bounce occurs and the settling time is increased. Additionally, with damping removed, the cantilever strikes the drain with increased force which increases the likelihood of an adhesion failure. At UHV pressure levels, contaminant film layers on the contacts are removed from the surface. Furthermore at low pressures and low temperature, the atmosphere condenses on the contact creating variability in the resistance measurement. This will be discussed further in the next chapter.

High pressure results in increased viscosity, damping force, and spring force. With the increase in damping force the switching time is increased, but bouncing and settling time are decreased. The increase in pressure also affects the cleanliness of the contact surfaces.

At high pressures, contaminant films form at the switch contacts and increase the contact resistance.

The work contained in this chapter relates observed and measured beam dynamics to pressure, but to complete this work the following would be required:

- Find the electrostatic and damping forces for all three switches.
- Model the switch dynamics for the wiSpry and RFMD switches in the same manner as the NEU switch in [12].
- Find the ratio of F_d to F_e for each switch at 760 Torr.
- Determine the ratio of F_d to F_e for the wiSpry switch at 60 Torr, where the onset of bouncing was measured. This is the minimum ratio required to mitigate bounce for a cantilever switch.
- Calculate the cantilever area and gap distance required for a given actuation force that will meet the minimum ratio requirement to mitigate switch bouncing.
- Calculate the pressure needed to create the minimum ratio for the NEU and RFMD switches. Expect this pressure to be greater than 760 Torr.
- Experimentally verify the minimum ratio with the NEU and RFMD switches by incrementally increasing the pressure until switch bounding stops.
- Verify impact of changing pressure on surface topography by cycling two switches, each at a different pressure (one above the minimum ration with no bounce and one below the minimum ratio with bounce). Image contact surfaces after failure, comparing them with each other and an unused switch.

4.7 References

¹ A.H. Nayfeh and M.I. Younis, “A new approach to the modeling and simulation of flexible microstructures under the effect of squeeze-film damping,” *J. Micromech. Microeng.*, 14, pp. 170–181, 2004.

² Z.J. Guo, N.E. McGruer, and G.G. Adams, “Modeling, simulation and measurement of the

dynamic performance of an ohmic contact, electrostatically actuated RF MEMS switch,” *J. Micromech. Microeng.*, 17, pp. 1899–1909, 2007.

³ M.I. Younis and A.H. Nayfeh, “Simulation of Squeeze-Film Damping of Microplates Actuated by Large Electrostatic Load,” *Journal of Computational and Nonlinear Dynamics*, no.2, pp. 233-241, 2007.

⁴ W.E. Newell, “Miniaturization of Tuning Forks,” *Science*, vol. 161, no. 3848, pp. 1320-1326, 1968.

⁵ R.K. Gupta and S.D. Senturia, “Pull-in time dynamics as measure of absolute pressure,” *Micro Electro Mechanical Systems, 1997. MEMS '97, Proceedings, IEEE., Tenth Annual International Workshop on*, pp.290-294, 26-30 Jan 1997.

⁶ G. M. Rebeiz, *RF MEMS Theory, design, and technology*, New Jersey: John Wiley & Sons, Inc. 2003, pp 59-63.

⁷ M. Andrews, I. Harris, and G. Turner, “A comparison of squeeze-film theory with measurements on a microswitch,” *Sensors and Actuators*, vol. 36, pp. 79-87, 1993.

⁸ E.R. Brown, “RF MEMS switches for reconfigurable integrated circuits,” *IEEE Trans. Microw. Theory Tech.*, vol. 46, pp. 1868–1680, 1998.

⁹ D. Hyman *et al*, “Surface-Micromachined RF MEMS Switches on GaAs Substrates,” *Int. J. RF Microw. CAE*, vol. 9, pp. 348–361, 1999.

¹⁰ B. McCarthy, G.G. Adams, N.E. McGruer, D. Potter, "A dynamic model, including contact bounce, of an electrostatically actuated microswitch," *Microelectromechanical Systems, Journal of*, vol.11, no.3, pp.276-283, Jun 2002.

¹¹ P.G. Steeneken, G.S.M. Rijks, J.T.M van Beek, M.J.E. Ulenaers, J. De Coster, and R. Puers, "Dynamics and squeeze film gas damping of a capacitive RF MEMS switch," *J. Micromech. Microeng.*, vol. 15, pp. 176-184, 2005.

¹² Z.J. Guo, N.E. McGruer, and G.G. Adams, "Modeling, simulation and measurement of the dynamic performance of an ohmic contact, electrostatically actuated RF MEMS switch," *J. Micromech. Microeng.*, 17, pp. 1899–1909, 2007.

¹³ Z.J. Guo, N.E. McGruer, and G.G. Adams, "Modeling, simulation and measurement of the dynamic performance of an ohmic contact, electrostatically actuated RF MEMS switch," *J. Micromech. Microeng.*, 17, pp. 1899–1909, 2007.

¹⁴ B. McCarthy, G.G. Adams, N.E. McGruer, D. Potter, "A dynamic model, including contact bounce, of an electrostatically actuated microswitch," *Microelectromechanical Systems, Journal of*, vol.11, no.3, pp.276-283, Jun 2002.

CHAPTER 5

Cryogenic Performance of Gold RF MEMS Switch Contacts

C. Brown^a, A.S. Morris III^b, A.I. Kingon^c, and J. Krim^a

^a Department of Physics
North Carolina State University
Raleigh, NC 26795

^b wiSpry, Inc.
Fairbanks, Suite 198
Irvine, CA

^c Division of Engineering
Brown University
Providence, RI 02912

Journal of Microelectromechanical Systems in press 2008.

This work was supported by AFOSR MURI Grant No. FA9550-04-1-0381 entitled “Multifunctional Extreme Environment Surfaces: Nanotribology for Air and Space” and DARPA S&T Fundamentals Program, “Center for RF MEMS Reliability and Design Fundamentals,” Grant No. HR0011-06-1-0051.

5.1 Abstract

A series of experiments were performed to characterize RF MEMS switch performance under variable environmental conditions and cryogenic temperatures. Data were recorded in helium and nitrogen environments to lower stiction failure rates, as well as to circumvent switch bouncing arising from low pressure at cryogenic temperatures. Contact resistance values were observed to be lower at cryogenic temperatures but still two orders of magnitude higher than values predicted for the constriction resistance of gold asperity contacts, consistent with the presence of adsorbed films on the contacts. An asperity-heating model was applied, from which it was deduced that contact voltages can selectively disassociate adsorbed films from the contact surface while not softening the gold asperity contacts. The results are consistent with reduced mobility of the adsorbed surface films at cryogenic temperatures.

5.2 Introduction

Understanding the failure mechanisms for metal contact switches is a complex challenge. There is strong interplay between variables such as mechanical creep [1], deformation, contact heating [2],[3], contact asperity size, real contact area and current flow [4] leading to the eventual demise of the switch. Stiction failures moreover are highly sensitive to ambient conditions and adsorbed film layers at the switch contact.

Most prior work for extending switch lifetime has focused on mechanical factors, contact materials and operational parameters. Prior work documenting RF MEMS switch performance in terms of the environmental conditions has been very limited [2],[5]-[11]. Understanding the effects of cryogenic temperatures and large fluctuations in temperature on switch performance is becoming increasingly important to system designers as they integrate the switches into microwave systems, satellite communications, and space and air flight monitoring systems [7],[9]. Interest also exists for integrating RF MEMS devices with high- T_c superconductors (HTS); demonstrated applications with integrated MEMS include a HTS microstrip resonator [12] and a tunable HTS filter [13]. Cryogenic temperatures have adverse effects on the operational stability and longevity of capacitive MEMS switches. The

pull-in voltage substantially increases and capacitance decreases with decreasing temperature [6]-[12]. An increased mortality rate for switches operating at cryogenic temperatures has also been reported [9].

No prior work on contact resistance at cryogenic temperatures for metal contacting RF MEMS switches has been published, but an observation of decreased contact resistance with increasing temperature ranging from room temperature to 373 Kelvin [2] has been reported in the literature. In the latter case, the experimental results were unable to discern the individual contributions from surface morphology changes and adsorbed film effects on the overall contact resistance value.

This paper covers the performance characteristics of an RF MEMS device across a range of operational environments. The data presented here suggests that decreasing the ambient temperature to liquid nitrogen levels can lower contact resistance and mitigate some stiction events. Three sets of data are presented: 1) the correlation between contact resistance and ambient atmosphere at cryogenic temperatures and 3) the contact resistance as a function of both time and temperature under constant actuation force.

The data presented herein collectively indicate that substantial changes can be made to the switch's performance by altering the operating conditions. Possible causes for contact resistance change are discussed and correlated to contact theory, which is reviewed in the following section. The improved understanding of switch behavior and contact resistance facilitates improved switch design and performance.

5.3 Contact theory

Roughness of the contact surfaces plays a key role in the contact resistance. Current is confined to flowing through the contacting asperities, and the flow is governed by the size of those asperities. Only a few gold asperities come into contact when the switch is closed, so the area through which the current flows is initially small. After being closed for an extended time period or alternatively opened and closed repetitively, the true contact area is observed to increase, resulting in decreased contact resistance. If the contact temperature rises, the contacts may soften, which leads to increased contact area under applied load. Such

“softening” of the contacts has been reported for temperatures ranging from 65 to 100°C [2],[3]. The authors who reported the lower temperature did not rule out thermal breakdown of bonds between the gold and an adsorbed film layer as the mechanism producing decreased resistance at 65 °C [2].

An accurate representation of the surface roughness is needed to generate meaningful predictions for contact area and resistance. A multi-scale three-dimensional surface topography was generated for the switch contacts using a Weierstrass-Mandelbrot function paired with the fractal dimension and fractal roughness measurements from an AFM [14]-[16]. Modeling of the contact surfaces, when left in the closed position for extended periods of time, predicted the true contact area to reach a maximum of 7% of the total possible contact area [17]. Switches subjected to high contact forces or repeatedly cycled deform plastically leaving a greater contact area for subsequent switch cycling [18]. The switches used for experimentation had been under frequent prolonged cycling and it is assumed that they maintained the 7% true contact area for the duration of the tests.

RF MEMS contact asperity dimensions are on the order of the mean free path of electrons in gold. The spatial constriction on the current produces lattice and boundary scattering of electrons. The contact resistance, R_c , of an asperity with radius a is [19],[20]:

$$R_c = f\left(\frac{\lambda}{a}\right)R_M + R_S = \frac{1+0.83(\lambda/a)}{1+1.33(\lambda/a)} \frac{\rho}{2a} + \frac{4\rho\lambda}{3\pi a^2}, \quad (5.1)$$

where ρ is the electrical resistivity and λ is the electron mean free path, which is approximately 38 nm in gold [21]. R_M is the Maxwell resistance due to lattice scattering and R_S is the Sharvin resistance due to boundary scattering. The Maxwell term is representative of the resistance found when the contact spot size is much greater than the mean free path of the electrons. The Sharvin term contributes to the overall contact resistance when the contact spot size is on the order of the mean free path and the electrons are ballistically projected through the asperities without any scattering. The scaling factor $f(\lambda/a)$, accounts for the transition between resistance regimes. It has a maximum value of 1 as $a \gg \lambda$ and a minimum value of 0.624 as $a \ll \lambda$.

The contact resistance can range between an upper and lower limit depending on how

the real contact area is represented. The lower limit assumes that the contact spots do not interact and can be represented as a number of parallel resistance points. The lower contact resistance limit R_L can be approximated as:

$$\frac{1}{R_L} = \sum_{i=1}^N \frac{1}{R_{ci}}, \quad (5.2)$$

where N is the number of asperities in contact, and R_{ci} is the contact resistance of the i^{th} contact spot. The upper limit for the contact resistance is set by approximating the area of all individual asperity contacts with one single large asperity of equal area. The radius of the single asperity is a_{eff} and the upper limit R_U is

$$R_U = f\left(\frac{\lambda}{a}\right) \frac{\rho}{2a_{eff}} + \frac{4\rho\lambda}{3\pi a_{eff}^2}, \quad (5.3)$$

The contact resistance value from (5.1) is an integral part of the asperity-heating model, which relates the contact voltage V_c to the contact spot temperature T_c . The contact spot temperature can be stated as

$$T_c = \sqrt{\frac{f(\lambda/a)R_M}{4LR_c} V_c^2 + T_o^2}, \quad (5.4)$$

where $L = 2.45 \times 10^{-8} \text{ W}\cdot\Omega/\text{K}^2$ is the Lorentz constant and T_o is the ambient temperature [2]. It is important to note that the asperity-heating model accounts for the size of the contact spots and the increased boundary scattering contributions due to the small spot size. Additionally it eliminates an overestimation of contact spot temperature by assuming only the Maxwell term leads to contact heating with no contribution from the boundary scattering term [22].

5.4 Device

The experiments have been performed on a single-pole double-throw (SPDT) cantilever type switch produced by wiSpry (Fig. 5.1). The devices actuate to the closed state when a voltage differential of approximately 35 Volts is applied between the upper and lower electrodes. Upon actuation the contacts at the leading edge of the cantilever are brought into contact with two lower contact dimples attached to the transmission line. This allows current

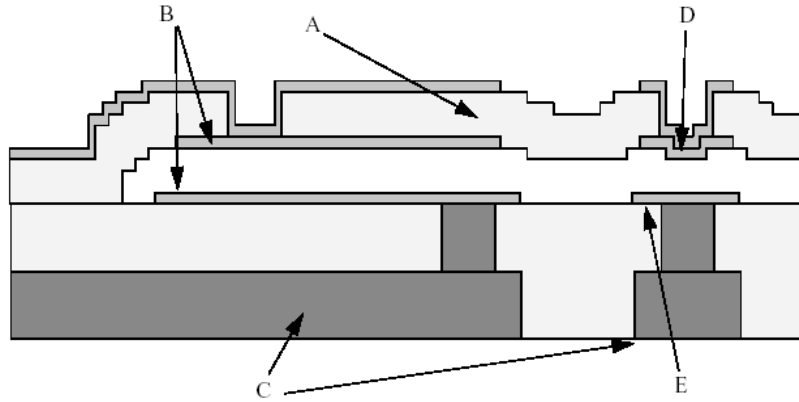


Figure 5.1 – Side view of RF MEMS switch cantilever. A is the Silica cantilever. B are the gold capacitive plates used for actuating the switch into the closed position forcing the contact bumps at D against the transmission line at E. Interlaced are conducting copper paths, C, for carrying the signal and actuation voltages.

to flow from the transmission line through the contact dimples, across the cantilever and back through the other set of contact dimples to the outbound transmission line. Once the actuation voltage is removed, the stiffness in the root of the cantilever arm pulls the switch into its open position.

The switches are fabricated using the wiSpry metal surface micromachining process. The die substrate is silicon. Gold and copper transfer lines are interlaced with silicon and sacrificial layers during the stack process. Sacrificial layers are subsequently etched away creating the three dimensional cantilever structure and exposing the electrode plates used for actuation as well as the contact dimples which transfer the RF signal. Each die has four sets of SPDT switches. The cantilever beam is 135.5 μm in length and 251 μm in width. The upper contact bumps are 6 μm in diameter and separated by 55 μm . The travel distance from upper to lower contact dimples is 2 μm .

Prior to testing the devices were stored in uncontrolled room ambient conditions. Initial resistance measurement taken in a helium gas environment at room temperature ranged from 0.7 Ω to 6 Ω , with most devices in the 1.8 Ω to 2.0 Ω range. Each device was tested for the voltage needed to make contact, create stable contact resistance, and break

contact. The average voltage needed to create stable contact resistance was 42 Volts. Five different devices were used for the resistance versus temperature measurements.

5.5 Experimental setup

The switches were tested in a vacuum system to alleviate stiction events (Fig. 5.2). The test chamber consisted of a thin steel 3.75 inch diameter cylinder fitted with a 20 pin electrical feedthrough at the lower end allowing a four-point dc measurement of the device's contact resistance. A 28 inch extension arm is fitted to the top of the cylinder to ensure the environmental chamber is as low as possible in the cryostat dewar. The top of the transfer arm meets with a four-way cross that allows for pressure measurement, vacuum access and ports for backfilling gas environments.

Electrical connections inside the chamber were made with standard braided copper vacuum wire between the feedthrough and a zero insertion force (ZIF) socket. The switch

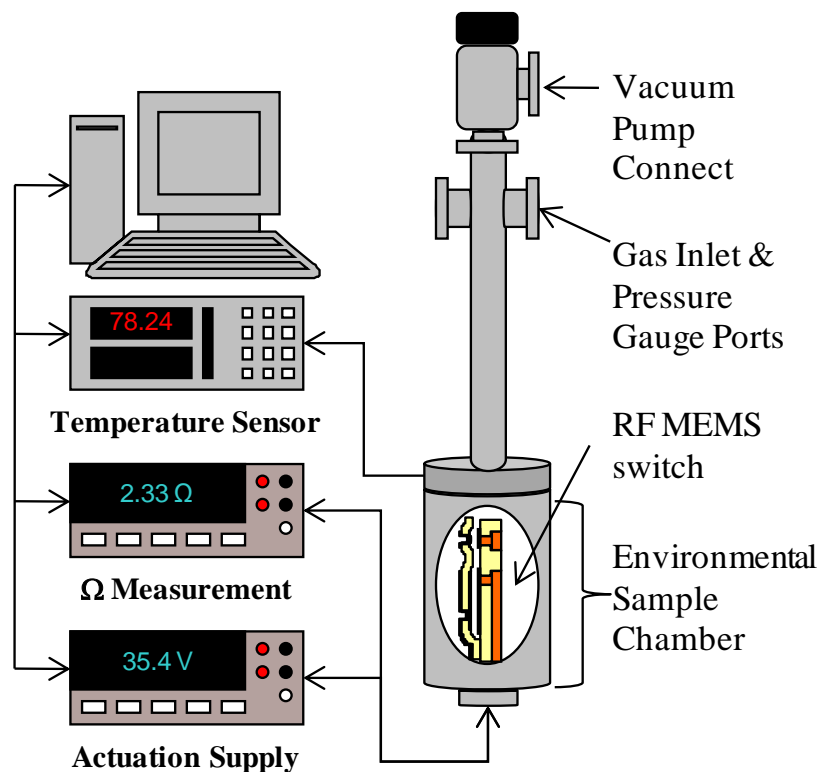


Figure 5.2 – Experimental setup.

was attached to a ceramic side braze package with gold leads. One mil (25 μm) gold wires were wirebonded between the device and ceramic package. The packages were then inserted in the ZIF socket during testing. Electrical connections outside the chamber between the feedthrough and test circuitry were made using constantan wire to ensure no additional resistance changes were measured as a result of thermal fluctuations from wire exposed to liquid nitrogen during testing.

Two Keithley 2400 source meters were used for actuating the switch and performing a four-point dc contact resistance measurement across the device contacts. For the four-point measurement, a 1 mA current was sourced and limited to a voltage compliance of 1 V. Actuation currents were limited to 10 μA . All instrumentation was controlled via LabView.

The environmental chamber was cooled by immersing it in a liquid nitrogen bath at 77.4 Kelvin. The nitrogen was contained in a Cryofab CSM type vacuum insulated stainless steel dewar which in turn was immersed in an outer heat shield filled with liquid nitrogen. A Lake Shore 330 Temperature Controller measured temperature with both silicon diode and platinum resistance thermometers.

The experimental variables were the contact voltage V_c and ambient temperature T_o . During testing, 1 mA dc current was supplied that resulted in a V_c of approximately 2 mV. The ambient temperature was chosen for each experiment to aid in differentiating changes in contact resistance due to adsorbed surface films and morphology of the contact surfaces. Since the 7% true contact area is large compared to the single asperity size and the mean free path of the electrons in gold, the upper limit for contact resistance is assumed for correlating the theory with experimental data.

Initially measurements were planned to be in UHV to avoid stiction problems by removing moisture and to clean the gold contacts by removing the hydrocarbon layers on them. However it was found during testing that severe switch bounce commenced at pressures below 80 Torr. As a result, the system was evacuated of air and backfilled to a pressure of 760 Torr with helium before being cooled with liquid nitrogen.

5.6 Experimental results

5.6.1 Gas dependence

A series of tests were also performed to investigate the effects of atmospheric conditions on the contact resistance. For this round of testing, the chamber was filled with either helium or nitrogen. The switch was actuated to the closed position and a resistance measurement was taken once per second with the current on continuously. Measurements were taken on the same device for both gasses at room temperature, during a rapid cool down to 77 Kelvin and at a steady state of 77 Kelvin. Rapid cool down measurements were taken over the range of 293 Kelvin to 77 Kelvin as the vacuum system was immersed in liquid nitrogen.

At room temperature there was no difference in the contact resistance as a function of

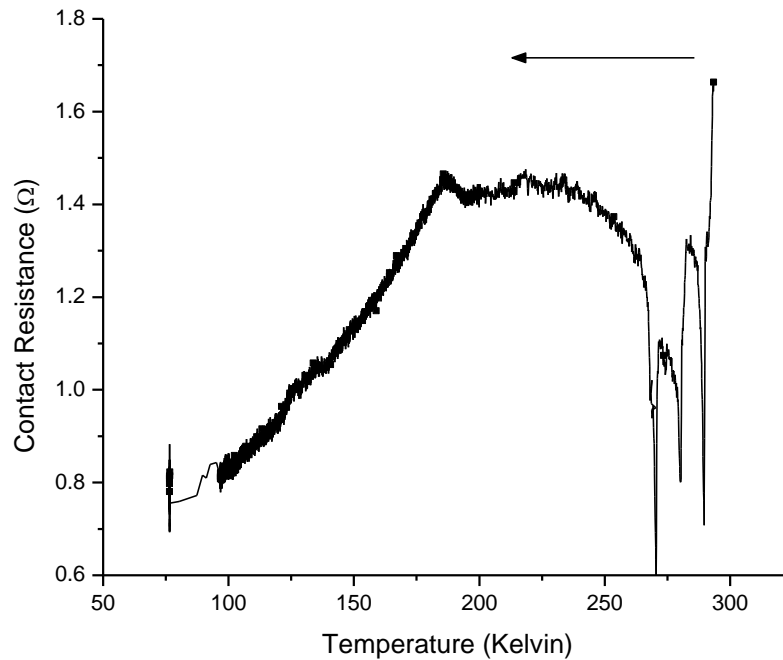


Figure 5.3 – Rapid cooldown of the device by boiling off liquid nitrogen directly on the vacuum system induces large fluctuations in contact resistance. These fluctuations are not present in data taken when the device is allowed to slowly warm after being maintained at 77 Kelvin for several hours.

the gas environment. However fluctuations in the contact resistance did arise during the rapid cool down and 77 Kelvin steady state measurements. During the rapid cool down, both the helium and nitrogen environments exhibited sharp fluctuations in contact resistance (Fig. 5.3). The device was also cooled over a 10 hour period from 293 Kelvin to 100 Kelvin by filling only the outer heat shield of the dewar. Neither the helium nor nitrogen gas atmospheres produced rapidly changing fluctuations in contact resistance during a slow cool down.

Additional tests were taken when the device had reached thermal equilibrium at 77 Kelvin. The device was allowed to cool for 12 hours with both the inner and outer dewar filled with liquid nitrogen. The switch was then actuated and a resistance measurement was taken once per second while a 1mA current was left on continuously. Figure 5.4 shows the contact resistance for helium and nitrogen atmospheres at liquid nitrogen temperature. The

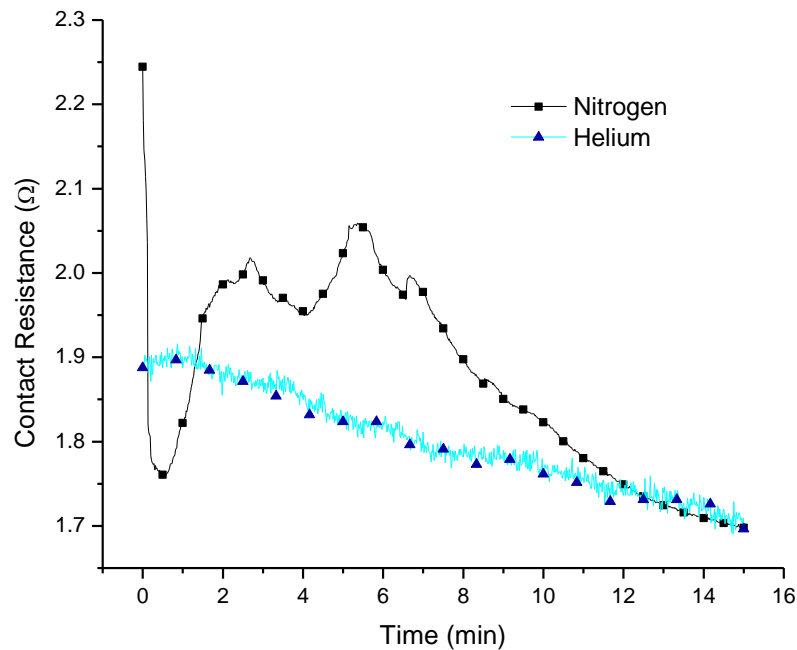


Figure 5.4 – Contact resistance fluctuations are seen just after switch closure for a nitrogen atmosphere at liquid nitrogen temperatures, but not for a helium atmosphere. This variable resistance may be due to condensed nitrogen boiling off at the switch contacts when current is applied.

helium atmosphere showed no fluctuations in contact resistance, while the nitrogen atmosphere showed some fluctuations in resistance just after closing. It is believed this fluctuation was due to condensed nitrogen boiling off at the contacts as the local temperature was rapidly rising due to the current flow. It is highly probable that the same type of data would be seen for a helium atmosphere when cooled to liquid helium temperatures.

5.6.2 Time dependence

During the resistance versus temperature experimentation it was noted at room temperature that switches closed for extended periods of time would decrease in contact resistance. However, when the switch was opened and allowed to dwell, even for short periods of time, the contact resistance would immediately return to the level measured before the extended period of closure. It was also noted that the same effect was greatly diminished or non-existent when the switches were cooled to 77 Kelvin.

A set of experiments was performed to explore the contact resistance as a function of temperature for extended periods of time in the closed state. The resistance versus time data were taken at both room temperature and 77 Kelvin. Due to the contact resistance variability induced by nitrogen gas at near liquid nitrogen temperatures, only helium was used for cryogenic portion of the experiment. Before each measurement run, the switch was cycled 200 times. A resistance measurement was taken once per second for the duration of the experiment using a 1 mA source. Measurements were taken by two methods. For the first set of data runs the switch was cold cycled and left in the open position between measurements. In the second set of runs, the switch was closed for the duration of the test, and opened to dwell between runs.

Room temperature experiments had a rapid reduction in resistance during the first minutes of closure as seen in Trace A of [Fig. 5.5](#). The resistance decreased over time while the switch was cycling and for tests where the switch was continuously closed. As soon as the contacts were allowed to dwell in the open position the resistance values immediately returned to their initial values. Resistance measurements were taken for various amounts of dwell time in the open position ranging from 1 day to 10 seconds while still contained in the

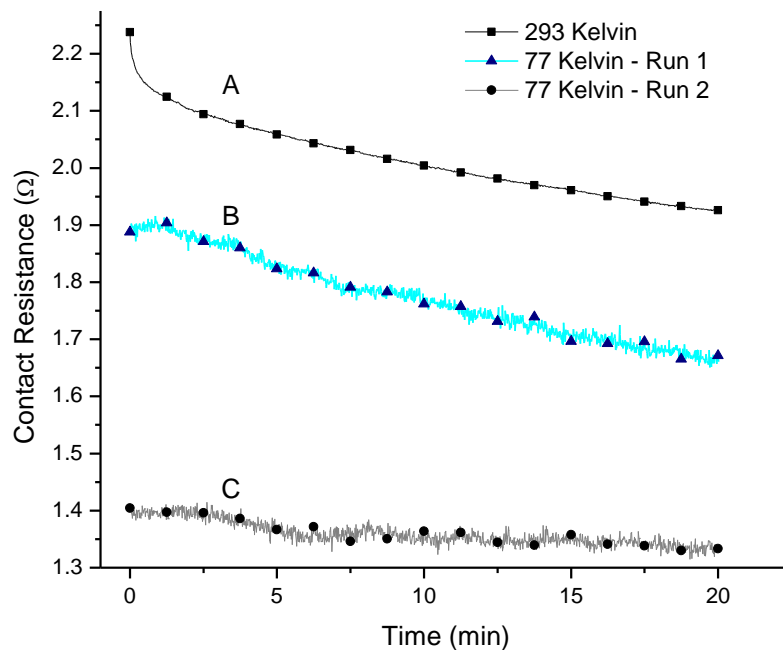


Figure 5.5 – Contact resistance decreases over time while a switch is left in the actuated position at room temperature and at 77 Kelvin. When the switch is allowed to dwell for a short period of time in the open state at room temperature the contact resistance returns to its initial value while it remains below the initial value for a second run at 77 Kelvin. This indicates the adsorbed film is less mobile at lower temperatures.

nitrogen and helium atmospheres. In every case at room temperature, the resistance returned to the initially measured value after the dwell. Resistance measurements versus time subsequent to the dwell showed the same drop-off in resistance as seen in Trace A.

To measure the effects of cryogenic temperatures on the resistance values over time, the devices were cooled for 24 hours and then tested with the inner dewar and outer heat shield filled with liquid nitrogen to ensure the device remained at 77 Kelvin throughout testing. The initial resistance of the switch is significantly lower for the cryogenic temperatures than at room temperature. Trace B of Fig. 5.5 shows the same drop in resistance as a function of time as seen in Trace A for the room temperature measurements. However, when allowed to dwell in the open position for the same lengths of time as the room temperature experiments, the return to higher resistance values did not manifest itself.

Trace C of Fig. 5.5 is a resistance versus time curve taken with five minutes of dwell time between measurements. The cryogenic data shows that, in contrast to room temperature data, the resistance has not returned to its original value between runs, but has remained near the same value recorded at the end of the previous run.

Upon completion of the cryogenic resistance versus time experimentation, the device was allowed to warm slowly back to room temperature. Measurements once again showed the device had higher initial resistance than at cryogenic temperatures and that even with very short dwell times between measurements, the resistance returned to its initial peak value.

5.7 Analysis

It is evident that environmental conditions play an important role in operation of the MEMS devices. The switches showed no changes in mechanical stability during or after testing at cryogenic temperatures. The increased pull-in voltage for fixed-fixed capacitive switches at cryogenic reported in [6]-[12] was not observed at 77 Kelvin for the cantilever type switches used for experimentation. Additionally, the hysteresis in pull-in voltage reported in [11] after temperature cycling was not present. A differential in pre and post-cooling pull-in voltages indicates that the switching structure has sustained permanent deformation. The wiSpry devices tested reached stable contact resistance at the same pull-in voltage for both room temperature and 77 Kelvin. Goldsmith and Forehand's model shows pull-in voltage as a function of temperature for fixed-fixed capacitive switches is mostly due to the buildup of residual stresses on the bridge structure produced [10]. Cantilever designed switches do not exhibit the fluctuations in pull-in voltage as a function of temperature or the thermal cycling hysteresis because they are not subjected to biaxial thermal stresses found in fixed-fixed switches [11]. Additionally, none of the wiSpry devices became stuck or failed during the cryogenic testing.

Ideally, the switch should be run in UHV to eliminate stiction events and formation of adsorbed films common to exposure with normal atmospheric conditions. However, for this switch to operate properly the device requires pressures above 80 Torr. The addition of

alternative atmospheres such as nitrogen and helium can help eliminate bouncing problems by maintaining sufficient operational pressure at cryogenic temperatures, however the gas choice is dependent on the temperature range over which the device will operate. Nitrogen is adequate for temperatures above 77 Kelvin, but near or below 77 Kelvin helium was more effective.

Changing the gas composition of the atmosphere can solve the bouncing and moisture-induced adhesion events, however the apparent presence of an adsorbed film layer on the gold contacts has substantial impact on the contact resistance. The contact resistances measured in this experiment are two orders of magnitude higher than values predicted by current contact theory. It is the presence of these less conductive adsorbed films that generates the higher contact resistance. It should be noted that while the films do create higher contact resistance, they also play an important role in preventing adhesion failures [23]. The film layer prevents the gold-gold adhesion forces from forming. While pure ohmic contact would be optimal for signal throughput, even small amounts of clean surface area generated by many tens of asperities would create an attractive adhesion force greater than the restoring force used to open the contacts. This provides a possible explanation for the device that immediately failed in UHV during this experiment.

A more in-depth treatment of the surface contamination as it relates to the contact asperity model is required to understand the variances in contact resistance seen in the experiments. Adsorbed films on the contact surfaces have been suggested as the most likely contributor for large-scale resistance changes on MEMS contacts [2]. Heating the contacts has been shown to generate a drop in resistance, however it is difficult to discern how much of this drop is due to the physical changes in contact topography from asperity softening and how much is due to the dissociation of adsorbed films at the contact points. The impact of adsorbed surface films on the measured contact resistance for a MEMS device can be partially explained by exploring the existing theory for asperity contact and application of an asperity-heating model. Application of the asperity-heating model for low temperatures is helpful in showing that the change in resistance must be due mostly to film effects rather than changes in surface characteristics of the gold asperity contacts.

5.7.1 Comparison to temperature dependence

Several key features are apparent when comparing the experimental contact resistance data with theoretical values. Foremost is the difference of nearly two orders of magnitude between the predicted and experimentally measured value for contact resistance. Some of the additional contact resistance can be accounted for by how the measurement was taken. The four point probe measurement included resistance contributions from the transmission lines on the device itself, gold wirebond, and the ceramic package. Using device geometries and wirebond lengths, it is estimated that their contribution is approximately 1.54Ω . For the average device at 293 K, this still leave $\sim 0.3 \Omega$ of resistance attributed to the contacts, which is still one order of magnitude greater than the predicted value of 0.03Ω . Adsorbed films at the contact interface are a likely contributor to the difference in measured and expected contact resistance.

Data from this experiment and calculations show resistance is reaching its maximum value at room temperature; however published data shows that resistance decreases as the temperature increases over a range of 300 to 363 Kelvin [2]. Pairing the data sets together shows the resistance reaches a local maximum at room temperature. A possible explanation for this is that near room temperature the film is reaching its maximum mobility and is being pressed in to the contact areas due to the mechanical cycling of the switch. However, as discussed in the next section, the lower temperatures may limit the adsorbed film's ability to move into the contact areas during cycling and the higher temperatures may disassociate the adsorbed films from the gold surface. In either case additional real contact area would be generated leading to a lower contact resistance.

5.7.2 Comparison to time and temperature dependence

The resistance versus time data offers further explanation for significant role surface films may play in the overall contact resistance. Solving (4) for the contact voltage V_c as a function of ambient temperature T_o yields:

$$V_c = \sqrt{\frac{R_c}{f(\lambda/a)R_M} 4L(T_c^2 - T_o^2)} \cong \sqrt{4L(T_c^2 - T_o^2)}, \quad (4.5)$$

In the case of the upper limit of contact resistance $R_c \approx R_M$ and the scaling factor is approximately one. [Figure 5.6](#) shows the contact voltage plotted as a function of ambient temperature. The function is plotted for contact temperatures of 338 and 373 Kelvin. The upper curve corresponds to contact voltages needed to create temperatures at the contacts high enough to soften gold asperities based on the 373 Kelvin softening value reported by Holm. The lower curve represents the contact voltage needed to create contact temperatures of 338 Kelvin which disassociate adsorbed film layers as reported in [\[2\]](#).

The area below the upper curve contains the possible contact voltages and corresponding ambient temperatures that could be applied to the experimental system and not soften the gold asperities. If a contact voltage is chosen in the area below the upper curve and held constant, any large fluctuation in resistance would result from changes in the system other than the creation of real contact area through asperity softening.

Additionally, there should be a preferential range of ambient temperatures and contact voltages for which the temperature at the contact spot is high enough to remove the adsorbed film from the contacts, but not elevated enough to cause asperity softening. This provides the optimum case where the insulating film thickness has decreased, generating a lower contact resistance, however the temperature has not increased to the point where asperity softening could generate surface areas large enough to produce adhesion failures. This region lies between the two curves in [Fig. 5.6](#).

Resistance versus time data collected at room temperature and 77 Kelvin supports this. Traces A and B in [Fig. 5.5](#) show the resistance change as a function of time where the ambient temperature was held constant at 293 and 77 Kelvin respectively. Comparing room versus cryogenic temperature initial resistance shows a higher resistance for room temperature contacts, which is to be expected. In both cases the resistance dropped off quickly in the first few minutes of contact. In the case of the room temperature run, when allowed to dwell for a short period of time the initial contact resistance would return to the elevated contact resistance and decrease over time again. For a well-worn switch in which

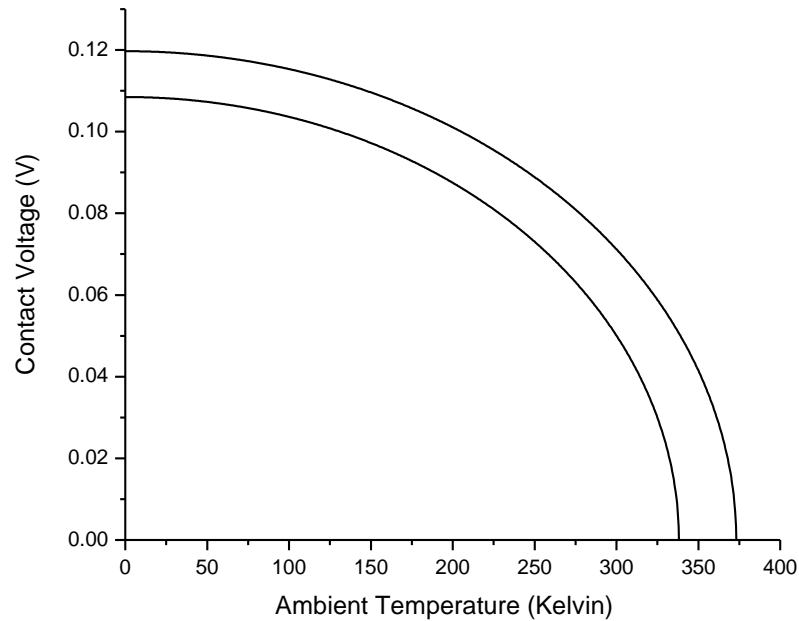


Figure 5.6 – According to the asperity-heating model, a contact voltage chosen between the two curves will generate a contact temperature high enough to disassociate the adsorbed films on the contacts but low enough to keep gold asperities from softening.

the contact area is approximately the same throughout testing and there are no changes in the ambient and experimental conditions, the contact resistance should not increase appreciably during the dwell time. The contact resistance increase during dwell strongly indicates the presence of an adsorbed film that is highly mobile at room temperatures.

In the case of the 77 Kelvin tests, after the same length of dwell the contact resistance had not returned to the initial resistance measured in the first run but remained near the last measured value of resistance from the previous run. In this experiment, no physical changes, such as external heating or changes in surface topography have occurred during the dwell period. Thus, none of the variables from standard asperity-heating model can be used to determine what initiated the change in resistance during the dwell period. The data again indicates that an adsorbed film is present, and once removed from the contact points, it does not rapidly return. This implies the adsorbed film is less mobile at lower temperatures.

The contact resistance of the switch contacts was modeled using contact area

information from aforementioned multi-scale model for continuous closure at room temperature. The model did not take into account adsorbed film effects, but did relate the contact resistance to the real contact area, contact pressure and material properties. At each time step of the model, the number of asperities in contact and their effective radius was determined. The simulation yielded predictions for contact resistance versus time consistent with the data collected from the RF MEMS switches in that the resistance rapidly decreased in the initial moments of contact and then the rate of decrease slowed over time. The model assumes in the initial moments that increased contact area dominates the change in resistance, and as the asperities become strain hardened, the resistivity increases, slowing the rate of change in resistance [17].

While the effects of increased contact area from asperity softening and strain hardening can partially explain the changes in contact resistance, it cannot explain why the initial resistance was so high or why resistance increases during prolonged cycling. The experimental data and the simulations are qualitatively similar because in both cases it is the creation of real contact area creating the drop in resistance. While the simulation assumes that new contact area is generated from asperity softening, the data suggests the decrease in contact resistance is in fact from decreasing the adsorbed film thickness between the gold contacts or the removal of adsorbed film between the contacts leading to more gold on gold contact.

The experimental results indicating the presence of an insulating film and the impact of environmental conditions are similar to those reported in prior publications [2],[5],[18],[24]. The authors of [5] tested RF MEMS switches in both nitrogen and air environments at room temperature and found no change in contact resistance due to atmospheric conditions. Experimental results were similar to those for the switches used in this experiment. Both switches used similar contact areas with initial contact resistance in the 1-ohm range, a full order of magnitude above the upper limit predicted values in (3). Those studies concluded the discrepancy between the model and experimental results was due to the presence of insulating films on the contacts. This assertion was further supported by the fact no adhesion failures occurred even when a contact force on the order of 10^{-2} N

was applied.

Modifications to the current contact resistance equations must be performed in order to account for the surface film contribution to the total resistance. Efforts have already started in this area [25],[26]. Additional contact resistance is accounted for in the system due to tunneling effects through the adsorbed film. However, the model assumes that the film is present throughout the simulation. This works well for simulating contact resistance response for light loads and small currents on a single closure. The next logical step would be introducing the effects of ambient temperature and contact temperature. The data shows that the adsorbed film is at the very least compressed to a smaller thickness, thus lessening the height of the potential barrier that the current flow must cross, and in the most extreme case, it may be completely removed. A valid model should be cognizant of adsorbed film's response for low ambient temperatures where it appears to be less mobile and can be mechanically removed from the surface. Additionally it should take into account high contact temperatures where the adsorbed film may disassociate from the local gold contact surfaces.

5.8 Summary

A series of experiments were performed to investigate RF MEMS switch performance under variable temperature, pressure, and atmospheric conditions. Several features in the operational characteristics of the RF MEMS devices were observed:

1. Proper environmental conditions must be selected for optimal switch functionality. Switch bouncing occurs when the atmospheric pressure is too low to dissipate the energy stored in the cantilever arm during closure.
2. UHV environment would be optimal for removing adsorbed films at the contacts; however it produces adhesion failures due to attractive forces between the clean gold-gold asperity contacts and leads to extreme bouncing problems.
3. Nitrogen and helium atmospheres have no impact on cold-switching operation or contact resistance except at cryogenic temperatures where the gaseous atmosphere is reaching its liquid state. At 77 Kelvin, nitrogen gas appears to condense at the

switch contacts and create resistance variability; however, this contact variability is not seen for a helium gas atmosphere at 77 Kelvin. Therefore, the atmosphere must be chosen according to the operational environment.

4. The experimentally measured resistance values and predicted contact resistance values differ by orders of magnitude. The current contact resistance and asperity heating models only take into account constriction resistance at the gold asperities and do not take into account the effect of adsorbed thin films between the contacts. Changes in measured resistance are most likely due to changes in the thickness and composition of thin films at the contacts. Improved models are required that include these critical aspects of contact operation.
5. Cryogenic temperatures lower the contact resistance by lowering the resistivity of the gold. The data also shows that low temperatures allow surface films to be mechanically removed and retard their reformation on the contacts when the switch is allowed to dwell. At lower temperatures, more voltage can be applied at the contacts before asperity softening occurs, allowing the switch to maintain its surface characteristics while using higher voltages.
6. Application of the asperity-heating model shows a contact voltage can be chosen for a given ambient temperature that results in contact temperatures high enough to disassociate the films at the surface but not so high as to soften the gold asperities.

5.9 References

- [1] G. Gregori and D. Clarke, "Mechanical creep as a life-limiting factor of radio frequency microswitches," *Appl. Phys. Lett.*, **87**, 2005.
- [2] B. Jensen, L. Chow, K. Huang, K. Saitou, J. Volakis, and K. Kurabayashi, "Effect of nanoscale heating on electrical transport in RF MEMS switch contacts," *J. Microelectromech. Syst.*, vol. 14, no. 5, pp. 935-946, 2005.

- [3] R. Holm, *Electric Contacts – Theory and Applications*, 4th ed. Berlin, Germany: Springer-Verlag, 1967.
- [4] S. Patton and J. Zabinski, “Fundamental studies of Au contacts in MEMS RF switches,” *Tribology Letters*, vol. 18, no. 2, pp. 215-230, 2004.
- [5] S. Majumder, N. McGruer, and P. Zavracky, “Electrostatically actuated micromechanical switches,” *Journal of Vacuum Science and Technology*, vol. 15, no. 3, pp. 1246-1249, 1997.
- [6] X. Yuan, Z. Peng, J.C.M. Hwang, D. Forehand, and C. Goldsmith, “Temperature acceleration of dielectric charging in RF MEMS capacitive switches,” *Microwave Symposium Digest 2006*, IEEE MTT-S International, pp. 47-50, 2006.
- [7] Y. Zhu and H. Espinosa, “Effect of temperature on capacitive RF MEMS switch performance – a coupled-field analysis,” *Journal of Micromechanics and Microengineering*, vol. 14, pp. 1270-1279, 2004.
- [8] Y. Hijazi, A. Bogozi, M. Brzhezinskaya, J. Martinez, J. Burke, J. Noel, Y.A. Vlassov, and G.L. Larkins Jr., "Effect of temperature on impedance behavior of insulation layer in a HTS MEMS switch for RF applications," *Applied Superconductivity, IEEE Transactions on*, vol.15, no.2, pp. 952-955, June 2005.
- [9] H.T. Su, I. Llamas-Garro, M.J. Lancaster, M. Prest, J.-H. Park, J.-M. Kim, C.-W. Baek, and Y.-K. Kim, "Performance of RF MEMS switches at low temperatures," *Electronics Letters*, vol.42, no.21, pp.1219-1220, 12 Oct. 2006.

- [10] C.L. Goldsmith and D.I. Forehand, "Temperature variation of actuation voltage in capacitive MEMS switches," *Microwave and Wireless Components Letters, IEEE*, vol.15, no.10, pp. 718-720, Oct. 2005.
- [11] P. Rantakari and T. Vaha-Heikkila, "Characterization of CMOS Compatible RF MEMS Switch at Cryogenic Temperatures," *Solid-State Sensors, Actuators and Microsystems Conference, 2007. TRANSDUCERS 2007. International*, pp.639-642, 10-14 June 2007.
- [12] J. Noel, Y. Hijazi, J. Martinez, Y.A. Vlasov, and G.L. Larkins Jr., "A switched high-Tc superconductor microstrip resonator using a MEM switch," *Supercond. Sci. Technol.*, vol. 16, pp. 1438–1441, 2003.
- [13] E.M. Prophet, J. Musolf, B.F. Zuck, S. Jimenez, K.E. Kihlstrom, and B.A. Willemsen, "Highly-selective electronically tunable cryogenic filters using monolithic, discretely-switchable MEMS capacitor arrays," *IEEE Trans. Appl. Supercond.*, 15, (2), pp. 956–959, 2005.
- [14] F. Borodich and D. Onishchenko, "Similarity and fractality in the modeling of roughness by a multilevel profile with hierarchical structure," *International Journal of Solids and Structures*, vol. 36, pp. 2585-2612, 1999.
- [15] B. Mandelbrot, *The Fractal Geometry of Nature*, New York: Freeman, 1983.
- [16] W. Yan and K. Komvopoulos, "Contact analysis of elastic-plastic fractal surfaces," *J. App. Phys.*, vol. 84, pp. 3617-3624, 1998.
- [17] M. Zikry, O. Rezvanian, C. Brown, and J. Krim, "Surface roughness, asperity contact and gold RF MEMS switch behavior," Submitted to *Journal of Micromechanics and Microengineering*, May 2006.

- [18] S. Majumder, N. McGruer, G. Adams, P. Zavracky, R. Morrison, and J. Krim, "Study of contacts in electrostatically actuated microswitch," *Sens. Actuators A: Phys.*, vol. 93, pp. 19-26, 2001.
- [19] G. Wexler, "The size effect and non-local Boltzmann transport equation in orifice and disk geometry," *Proceedings of the Physics Society*, vol. 89, pp. 927-941, 1966.
- [20] B. Nikolic and P.B. Allen, "Electron transport through a circular constriction," *Physical Review B*, vol. 60, pp. 3963-3969, 1999.
- [21] N. Ashcroft, N. Mermin, D. Mermin, *Solid State Physics*, 1st ed. New York: Holt, Rinehart and Winston, 1976.
- [22] L. Weber, M. Lehr, and E. Gmelin, "Investigation of the transport properties of gold point contacts," *Physica B: Condensed Matter*, vol. 217, pp. 181-192, 1996.
- [23] J. Tringe, T. Uhlman, A. Oliver, and J. Houston, "A single asperity study of Au/Au electrical contacts," *J. App. Phys.*, vol. 93, no. 8, pp. 4661-4669, 2003.
- [24] S. Majumder, N. McGruer, G. Adams, A. Zavracky, P. Zavracky, P. Morrison, and J. Krim, "Study of contacts in an electrostatically actuated microswitch," *Proc. 44th IEEE Holm Con. on Electrical Contacts*, 1998, pp. 127-132.
- [25] L. Kogut and K. Komvopoulos, "Electrical contact resistance theory for conductive rough surfaces separated by a thin insulating film," *J. App. Phys.*, vol. 95, no. 2, pp. 576-585, 2005.
- [26] L. Kogut and K. Komvopoulos, "Analytical current-voltage relationships for electron tunneling across rough interfaces," *J. App. Phys.*, vol.97, no. 1, pp. 1-5, 2004.

CHAPTER 6

Surface Roughness, Asperity Contact, and Gold RF MEMS Switch Behavior

O. Rezvanian^a, M.A. Zikry^a, C. Brown^b, and J. Krim^b

^a Department of Mechanical and Aerospace Engineering

^b Department of Physics

North Carolina State University

Raleigh, NC 26795

Journal of Micromechanics and Microengineering, **17** (2007) 2006–2015

This work was funded by the AFOSR Extreme Friction MURI program, AFOSR grant FA9550-04-1-0381

6.1 Abstract

Modeling predictions and experimental measurements were obtained to characterize the electro-mechanical response of radio frequency (RF) microelectromechanical (MEM) switches due to variations in surface roughness and finite asperity deformations. Three-dimensional surface roughness profiles were generated, based on a Weierstrass-Mandelbrot fractal representation, to match the measured roughness characteristics of contact bumps of manufactured RF MEMS switches. Contact asperity deformations due to applied contact pressures, were then obtained by a creep constitutive formulation. The contact pressure is derived from the interrelated effects of roughness characteristics, material hardening and softening, temperature increases due to Joule heating, and contact forces. This modeling framework was used to understand how contact resistance evolves due to changes in real contact area, the number of asperities in contact, and the temperature and resistivity profiles at the contact points. The numerical predictions were qualitatively consistent with the experimental measurements and observations of how contact resistance evolves as a function of deformation time history. This study provides a framework that is based on an integrated modeling and experimental measurements, which can be used in design of reliable RF MEMS devices with extended life cycles.

6.2 Introduction

Surface roughness and asperity behavior are critical factors that affect contact behavior at scales ranging from the nano to the micro in microelectromechanical, electronic, and photonic devices. Specifically, in MEMS devices, large surface to volume ratios underscores that it is essential to understand and accurately predict how asperities behave in contact devices. MEMS switches, particularly those with radio frequency (RF) applications have demonstrated significantly better performance over current electromechanical and solid-state technologies, which renders them as highly attractive alternatives for a variety of commercial and military applications [1-6].

One of the major objectives in the design of RF MEMS with metal contacts is to make repeatable and reliable electrical contacts. However, the complex physical interactions

between thermo-mechanical deformation, current flow, and heating at the contact, has made it extremely difficult to obtain accurate predictions of RF MEMS behavior, such that reliable devices can be designed for significantly improved life-cycles (see for example, [7]-[8]). Validated modeling methods can provide MEMS switch designers with insights on how the interrelated effects of the contact resistance, the surface roughness of the contact surfaces, and the contact pressure evolve. Hence, guidelines can be incorporated in the design and fabrication process to effectively size critical components and forces to provide stable contact resistance for significantly improved device durability and performance.

Various analytical and numerical methods have been employed to study the contact mechanics of ideally smooth surfaces [9-14]. Since surface topographies are critical in MEMS devices, some probabilistic models have been proposed to account for asperity height variations (For example, see [15]-[16]). However, these studies do not account for the actual surface topographies related to the roughness of contact surfaces in MEMS devices. The random and multiscale nature of the surface roughness can be better described by fractal geometry [17-21]. The use of fractals to represent the surface roughness into contact analyses of MEMS devices has been used to relate contact parameters, such as the real area of contact, contact pressure, and contact resistance [12, 20, 22-26].

However, what has been generally lacking is an integrated modeling framework that couples three dimensional surface roughness representations with the thermo-mechanical deformation of surface asperities, and to relate these to device performance over time. Hence, in this study a three dimensional fractal representation of surface roughness is used with a numerical framework to obtain predictions of thermo-mechanical asperity deformations of contacting surfaces as a function of time. Contact resistance behavior is then investigated and categorized for two surface roughness models with different roughness characteristics. Several resistance measures are then presented and their connection to other contact parameters, such as real contact area and the number of asperities in contact, is categorized. The resistivity of the contact material is assumed to vary by strain hardening, and also by softening effects due to Joule heating at the asperity micro-contacts. The contact material used in this investigation is gold, which is one of the widely used contact materials

for low-current MEMS switches [27]. To validate our approach, we also compared our predicted results with a set of experiments that were undertaken to characterize the contact resistance of RF MEMS switches.

This paper is organized as follows: in Section 2, the contact mechanics and topography of microscale contacts are presented. In Section 3, the physics of contact resistance is discussed. The fabrication and experimental setup is presented in Section 4. The fractal roughness models, the contact conditions, and the numerical scheme are outlined in Section 5. The results and discussion are given in Section 6, followed by the summary and conclusions in Section 7.

6.3 Contact mechanics and topography

Accurate modeling of the normal contact at the interface of the contact bump and the drain electrode in a RF MEMS switch requires that the roughness profile of the two surfaces to be known. However, to simplify the contact problem, it can be assumed that the contact is between a rough and an infinitely smooth surface. This assumption is based on that the drain electrode is generally significantly smoother than the contact bumps [20]. Furthermore, based on the composite theory of roughness, two rough surfaces in contact are equivalent to one infinitely smooth surface in contact with a rough surface, for which the composite roughness parameters are defined in terms of the roughness parameters of the original two surfaces.

Following the asperity-based model of Greenwood and Williamson [15], the asperities are dealt with individually. However, the deformation behavior of a contact asperity is influenced by other contact asperities, in that the share of the total applied load for each individual contact asperity will be determined by the set of all asperities that are in contact. In this study, the asperities are randomly distributed and the deformation of the asperities is obtained from the constitutive creep relations, and the contact areas are obtained from the deformed geometrical shapes of the contact asperities.

Fractal geometry can be used to obtain the random and multiscale topographies that pertain to most microscale engineering applications and devices [18-21]. Majumder and

Bhushan [25] used a fractal description of the surface topography in a contact problem to analyze the deformation behavior of the contacting asperities. Yan and Komvopoulos [26] used a three-dimensional fractal mechanics theory for elastic-plastic surfaces in normal contact, and they obtained numerical estimates for the average contact pressure and the real area of contact.

A realistic multi-scale three-dimensional fractal surface topography can be generated using a Weierstrass-Mandelbrot function [21], [18] and can be expressed as [26]

$$z(x,y) = L_0 \left(G/L_0 \right)^{D-2} (\ln(\gamma)/M)^{1/2} \sum_{m=1}^M \sum_{n=0}^{n_{\max}} \gamma^{(D-3)n} \left\{ \cos \phi_{m,n} - \cos \left[(2\pi/L_0) \gamma^n (x^2 + y^2)^{1/2} \cos(\tan^{-1}(y/x) - \pi m/M) + \phi_{m,n} \right] \right\}, \quad (6.1)$$

where L_0 is the sample length, G is the fractal roughness, which is a height scaling parameter independent of frequency, D is the fractal dimension ($2 < D < 3$), which its magnitude determines the contribution of high and low frequency components in the surface function z , γ is a scaling parameter, which is based on surface flatness and frequency distribution density, M is the number of superposed ridges used to construct the surface, $\phi_{m,n}$ is a random phase, n is a frequency index, where its maximum n_{\max} is equal to $\text{int}(\text{Log}(L_0/L_s)/\text{Log}(\gamma))$, and L_s is a cut-off length.

During the first few contacts, the applied pressure is normally higher than the yield stress of the contact material. The initial contact pressure depends on the contact force and the size and the number of the asperities that are initially in contact. The contact force can be obtained from the electromechanical modeling of the cantilever beam, and the electrostatic field generated over the gate. During the period after the initial asperity deformation, contacting asperities are susceptible to creep under compressive strain. Creep deformation has been reported at micro-Newton level contact forces and low current levels ([27], [28], [29]). The rate of creep deformation is assumed to have a power-law dependence on the stress, and it can be stated as

$$\dot{\epsilon} = A \sigma^p \exp\left(-\frac{Q_c}{kT}\right), \quad (6.2)$$

where $\dot{\epsilon}$ is the strain-rate, A is a parameter relating to the material properties and the creep mechanism, σ is the stress, Q_c is the activation energy for creep, T is the absolute temperature, and k is the Boltzmann constant ($k=1.38\text{E-}23$ J/K). The stress exponent p in (6.2) is usually between 3 and 10, and is determined by the material composition.

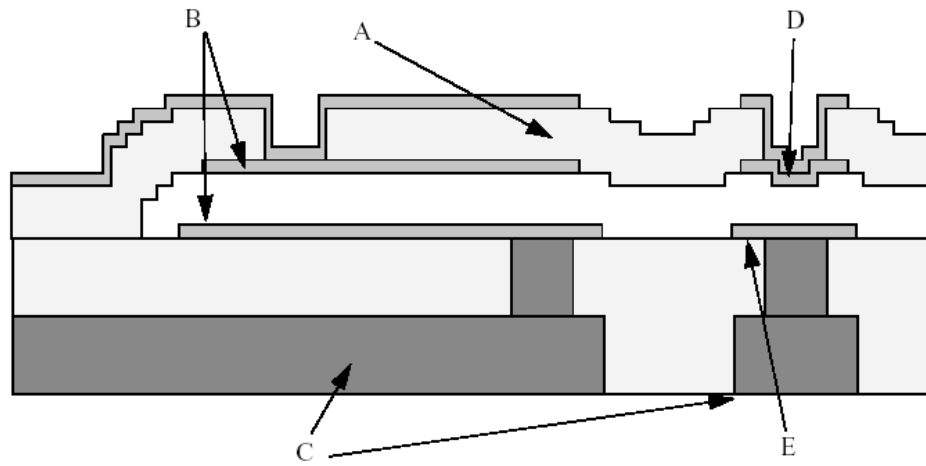
6.4 Physics of contact resistance and surface roughness

Due to the surface roughness, when two surfaces are in contact, the contact is made at a finite number of points, where the asperities on the both sides touch (Fig. 6.1(b)). These asperity contacts have different sizes, and since the electrical current is constricted to flow through these regions, it is essential to have an accurate representation of the contact area for predictions of the contact resistance. In addition to the role that the roughness has in limiting the contact area in the diffusive transport of electrons and increasing the regular ohmic resistance, for an asperity contact radius on the order of the electron mean free path, more electrons will be ballistically transported, and the contribution of the boundary scattering of electrons to the total constriction resistance can increase. Based on the range of the electron mean free path, which is approximately 50 nm in Au [30], and considering that MEMS contacts have been observed to have contact spots on the order of the electron mean free path [30], the boundary scattering effect can be critical for MEMS applications.

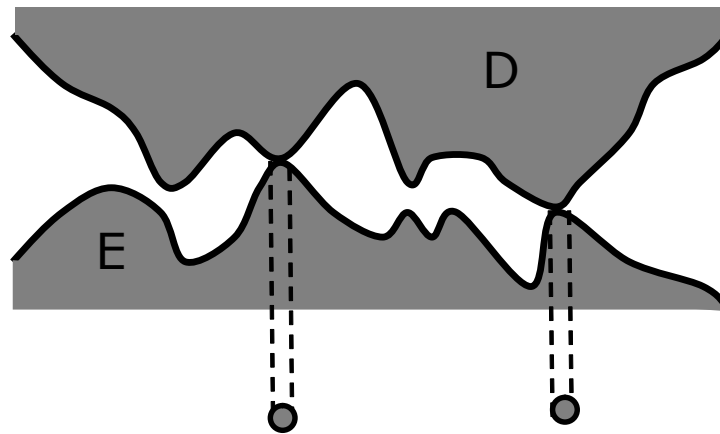
For a contact spot of radius a , and considering both ohmic and boundary scattering effects, the constriction resistance R_c can be given as [31], [32]

$$R_c = f\left(\frac{\lambda}{a}\right)R_M + R_S = f\left(\frac{\lambda}{a}\right)\frac{\rho}{2a} + \frac{4\rho\lambda}{3\pi a^2}, \quad (6.3)$$

where ρ is the electrical resistivity, and λ is the electron mean free path. R_M denotes the Maxwell resistance, which is the resistance due to lattice scattering mechanism [33], and R_S denotes the Sharvin resistance, which is due to the boundary scattering of electrons [34, 35]. In (6.3), $f(\lambda/a)$ is an interpolation function, which accounts for the transition between the two resistance regimes, and has the limiting values of 1 as the Knudsen number λ/a approaches zero for $a \gg \lambda$, and 0.624 as λ/a approaches infinity for $a \ll \lambda$. A commonly



(a)



Real contact area

(b)

Figure 6.1 – (a) Side view of RF MEMS switch. A is the silica cantilever. B are gold actuation capacitors used to pull the cantilever downward to the contact bump D. When the contact bump and the gold contact on the signal line, E, are touching the switch is closed and signal can be transferred. C are copper transfer lines encapsulated in silica during the stack process (b) Schematic of the surface asperities of the contact bump D, and the gold contact E. Micro-contacts are established when the two surfaces touch.

used expression for $f(\lambda/a)$ is [31], [32]

$$f\left(\frac{\lambda}{a}\right) = \frac{1 + 0.83(\lambda/a)}{1 + 1.33(\lambda/a)}. \quad (6.4)$$

To link the resistance of individual asperity contacts to the contact resistance, an effective contact resistance range has to be defined. In this study, we define a lower and an upper limit for the contact resistance. For the lower limit, it is assumed that contact spots do not interact with each other, and are in parallel. Hence, a lower limit for the effective contact resistance R_l , can be approximated as

$$\frac{1}{R_l} = \sum_{i=1}^N \frac{1}{R_{ci}}, \quad (6.5)$$

where N is the number of asperity contacts, and R_{ci} is the resistance of contact spot i . An upper limit for the effective contact resistance can be obtained by replacing all asperity contacts with a single asperity with a contact area equal to the total contact area of all the individual asperity contacts with an effective radius a_{eff} and an average resistivity ρ_{av} . Using (6.2), the upper limit for the contact resistance R_u is

$$R_u = f \frac{\rho_{av}}{2 a_{eff}} + \frac{4 \rho_{av} \lambda}{3 \pi a_{eff}^2}. \quad (6.6)$$

Inelastic deformations result in the hardening of the contact material, which in turn, increases the resistivity. On the other hand, as the contact asperities become extensively deformed, the contact area increases. Hence, there are two competing events in which the net effect will be highly dependent on the roughness characteristics. These interactions are further exacerbated by the increases in the contact temperature due to Joule heating. In addition to the contact heating direct effect on resistivity, if the temperature becomes high enough, the contact material can soften [33],[30], countering the hardening effects of inelastic deformations. At the same time, increases in temperature, can also accelerate the material's creep response over a rather long period of time, which can subsequently lead to device failure.

In the present model, strain-hardening and softening effects on resistivity are accounted for through a power-law formulation [36] as

$$\rho = \bar{\rho} \left(1 + \frac{\varepsilon_p}{\varepsilon_{ref}} \right)^q \left(1 - \exp\left(-\frac{Q}{kT_c} \right) \right), \quad (6.7)$$

where $\bar{\rho}$ is the average resistivity of a contact spot at temperature T_c , ε_p is the plastic strain, ε_{ref} is a reference strain, q is a material dependent parameter, Q is the activation energy for the mechanism by which stored dislocations are recovered or annihilated, and k is Boltzmann constant.

Using the basic definitions of the Joule heating and the heat flow, some contact heating models relate the contact spot temperature T_c , controlled by the joule heating mechanism, to the contact voltage V_c , without considering the size effects of the asperities in contact [33],[8],[37]. With the size of the contact spots being close to the electron mean free path of the contact material [30], boundary scattering contribution to the contact resistance increases. However, boundary scattering does not result in the Joule heating of the contact spots [38]. Hence, following the asperity-heating model of [30], contact spot temperature can be stated as

$$T_c = \sqrt{\frac{\gamma R_M}{4LR_c} V_c^2 + T_0^2}, \quad (6.8)$$

where L is Lorenz number ($L = 2.45\text{E-}8 \text{ W} \cdot \Omega / \text{K}^2$), and T_0 is the ambient temperature.

6.5 RF MEMS fabrication and experimental setup

A number of experiments were carried out at the Nanoscale Tribology Laboratory at North Carolina State University, with the goal that a comparison can be made between the experimental and numerical modeling results. The RF MEMS devices used for these experiments are commercially available single pole double throw switches by wiSpry Inc. Each die contains four double throw pairs. The switch consists of a cantilever arm with a pair of gold contacting dimples at the termination (Fig. 6.1(a)). The switches are fabricated using the wiSpry metal surface micromachining process. The die substrate is a silicon wafer. Gold and copper transfer lines are interlaced with silicon and oxide layers during the stack process. Sacrificial layers are subsequently etched away creating the three dimensional

cantilever structure and exposing the electrode plates used for actuation and the contact dimples which transfer the input signal. An electrostatic force is used to pull the cantilever arm down forcing the upper contacts dimples with the lower electrodes. The beam length is 135.5 μm with a width of 251 μm . The contact bumps are 6 μm in diameter and are separated by 55 μm . The travel distance of closure is 2 μm .

The devices are mounted on gold sidebrazed ceramic packages with 1 mil (25 μm) gold wirebonds connecting the device to the package, and the package is mounted inside of a vacuum system. The vacuum system is pumped to 1-5 mTorr, and then backfilled with Helium. The helium pressure was held at 760 Torr and at 293 Kelvin. This helium environment was also used to control stiction events. The vacuum environment created before backfilling the helium sufficiently removes moisture; however a thin layer of hydrocarbon is most likely present during testing. Two Keithley 2400 source-meters were used to actuate the switch and to record the resistance across the contacts using the four-point probe technique. Varying the output voltage from the source-meter changes the contact force. For the test device, 33 Volts generated a stable contact resistance for testing. Both source meters were controlled using LabVIEW software. Before each test, the switch was cold-switched 250 times. After this, the switch remained in the closed position, and a current of 100 μA was applied. A resistance measurement was taken from only one switch on the double throw, once per second for the duration of the testing period.

6.6 Contact models

Two surface roughness models were obtained using (6.1), over an area of 4 by 4 microns, which is close to the area of the contact bumps in our fabricated RF MEMS switches. The topography was varied, so that we can understand how roughness can affect contact behavior. In Model 1 (Fig. 6.2(a)) a surface roughness profile with a peak-to-valley of 12.8 nm, and an RMS of 7.2 nm was generated. Model 2 (Fig. 6.2(b)) has a peak-to-valley of 27.1 nm and an RMS of 14.9 nm. These values are representative of roughness profiles for gold RF MEMS switches. The mating surface is assumed to be flat and infinitely smooth. The parameters used in (6.1) for each model, are given in Table 6.1. As noted earlier, the

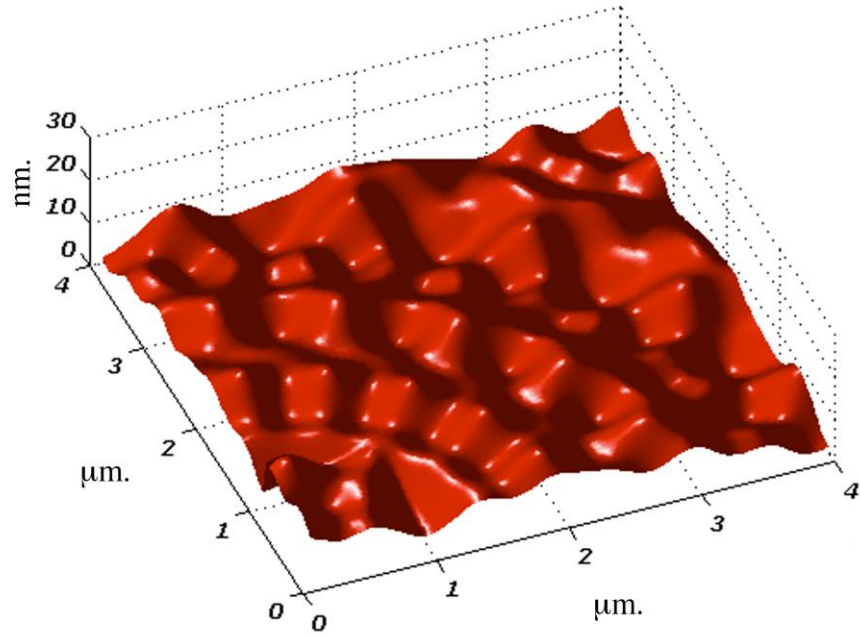
contact material is gold, and its electro-mechanical properties are given in [Table 6.2](#). For the current model, it is assumed that the ambient temperature is 293 K.

Table 6.1 – Roughness parameters.

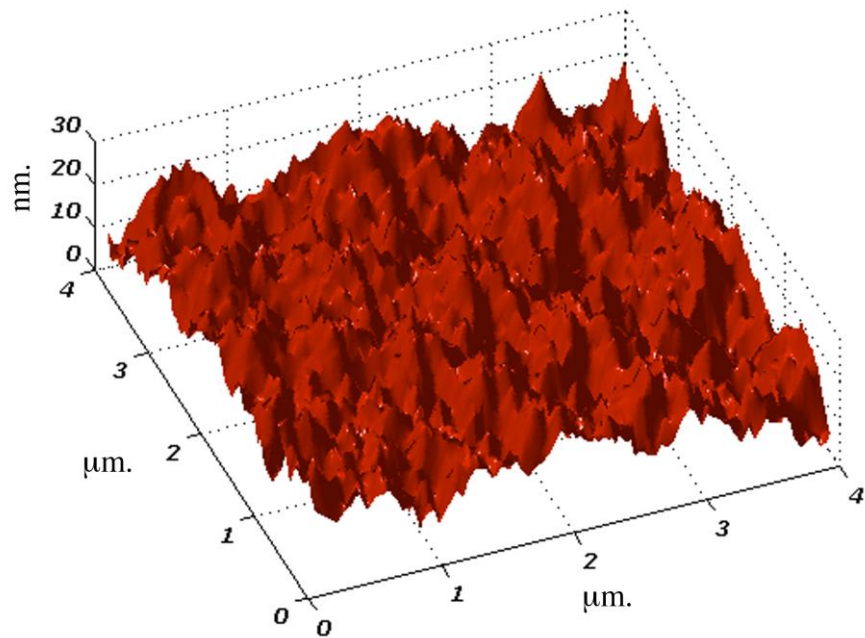
Parameter	Unit	Model 1	Model 2
L	m	4E-06	4E-06
G	m	0.5E-11	9.5E-11
D	—	2.5	2.6
γ	—	1.5	1.5
M	—	10	10
L_s	m	600E-09	3E-09

Table 6.2 – Electromechanical properties of Gold.

Electrical resistivity, ρ	2.5E-08 Ω .m
Power exponent in (2), p	7
Coefficient in (2), A	9E-16
Activation energy in (2), Q_c	3E-19 J
Reference strain in (7), ε_{ref}	0.001
Power exponent in (7), q	0.1



(a)

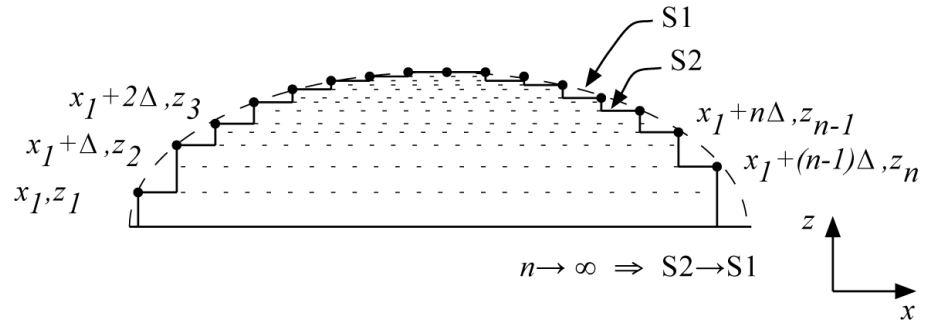


(b)

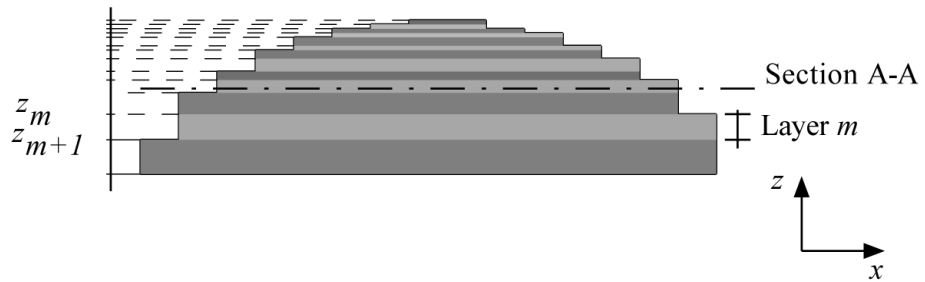
Figure 6.2 – Three-dimensional fractal surface topographies generated using a Weierstrass-Mandelbrot function (a) Model 1 has a peak-to-valley of 12.8 nm, and an RMS of 7.2 nm (b) Model 2 has a peak-to-valley of 27.1 nm and an RMS of 14.9 nm.

Contact forces in MEMS switches are typically in the range of a few μN s to as high as about one mN [27]. In this model, the applied contact force was chosen as $50 \mu\text{N}$, pertaining to a gold cantilever beam with dimensions of $150 \times 250 \times 0.5 \mu\text{m}$, and a gap of $2 \mu\text{m}$. The switch is assumed to remain in close position for the duration of the simulation, and it is also assumed that there is no insulating film effect. This is done so that we can better understand the direct effects of surface roughness on electro-mechanical behavior of RF MEMS switches with normal contact. Also the current model does not account for the generated debris from the fracture and crushing of the contact asperities, which is known to influence the electro-mechanical response of the RF MEMS switches [39].

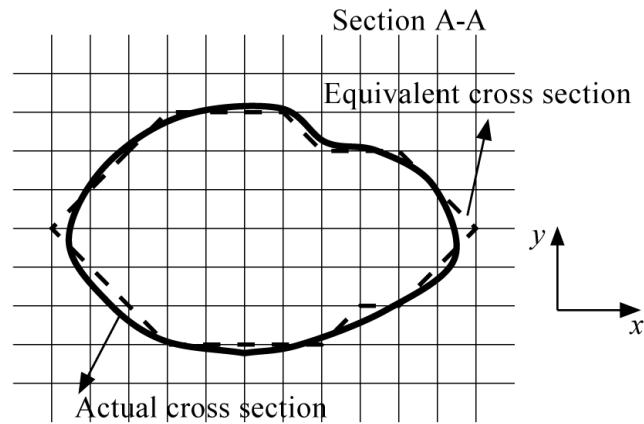
In RF MEMS switches with normal contact, the lateral deformations of asperities can be assumed to be negligible. Since creep is a long-term deformation mechanism, the normal finite deformations of contact asperities can then be obtained by a power-law constitutive relation (6.2). Since the generated surface roughness models do not necessarily have any prescribed asperity geometries, a numerical scheme has to be used to generate asperity geometries, which instead of having smooth surfaces (S1 in Fig. 6.3(a)) have irregular surfaces (S2 in Fig. 6.3(a)). A grid of x and y coordinates has been used to take sampling points on the surface of the asperities. The asperity geometries are obtained by connecting these sampling points. S2 approaches S1, when the number of sampling points increases (Fig. 6.3(a)). In this scheme, asperities can have any arbitrary geometry. The asperity geometries are constructed from layers that stack upon each other in z direction (Fig. 6.3(b)-(c)). The cross sectional area of each layer is assumed to be constant along its thickness, and is determined by using the x and y coordinates of the sampling points, which define that layer (Fig. 6.3(c)). The thickness of each layer is obtained by the z coordinates of the sampling points. The stresses and strains for each individual asperity in contact are then obtained for each individual layer, and the far-field approach is determined from the collective creep response of the contact asperities. The asperity tips that establish contact are identified at each time step by comparing the far-field approach with the asperity heights. An 80 by 80 grid of x and y coordinates is used to obtain the updated contact areas. Consequently the contact pressure, the resistance, the temperature, and the material properties are updated at



(a)



(b)



(c)

Figure 6.3 – (a) Schematic front view of a cross section of the actual asperity geometry with smooth surface (S1), and its equivalent geometry with an irregular surface (S2) that is obtained by connecting the sampling points. (b) The Asperity geometry that is assumed as stacked layers with uniform cross sectional areas along the thickness direction. (c) A schematic top view of a cross section of actual asperity, and its equivalent geometry that is obtained by connecting the corresponding sampling points.

each time step. Based on the deformations induced by the contact and asperity interactions, the number of asperities in contact and an effective radius for the contact area of each individual asperity are determined at each increment. Since the asperity contact layers are not necessarily circular, as an approximation the contact radius used in (6.3) is taken as the radius of a circle of equal area (see Fig. 6.3(c)). It is also assumed that the thermal boundary conditions are fixed.

6.7 Results and discussion

The ratio of the real contact area to the total area for the two roughness models is shown in Fig. 6.4. It is seen that the contact area increases with a steep slope at the beginning, which is due to the initial high applied pressure. The high applied pressure results

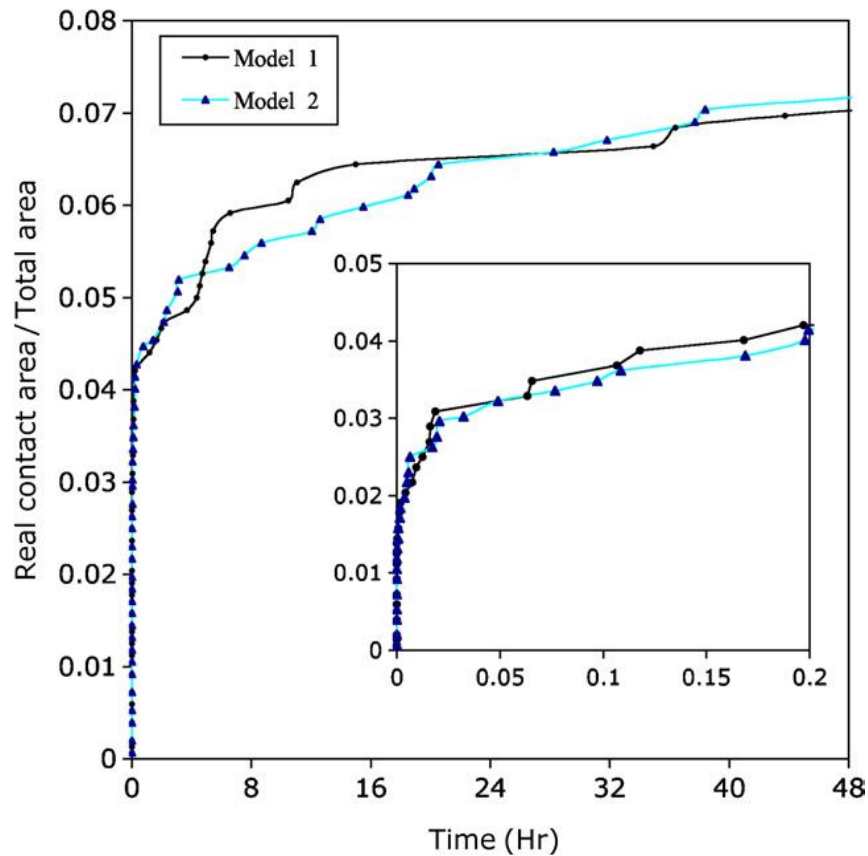


Figure 6.4 – Ratio of the real contact area to the apparent area over a 48-hour time span for the two surface roughness models. The inset magnifies the initial 12 minutes.

in large deformations in the contact asperities. The asperity deformations, in turn, lower the applied pressure in two different ways. Firstly, as the asperities deform, more asperities come into contact. Secondly, cross sectional area of asperities generally increases as they are pressed down. Hence, the real contact area increases. The decreased applied pressure, then, along with the strain hardening of the material reduces the rate of increase of the contact area. It is also seen from Fig. 6.4 that in both roughness models the real contact areas are almost equal and reach to about 7% of the apparent area after 48 hours. As noted earlier, roughness parameters have been selected in such a way that generate approximately equal real contact areas for the two models, but with different number of contact asperities. The number of micro-contact spots for the two roughness models is shown in Fig. 6.5.

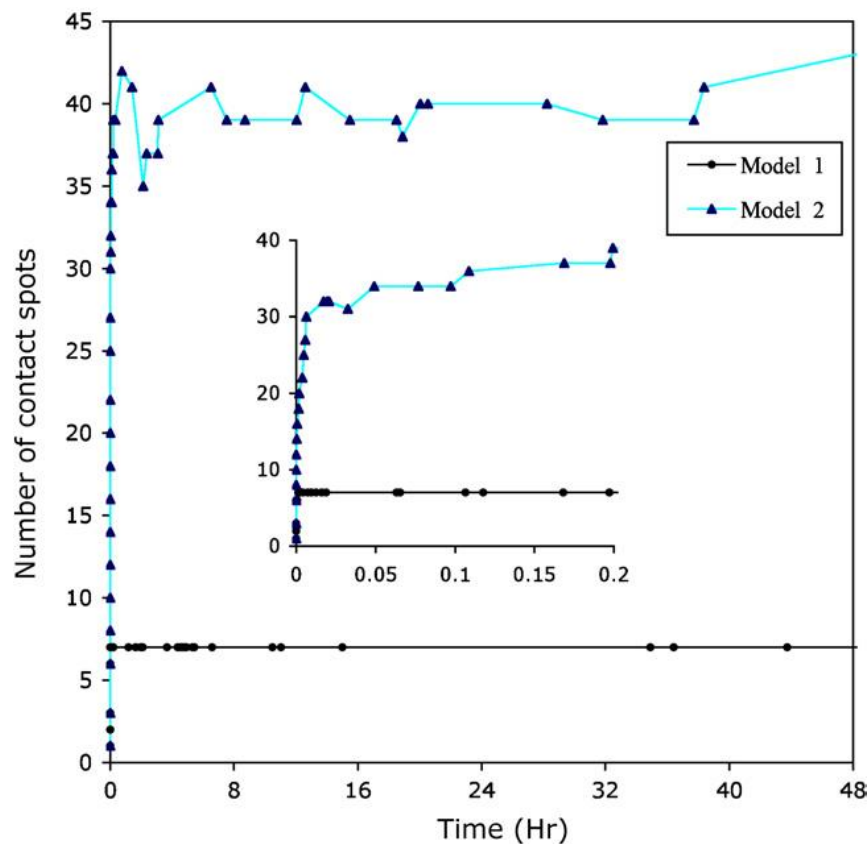


Figure 6.5 – Number of the contact spots over a 48-hour time span for the two surface roughness models. The inset magnifies the initial 12 minutes.

Model 1 has very few asperities in contact, with their number being almost constant over the contact period. In contrast, Model 2 has considerably more asperities in contact with their numbers increasing initially, and then fluctuating over time. The number of micro-contacts decreases when some micro-contacts coalesce, and it increases when new micro-contacts are established. The coalescence and generation of micro-contacts, changes the constriction resistance, which is also affected by how the micro-contacts are distributed over the apparent area. Based on this, two limit cases can be considered for how the micro-contacts are distributed, and accordingly two limits can be determined for the contact resistance.

For the two roughness models, the lower and upper limits of contact resistance have been calculated over time, and the results are shown in Fig. 6.6. The lower limit corresponds to the case for which each micro-contact is assumed to be far enough from the others so that there will be no neighboring asperity effects. The upper limit corresponds to the case for which a large micro-contact is assumed to form by the coalescence of all the micro-contacts. Two stages of decrease can be seen in the curves of Fig. 6.6. The contact resistance initially decreases sharply until it reaches a rather stable level, during which the contact resistance continues to gradually decrease. The initial rate of reduction of contact resistance is associated with the initial deformation rate of asperities. Consequently, the increased contact area and the number of contact spots, reduces the applied pressure, which in turn decreases the deformation rate of asperities. The results show that for the selected roughness parameters for both roughness models, the overall effect of increased resistivity at the asperity contacts due to the strain hardening is dominated by the contact area effect. Model 1 has an initial lower limit contact resistance of 44 m Ω , and an upper limit of about 125 m Ω . After the initial deformation of the asperities for 10 minutes, the contact resistance decreases to between 32 and 88 m Ω . After 48 hours, the contact resistance reduces to between 20 and 63 m Ω , which on average is about 47% of the initial value (Fig. 6.6). Model 2 has an initial contact resistance between 40 and 127 m Ω , which after 10 minutes decreases to between 20 and 84 m Ω . The contact resistance level after 48 hours falls between 11 and 57 m Ω , which on average is about 37% of the initial value (Fig. 6.6). After 48 hours, contact resistance in

Model 1 is about 1.22 times the contact resistance of Model 2, which with having almost equal contact areas, the difference can be attributed to the number of the micro-contacts in each model. Reported minimum contact resistance, in previous studies, varies from less than 0.1Ω to several ohms at loads from $25 \mu\text{N}$ to $300 \mu\text{N}$ for gold-on-gold contacts in different environments [27]. Majumder *et al.* [20] reported a contact resistance between 60 and 130 $\text{m}\Omega$ for a population of 50 asperities, and a contact resistance between 80 and 110 $\text{m}\Omega$ for a population of five asperities, both pressed by a $50 \mu\text{N}$ contact force. Hence, it is seen that the predicted contact resistance values for the two roughness profiles of this study are within the same range of these cited studies.

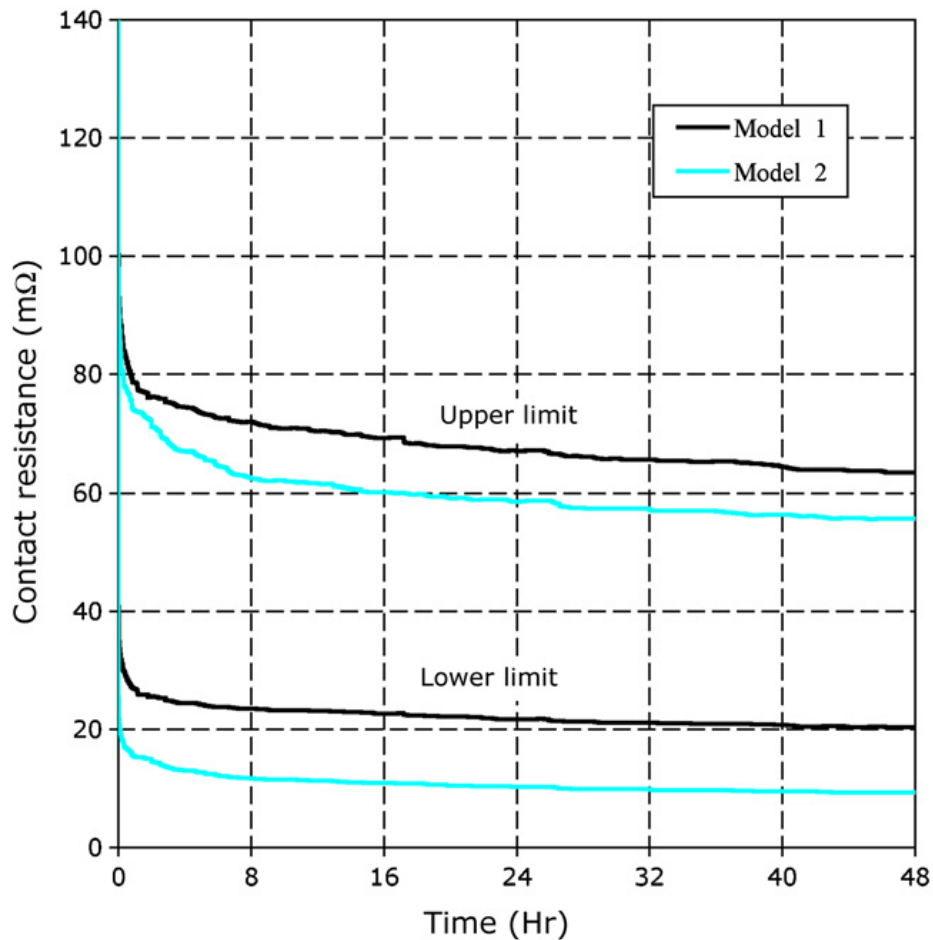


Figure 6.6 – The lower and upper limits of the contact resistance over a 48-hour time span for the two surface roughness models.

To further validate our model, we also compared the predicted contact resistance of the roughness models with experimental measurements described in Section IV. Three experimentally measured contact resistance curves over a 90-minute time span are shown in Fig. 6.7, along with the predicted upper limits of the contact resistance for the two roughness models. To be able to make a meaningful comparison, each data set is normalized by its respective maximum value. The experimental and the predicted results show a similar evolution for the contact resistance. Quantitatively, however, the experimental measurements show a less resistance drop over the time. On average, the experimental measurements show that contact resistance drops to about 80% of its initial maximum value

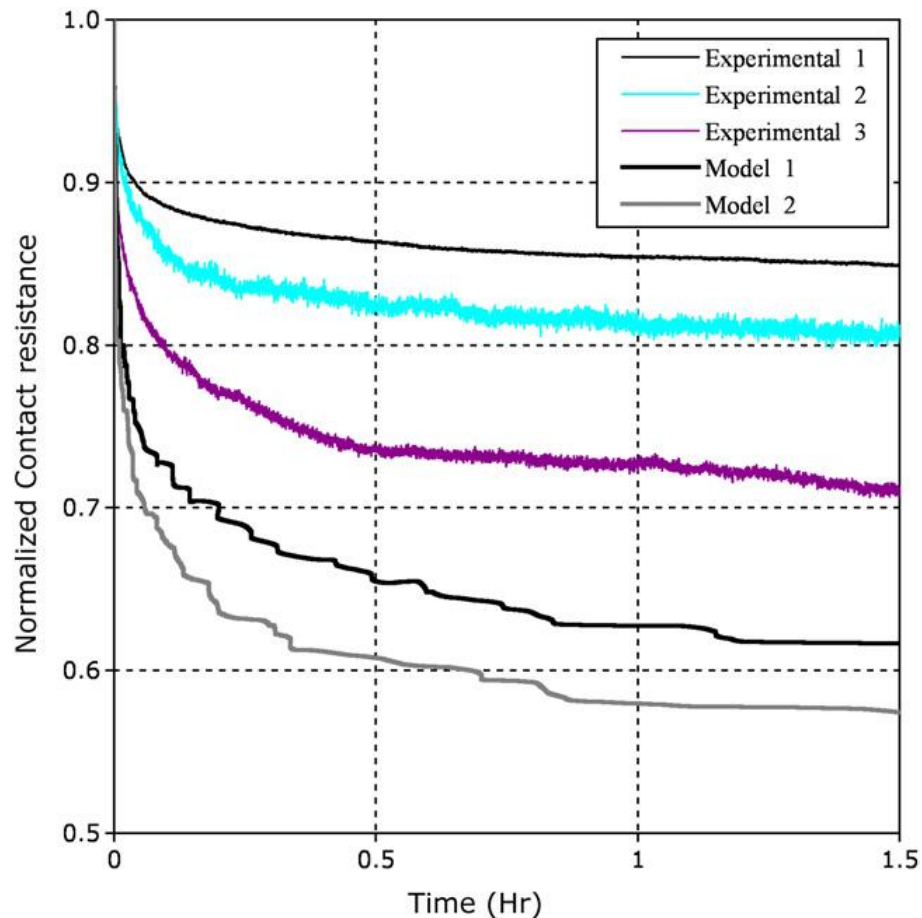


Figure 6.7 – Normalized Contact resistance over a 90-minute time span.

after 90 minutes, while the simulations predict a 40% drop (60% of their initial value).

Another resistance measure that can be used to better understand the effects of roughness characteristics on the total resistance response of a population of micro-contacts is the average resistance of the individual contact asperities (Fig. 6.8). By comparing Fig. 6.6 and Fig. 6.8, it can be seen that the estimated upper limit for the contact resistance, when stabilized, is significantly lower than the average resistance of the individual contact spots. The average resistance of individual micro-contacts of Model 2 initially increases to about 1.4 Ω , and then fluctuates around 1.2 Ω . The initial increase is due to strain hardening and increased resistivity, which locally surmounts the contact area effects.

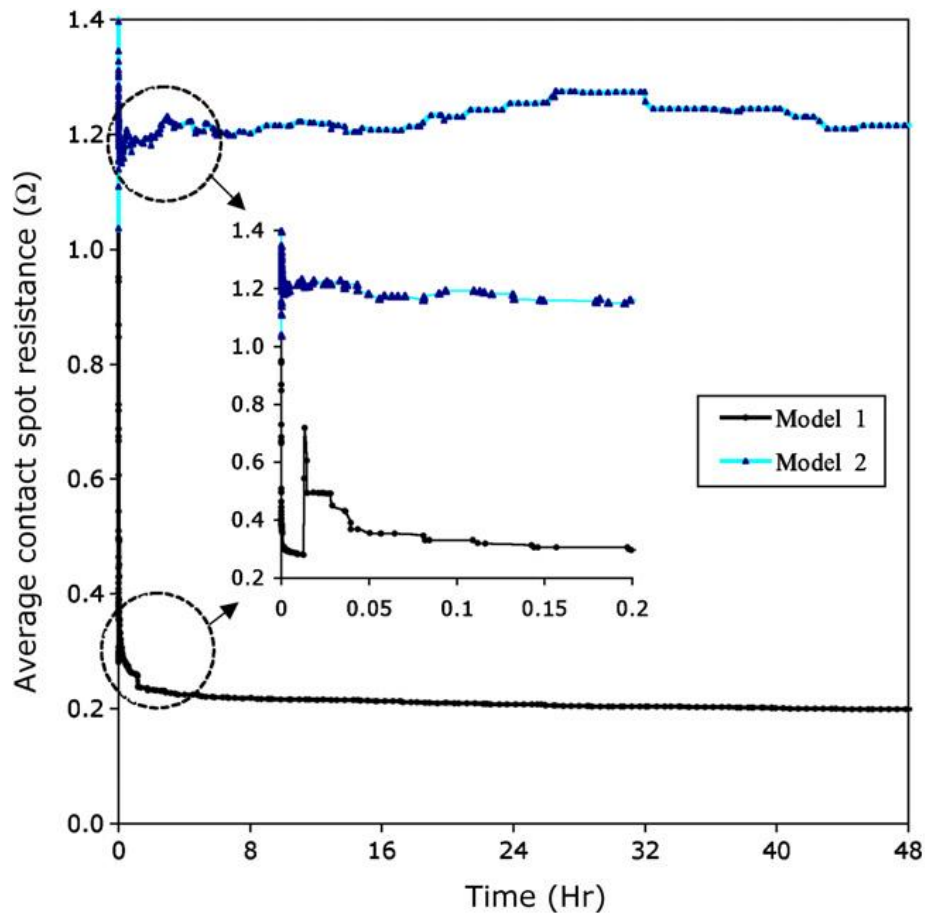


Figure 6.8 – Average contact spot resistance of the two surface roughness models over a 48-hour time span. The inset magnifies the initial 12 minutes.

In contrast, the average resistance of micro-contacts in Model 1 is initially about 1.15 Ω , which falls down to between 0.2 and 0.3 Ω , then increases and falls down again. The fluctuations best show how strain hardening and increased resistivity compete with contact area effects. Fig. 6.9 then shows to what extent the strain hardening can increase the resistivity of the contact material. It is seen from the curves of Fig. 6.9 that in Model 1, maximum resistivity increases to about 4.1E-08 Ωm at deformed asperity contacts, which is 1.64 times the initial resistivity. In Model 2, the maximum resistivity reaches to about 4.4E-08 Ωm , which is 1.76 times the initial resistivity. Higher resistivity in Model 2 is an indication of asperities with higher curvatures, which can also be seen in Fig. 6.2.

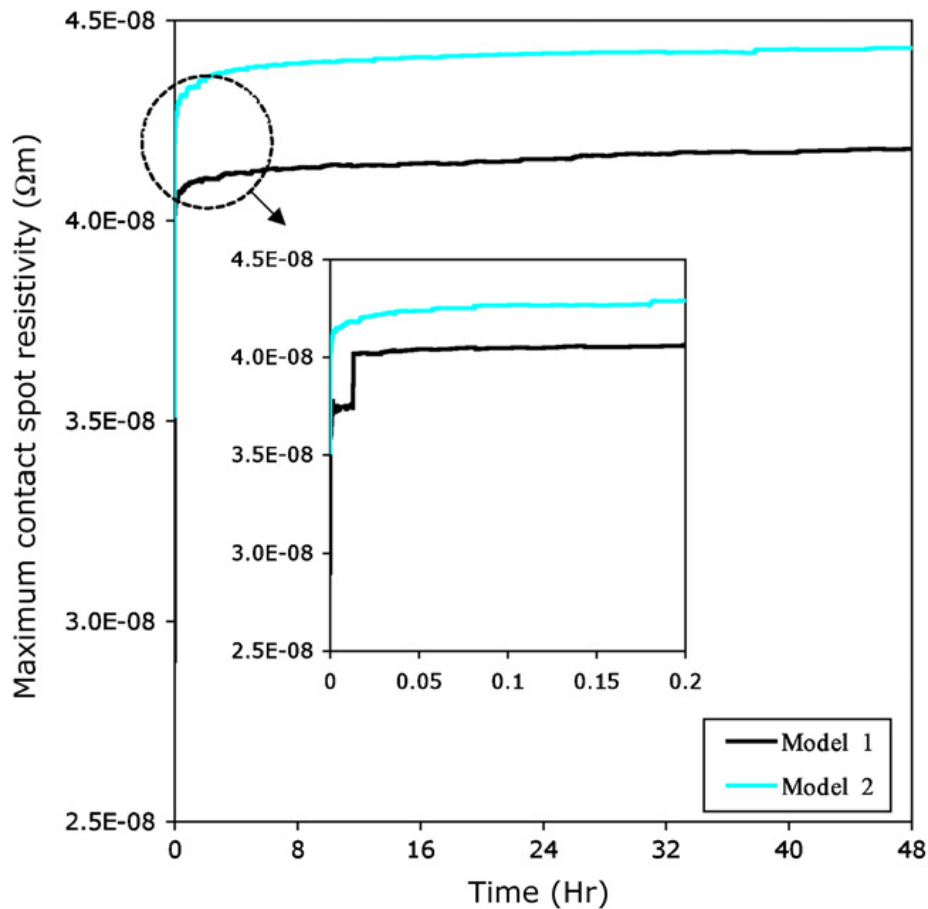


Figure 6.9 – Maximum resistivity at the contact spots for the two surface roughness models over a 48-hour time span. The inset magnifies the initial 12 minutes.

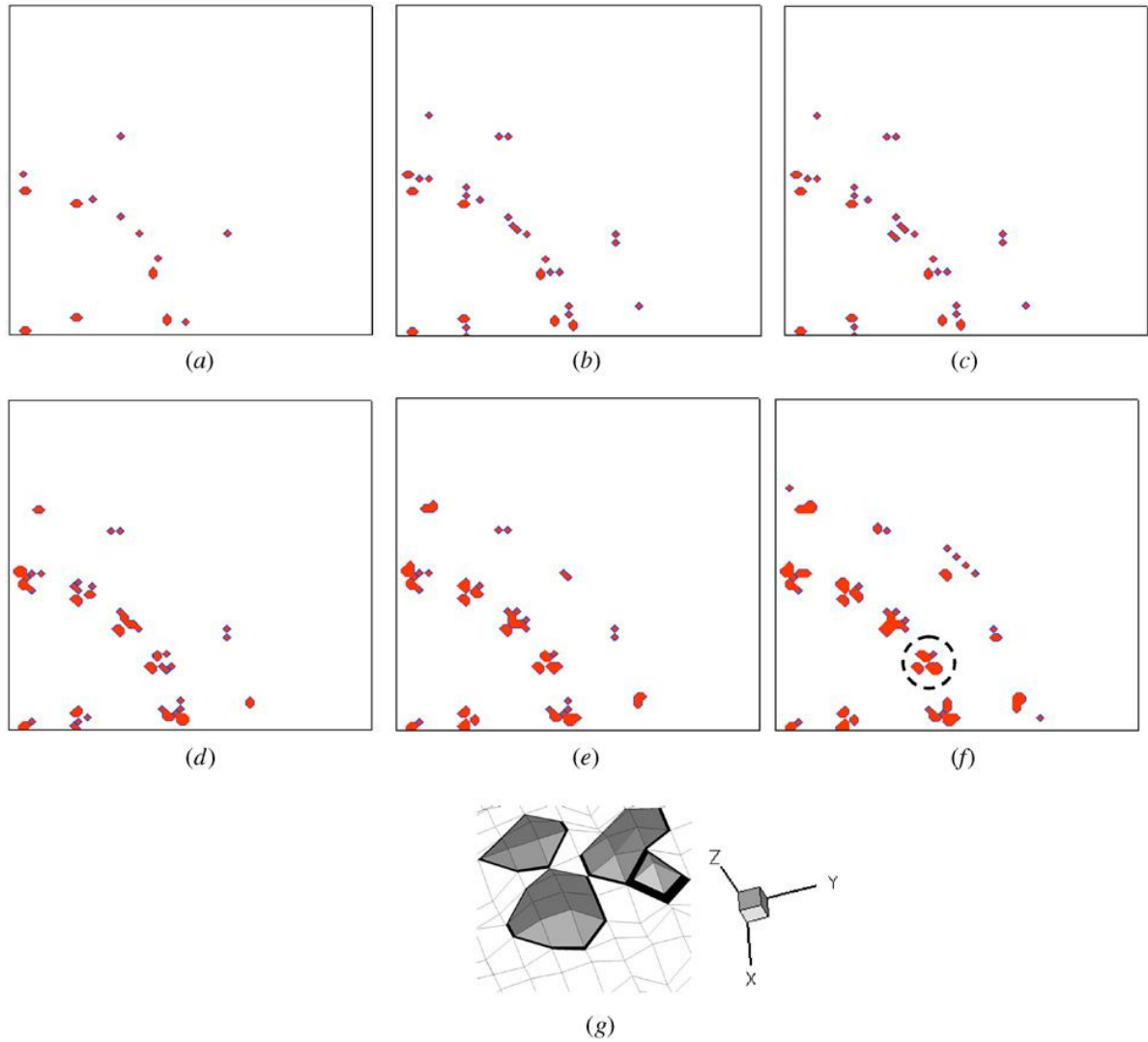


Figure 6.10 – Top-view snap shots of the contact evolution for Model 2 (a) after 1 sec., real contact area is 1.31%, contact resistance is 27 ~ 77 m Ω , and applied pressure is 237 MPa (b) after 30 sec., real contact area is 2.50%, contact resistance is 14 ~ 56 m Ω , and applied pressure is 125 MPa. (c) after 1 min, real contact area is 2.63%, contact resistance is 14 ~ 55 m Ω , and applied pressure is 119 MPa (d) after 1 hr., real contact area is 4.47%, contact resistance is 9 ~ 42 m Ω , and applied pressure is 70 MPa (e) after 10 hr., real contact area is 5.60%, contact resistance is 8 ~ 37 m Ω , and applied pressure is 56 MPa (f) after 40 hr., real contact area is 7.0 %, contact resistance is 7 ~ 34 m Ω , and applied pressure is 44 MPa (g) magnified 3D view of the asperity cluster circled in (f).

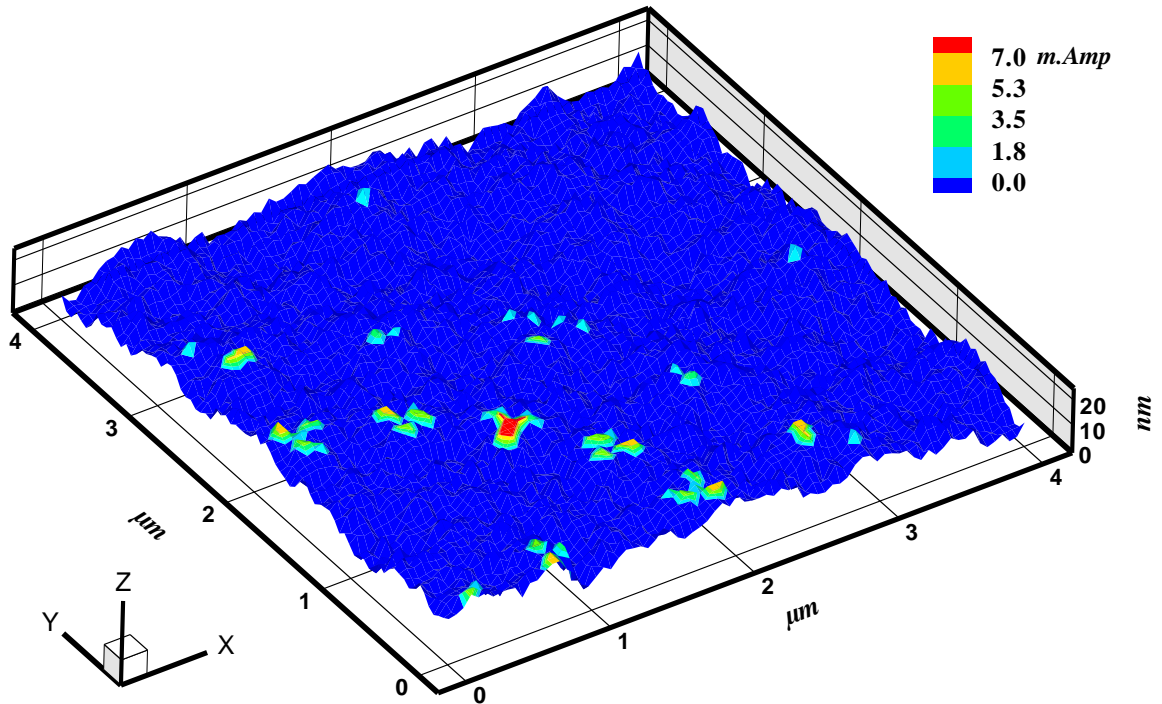


Figure 6.11 – Contour of current magnitude for a voltage drop of 1 mV.

Top-view snap shots of contact evolution over the 48-hour time span for Model 2 are also shown in [Fig. 6.10](#). The snap shots show how micro-contacts are distributed and clustered over the apparent contact area. Contact area, resistance, and applied pressure are also given for each snapshot.

The temperature increase at contact spots is insignificant in both models for the voltage drop of 1 mV. However, for a voltage drop of 0.1 V, a very high current flows through the micro contacts, which results in temperatures of up to 370 K at the contact spots.

The current contour for a 1 mV voltage drop applied to Model 2 is shown in Fig. 6.11. The 3-D contour shows that, after 48 hours, current flow has increased to about 7 mA at some contact spots, which is within the reported range for gold contacts [27]. Furthermore, the maximum allowable current for gold contacts has been reported to be from 20 to 500 mA in different environments [27].

6.8 Conclusions

Modeling predictions and experimental measurements were obtained to characterize the electro-mechanical response of RF MEMS switches due to variations in surface roughness and finite asperity deformations. Three-dimensional surface roughness profiles were generated based on a Weierstrass-Mandelbrot fractal representation, to match the measured roughness characteristics of contact bumps of manufactured RF MEMS switches. Real areas of contact and the number of contact asperities were then obtained over the time, as a function of the asperity deformations under applied pressure.

The interrelated effects of roughness characteristics, material hardening due to creep deformation, and softening due to temperature increases from Joule heating were investigated on contact resistance. Changes in the constriction resistance of individual asperities were shown to depend on the two competing events of increase in the contact area and the increase in electrical resistivity. The numerical predictions and the experimental measurements indicate that there are two main stages related to the variation of the contact resistance. An initial decrease with a steep slope, with a subsequent gradual decrease was characteristic of the contact resistance behavior. In the initial stage, the decrease is attributed to the high applied pressure, and the slightly strain-hardened contact material. In the second stage, the applied pressure had considerably decreased, and the contact material had extensively strain hardened.

The results indicate that a very small percentage of the apparent contact area, in both cases less than 10%, conducts the electrical current. They also indicate that asperity coalescence prevents the unlimited increase of the number of the micro-contacts. Furthermore, based on the distribution, size and number of the micro-contacts, the results

indicate that the electrical interactions of the neighboring micro-contacts cannot be neglected in the design of RF MEMS devices. The results also show different characteristic contact resistance behaviors for a population of asperities versus individual asperities. This modeling approach, in conjunction with the experimental measurements and observations, can be used as a framework to design reliable RF MEMS devices with extended lifetimes.

6.9 Acknowledgements

The authors gratefully acknowledge useful support and interactions with Art Morris of wiSpry, Inc. This work was funded by the AFOSR Extreme Friction MURI program, AFOSR grant FA9550-04-1-0381.

6.10 References

- [1] Barker NS, Rebeiz GM 1998 Distributed MEMS true-time delay phase shifters and wide-band switches *IEEE Transactions on Microwave Theory and Techniques* **46** 1881-1890
- [2] Brown ER 1998 RF-MEMS switches for reconfigurable integrated circuits *IEEE Transactions on Microwave Theory and Techniques* **46** 1868-1880
- [3] Hah D, Yoon E, and Hong S 2000 A low-voltage actuated micromachined microwave switch using torsion springs and leverage *IEEE Transactions on Microwave Theory and Techniques* **48** 2540-2545
- [4] Park JY, Kim GH, Chung KW, and Bu JU 2001 Monolithically integrated micromachined RF MEMS capacitive switches *Sensors and Actuators A: Physical* **89** 88-94
- [5] Taylor WP, Brand O, and Allen MG 1998 Fully integrated magnetically actuated micromechanical relays *Journal of Microelectromechanical Systems* **7** 181-191

- [6] Yao ZJ, Chen S, Estelman S, Denniston D, and Goldsmith C 1999 Micromachined low-loss microwave switches *Journal of Microelectromechanical Systems* **8** 129-134
- [7] Rebeiz GM 2003 *RF MEMS, Theory, Design, and Technology*. New York Wiley.
- [8] Hyman D, Mehregany M 1999 Contact physics of gold microcontacts for MEMS switches *IEEE Transactions on Components and Packaging Technologies* **22** 357-364
- [9] Johnson KL 1985 *Contact Mechanics*. Cambridge, UK Cambridge University Press.
- [10] Kennedy FE, Ling FF 1974 Elasto-plastic indentation of a layered medium *Journal of Engineering Materials and Technology* **96** 97-103
- [11] Komvopoulos K 1988 Finite element analysis of a layered elastic solid in normal contact with a rigid surface *Journal of Tribology* **110** 477-485
- [12] Komvopoulos K, Ye N 2001 Three-dimensional contact analysis of elastic-plastic layered media with fractal surface topographies *Journal of Tribology* **123** 632-640
- [13] Kral ER, Komvopoulos K 1996 Three-dimensional finite element analysis of surface deformation and stresses in an elastic-plastic layered medium subjected to indentation and sliding contact loading *Journal of Applied Mechanics* **63** 365-375
- [14] Mesarovic SDj, Fleck NA 1999 Spherical indentation of elastic-plastic solids *Proceedings of the Royal Society of London. Series A* **455** 2707-2728
- [15] Greenwood JA, Williamson JBP 1966 Contact of nominally flat surfaces *Proceedings of the Royal Society of London. Series A* **295** 300-319
- [16] Larsson J, Biwa S, Storakers B 1999 Inelastic flattening of rough surfaces *Mechanics of Materials* **31** 29-41

- [17] Berry MV, Lewis ZV 1980 On the Weierstrass-Mandelbrot fractal function
Proceedings of the Royal Society of London. Series A **370** 459-484
- [18] Borodich FM, Onishchenko DA 1999 Similarity and fractality in the modeling of roughness by a multilevel profile with hierarchical structure *International Journal of Solids and Structures* **36** 2585-2612
- [19] Majumder A, Tien CL 1990 Fractal characterization and simulation of rough surfaces *Wear* **136** 313-327
- [20] Majumder S, McGruer NE, Adams GG, Zavracky PM, Morrison RH, and Krim J 2001 Study of contacts in an electrostatically actuated microswitch *Sensors and Actuators A* **93** 19-26
- [21] Mandelbrot BB 1983 *The Fractal Geometry of Nature*. New York Freeman.
- [22] Blackmore D, Zhou JG 1998 Fractal analysis of height distributions of anisotropic rough surfaces *Fractals* **6** 43-58
- [23] Ciavarella M, Demelio G, Barber JR, and Jang YH 2000 Linear elastic contact of Weierstrass profile *Proceedings of the Royal Society of London. Series A* **456** 387-405
- [24] Komvopoulos K 2000 Head-disk interface contact mechanics for ultra-high density magnetic recording *Wear* **238** 1-11
- [25] Majumder A, Bhushan B 1991 Fractal model of elastic-plastic contact between rough surfaces *Journal of Tribology* **113** 1-11
- [26] Yan W, Komvopoulos K 1998 Contact analysis of elastic-plastic fractal surfaces *Journal of Applied Physics* **84** 3617-3624

- [27] Patton ST, Zabinski JS 2005 Fundamental studies of Au contacts in MEMS RF switches *Tribology Letters* **18** 215-230
- [28] Budakian R, Putterman SJ 2002 Time scales for cold welding and the origins of stick-slip friction *Physical Review B* **65**
- [29] Gregori G, Clarke DR 2006 The interrelation between adhesion, contact creep, and roughness on the life of gold contacts in radio-frequency microswitches *Journal of Applied Physics* **100** 094904-1
- [30] Jensen BD, Chow LL, Huang K, Saitou K, Volakis JL, and Kurabayashi K 2005 Effect of nanoscale heating on electrical transport in RF MEMS switch contacts *Journal of Microelectromechanical Systems* **14** 935-946
- [31] Wexler G 1966 The size effect and the non-local Boltzmann transport equation in orifice and disk geometry *Proceedings of the Physical Society* **89** 927-941
- [32] Nikolic B, Allen PB 1999 Electron transport through a circular constriction *Physical Review B* **60** 3963-3969
- [33] Holm R 1967 *Electric Contacts-Theory and Applications* 4th ed. Berlin, Germany Springer-Verlag.
- [34] Jansen AGM, van Gelder AP, and Wyder p 1980 Point-contact spectroscopy in metals *Journal of Physics C13* 6073-6118
- [35] Sharvin YV 1965 A possible method for studying Fermi surfaces *Journal of Experimental and Theoretical Sciences* **21** 655-656
- [36] Zikry MA 1994 An accurate and stable algorithm for high strain-rate finite strain plasticity *Computers & Structures* **50** 337-350

- [37] Yan X, McGruer NE, Adams GG, and Majumder S, "Finite element analysis of the thermal characteristics of MEMS switches," in *Proc. 12th Int. Conf. on Transducers, Solid-State Sensors, Actuators, and Microsystems*, Jun. 2003.
- [38] Weber L, Lehr M, and Gmelin E 1996 Investigation of the transport properties of gold point contacts *Physica B: Condensed Matter* **217** 181-192
- [39] Alsem DH, Stach EA, Dugger MT, Enachescu M, and Ritchie RO 2007 An electron microscopy study of wear in polysilicon microelectromechanical systems in ambient air *Thin Solid Films* **515** 3259-3266

CHAPTER 7

The Role of Creep in the Time-Dependent Resistance of Ohmic Gold Contacts in RF-MEMS Devices

*O. Rezvanian^a, C. Brown^b, M.A. Zikry^a, A.I. Kingon^c, J. Krim^b,
D.L. Irving^c, and D.W. Brenner^c*

^a Department of Mechanical and Aerospace Engineering

^b Department of Physics

^c Department of Materials Science and Engineering

North Carolina State University

Raleigh, NC 26795

Journal of Applied Physics in press 2008.

This work has been supported by the Extreme Friction MURI program, AFOSR grant FA9550-04-1-0381 entitled “Multifunctional Extreme Environment Surfaces: Nanotribology for Air and Space. C.B. and J.K. were also supported by the DARPA Center for RF MEMS reliability and Design Fundamentals Grant # HR0011-06-1-0051.

7.1 Abstract

It is shown that measured and calculated time-dependent electrical resistances of closed gold Ohmic switches in RF MEMS devices are well described by a power law that can be derived from a single asperity creep model. The analysis reveals that the exponent and prefactor in the power law arise respectively from the coefficient relating creep rate to applied stress and the initial surface roughness. The analysis also shows that resistance plateaus are not in fact limiting resistances, but rather result from the small coefficient in the power law. The model predicts a transition from a constant contact resistance to the power law that occurs at increasingly longer times for successive switch opening and closing that is caused by asperity blunting. Analysis of the first few seconds of the measured resistance for three successive openings and closings of one of the MEMS devices supports this prediction. This work thus provides guidance toward the rational design of Ohmic contacts with enhanced lifetimes and reliabilities by better defining variables that can be controlled through material selection, interface processing, and switch operation.

7.2 Introduction

Radio frequency micro-electromechanical system (RF-MEMS) devices use two types of switches, capacitive switches, which have dielectric contacts, and Ohmic switches, which have conducting contacts ¹. For most applications, capacitive switches traditionally have longer lifetimes and better reliabilities than Ohmic switches. This is due in part because the adhesion of capacitive contacts can be made relatively weak, while the requirement of small contact resistances for Ohmic switches require metal-metal contacts that can be susceptible to cold welding and strong adhesion. To effectively engineer Ohmic switches with optimized performance, a better understanding of the mechanics of metal contacts is needed, as well as how the associated processes are related to contact resistance.

In a recent study, Zikry, Krim and co-workers compared the time-dependent contact resistance between two loaded rough gold surfaces calculated by a specialized finite-element plasticity model to experimental measurements of the time-dependent resistance of an RF-MEMS device containing a closed gold Ohmic switch ². The calculated and experimental

measurements had very similar trends. Both showed a relatively large initial drop in resistance over a time period of up to a few minutes, followed by an apparent plateau in the resistance. For the experiment, the initial closure of the switch resulted in a plateau value of about 2Ω , while opening and then closing the switch two times resulted in plateau values of about 2.8Ω and 4Ω , respectively. The plateau values for the contact resistance in the modeled system were of the order of tens of $m\Omega$, with initially rougher surfaces producing higher plateau contact resistances. While the calculated and experimental data were qualitatively similar, the quantitative behavior appeared to be very different. For example, scaling the experimental and calculated resistances to the same initial value did not produce overlaying curves. In a related paper, Brown *et al.* characterized the resistance of an Ohmic gold switch in an RF-MEMS device in the temperature range 77-300K³. At room temperature the device showed a similar drop in resistance with time as the switch used in [2].

In this paper we examine the computational and experimental resistances reported previously in [2] and [3] in terms of asperity creep. Our analysis shows that after a maximum of a few minutes, all of the experimental data near room temperature are well described by a power law in time, and that the same power law relation with a similar exponent also describes the prior modeling data. This fitting suggests that while the apparent plateau regions define the practical contact resistances for most device applications, they do not in fact define the limiting resistances. Rather the plateaus are a consequence of the small exponential in the power law relations. Using an analytic single-asperity model it is shown that creep deformation can lead to the same power law relation, and more importantly that the power law exponent can be directly calculated from the constitutive relation between creep rate and load. This analysis also shows that the prefactor in the power law relation depends on the initial surface structure.

7.3 Analysis of experimental and calculated resistance data

Details of the computational plasticity model have been presented previously², and therefore only a brief description is given here. A square contact with total dimensions of

4 μm x 4 μm subject to a total load of 50 μN was assumed. These load and contact dimensions are based on the properties of the fabricated RF MEMS switches described below. For simplicity, the two gold rough surfaces at the contact were replaced with a rough surface contacting a perfectly smooth surface. This is justified by the composite theory of roughness that demonstrates that with an appropriate transformation a combined contact roughness can be replaced with a smooth plus rough interface ^{4,5}. Each asperity contact was treated independently, and the distribution of contact geometries was determined from a Weierstrass-Mandelbrot function ⁶. The load on each individual asperity was determined by distributing the overall load according to the shapes and heights of the collection of asperities produced by a given set of roughness parameters. Two sets of roughness parameters were used that differed in the fractal roughness and dimension, as well as in the cut-off length that determined the maximum in the frequency index.

In the initial stages of the computation, the applied pressure was larger than the yield stress and therefore the asperities deformed plastically. For subsequent loading, the asperities deformed via creep with an assumed power law dependence of

$$\dot{\epsilon} = C\sigma^p e^{(-Q_c/kT)} \quad (7.1)$$

where $\dot{\epsilon}$ is the creep rate, C depends on the material and creep mechanism, σ is the applied stress, p is the stress exponent, Q_c is the activation energy for creep, k is the Boltzmann constant, and T is temperature. Redistribution of material at the contact due to creep was neglected for simplicity in the prior modeling. Therefore the resistances of individual asperities are slightly over estimated.

Because the dimensions of some the individual asperity contacts are of the order of the electron mean free path, an expression incorporating both the Maxwell and Sharvin resistance was used to calculate the resistance of an individual asperity ⁷. This expression includes an interpolating function that depends on the ratio of the electron mean free path to the contact spot radius. A power law formulation was used to relate the resistivity of an asperity to strain hardening that included a temperature dependence to recovery and annihilation of stored dislocations due to plastic deformation. Two models were used to combine the resistances of the individual asperities. The first assumes that the contacts

remain isolated and act in parallel. The second model replaces the collection of contacts with a single contact with area equal to sum of the single asperities areas and a resistivity equal to the average of the individual contacts. The first and second models represent lower and upper limits to the true contact resistance, respectively.

Two different commercially available single pole double throw switches by wiSpry Inc. were used for the prior experimental measurements. Herein device one refers the device used in [2], which is the original paper comparing the detailed modeling to the experimental device resistances; device two refers to the device used for the room temperature and low temperature experiments discussed in [3]. To remove residual moisture, both devices were placed in a vacuum that was backfilled with helium and then held at a pressure of 760 Torr and a temperature of 293K. A four point probe technique was used to measure resistance across the switches. Before the first measurement device one was cold-switched (e.g. switched without an applied voltage) 250 times, and then a 100 μ A DC current was applied across the device as the switch was held closed. The switch was then opened, cold switched 250 times, and closed again during a resistance measurement for two additional times for a total of 3 data measurements. For the data shown below, device two was cold switched 200 times, closed, and the resistance was measured with an applied 1 mA DC current. For both devices resistance measurements were taken each second from only one switch on the double throw for the duration of each experiment. Further manufacturing and operating details of these devices are given in the respective references.

The results of the prior detailed computations were analyzed in terms of the time dependence of the ratio of the true to apparent contact areas, the number of contacting asperities, the size and shape of the asperities, the current through each asperity, and the total contact resistance. The latter was compared to the experimental measurements, and so the present analysis focuses on this relation. Plotted as the discrete points in the bottom panel of Fig. 7.1 is the calculated lower limit contact resistance for the two roughness models. Plotted as solids lines in the top panel are the measured resistances from the MEMS devices. Curves labeled I, II and III denote measurements from the first, second and third runs from device one. The curve labeled IV is the measurement from device two. As described above, each

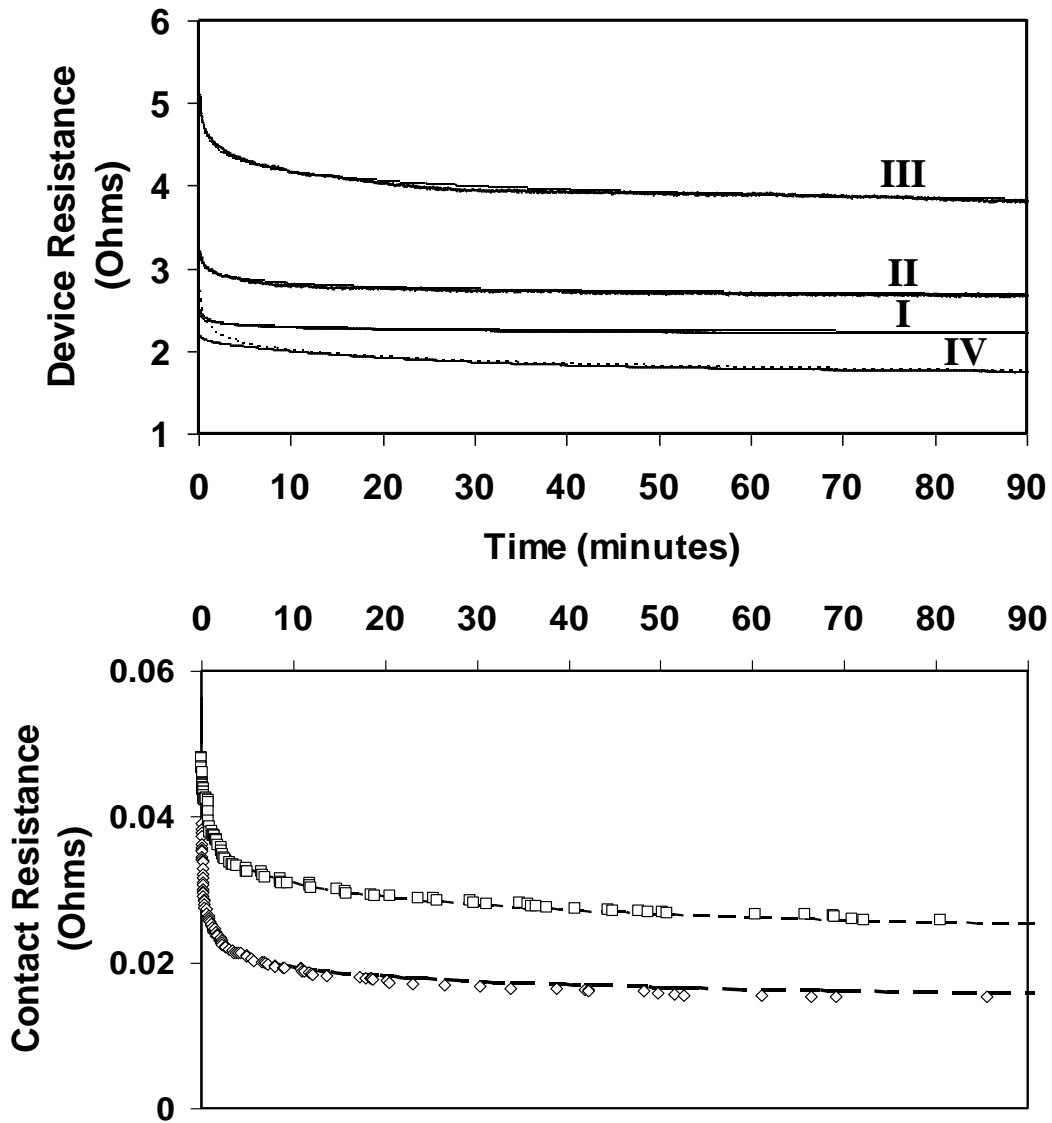


Figure 7.1 – Resistances across gold-gold contacts as a function of time. Bottom Panel: Symbols denote calculated values from [2]. The solid line is a fit of (7.2) to the computational data. Top Panel: Solid lines are experimental measurements for a closed Ohmic switch in two RF MEMS devices. Curves denoted I, II and III correspond to the first, second and third measurements on switch one, respectively. The curve denoted by IV is for switch two. Dashed lines represent fits of (7.2) to the experimental data. Except for the early stages of curve IV, the dashed and dotted lines are indistinguishable from one another on this graphing scale.

Table 7.1 – Resulting parameters from the fit of (7.2) to the prior experimental and modeling data.

Fitting Data	α	A (Ohms-minutes)	B (Ohms)
First measurement on switch one (curve I in top panel of Fig. 7.1)	0.073	0.45	1.90
Second measurement on switch one (curve II in top panel of Fig. 7.1)	0.073	1.08	1.90
Third measurement on switch one (curve III in top panel of Fig. 7.1)	0.073	2.68	1.90
Measurement on switch two (curve IV in top panel of Fig. 7.1)	0.073	2.01	0.30
Computational data from [2] (bottom curve in bottom panel of Fig. 7.1)	0.094	0.024	0
Computational data from [2] (top curve in bottom panel of Fig. 7.1)	0.094	0.038	0

resistance curve shows an initial drop, followed by a plateau region. However, the resistances in each of the plateau regions are all different for the different roughness models and experimental runs. Furthermore, the experimentally measured device resistances are roughly two orders of magnitude larger than the calculated contact resistances.

Plotted as dotted lines in Fig. 7.1 are fits of the function

$$\rho = At^{-\alpha} + B \quad (7.2)$$

to all of the experimental measurements and the calculated resistances. The corresponding parameter values are given in Table 7.1. Except for the first few minutes of curve IV, the fitted lines and the lines connecting the experimental measurements are indistinguishable from one another at this plotting scale. All four of the experimental fitting curves use the same value for α . For device one, all three fitting curves use the same value for B with different A values. The fit to curve IV (device two) uses different A and B values. The fit of

(7.2) to the calculated resistances is equally impressive. Both fitted expressions use the same values for α and B , and different A values.

The relatively accurate fit provided by (7.2) to both the detailed modeling and experimental measurements suggests that the resistance as a function of time of the gold Ohmic contact within these devices can be understood from a few properties of the switch. The parameter B represents the resistance in the $t = \infty$ limit. For the computational results, which directly yield the contact resistance, a value of zero for B implies that the limiting resistance corresponds to an ideal interface at which the asperities have been completely flattened and plastic damage removed. The experimental studies, on the other hand, measure the total resistance of the device, hence yielding a combination of the contact resistance across the switch and other resistance contributions from the device. The common value of B for all three runs for device one supports this interpretation. Adding the resistances of the wire bond and the conduction path within the device (excluding the contact resistance across the switch) yields an estimate for the device resistance of 1.54Ω , which is intermediate between the fitted B values for the two devices (both of which are from the same wiSpry design).

The common value of α for the experimental curves, and the small difference between the experimental and computational values, suggests that this parameter reflects an intrinsic material property of the gold in the switch. The two roughness models used in the computational studies yield different values for A in (7.1), suggesting that this parameter reflects the initial state of the surfaces prior to contact. Interestingly, the rougher surface yields a higher A value. This is discussed more below.

7.4 Analytic single asperity model

The following analytic single asperity deformation model can be used to derive the form of (7.2). More importantly it demonstrates the origin of the α and A parameters. The geometry of the model is illustrated in Fig. 7.2. It is composed of a single conical asperity with initial height L and radius r_l whose shape is designated by the angle β with respect to the interface plane. This assumed geometry is used because it leads to a relatively straight-

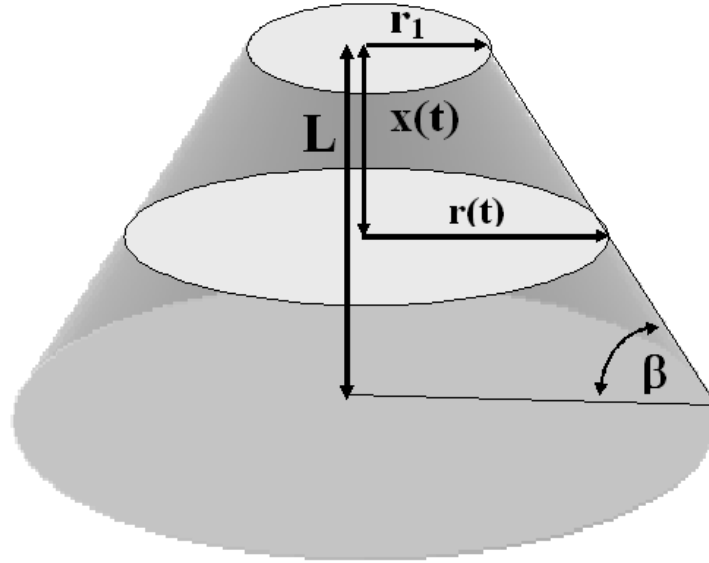


Figure 7.2 – Illustration of the conical geometry used in the single asperity model. L and r_1 are the initial asperity height and radius, respectively, β is the angle of the side of the asperity with respect to the surface plane, and $x(t)/L$ and $r(t)$ are the time dependent strain and radius, respectively.

forward derivation that justifies (7.2). The time-dependent strain is defined as the change in height $x(t)$ normalized by the initial asperity height L . With this definition the strain rate is given by

$$\dot{\varepsilon}(t) = \frac{\dot{x}(t)}{L} \quad (7.3)$$

and the stress due to load F on the asperity is defined as

$$\sigma = \frac{F}{\pi r^2(t)}. \quad (7.4)$$

With this geometry

$$\dot{r}(t) = \frac{\dot{x}(t)}{\tan(\beta)}, \quad (7.5)$$

which combined with (7.3) leads to

$$\dot{\varepsilon}(t) = \frac{\tan(\beta)}{L} \dot{r}(t), \quad (7.6)$$

Substituting (7.4) and (7.6) into (7.1) gives

$$\dot{r}(t) = C e^{(-Q_c / kT)} \left(\frac{L}{\tan(\beta)} \right) \left(\frac{F}{\pi r^2(t)} \right)^p, \quad (7.7)$$

which can be integrated with respect to time to yield the relation

$$r(t) = \left[\left(\frac{L C e^{(-Q_c / kT)} F^p (1 + 2p)}{\tan(\beta) \pi^p} \right) t + r_1^{(1+2p)} \right]^{\frac{1}{1+2p}} \quad (7.8)$$

for the radius as a function of time. Equation 7.8 reduces to the initial asperity radius for time $t=0$, and is only valid for $r(t)$ less than or equal to the radius of the base of the asperity (i.e. strains between 0 and 1). If r_1 is sufficiently small, $r_1^{(1+2p)}$ can be ignored with respect to the first term in the brackets in (7.8) at some finite time, which yields

$$r(t) = \left(\frac{L C e^{(-Q_c / kT)} F^p (1 + 2p)}{\tan(\beta) \pi^p} \right)^{\frac{1}{1+2p}} t^{\frac{1}{1+2p}} \quad (7.9)$$

for (7.8). Finally, combining (7.9) with a Maxwell spreading resistance $R(t)$ of the form ⁸

$$R(t) = \frac{\rho}{2r(t)} \quad (7.10)$$

gives a time-dependent resistance due to creep of the form

$$R(t) = \frac{\rho}{2 \left(\frac{L C e^{(-Q_c / kT)} F^p (1 + 2p)}{\pi^p \tan(\beta)} \right)^{\frac{1}{1+2p}} t^{\frac{-1}{1+2p}}} \quad (7.11)$$

Equating (7.11) to (7.2) yields

$$A = \frac{\rho}{2} \left(\frac{L C e^{(-Q_c / kT)} F^p (1 + 2p)}{\pi^p \tan(\beta)} \right)^{\frac{-1}{1+2p}} \quad (7.12)$$

and

$$\alpha = \frac{1}{1 + 2p} \quad (7.13)$$

By using (7.10) the contribution of the Sharvin resistance is neglected compared to the Maxwell spreading resistance. The overall contact resistance is governed by the asperity with

the lowest resistance and hence largest contact area, which is where the Sharvin resistance is smallest compared to the Maxwell spreading.

The form of (7.12) and (7.13) supports observations made above regarding the physical origin of the A and α parameters in (7.2), and it provides a plausible explanation for why the A value increased for multiple measurements on switch one. It was suggested above that the α in (7.2) is related to an intrinsic property of the material out of which the switch is composed. Equation 7.13 suggests that this is indeed the case, and that the value for α can be specifically related to the creep coefficient in (7.13). The values of α of 0.073 determined by fitting to the experimental data and 0.094 by fitting the plasticity model give creep coefficients of 6.35 and 4.82, respectively. Creep coefficients are typically between about 4 and 10 depending on the creep mode. Also from (7.13) the value of A in (7.2) is proportional to $(L/\tan(\beta))^{-\alpha}$. Therefore larger angles of the asperities with respect to the surface plane, which correspond to rougher surfaces, produce larger A values, consistent with the detailed plasticity modeling². Finally (7.13) implies that for the same angle shorter asperities produce larger A values in (7.2). This result suggests that asperity blunting is contributing to the increasing A values observed for device one for the second and third runs. However, this does not explain why for each consecutive run the initial resistance increases. This could be due to roughening during switch opening, the formation of a contamination film after opening^{7,9}, or some other contribution (or combination of contributions).

The approximation that leads from (7.8) to (7.9) for this single asperity model yields a prediction for the contact resistance that has not been previously recognized. For multiple switching, the blunting of asperities decreases the value of the first term and increases the value of the second term in the brackets in (7.8). Hence this analysis predicts that it will take a longer time (i.e. a larger value for t in the first term in the brackets in (7.8)) for the contact resistance to attain a power law relation with each successive closing of the switch. Plotted in Fig. 7.3 is a blow-up of the experimental data plotted in Fig. 7.1 for device one (curves I, II and III) during the first 10 seconds of switch operation. The solid lines are the results of (7.2) with parameters fit to the entire 90 minute data run as described above. For curve I, which is the first closing of the switch, the power law relation for the entire run fits the first

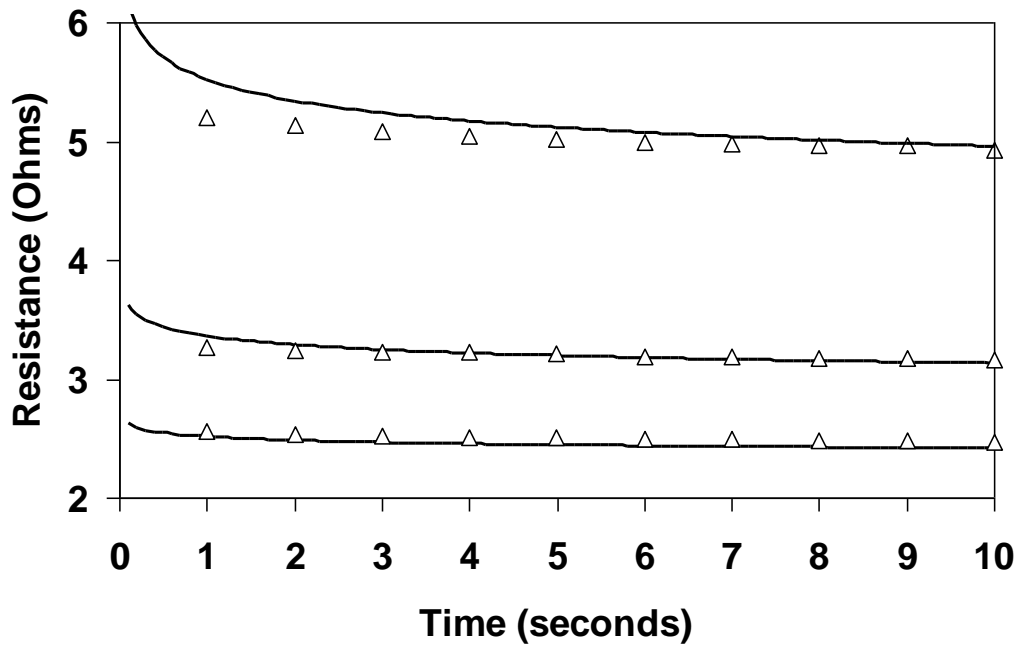


Figure 7.3 – Curves I, II and III from Fig. 7.1 for the first 10 seconds. Symbols are the experimental data; solid lines are the fit of (7.2) to each entire data set.

few data points very well. For the second closing (middle plot), the experimental measurement is flatter than the power law prediction up until about 4 seconds, after which the power law provides a good description of the data. The same trend is seen for the third switching (the top plot), except that it requires about 9 seconds for the experimental data to be well described by the power law. This behavior qualitatively matches the prediction of our single asperity analytic analysis.

7.5 Summary

We have shown that the measured resistance as a function of time for two MEMS switches as well as a comparable resistance calculated using a specialized finite-element plasticity model is well described by a power law relation. This relation is derived analytically from a single asperity model, which demonstrates that the coefficient of the

power law is directly related to the creep coefficient, and that the prefactor to the power law is related to the initial roughness of the contact. The analytic model also predicts a transition from a constant contact resistance to the power law that occurs at increasingly longer times for successive switch opening and closing that is caused by asperity blunting. Analysis of the first few seconds of the measured resistance for three successive openings and closings of one of the MEMS devices supports this prediction. This work thus provides guidance toward the rational design of Ohmic contacts with enhanced reliabilities by better defining variables that can be controlled through material selection, interface processing, and switch operation.

7.6 Acknowledgements

Interactions with Art Morris of WiSpry, Inc are gratefully acknowledged. This work has been supported by the Extreme Friction MURI program, AFOSR grant FA9550-04-1-0381 entitled “Multifunctional Extreme Environment Surfaces: Nanotribology for Air and Space. C.B. and J.K. were also supported by the DARPA Center for RF MEMS reliability and Design Fundamentals Grant # HR0011-06-1-0051.

7.7 References

¹ See for example G.M. Rebeiz, “RF MEMS: Theory, Design and Technology” (Wiley, Hoboken, 2003)

² O. Rezvanian, M. Zikry, C. Brown and J. Krim, *J. Micromechanics and Microengineering* **17**, 2006 (2007).

³ C. Brown, A. S. Morris, A.I. Kingon and J. Krim, *IEEE J. Microelectromechanical Systems* , in press.

⁴ H.A. Francis, *Wear* **45**, 221 (1977)

⁵ M. O’Callaghan and M.A. Cameron, *Wear* **36**, 79 (1976).

⁶ W. Yan and K. Komvopoulos, *J. Appl. Phys.* **84**, 3617 (1998).

⁷ B.D. Jenson, L. L.-W. Chow, K. Huang, K. Saitou, J.L. Volarkis and K. Kurabayashi, *J. Microelectromech. Systems* **14**, 935 (2005).

⁸ “Electrical Contacts: Principles and Applications”, P.G. Slade, ed. (Dekker, New York, 1999).

⁹ H.P. Koidl and F.R. Werner, *IEEE Trans. Components, Packaging and Manufacturing Tech.* **22**, 439 (1999)

CHAPTER 8

Additional Contact Resistance Measurements

8.1 RF MEMS contact resistance temperature dependence

In addition to the work present in Chapter 5 a set of contact resistance versus temperature data were taken. The present work provides data for a range of temperatures extending from room temperature to liquid nitrogen temperatures that are highly complementary to those reported in by Jensen *et al*¹.

The resistance versus temperature data were taken by cooling the chip to 77.4 Kelvin and maintaining the system at temperature for 24 hours to ensure the device and system were at a steady state temperature. The outer heat shield was purged of liquid nitrogen and the liquid nitrogen in the inner dewar was allowed to boil off. This ensured a slow and steady temperature rise and removed rapid temperature fluctuations during the data taking. At the start of the data run, the switch was cold cycled 250 times. Cold cycling resistance measurements were collected for every 0.01 Kelvin change in temperature from 77.4 Kelvin to room temperature. For every detected temperature change, the switch was actuated to the closed position, a current of 1 mA applied, the resistance value recorded, current removed, and the switch opened. The normal run length of the experiment was 72 hours.

The same procedure was followed for several switches fused in the closed state and also for a MEMS switch package which had only a gold wire between the in and out signal line. Additionally, all experiments were repeated with an identical run in nitrogen gas instead of helium. Other than the variable resistance immediately following the switch closure, as discussed in Chapter 5, there were no differences in contact resistance due to the different atmospheres.

For a fully operational switch that was able to open and close throughout the duration of the entire experiment, several key features were noted in the data (Fig. 8.1). First, as expected there was a significant drop in the initial contact resistance at lower temperatures when applying the same actuation voltage. The drop in resistance can be attributed to a decrease in the resistivity of gold at cryogenic temperatures. It was also found that the same actuation voltage which produced the lowest contact resistance at room temperature also produced the lowest contact resistance at low temperature. Thus it can be assumed that the device contacts were in the stable contact resistance regime throughout testing.

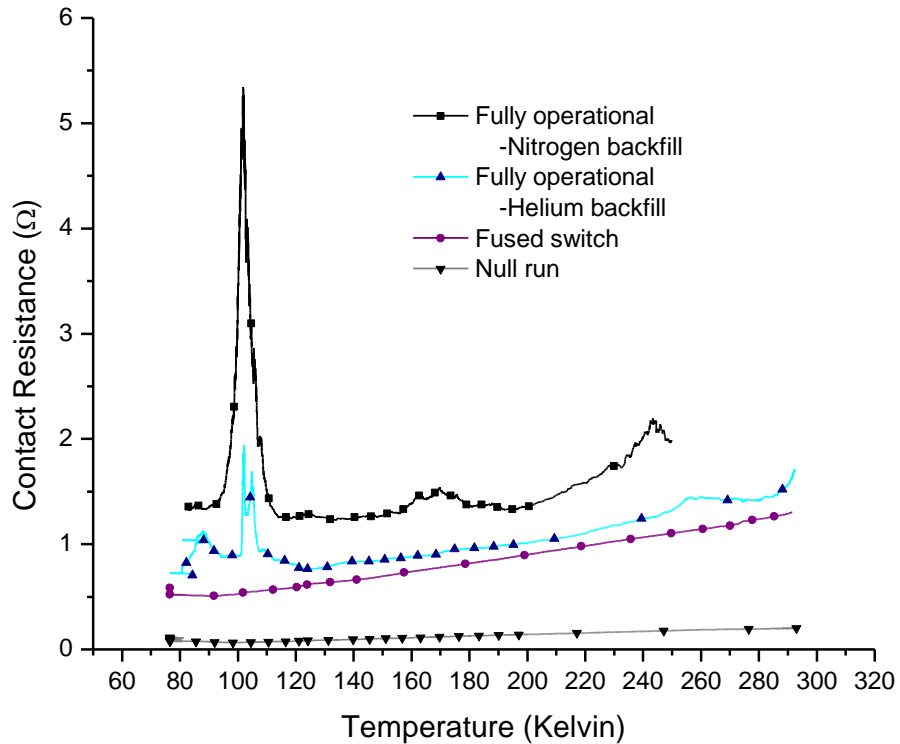


Figure 8.1 – Contact resistance as a function of temperature for a wiSpry RF MEMS switch.

The second and most prominent feature was the resistance spike at 104 Kelvin. To test the reproducibility of the data, the experiment was repeated 8 more times on four more switches. Data were recorded on two different devices to ensure that the resistance peak was not a function of the single device or a characteristic of the lot received for testing. In all cases, the peak at 104 Kelvin is present. In every case the peak begins to manifest itself at 100 Kelvin and returns to normal resistance levels at 109 Kelvin. While most switches show elevated contact resistance at 104 Kelvin, two devices produced data showing the switch contact having infinite resistance over the same temperature range. As with the other switches, the resistance returned to normal levels at 109 Kelvin.

To ensure the resistance peaks could not be attributed to the operational functionality of the switch, test system or gas environment, a series of additional experiments were carried out. These tests used the same testing procedures for cool down and testing methodology. In

the case of operational functionality, switches which were fused at the contacts were tested. Initial tests on these switches showed no change in contact resistance at room temperature or 77.4 Kelvin and no changes when under actuation loads ranging from 20 Volts to 80 Volts at either temperature. The device showed no peak at 104 Kelvin; however it did have the characteristic rise in resistance as a function of increasing temperature as seen in the fused switch trace of [Fig. 8.1](#).

The experiment was then repeated using piece of gold wire consistent with the materials found in the leads on the ceramic package used to mount the devices. The gold wire was inserted shorting the system between in and out signal lines on the ZIF socket. For this experiment, the only component missing from the experimental setup was the device itself and its 1 mil gold wirebond connections to the package. The null run trace of [Fig. 8.1](#) shows that resistance remained relatively flat over the same temperature range.

Several key features are apparent when comparing the experimental contact resistance data with theoretical values. Foremost is the difference of nearly two orders of magnitude between the predicted and experimentally measured value for contact resistance. Qualitatively, both fully functioning switches and switches fused at the contacts show the general increase in resistance with increasing temperature. The fully functioning switches have a sharp peak in resistance at 104 Kelvin. The peak only appears in switches which were cycled during testing. In every case the peak appears at 104 Kelvin and resistance values measured afterward return to levels measured before its occurrence. While the exact cause of the peak is not known, it is likely that its existence is due to the adsorbed film layers on the contacts.

Data from this experiment and calculations show resistance is reaching its maximum value at room temperature; however, published data ([Fig 8.2](#)) shows that resistance decreases as the temperature increases over a range of 300 to 363 Kelvin [1]. Pairing the data sets together shows the resistance reaches a local maximum at room temperature. A possible explanation for this is that near room temperature the film is reaching its maximum mobility and is being pressed into the contact areas due to the mechanical cycling of the switch. However, as discussed in the next section, the lower temperatures may limit the adsorbed

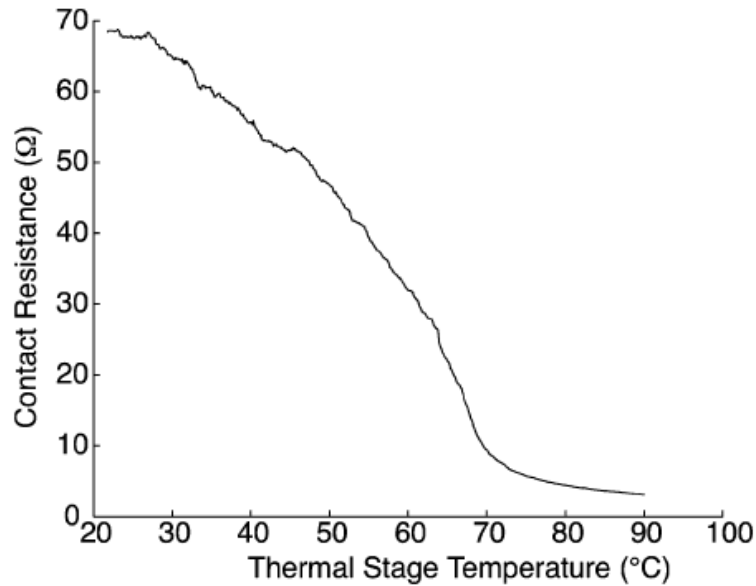


Figure 8.2 – Contact resistance versus temperature from 293 to 363 K [1].

film’s ability to move into the contact areas during cycling and the higher temperatures may disassociate the adsorbed films from the gold surface. In either case additional real contact area would be generated leading to a lower contact resistance.

8.2 Thermometer calibration

Cryogenic temperature data for this thesis was taken with two thermometers mounted to the outside of the vacuum chamber at the same level as the device under test. Optimally the temperature measurement should be taken directly at the device; however the limited number of electrical feedthrough slots had to be used for actuation and measurement of the RF MEMS switches.

The typical procedure for making a range of measurements at cryogenic temperatures is to warm the sample to the desired temperature, wait twenty minutes while the sample reaches thermal equilibrium, and then record the temperature. In the case of this experiment, the warming period extended over three to four days, and it was believed that the inside and outside of the system were in near thermal equilibrium. This theory was called into question

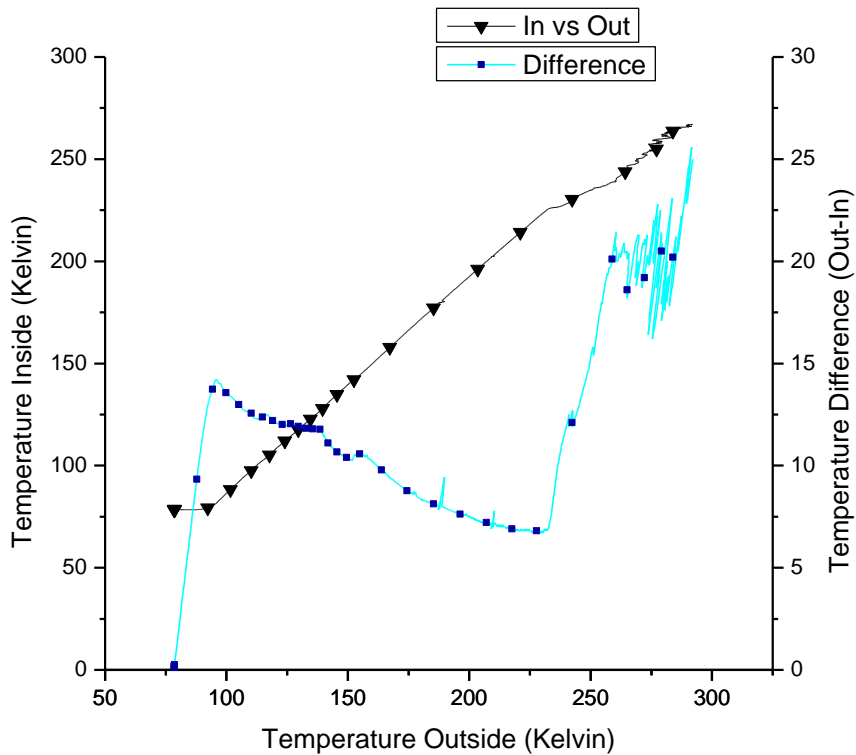


Figure 8.3 – Thermometer calibration data.

as the stainless-steel from which the vacuum chamber is constructed, is a non-linear thermo conductor.

A set of data was taken to show the equivalency of the inside and outside temperatures. A platinum resistance thermometer was mounted on a ceramic package that normally holds the RF MEMS switch and was placed inside the chamber. Temperature from inside and outside the chamber were recorded across the temperature range of 77.4 to 290 K every time the outside temperature changed by 0.01 K or greater.

Plotting a trend line to fit the data points to a nearly linear fit, but further inspection of the data reveals that this is not the case. Starting at 77.4 K the outer temperature begins to rise while the inside temperature remains steady. This continues until the outside temperature reaches about 92 K. From this point until the outside temperature reaches approximately 225 K, the rise in the outside and inside temperatures are nearly linear, but the

inside temperature trails the outside by 17 Kelvin across the entire range. The average difference in temperature between the outside and inside from 77.4 to 290 K is 10 K.

This clearly calls into the question the exact temperature reported in A.1, but does not negate the contact resistance data. It simply means that the outside temperature is not indicative of the temperature at the device, and that the changes in contact resistance are happening at a slightly different internal temperature.

8.3 Additional contact resistance versus time data

Nearly all of the room temperature contact resistance versus time data fit the power law relationship described in Chapter 7. One data set exhibited the power law relation for several periods during a long duration closure. Two other data sets showed upwardly trending contact resistance versus time. The data for these plots were taken using the same procedure as those that produced theory matching traces. The switch was closed, and a 1 mA current was applied for the duration of the measurement, with a contact resistance measurement recorded once every second. All measurements were taken on a wiSpry switch.

The data in [Fig. 8.4](#) show a 1500 minute closure for a fully functional wiSpry switch. The first 900 minutes fit the power law expression derived in Chapter 7. After 900 minutes several drops in contact resistance are recorded. Each begins with large drop in contact resistance, followed by the beginning of a plateau in contact resistance. The data here can be partially explained by the single asperity creep model. Given the long duration of the measurement it is possible that additional asperities will come into contact due to creep in the already contacting ones. The addition of new contact asperities will result in more real contact area, and in turn lower the contact resistance. While the modeling of Chapter 6 does show variation in contact resistance over time, it has not produced the large drops seen in the data here.

The argument of increasing contact area with time due to creep is not well supported by two additional data sets where the contact resistance increases with time. These two data sets represent the first time a fully functioning switch produced an upward trend in contact

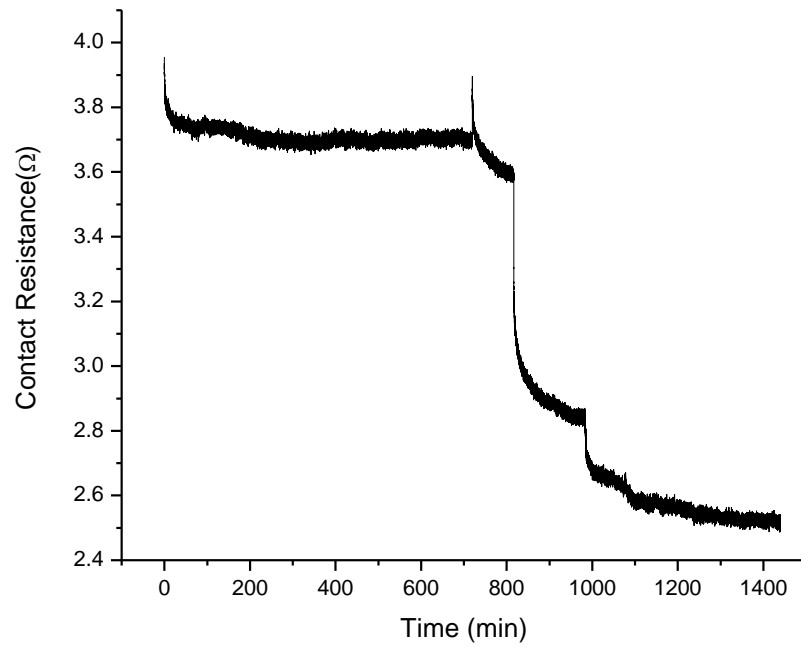


Figure 8.4 – Contact resistance versus time for 1500 minutes showing multiple drops in resistance.

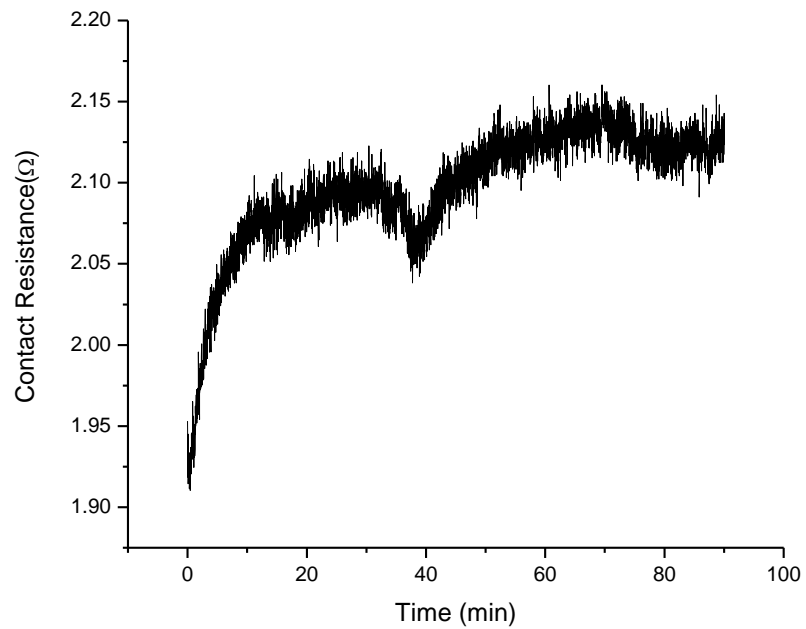


Figure 8.5 – Upwardly trending contact resistance versus time.

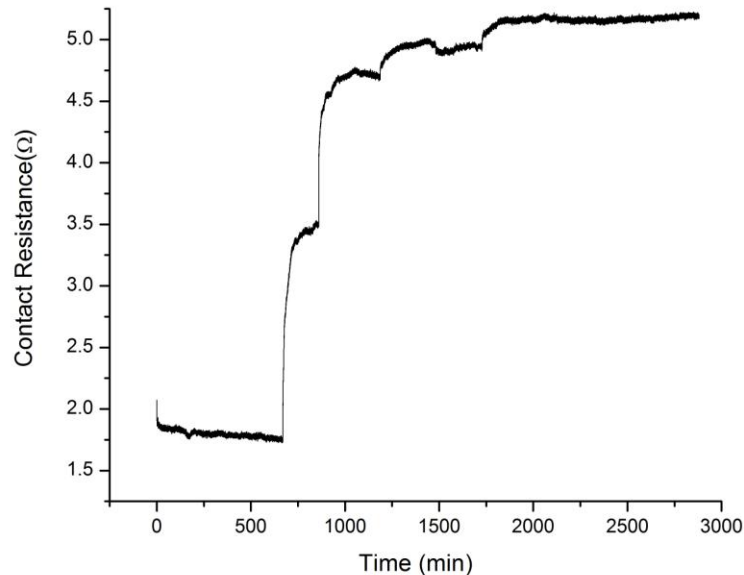


Figure 8.6 – Contact resistance versus time for 2900 minutes showing multiple increases in resistance.

resistance as a function of time. The only other recorded increases in contact resistance have been seen in switches fused at the contacts and for contact resistance measurements taken at cryogenic temperatures with high input voltages (covered in A.4).

As 90 minute closure and a 2900 min closure are shown in Fig. 8.5 and Fig. 8.6. The upwardly trending contact resistance is similar in shape in both graphs; however, the onset of the increase is different in the two cases. In the shorter closure, the contact resistance immediately rises upon closure and continues upward until shouldering off, and is followed by another upward jump. The longer closure starts off with the characteristic drop in contact resistance indicative of plastic yield and creep, and later experiences an upward jump in contact resistance after 700 min.

The data sets in Fig. 8.4 and Fig. 8.6 may possibly arise from the same mechanism. Given that both switches were actuated for prolonged periods of time with the same amount of current supplied to both contacts, it is unlikely that the differing shifts in contact resistance were solely from creep. Also, since the switches were closed and not cycled, it is unlikely

that adsorbed films in the contact area precipitated the upward trend in contact resistance. It is plausible that both the downward and upward trends in contact resistance are the product of interfacial slip or lateral contact movement.

In the case of the multiple decreasing contact events, lateral movement could have brought more asperities into contact with each shift. A large shift in the contact would produce the plastic yielding seen in the first minutes after the shift followed by the onset of creep and the slowly evolving contact resistance with time. The upwardly trending contact resistance would then be the opposite effect, where the switch is laterally sliding into positions with less contact area, or even pulling away from the contacts, so that fewer asperities are in contact.

Cantilever creep provides one possible explanation for the lateral slip. With the wiSpry switches, contact is not normal between the gold surfaces. The upper contact approaches the lower contact at a 1.5° angle. With the asperity radius on the order of 100 nm and a small difference in the height distribution, a significant number of asperities can come in and out of contact as the cantilever changes position over time.

8.4 Contact heating

Upwardly trending contact resistance is not only a function of decreased contact area, but also arises from asperity heating. In cases where the contact area changes little with time, for example in a switch fused at the contacts or at cryogenic temperatures where creep is negligible, changes in the contact resistance must be due to heating at the asperity level. Changes in the local asperity temperature increase the resistivity of gold, and this change in resistivity is reflected in an increase in the measured contact resistance.

In Chapter 5 cryogenic temperatures slowed the creep mechanism and lowered the resistivity. The voltage drop across the contacts was insufficient for generating enough heat to create more contact area or appreciably change the resistivity; therefore creep was the dominate time dependent contact resistance factor. In Chapter 9, cryogenic temperature were again employed to control creep, and high contact voltages were used to induce asperity heating sufficient enough to raise the resistivity of gold.

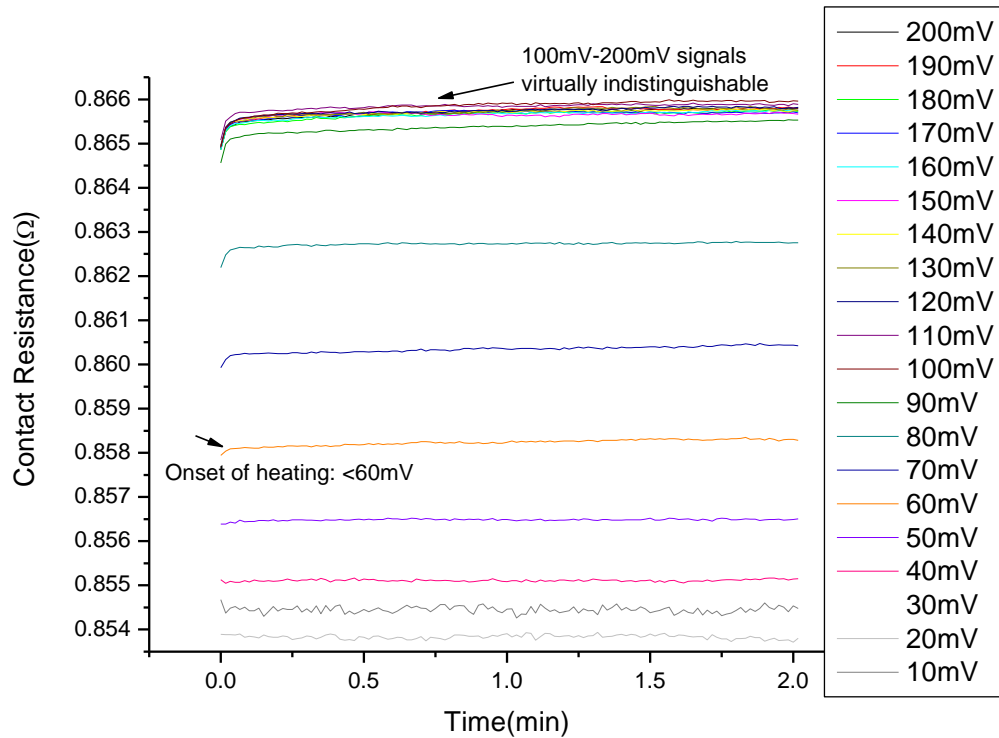


Figure 8.7 – Onset of asperity contact heating as a function of contact voltage.

The data presented here is a room temperature supplement to the asperity heating reported at cryogenic temperatures in Chapter 9. In Fig. 8.7 heating effects are shown for a fused switch. Heating induced increases in resistivity are indicated by the generally upward trend in contact resistance as well as the shouldering effect at the start of each run. Beyond 10 mV the overall contact resistance increases with increased contact voltage and beyond 60 mV the shoulder effect becomes apparent. The noticeable increase in contact resistance as the run is initiated is from the dramatic rise in local asperity temperature. Beyond 100 mV, increases in contact voltage do not significantly change the overall contact resistance or size of the initial jump in resistance as the temperature at the switch contacts increases. In Fig. 8.8 a small step size is used between 50 mV and 60 mV to obtain a refined look at the increase in contact resistance and the onset of the shouldering effect.

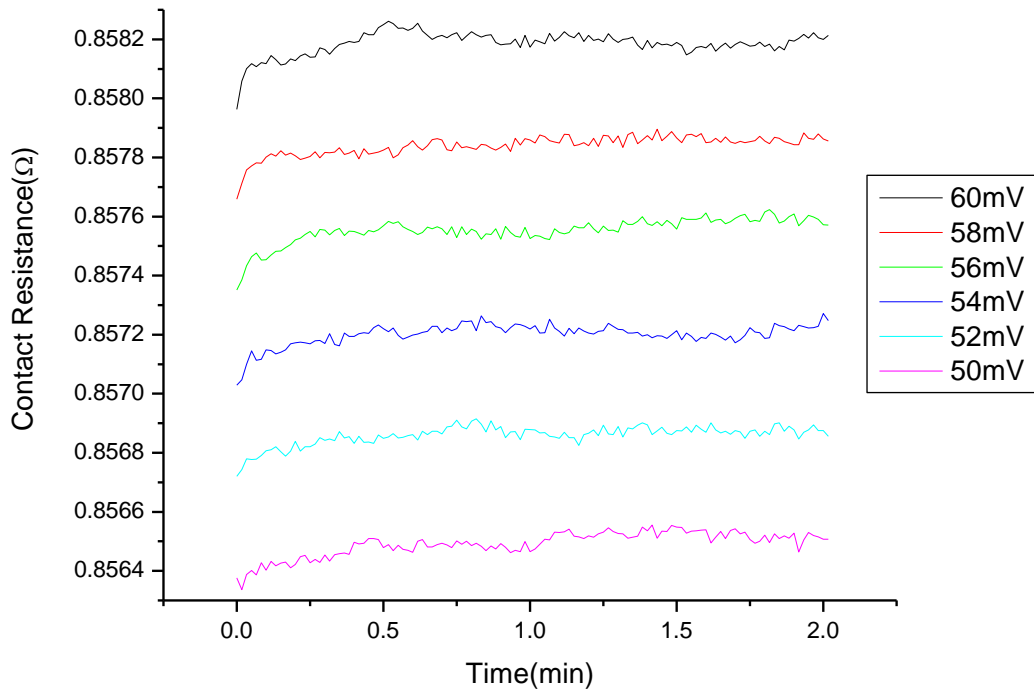


Figure 8.8 – Initial Onset of asperity contact heating between 50 mV and 60 mV.

Figure 8.7 also shows the transition from heating dominated contact resistance values to real contact area creation dominated contact resistance values. The two concentric arcs in Fig. 8.9 show the ambient temperature and voltage drop across the contact combinations that result in disassociation of adsorbed films from the contacts (inner arc) and the softening of gold asperities (outer arc). Inside the first arc little contact area is created with increases in contact temperature induced by the voltage drop across the asperities, and heating, which increases the resistivity of the gold contacts, dominates the measurement. For the fused switch there is a clear transition after 80 mV where heating no longer creates an increase in contact resistance with increasing contact voltage.

Beyond 80 mV there is relatively little increase in the contact resistance despite increasing the contact voltage to 200 mV. Although the switch is fused, there is still some availability for additional contact area creation, which in turn decreases the contact

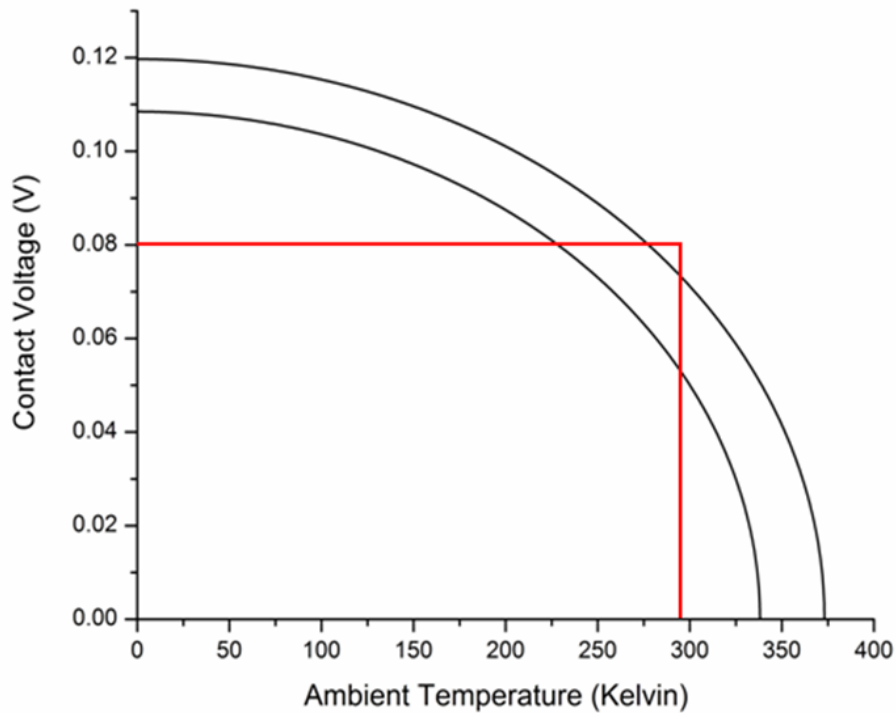


Figure 8.9 – Transition point from heating dominated to real contact area creation dominated contact resistance measurement for a RF MEMS switch at room temperature as measured in Fig. 8.7.

resistance. This small increase in contact area is large enough to offset the increase in contact resistance created by heating effects. It is hypothesized for a fully functioning switch the increase in contact area would be substantial enough to create a more pronounced decrease in contact resistance as well as a downward trend over the length of the measurement, much like those seen in previous chapters covering the creep mechanism. For the same switch at a lower temperature, a greater contact voltage drop would be required to generate enough heat to initiate asperity softening and achieve the same effect seen in Fig. 8.7. For example, at 5.6 K a contact voltage of 120 mV is required to soften asperities.

8.5 Contact resistance as a function of switch cycles

As discussed in Chapter 2, one of the most prevalent failure modes in metal contacting switches is the increase in contact resistance with the number of cycles. Normally the contact resistance will start out above normal levels, and after a short number of cycles it will decrease. The decrease in contact resistance is from asperity blunting which creates additional contact area and from the removal of adsorbed film layers. The switch will continue in this stable, low contact resistance regime until a large number of cycles are reached. Typically as the cycle number increases the contact resistance becomes more variable.

The wiSpry RF MEMS switch was cold switched in excess of 1.6×10^6 cycles. The switch started with abnormally high contact resistance which increased with cycling. As the

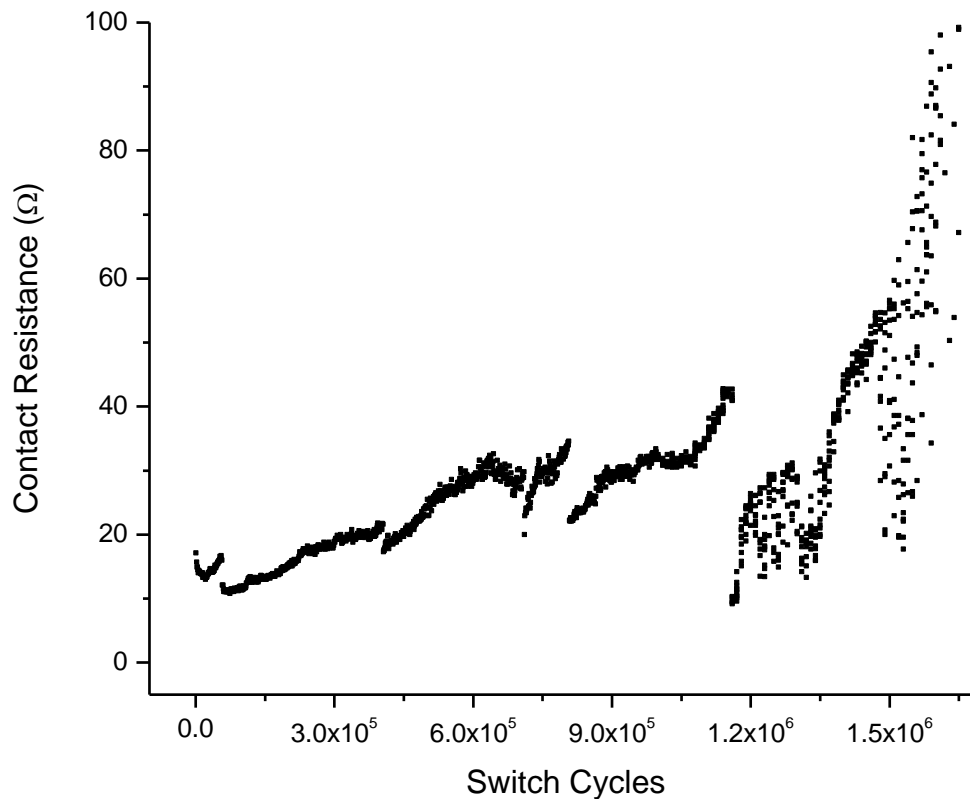


Figure 8.10 – Contact resistance as a function of switch cycles for a wiSpry RF MEMS switch.

number of cycles increased the contact resistance became increasingly variable, until the contact resistance reached was on the order of $M\Omega$ (Fig. 8.10).

8.6 References

¹ B. Jensen, L. Chow, K. Huang, K. Saitou, J. Volakis, and K. Kurabayashi, “Effect of nanoscale heating on electrical transport in RF MEMS switch contacts,” *J.*

Microelectromech. Syst., vol. 14, no. 5, pp. 935-946, 2005.

CHAPTER 9

Temperature Dependence of Asperity Contact and Contact Resistance in Gold RF MEMS Switches

C. Brown^a, O. Rezvanian^b, M.A. Zikry^b, and J. Krim^a

^a Department of Physics

^b Department of Mechanical and Aerospace Engineering

North Carolina State University

Raleigh, NC 27695

Submitted to *Journal of Micromechanics and Microengineering*

This work was supported by AFOSR MURI Grant No. FA9550-04-1-0381 entitled “Multifunctional Extreme Environment Surfaces: Nanotribology for Air and Space” and DARPA S&T Fundamentals Program, “Center for RF MEMS Reliability and Design Fundamentals,” Grant No. HR0011-06-1-0051.

9.1 Abstract

Experimental measurements and modeling predictions were obtained to characterize the electro-mechanical response of two different gold contact RF MEMS switches due to variations in the temperature and applied contact voltage. A three-dimensional surface roughness profile from AFM measurements of the top contact surface of a sample RF MEMS switch was used to obtain modeling predictions of the transient-dependent deformation of the asperity micro-contacts, real areas of contact, number of asperity micro-contacts, and constriction resistance. The experimental data indicated a decrease in the overall resistance and a decrease in the creep mechanism at 77 K and 5.6 K when compared to measurements at 293 K. At 293 K, there is more contact area per unit time, and the resistance drop from the increase in real contact area dominates the resistance increase from asperity heating. At 77 K, the creep rate is reduced as fewer asperities come into contact over time. Real contact area as a percentage of apparent contact area increases with time, but not at the same rate as at 293 K. At 5.6 K, the change in contact area over time is small, and the contact resistance measurement is dominated by asperity heating. The data presented and constriction resistance modeling for gold RF MEMS show that temperature plays a significant role in the creep deformation and heating of switch contacts.

9.2 Introduction

RF MEMS switches have demonstrated significantly improved performance over their current solid-state and electromechanical counterparts. They are highly attractive for a variety of commercial and military applications looking to utilize the switch's large potential for use in low and medium power applications as replacements for current switching technology and the potential to create new highly flexible RF systems ¹. To date, RF MEMS switches have lagged the lofty expectations placed upon them, mostly because the physics behind the failure modes is not well understood. In RF MEMS switch applications it has been difficult to obtain an accurate prediction of switch behavior due to the complex physical interactions between thermo-mechanical deformation, current flow, and contact heating. In order to improve device reliability it is essential to understand the evolution of asperity

contact at the surface and the underlying physics that drive surface and stiction related failure modes.

The evolution of asperity contacts and stiction events are especially important for RF MEMS switches in high power sensing applications. Individually, the MEMS switches are less capable of handling high power signals than conventional mechanical switches used as circuit breakers. However, when arranged in series and parallel in a large array the MEMS switches have improved power handling capability and superior switching speed. The switches remain in the closed position, until a large fluctuation in current occurs or they are taken off-line for maintenance. The time spent in the actuated state can range into years, therefore understanding and accurately predicting the creep characteristics of extended closure are an integral part of switch design for these applications ^{2,3}.

In a previous paper by the authors, modeling predictions and experimental measurements were published that characterized the electro-mechanical response of the RF MEMS switches due to the variations in surface roughness and finite asperity deformations at room temperature ⁴. The interrelated effects of roughness characteristics, material hardening due to creep deformation, and softening due to temperature increases from Joule heating were investigated on contact resistance. Changes in the constriction resistance of individual asperities were shown to depend on two competing events of increases in contact area and the electrical resistivity. The creep and contact resistance were later related through the use of a power law fit ⁵.

This paper is an extension of [4] with a focus on temperature-induced changes in asperity deformation and contact resistance. Creep at cryogenic temperatures has been researched for many metals including copper, aluminum, and steel, but has yet to be studied in MEMS devices ^{6,7,8,9,10,11,12}. Understanding the effects of cryogenic temperatures on switch performance is becoming increasingly important to systems designers as they integrate switches into microwave systems, satellite communications, space flight monitoring systems, and integration with high- T_c superconductors ^{13,14,15,16}. The impact of cryogenic temperatures on contact resistance for metal-metal contacting switches is explored in [17].

This paper is organized as follows. In section 9.3, the RF MEMS experimental device and apparatus are described. Experimental results are presented in section 9.4. Modeling predictions supporting the experimental data are discussed in section 9.5, followed by a summary and conclusion in section 9.6

9.3 Experimental device and apparatus

The devices used for experimentation were provided by Northeastern University (NEU) and wiSpry. The NEU switch is an inline metal contacting switch (Fig. 9.1). The transmission signal enters at the anchor or fixed end, and travels the length of the cantilever beam and exits to the transmission line through the contacts at the end of the cantilever beam. Because the signal must travel through the cantilever beam and the beam must be stiff enough to overcome the force of adhesion at the contacts, the cantilever is fabricated using a thick layer of electroplated gold ($\sim 9 \mu\text{m}$). The cantilever is $75 \mu\text{m}$ long by $30 \mu\text{m}$ wide. The pull-down electrode is $15 \times 25 \mu\text{m}^2$ and separated from the cantilever by $0.6\text{--}1.2 \mu\text{m}$. The short, thick design results in a stiff structure and requires $60\text{--}80 \text{ V}$ and a current of $\sim 6\text{--}10 \mu\text{A}$ to actuate into the closed position. The switch has two contacts in parallel separated from the transmission line (drain) by $0.4\text{--}0.6 \mu\text{m}$. The contact area is $\sim 5 \mu\text{m}^2$. Contact resistance is $2\text{--}3 \Omega$ at $100 \mu\text{N}$ of contact force.

The wiSpry switch is broadside metal contacting switch in a single-pole double-throw

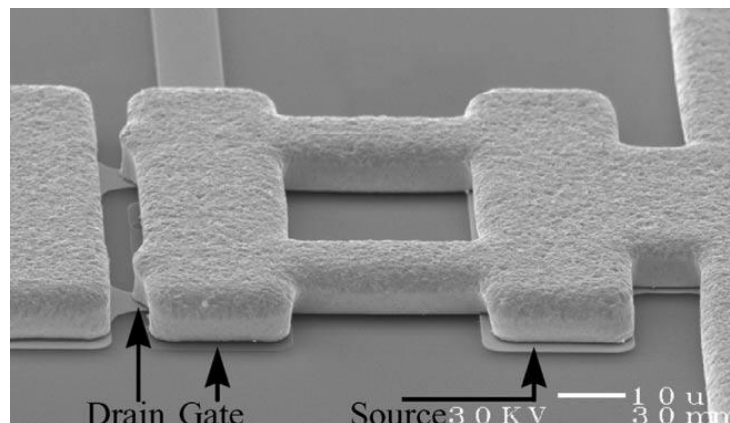


Figure 9.1 – Northeastern University (NEU) RF MEMS switch ¹⁸.

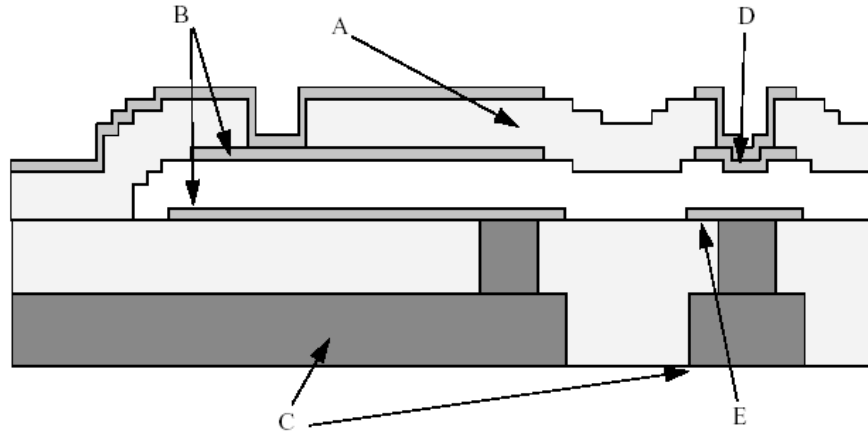


Figure 9.2 – Side view of RF MEMS switch cantilever. A is the Silica cantilever. B are the gold capacitive plates used for actuating the switch into the closed position forcing the contact bumps at D against the transmission line at E. Interlaced are conducting copper paths, C, for carrying the signal and actuation voltages.

(SPDT) configuration (Fig. 9.2). The transmission line is fabricated with a gap that is bridged by the contacts while the switch is in the closed state. The non-contact portion of the cantilever is used for switch actuation. The cantilever is a single fixed end and is composed of SiO_x with gold embedded to form the actuation electrode and the contacts at the end of the beam. The cantilever beam is 135.5 μm in length and 251 μm in width. Actuation requires 30–40 V and a current of ~3–5 μA. The switch has two 5 μm in diameter contacts in series that are separated by 55 μm and are 2 μm above the drain, or transmission line. Contact resistance measurement taken in a helium gas environment at room temperature ranged from 0.7–6 Ω, with most devices in the 1.5–2.0 Ω range.

The switches were tested in a vacuum system to reduce moisture induced stiction events (Fig. 9.3). The test chamber consisted of a thin steel 3.75 inch diameter cylinder fitted with a 20 pin electrical feedthrough at the lower end allowing a four-point dc measurement of the device’s contact resistance. A 28 inch extension arm is fitted to the top of the cylinder to ensure the environmental chamber is as low as possible in the cryostat dewar. The top of the transfer arm meets with a four-way cross that allows for pressure measurement and vacuum access and has ports for backfilling gas environments.

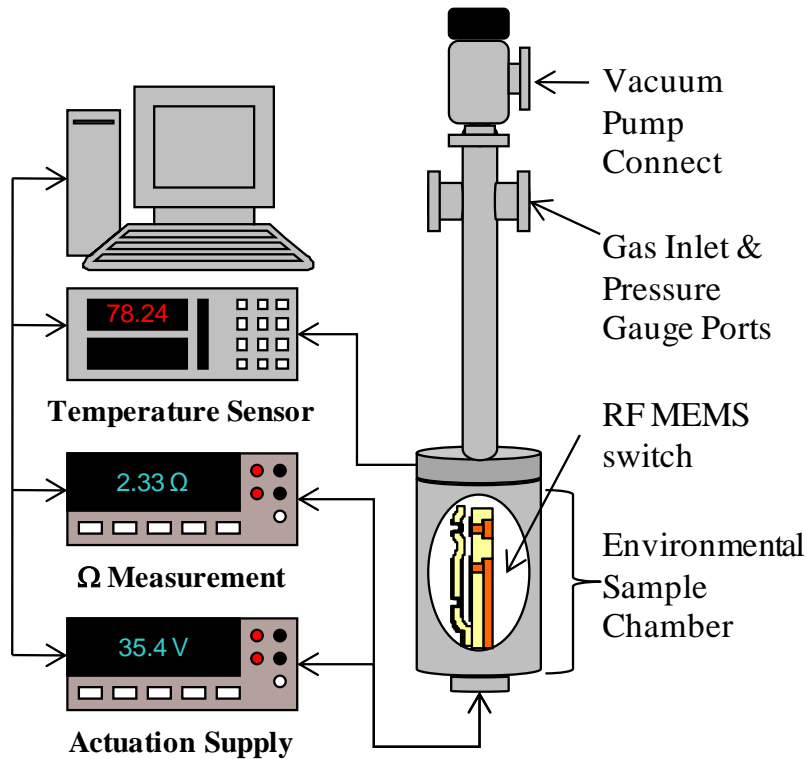


Figure 9.3 – Schematic of experimental setup.

Electrical connections inside the chamber were made with standard braided copper vacuum wire between the feedthrough and a ceramic zero insertion force (ZIF) socket. The switch was mounted on a ceramic side braze package with gold leads and wirebonded with one mil (25 μm) gold wires. The packages were then inserted in the ZIF socket during testing. Electrical connections outside the chamber between the feedthrough and test circuitry were made using constantan wire to ensure no additional resistance changes were measured as a result of thermal fluctuations from wire exposed to liquid nitrogen or liquid helium during testing. Two Keithley 2400 source meters were used for actuating the switch and performing a four-point dc contact resistance measurement. It should be noted that the four-point measurement is not solely the constriction resistance, but also includes contributions from the die components such as transmission lines, the wirebond and gold leads from the ceramic side braze package. Thus, the measured contact resistance values

nearly an order of magnitude greater than the predicted constriction resistance values of contacts of this size.

The environmental chamber was cooled by immersing it in a liquid nitrogen or helium bath contained in a Cryofab CSM type vacuum insulated stainless steel dewar, which in turn was immersed in an outer heat shield filled with liquid nitrogen. A Lake Shore 330 Temperature Controller measured temperature with both silicon diode and platinum resistance thermometers. All instrumentation was controlled via LabView.

9.4 Experimental results and analysis

Three sets of experimental results are presented in this paper. The first reports on contact resistance as a function of time at 293 K, 77.4 K, and 5.6 K. The second reports contact resistance as function of time at 5.6 K with supplied contact voltages of 1 mV and 100mV. The third reports contact resistance as a function of voltage at 5.6 K as the voltage is swept from 0 V to 150 mV.

9.4.1 Temperature-dependent creep

A series of tests were performed to investigate the effect of temperature on creep. NEU and wiSpry RF MEMS switches were used for testing. Tests were performed at 293 K, 77.4 K, and 5.6 K at a starting pressure of 10^{-7} Torr. At each temperature actuation voltage was applied to the switch until stable contact resistance was achieved. A Keithley 2400 sourcemeter supplied 1 mV to the contacts and recorded a four-point contact resistance measurement once per second for the duration of the test. The contact voltage was supplied continuously throughout the measurement.

The NEU switches were only actuated for 30 minutes rather than 60. This was done to prevent cantilever creep. Switches actuated for 60 minutes or more required more actuation voltage to reach stable contact resistance on subsequent measurements. No cantilever creep was observed for NEU switches closed for 30 minutes or less. The wiSpry switches have been actuated for up to 500 minutes without any shifts in contact resistance

during the measurement or increases in actuation voltage on subsequent measurements which would indicate cantilever creep.

Contact resistance versus time for different temperatures is shown for the NEU (Fig. 9.4) and wiSpry (Fig. 9.5) switches. The contact resistance versus time at 293 K for both the NEU and wiSpry switches are consistent with the power law fits previous published in [5].

$$R = At^{-\alpha} + B \quad (9.1)$$

The power law fits the contact resistance, R , as a function of time based on three parameters. A reflects the initial state of roughness prior to contact and increases as the roughness increases. The intrinsic material properties and relationship to the creep coefficient are contained in α . Theoretically B represents the limiting resistance value, or the resistance at $t=\infty$ when all the asperities have flattened and the contacts can be modeled as a short gold wire. However in the experimental case, B includes resistance contributions from other sources including switch die parts such as the signal transfer lines, the gold wirebonds connecting the die to the ceramic package, and contaminant films on the contact surfaces. Power law fits for the contact resistance versus time for the NEU and wiSpry switches are shown in Fig. 9.6 and Fig. 9.7 respectively.

On average, the α parameter is 0.073 for the wiSpry gold contacts, and the same value was used for fitting the NEU switch data. Both switches yielded similar A values, indicating that the surface roughness of both switches was similar. The B value for the wiSpry switch was double that of the NEU switch. This disparity is partially due to the difference in the contact designs. The wiSpry contacts are in series while the NEU contacts are in parallel. Additionally, the NEU contacts are smaller than the wiSpry contacts, which will contribute to increased contact resistance.

While the 293 K contact resistance versus time data is well described by the power law, the 77 K and 5.6 K data deviates from the power law fit. The lower curves in Figs. 9.4 and 9.5 are both flatter and lower in resistance than the curves for 293 K. At both cryogenic temperatures the steep initial drop in contact resistance is not present. The evolution of contact resistance is much more gradual at cryogenic temperatures. The decrease in contact resistance can be attributed to the decrease in resistivity of gold at cryogenic temperatures.

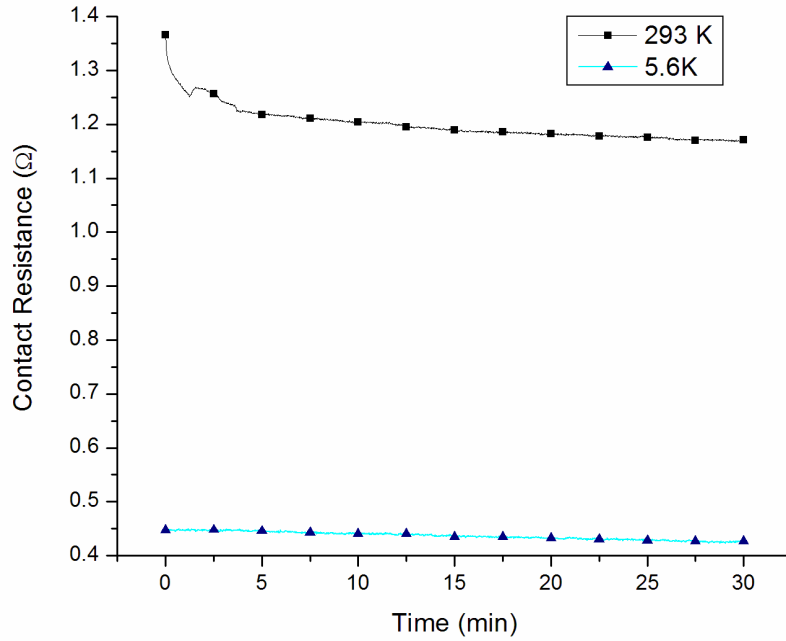


Figure 9.4 – Contact resistance versus time at 293 K, 77.4 K, and 5.6 K for the NEIJ switch.

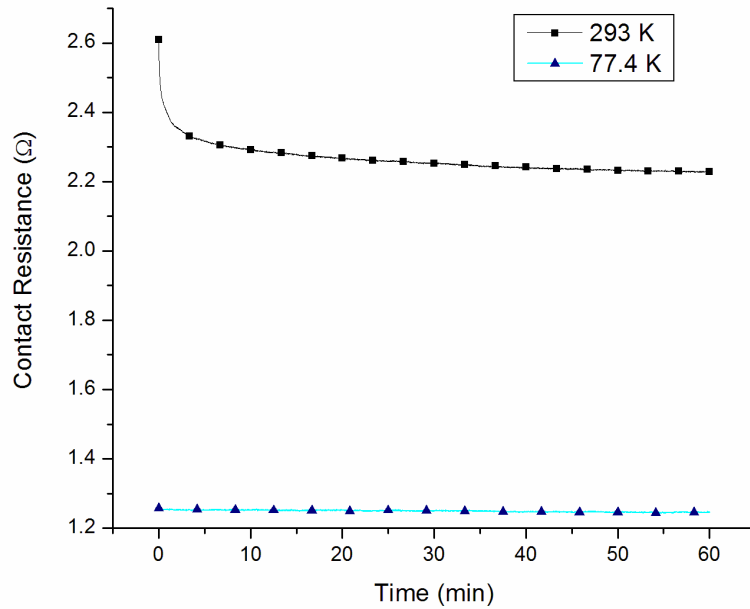


Figure 9.5 – Contact resistance versus time at 293 K and 77.4 K for the wiSpry switch.

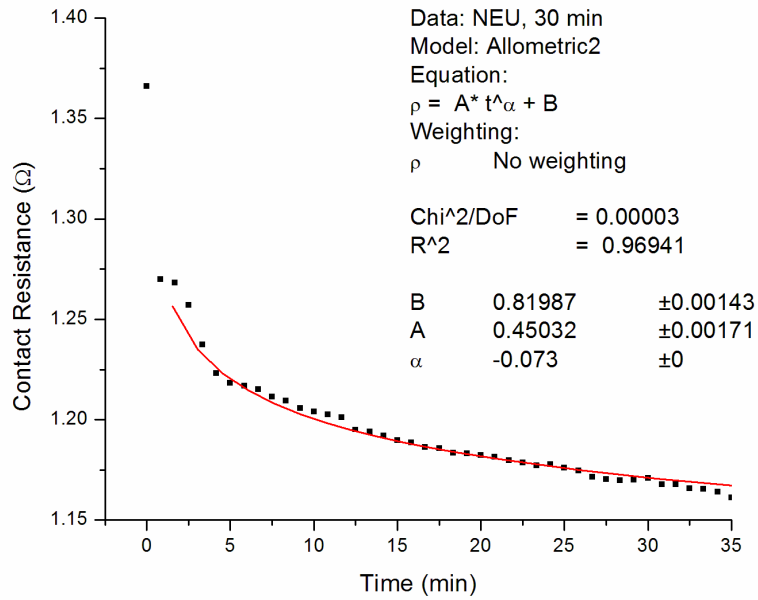


Figure 9.6 – Contact resistance versus time data from a NEU RF MEMS switch and the power law fit from [5] at 293°K.

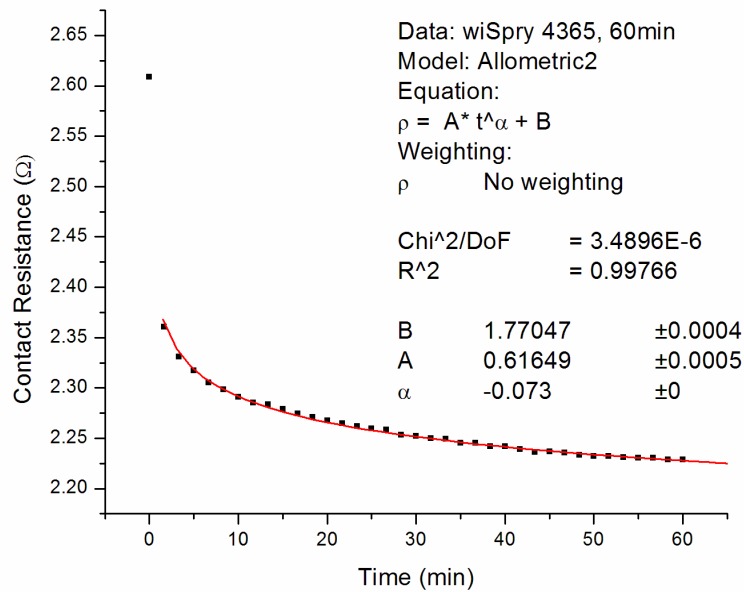


Figure 9.7 – Contact resistance versus time data from a wiSpry RF MEMS switch and the power law fit from [5] at 293°K.

The power law relation may not effectively fit the cryogenic temperature contact resistance versus time data, because the hardness of the gold asperities has increased at the low temperature. As an alternative to the power law fit, a measure of creep was taken by comparing the percent difference between contact resistance measurements taken 30 seconds after the experiment started and those taken after 30 minutes. Before the 30-second interval, the power law is not an exact fit to the data because the drop in resistance is driven by plastic deformation at the asperity level and by the removal of the adsorbed films at the contact surface. After 30 seconds, the main deformation mechanism for contact resistance change is creep.

The percent differences in contact resistance for the wiSpry and NEU switches at 293 K after 30 minutes were 7.4% and 9.3% respectively. The percent difference in contact resistance over a 30 minute period has been as high as 18% for a wiSpry switch. At cryogenic temperatures the percent difference is reduced. At 77 K it has dropped to 0.5% for the wiSpry switch, and at 5.6 K it has dropped to 4.6% for the NEU switch. Contact resistance versus time measurements at 5.6 K on four different NEU switches yielded percent differences ranging from 1.1% to 4.6%. The higher creep rate for the NEU switches can be attributed to the high actuation voltage required to close the switch which would also increase the load on the asperities.

9.4.2 Asperity heating

A series of tests were performed to investigate the impact of increased contact voltage on the creep mechanism at cryogenic temperature. The NEU switches were cooled to 5.6 K and contact resistance measurements were made using the same procedures enumerated in the previous section with currents of 1 mA, 100mA, and 200mA. 5.6 K was chosen as the testing temperature to ensure that adsorbed films on the gold surface would not have a significant impact on the contact resistance measurement. Prior to each test the switch was cycled for 200 cold cycles. Previous work has shown that the adsorbed film layers are less mobile at low temperatures and can be mechanically removed from the contacting area through cycling or application of sufficiently high current ¹⁷.

The measured data shows that some creep is present at 1 mA and 100 mA; however, when the current is raised to 100 mA, an initial increase in contact resistance is measured as the current is applied, after which the creep mechanism dominates for longer time periods (Fig. 9.8). When the current is raised to 200 mA, the initial increase in contact resistance becomes larger and the creep mechanism is no longer present. The contact resistance increases with time when large currents are applied.

It is hypothesized that the decrease in contact resistance with time for the 1 mA and 100 mA cases results from the normal creation of real contact area over time due to asperity deformation. The initial shouldering in contact resistance is created by resistivity changes in the gold due to increased heating at the contacts created by a voltage drop across the asperity micro-contacts. With the application of 200 mA, the contact resistance becomes a function of superposition of decreasing contact resistance from creep and increasing contact resistance from the change in resistivity due to heating, with the later being greater and driving an upward trend in the contact resistance.

To test this hypothesis, a voltage sweep was performed on the switch at 5.6 K. The

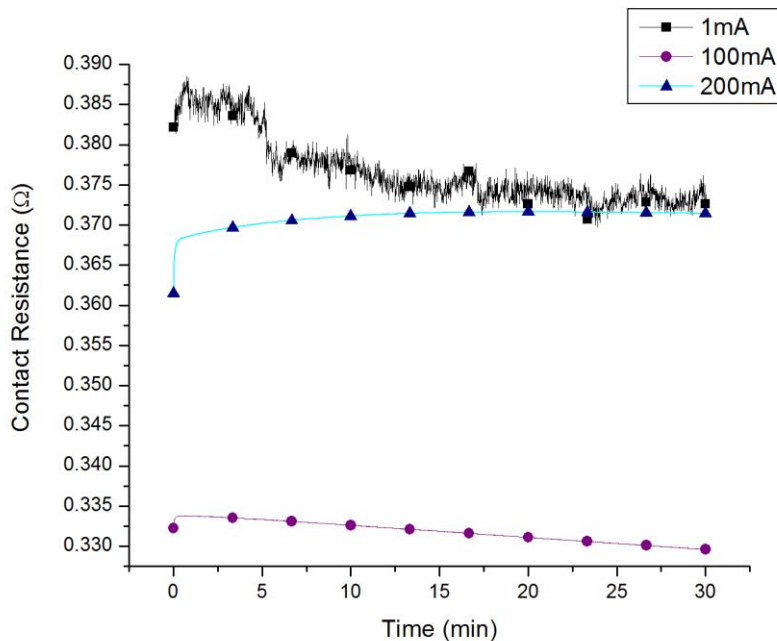


Figure 9.8 – Contact resistance versus time as a function of applied current for the NEU switch at 5.6 K.

switch was closed for 5 minutes with 1 mV applied to ensure that no large changes in creep or contributions from adsorbed film layers would affect the voltage sweep. The voltage was swept from 0 V to 0.12 V. According to the asperity-heating model, at 5.6 K a 0.12 V drop across the contacts is needed to reach the asperity softening temperature of 100°C. Above this voltage, changes in contact resistance would be due mostly to increases in real contact area as the soften asperities yielded to the applied actuation force. Below this value, changes in contact resistance will be driven by changes in resistivity from heating.

Figure 9.9 shows the contact resistance as a function of the voltage applied to the switch. As previously noted, all of the switch voltage is not dissipated at the contact constrictions because of the surrounding transmission lines and wirebonds. The contact resistance increases with increasing voltage.

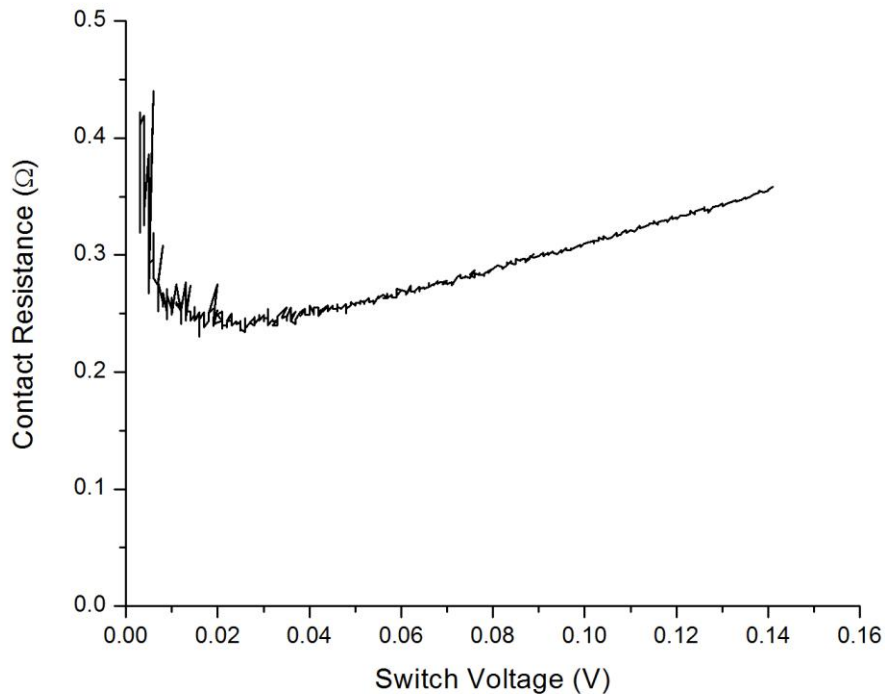


Figure 9.9 – Contact resistance versus switch voltage for the NEU switch at 5.6 K.

9.5 Modeling predictions

Modeling predictions of the electro-thermo-mechanical response of RF MEMS switches were obtained, such that comparisons can be made between the experimental and numerical modeling results and to gain a detailed understanding of the electro-mechanical behavior of RF MEMS switches. A three dimensional representation of the roughness of contact surface in a sample RF MEMS switch is obtained from AFM measurements (Fig. 9.10). This surface roughness model is then used with the numerical framework previously used in [4] to obtain predictions of time-dependent thermo-mechanical asperity deformations due to creep under applied contact pressures. Asperity deformations are then used to obtain contact parameters such as the real contact area, the constriction resistance of the micro-contacts, and the number of micro-contacts.

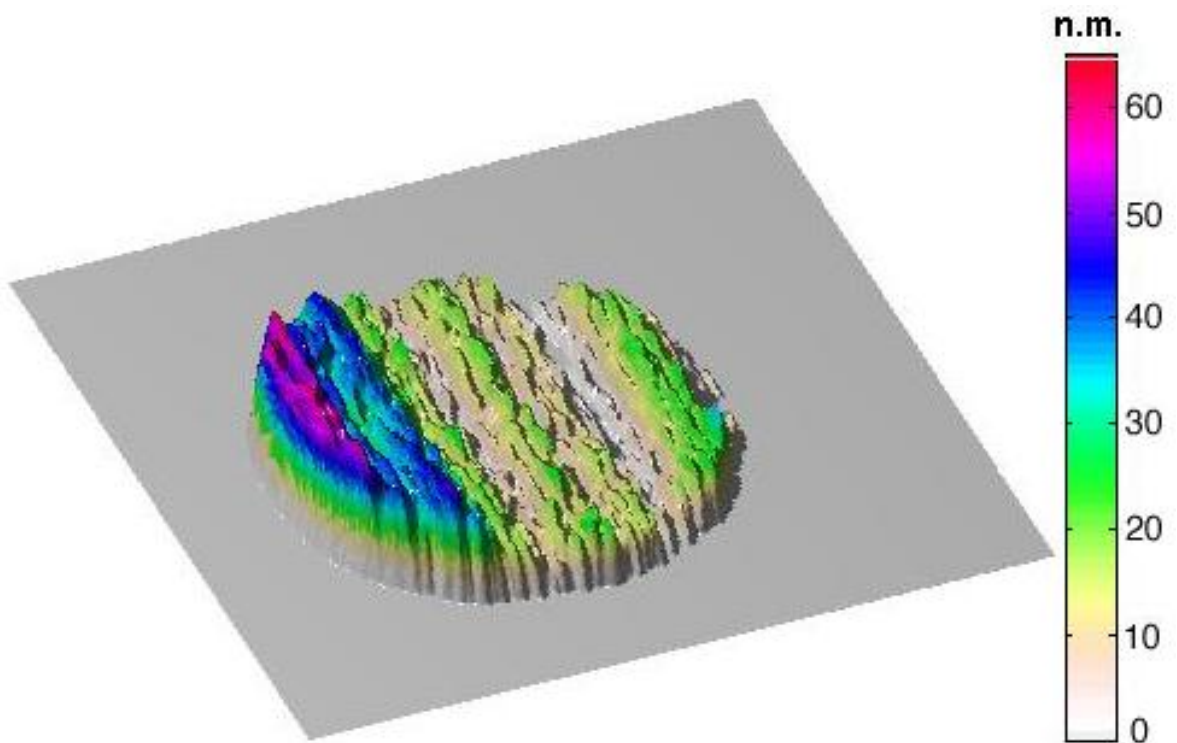


Figure 9.10 – Surface roughness simulation from AFM measurements of roughness of the top contact surface in a RF MEMS switch.

In RF MEMS switches with normal contact, the lateral deformations of asperities can be assumed to be negligible. As noted earlier, creep is considered the long-term deformation mechanism for asperity micro-contacts. Hence, the time-dependent normal finite deformations of contact asperities can be represented by a power law constitutive relation as

$$\dot{\varepsilon} = A_c \sigma^p \exp\left(-\frac{Q_c}{kT}\right), \quad (9.2)$$

where $\dot{\varepsilon}$ is the strain-rate, A_c is a parameter relating to the material properties and the creep mechanism, σ is the stress, Q_c is the activation energy for creep, T is the absolute temperature, and k is the Boltzmann constant ($k = 1.38\text{E-}23$ J/K). The stress exponent p in (9.2) is usually between 3 and 10, and it is determined by the material composition.

Assuming the mating surface to be flat and infinitely smooth, the far-field approach of the contact surfaces can be determined from the collective creep response of the asperities on one contact surface. This assumption is based on that the drain electrode is generally significantly smoother than the contact bumps. The asperity tips that establish contact can be identified at each time step by comparing the far-field approach with the asperity heights.

For a contact spot of radius a , and considering both ohmic and boundary scattering effects, the constriction resistance R_c can be given as

$$R_c = f\left(\frac{\lambda}{a}\right)R_M + R_S = f\left(\frac{\lambda}{a}\right)\frac{\rho}{2a} + \frac{4\rho\lambda}{3\pi a^2}, \quad (9.3)$$

where ρ is the electrical resistivity, and λ is the electron mean free path. R_M denotes the Maxwell resistance, which is the resistance due to lattice scattering mechanism¹⁹, and R_S denotes the Sharvin resistance, which is due to the boundary scattering of electrons²⁰. In (9.3), $f(\lambda/a)$ is an interpolation function, which accounts for the transition between the two resistance regimes, and has the limiting values of 1 as λ/a approaches zero for $a \gg \lambda$, and 0.624 as λ/a approaches infinity for $a \ll \lambda$ ^{21,22}. For the overall contact resistance, it is assumed that individual micro-contacts act in parallel.

With the size of asperity micro-contacts in the range of electron mean free path, steady state contact spot temperature T_c can be stated as²³:

$$T_c = \sqrt{\frac{f(\lambda/a)R_M}{4LR_c} V_c^2 + T_0^2}, \quad (9.3)$$

where L is Lorenz number ($L = 2.45\text{E-}8 \text{ W} \cdot \Omega / \text{K}^2$), V_c is the voltage drop across asperity micro-contacts and T_0 is the ambient temperature.

Table 9.1 – Electromechanical properties of Gold.

Electrical resistivity at 293K, ρ	2.5E-08 $\Omega \cdot \text{m}$
Power exponent in (2), p	7
Coefficient in (2), A_c	1.9E-15
Activation energy in (2), Q_c	3E-21 J

The surface roughness model is constructed over a circular area of 4 by 4 microns, using a grid of x and y coordinates with 31.4 nm intervals. The maximum asperity height is about 65 nm (Fig. 9.10), which is on top of 375 nm uniform thickness of the top contact (not shown in figure). The contact material is gold (Table 9.1). The applied contact force is 50 μN , which corresponds to a gold cantilever beam with dimensions of $150 \times 250 \times 0.5 \mu\text{m}$, and a gap of 2 μm . The switch is assumed to remain in close position for the duration of the simulation, and it is also assumed that there is no insulating film effect to match the experimental process, which tries to minimize the insulating film effects. This is done so that we can better understand the direct effects of surface roughness on electro-mechanical behavior of the RF MEMS switches. Also the current model does not account for the generated debris from the fracture and crushing of the contact asperities, which is known to influence the electro-mechanical response of the RF MEMS switches²⁴. It is also assumed that the thermal boundary conditions are fixed.

Modeling predictions for contact resistance over time at 293 K are shown in Fig. 9.11(a), and for temperatures of 77 K and 5.6 K are shown in Fig. 9.11(b). At room temperature, the initial contact resistance is approximately 56 m Ω . At 77 K it is approximately 10 m Ω and at 5.6 K it is approximately 0.5 m Ω . This difference in initial

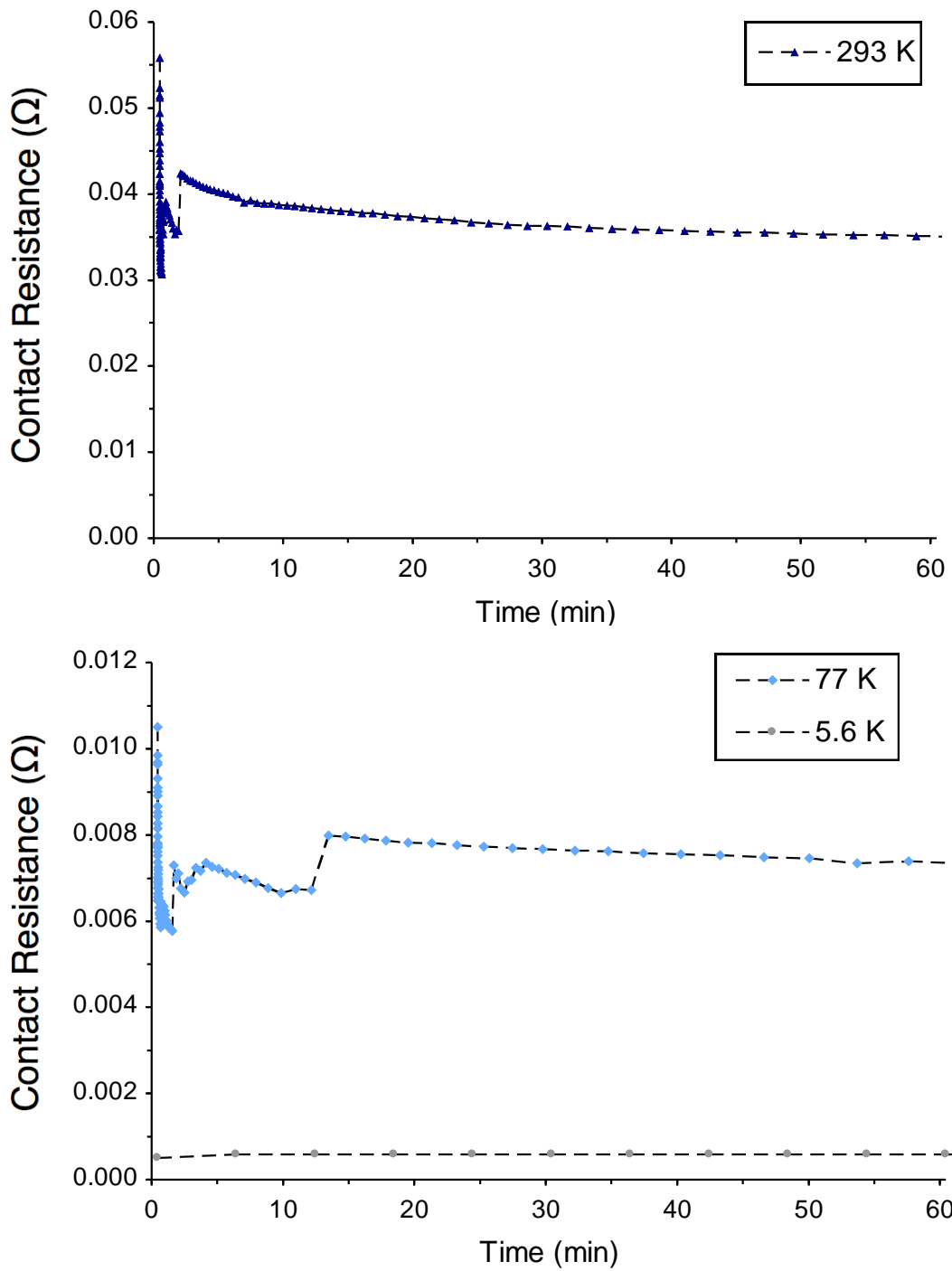


Figure 9.11 – Contact resistance versus time for the simulated surface roughness (a) at 293 K, (b) at 77.4 K, and 5.6 K.

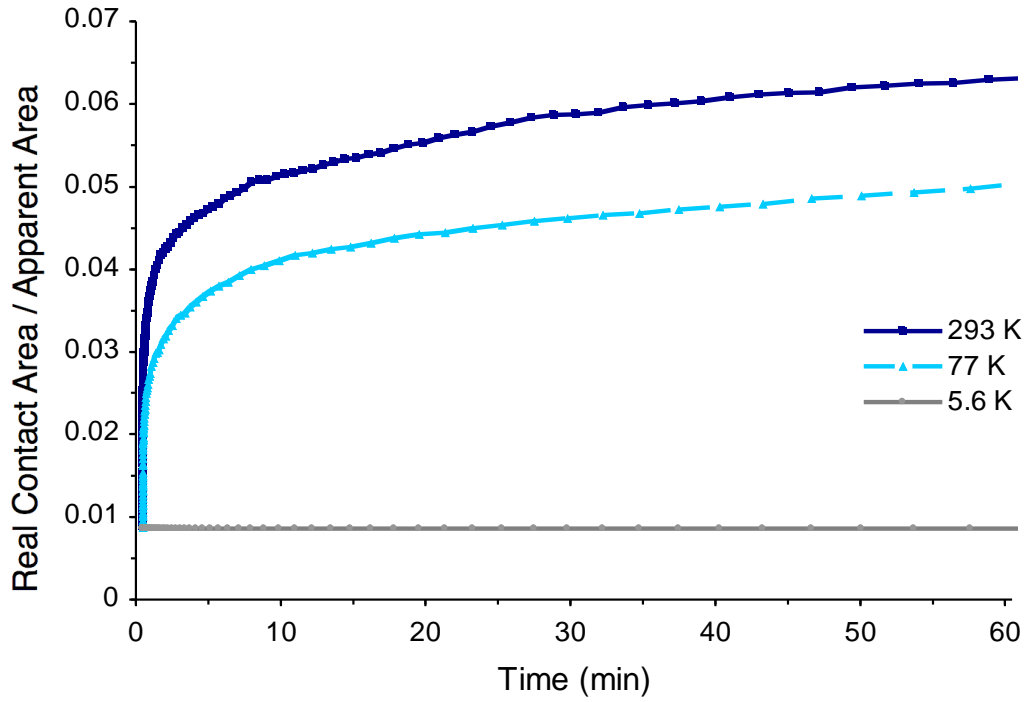


Figure 9.12 – Real contact area percentage with respect to apparent contact area versus time for the simulated surface roughness at 293 K, 77.4 K, and 5.6 K.

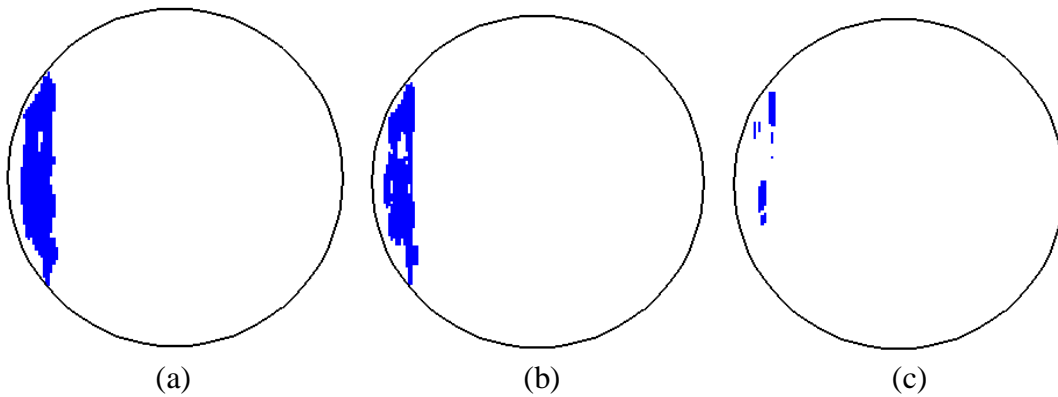


Figure 9.13 – Top view of the real contact area for the simulated surface roughness after 60 minutes (a) 293 K (b) 77.4 K and (c) 5.6 K.

contact resistance is due to the temperature dependence of the resistivity. For the applied contact voltage of 1mV, at a fixed ambient temperature, the change in contact resistance for clean contacts is a function of the competition between the increase of contact area due to asperity flattening and creep, and the resistivity increase due to contact heating from Joule heating. As is shown from Fig. 9.11(a-b), at 293 K and 77 K, contact resistance decreases by initial asperity flattening, and subsequently creep overcomes any increase by contact heating. At 5.6 K for the contact voltage of 1 mV the contact area remains almost unchanged over time, so the local heating of micro-contacts slightly increases the contact resistance from 0.5 mΩ to about 0.6 mΩ (Fig. 9.11(b)).

The change of contact area over time at 293 K, 77 K, and 5.6 K is shown in Fig. 9.12. The initial contact area is about 0.9% of the apparent area. At room temperature, the contact area reaches to approximately 6.6% of the apparent area after 60 minutes. Due to less deformation at 77 K the contact area reaches to only 5.2% after 60 minutes. At 5.6 K the contact area remains almost unchanged. The top views of contact area after 60 minutes (Fig. 9.13) clearly show the location, shape, distribution and number of asperity contacts at each ambient temperature level. The contact area at 5.6 K (Fig. 9.13(c)) is made of 7 individual micro-contacts. At 77 K, after 60 minutes, as the contact area has increased, asperity coalescence has resulted in the formation of one large asperity (Fig. 9.13(b)). At 293 K, over the same period of 60 minutes, the single contact has become larger (Fig. 9.13(c)).

To further examine the heating effect on resistivity and contact resistance, and to make valid comparisons with the experimental data from the voltage sweep at 5.6 K, modeling predictions were obtained for contact resistance for a voltage sweep from 1mV to 50 mV (Fig. 9.14). The temperature factor in the creep based constitutive relation is kept fixed at 5.6 K, so that the contact resistance change is only due to resistivity increase by contact heating. This is done to eliminate any heating effects on long-term asperity deformation and change in contact area. For the given contact surface, at 5.6 K contact resistance increases from 0.5 mΩ for a 1mV voltage drop at contact to 16.2 mΩ for a 50 mV voltage drop. Then the local heating effect on long-term creep is added to the contact resistance prediction. In this case, for each contact voltage, the contact resistance after 60

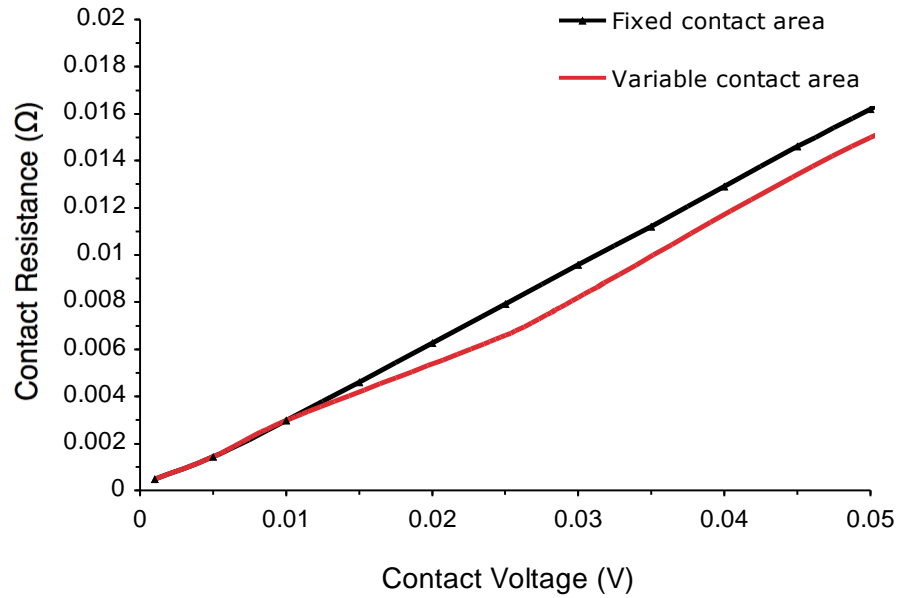


Figure 9.14 – Contact resistance versus switch voltage for the simulated surface roughness at 5.6 K.

minutes is taken so that the initial contact resistance fluctuations are not used. In the given voltage range, and at 5.6 K the local heating effect on contact area is seen to be minor in comparison to its effect on resistivity.

9.6 Conclusions

Experimental measurements and modeling predictions were obtained to characterize the electro-mechanical response of two different gold contact RF MEMS switches due to variations in the temperature and applied contact voltage. A three-dimensional surface roughness profile from AFM measurements of the top contact surface of a sample RF MEMS switch was used to obtain modeling predictions of the time-dependent deformation of the asperity micro-contacts, real areas of contact, number of asperity micro-contacts, and constriction resistance at various temperatures and contact voltage levels.

The experimental data indicated a decrease in the overall resistance and more significantly a decrease in the creep mechanism at 77 K and 5.6 K when compared to 293 K.

At 293 K the contact resistance as a function of time was consistent with the single asperity model and data obtained in [4]. The contact resistance as a function of time also followed the power law relation previously developed in [5]. The application of the power law fit to the contact resistance data generated similar A values, indicating the two switches to be similar in contact roughness. At 77 K and 5.6 K the power law no longer provided an effective fit for the change in contact resistance with time, but an inspection of the percent difference between initial contact resistance value and those after 30 minutes of closure indicated that creep was significantly reduced at cryogenic temperatures.

The modeling results showed that the room versus cryogenic temperature results to be a material competition between asperity flattening, which lowers contact resistance and heating, which raises the contact resistivity. At 293 K more area is in contact per unit time, and the resistance drop from the increase in real contact area dominates the resistance increase from asperity heating. At 77 K the creep rate is reduced as fewer asperities come into contact over time. Real contact area as a percentage of apparent contact area increases with time, but not the same percentage as at 293 K. At 5.6 K the change in contact area over time is small, and the contact resistance measurement is dominated by asperity heating.

To further examine contact heating, V-I sweeps were recorded at 293 K and 5.6 K for switches fused at the contacts. The experimental data indicated that contact resistance increased with increased voltage supplied over the switch contacts. The modeling of constriction resistance at 5.6 K for contacts with fixed contact area and variable contact area clearly shows that contact heating dominates the constriction resistance and the creation of real contact area has little effect.

The data presented and constriction resistance modeling for gold RF MEMS show that temperature plays an important role in the creep and heating of switch contacts. This modeling approach in conjunction with the experimental observations and measurements can be used as a framework to design reliable RF MEMS devices for prolonged contact and reliable operation in cryogenic temperatures.

9.7 Acknowledgements

This work was supported by AFOSR MURI Grant No. FA9550-04-1-0381 entitled “Multifunctional Extreme Environment Surfaces: Nanotribology for Air and Space” and DARPA S&T Fundamentals Program, “Center for RF MEMS Reliability and Design Fundamentals,” Grant No. HR0011-06-1-0051.

The authors would also like to thank Dr. Zhenyin Yang and Matt Walker for the AFM measurements.

9.8 References

- ¹ Rebeiz GM 2003 *RF MEMS, Theory, Design, and Technology*. New York Wiley.
- ² Kasim R, Kim BC, and Drobnik J 2005 MEMS circuit breakers for integrated shipboard power system *IEEE Electric Ship Technologies Symposium* 225-229, 25-27
- ³ Kim BC, and Kasim R 2007 Advanced MEMS Development for High Power Sensor Application *Sensors* 811-814, 28-31
- ⁴ Rezvanian O, Zikry MA, Brown C, and Krim J 2007 Surface roughness, asperity contact and gold RF MEMS switch behavior *J. Microelectromech. Syst.* 17 2006-2015
- ⁵ Rezvanian O, Brown C, Zikry MA, Kingon AI, Krim j, Irving DL, and Brenner DW 2008 The Role of Creep in the Time-Dependent Resistance of Ohmic Gold Contacts in Radio Frequency Micro-Electromechanical System Devices *J. Appl. Phys.* in press
- ⁶ Demchuk IS, Krakhmalev VI, and Lebedev DV 1979 Creep of cryogenic steels and alloys *Met. Sci. Heat Treat.* 21 547-553
- ⁷ Lebedev DV 1968 Creep of metals at low temperatures *Met. Sci. Heat Treat.* 10 780-781

-
- ⁸ McDonald LC, and Hartwig KT 1990 Creep of Pure Aluminum at Cryogenic Temperatures *Advances in Cryogenic Engineering* 36B 1135-1141
- ⁹ Roth L, Purushothaman S, and Tien JK 1979 A discussion of cryogenic creep using a back stress model *Scr. Metall.* 13 589-592
- ¹⁰ Roth LD, and Wetzel JT 1980 Creep of Copper at Cryogenic Temperatures *International Copper Research Assoc., Inc.* 31
- ¹¹ Yen C, Caulfield T, Roth LD, Wells JM, and Tien JK 1984 Creep of copper at cryogenic temperatures *Cryogenics* 24 371-377
- ¹² Zhang K, Weertman JR, and Eastman JA 2004 The influence of time, temperature, and grain size on indentation creep in high-purity nanocrystalline and ultrafine grain copper *Appl. Phys. Lett.* 85 5197-5199
- ¹³ Noel J, Hijazi Y, Martinez J, Vlasov YA, and Larkins Jr GL 2003 A switched high-Tc superconductor microstrip resonator using a MEM switch *Supercond. Sci. Technol.* 16 1438-1441
- ¹⁴ Prophet EM, Musolf J, Zuck BF, Jimenez S, Kihlstrom KE, and Willemsen BA 2005 Highly-selective electronically tunable cryogenic filters using monolithic, discretely-switchable MEMS capacitor arrays *IEEE Trans. Appl. Supercond.* 15 956-959
- ¹⁵ Su HT, Llamas-Garro I, Lancaster MJ, Prest M, Park JH, Kim JM, Baek CW, and Kim YK 2006 Performance of RF MEMS switches at low temperatures *Electron. Lett.* 42 1219-1220
- ¹⁶ Zhu Y, and Espinosa H 2004 Effect of temperature on capacitive RF MEMS switch performance – a coupled-field analysis *J. Micromech. Microeng.* 14 1270-1279

-
- ¹⁷ Brown C, Morris AS, Kingon AI, and Krim J 2008 Cryogenic performance of RF MEMS Switch Contacts *J. Microelectromech. Syst.* in press
- ¹⁸ S. Majumder, N.E. McGruer, G.G. Adams, P.M. Zavracky, R.H. Morrison, and J. Krim, "Study of contacts in an electrostatically actuated microswitch," *Sensors and Actuators A*, vol.93, pp. 19-26, 2001.
- ¹⁹ Holm R 1967 *Electric Contacts-Theory and Applications* 4th ed. Berlin, Germany Springer-Verlag.
- ²⁰ Sharvin YV 1965 A possible method for studying Fermi surfaces *J. Exp. Theor. Sci.* 21 655-656
- ²¹ Nikolic B, Allen PB 1999 Electron transport through a circular constriction *Phys. Rev. B* 60 3963-3969
- ²² Wexler G 1966 The size effect and the non-local Boltzmann transport equation in orifice and disk geometry *Proc. Phys. Soc.* 89 927-941
- ²³ Jensen BD, Chow LL, Huang K, Saitou K, Volakis JL, and Kurabayashi K 2005 Effect of nanoscale heating on electrical transport in RF MEMS switch contacts *J. Microelectromech. Syst.* 14 935-946
- ²⁴ Alsem DH, Stach EA, Dugger MT, Enachescu M, and Ritchie RO 2007 An electron microscopy study of wear in polysilicon microelectromechanical systems in ambient air *Thin Solid Films* 515 3259-66

CHAPTER 10

Summary and Future Work

10.1 Summary

Most studies in the RF MEMS field have focused on switch design and operating conditions (contact force, current, hot vs. cold switching, etc.) as a means of controlling switch failure mechanisms without revealing the underlying cause of the failure. In contrast, this thesis focuses on the impact of environmental conditions and links them to failure mechanisms in gold RF MEMS switches. Observations have been made and linked to theoretical predictions which show that environmental conditions play an important role in switch contact physics. The results presented specifically focus on temperature and pressure conditions that significantly impact adsorbed films on the contact surfaces, creep, and the cantilever beam mechanics that directly affect surface topography. All of these are leading contributors to early device failure.

As noted in Chapter 2, adsorbed films provide a significant barrier to reliability in low contact resistance RF MEMS switches. The film contribution to the overall contact resistance is much greater than the constriction resistance, and is believed to be the source of contact resistance variability late in switch lifetimes (Fig. 8.10). Results from Chapter 5 indicate that the role of adsorbed films is greatly reduced at cryogenic temperatures. At 77 K film mobility is reduced. The difference in contact resistance between consecutive runs at cryogenic temperature indicates that the film can be removed by mechanically cycling the switch or applying high enough heat at the asperity to disassociate the film from the gold surface (Fig. 5.5). Furthermore, the difference in slope between the two runs at 77K indicates the adsorbed film had indeed contributed to the overall contact resistance value and the time dependent change. With the film removed, the second run is more indicative of the temperature dependent creep results reported in Chapter 9. This thesis and associated publication is the first study reporting adsorbed film dynamics on a gold MEMS switch and the ability to isolate film effects through the use of cryogenic temperatures.

Creep is a component of the adhesion failure mechanism where the contact asperities yield under pressure creating more contact area. Heavy contact loads, extended cycling, and prolonged closure create additional contact area that generates an adhesive force large enough to cold weld the switch in the closed state. Creep was experimentally measured and

modeled in Chapter 6. Initial results showed the experimental and theoretical results to be qualitatively the same, differing only in the magnitude of measured contact resistance. In a subsequent publication covered in Chapter 6, the experimental and theoretical results for time dependent creep at 293 K were correlated using a power law relation. Previously, the time dependent nature of contact resistance in gold switches was reported as a simple logarithmic function. The power law developed here accounts for the material dependent properties, surface topography, and additional contributions from sources such as other switch components and adsorbed surface films.

The temperature dependence of creep is shown in Chapter 9. As in the case for room temperature creep, experimental data and modeling showed qualitatively similar creep characteristics at cryogenic temperatures, differing only in the magnitude of the contact resistance. Again this difference is attributable to adsorbed films and additional device components not measured out by the four point probe measurement. Creep is reduced at cryogenic temperatures. As seen in [Fig. 9.4](#), the change in contact resistance as a function of time becomes nearly linear at 77 K and lacks the steep initial drop off and continuing downward trend in resistance seen in the room temperature tests. At 5.6 K the creep effect is very limited, and the contact resistance as a function of time produces a nearly horizontal trace. This thesis and associated publication represent an iterative step forward in the understanding of creep by integrating temperature dependent effects to the formulation provided in Chapter 6.

Furthermore, it was noted that resistivity changes in the gold dominated contact resistance changes at cryogenic temperatures ([Fig. 9.14](#)). Per the explanation in Chapters 5 and 6, the time dependent nature of contact resistance is a balance between resistance decreasing phenomena such as the increase in contact area from creep and resistance increasing phenomena such as strain hardening and Joule heating. According to [Fig. 5.6](#), in the low temperature regime at contact voltages below 120 mV, asperity temperatures are below the threshold needed to allow creep; this allows heating mechanisms to dominate the change contact resistance over time. Isolation and measurement of this heating effect was achieved through cryogenic temperatures.

Investigation of temperature dependent characteristics of RF MEMS switches yielded more than increased understanding of creep and adsorbed films. During cryogenic testing, the switch contact resistance was observed to have a strong dependence on atmospheric conditions. Experimentation revealed that a nitrogen atmosphere at LN₂ temperature will condense on the switch contacts creating variability in the contact resistance as the liquid boiled off of the contacts (Fig. 5.4). Previously atmospheric conditions were only a consideration for limiting stiction events; however, this data definitively shows that atmospheric conditions have an impact on switch performance in the cryogenic temperature regime.

The pressure drop associated with a drop in temperature as prescribed by the ideal gas law was observed during cryogenic testing. The low pressure resulted in switch bouncing. A treatment of switch bounce as a function of pressure is presented in the thesis. Previously, bounce effects were attributed to and corrected by switch design. Here the data shows that without changing the switch design, switch bounce can be controlled by adjusting the ambient pressure. While this can be achieved through novel packaging techniques, it is easier to control bounce through design modifications and tailored actuation schemes. In Chapter 4, a treatment of the fluid mechanics governing squeeze film damping is paired with data from switches of differing geometries to suggest that a critical ratio of damping force to electrostatic pull-in force can be achieved through changes in pressure or design that will stop switch bounce.

10.2 Suggested future work

The convergence of experimental and theoretical understanding of the underlying physics leading to device failure mechanisms has opened a new avenue of understanding which provides RF MEMS switch designers with a larger knowledge base applicable to improving switch performance. The findings in this thesis should be paired with those emerging from other researchers exploring switch fundamentals in the area of contact materials and contact mechanics across a range of length scales. This will build a fuller, more robust understanding of the contact physics and allow multiple avenues for solving the

reliability issue in RF MEMS switches. Data from this thesis and other emerging work indicates that the solution to enhancing device reliability will require a combination of changes including harder contact materials and cantilever designs maximizing damping force to stop bounce and increasing the restoring force to overcome adhesion. Additionally, it is highly probable that no universal solution will be found, and switch designs will be application specific with the contact material and cantilever designed to meet the functional need. In this case, having a full understanding of the contact physics across a wide range of designs and materials is critical to meeting this demand.

In the case of gold contacts, further study should be committed to understanding the transition from heating effects to creep at cryogenic temperatures. At 5.6 K heating mechanisms will dominate the resistance measurements until a threshold voltage is applied which will soften the gold asperities and allow the creep mechanism to drive changes in the contact resistance. This data should be paired with experiments run at higher temperatures ranging from 77 to 350 K. Measurements at higher temperatures will require in-situ pre-test plasma or uv-ozone cleaning to remove films and isolate the creep mechanism. The temperature dependent set of creep data will validate accuracy of the asperity heating model and prediction of creep onset (Fig. 5.6).

The experimentation completed in this thesis and suggested future work should also be performed on contact materials other than gold. Z. Yang recently showed that a nickel gold alloy could improve switching performance without the tradeoff of high contact resistance seen in many hard contact material switches¹. The contact physics and creep phenomena seen in gold contact should be examined for gold alloy switches and the harder Ru and Rh switches that are now being fabricated. These harder metals should have decreased creep and a decreased likelihood of adhesion failures during prolonged closure and under heavy contact loads.

A final area of interest where continued work is of merit is the pressure dependent bounce of switches. Pressure plays a significant role in squeeze-film damping which offsets the downward force of impact on the contacts. Cycle testing over a range of pressures will provide insight to the contact physics and surface topography changes due to bounce and

initial impact speed. Decreased impact force and bouncing will reduce changes in surface topography and lessen adhesion failures in high cycle applications. Further work is required to determine the ratio of damping force to electrostatic force that will limit switch bouncing and decrease impact force. Understanding the physics of closure will translate to improved cantilever design.

10.3 References

¹ Z. Yang, “Contact Material Optimization and Contact Physics in Metal-contact Microelectromechanical Systems (MEMS) Switches,” Ph.D. dissertation, North Carolina State University, 2008.

APPENDIX

A.1 Cycle testing

Early literature on RF MEMS devices focused heavily on the number of switching cycles before failure as a gauge for switch robustness. Cycle testing has value when implemented during the proper stages of device development. Foremost it can be used as a proof of concept for a new device, and at the tail end of development, as the device moves into mass production and insertion into commercial applications, cycle testing can give the manufacturer a sense of the alpha and beta loss they can expect. A statistically based metric of the switch's lifetime is a must for a switch manufacturer, and the cycle test provides this.

Between the proof of concept stage and the prediction of failures in the field, the lifetime test yields limited information. What does it tell you about the switch other than it has failed? The work in this thesis obviates the fact that the lifetime of a switch is linked to its operating environment. Even the best switch (i.e. the one with the most cycles before failure) can fall short of its statistically proven lifetime when actuated in a less than optimum environment. The response to this has been to put the switch in hermetically sealed packaging where the environment is controlled and stable. While this is effective, it is costly and creates an additional layer of problems affecting switch lifetime. It is a surface fix for a much deeper problem.

Placing the switch in a controlled environment shows that switch manufacturers are cognizant that operating environment impact device performance; however placing the device in a hermetically sealed package and cycle testing it for increased longevity misses the real objective: to answer the question, "Why did this device fail, and what about the controlled environment extended the switch's lifetime?" A primary reason RF MEMS switches lag market expectations is because this question does not receive the attention it deserves.

The economic reality of intense competition in the open market often forces a mentality of "fix it enough to make it work" in place of "fix it right" in order to launch first and gain market share. This system has worked well so long as the science is well worked out and problems are mostly on the engineering level. As products become more complex and use less explored science as their foundation, more attention must be afforded to

fundamental understanding. In the case of MEMS and many emerging nanotechnology applications, the science is not well enough understood to transition directly to applications engineering and testing.

An appropriate amount of time needs to be spent laying a foundation of knowledge that can in turn be used to make a more robust product. The work cited and reported in this thesis needs to be applied early in the product development cycle where its impacts can be the most beneficial. The lessons learned through fundamental research can be rapidly applied while the product is in the design stage. With those modifications made the cycle test becomes useful. It provides quantifiable proof that the changes made at the design level based on an improved understanding of the fundamentals have positively impacted the reliability and performance of the switch. The cycle test is a necessity and is the ultimate proof of success, but it has limited meaning if not applied appropriately.

The proposed impacts of various environmental conditions are noted in [Table A.1](#).

Table A.1 – Impact of operating and environmental conditions on cycle lifetime.

Condition	Impact on cycles
UHV	1 cycle (experimentally measured); adhesion failure on first closure.
Inert atmosphere (N ₂ , He, Ar)	10 ⁶ increase in cycles for nitrogen versus air during hot cycling at high current ¹ ; Hypothesized increase in cycles as inert atmosphere does not contribute to surface films and related heating.
Carbon atmosphere (C ₅ H ₁₂ , CH ₃ (CH ₂) ₁₀ CH ₃)	Hypothesized decrease in cycles due to heating and increased resistance from adsorbed films on contacts.
Cryogenic temperatures	Hypothesized increase in cycles from increased material hardness.
Elevated temperatures (internal and external)	Hypothesized decrease in cycles for prolonged cycling at temperature greater than 100°C; adhesion failures expected.
Low ambient pressure	10x-40x reduction in cycle lifetime from bouncing; effects more pronounced under hot-switching.
High contact voltage (or current)	10 ⁶ increase in cycles for 5 mA versus 10 mA ¹ . Hypothesized decrease in cycles from adhesion failures and material transfer; dependent on ambient temperature (see Fig. 8.9)
Low contact voltage (or current)	1.6×10 ⁶ cycles (experimentally measured, Fig. 8.10); Hypothesized decrease in cycles from adsorbed film buildup at micro-contacts; dependent on ambient temperature (see Fig. 8.9)
Hard contact materials (Rh, Ru, Pt, AuNi)	Increase in cycles ² ; surface topography is maintained, and adhesion failures decrease (see Fig. 2.1).
Hot-switching	Decreased cycle lifetime ¹ ; failures from arcing, high resistance from pyrolyzed films, and material transfer.

A.2 Wiring diagrams

A common “failure mode” for switches is improper wiring. Inevitably the wrong connection will be made with the switch. The most detrimental misconnect is placing the high voltage actuation leads in contact with the connection intended for measuring the contact resistance. This will result in instant failure as the extreme voltage drop across the contacts will generate temperatures far beyond those needed to boil the gold asperities. For this reason all the wiring terminations for the experimental setup were fitted with d-sub connectors. The sockets were standardized for all the switches so that wiring was consistent for every data run and no switches were damaged from improper connections.

The wiring diagrams from the package to the device are often referred to as “straw man” diagrams. Contained in this section are the wiring diagrams for the wiSpry switches on 40 pin ceramic packages as well as the nomenclature used to identify the switch to bond pad to pin connection required to operate the switch.

The wiSpry switch wirebonding diagram is shown in [Fig. A.1](#). The wirebonding sites on the switch are referred to as pads. The bond sites on the ceramic package are referred to as pins, since each bond site leads to a pin on the side of the package. Pins 1 through 10 are required to operate one SPDT set. Pins 10 through 20 operate the next SPDT, etc. The pin to pad connections are listed in [Table A.2](#).

Table A.2 – Ceramic pin, switch bond pad, and function corresponding to wirebond diagram for wiSpry RF MEMS switch.

Pin	Pad	Function	Pin	Pad	Function
1	12	RFGround Signal	21	28	RFGround Signal
2	11	Out	22	27	Out
3	10	RFGround	23	26	RFGround
4	9	Vin - b	24	OPEN	
5	OPEN		25	OPEN	
6	OPEN		26	OPEN	
7	8	Vout	27	25	Vin - b
8	7	Vin - a	28	24	Vout
9	6	RFGround	29	23	Vin - a
10	5	Signal In	30	22	RFGround
11	4	RFGround	31	21	Signal In
12	3	Vin - a	32	20	RFGround
13	2	Vout	33	19	Vin - a
14	1	Vin - b	34	18	Vout
15	OPEN		35	OPEN	
16	OPEN		36	OPEN	
17	OPEN		37	17	Vin - b
18	32	RFGround Signal	38	16	RFGround Signal
19	31	Out	39	15	Out
20	30	RFGround	40	14	RFGround

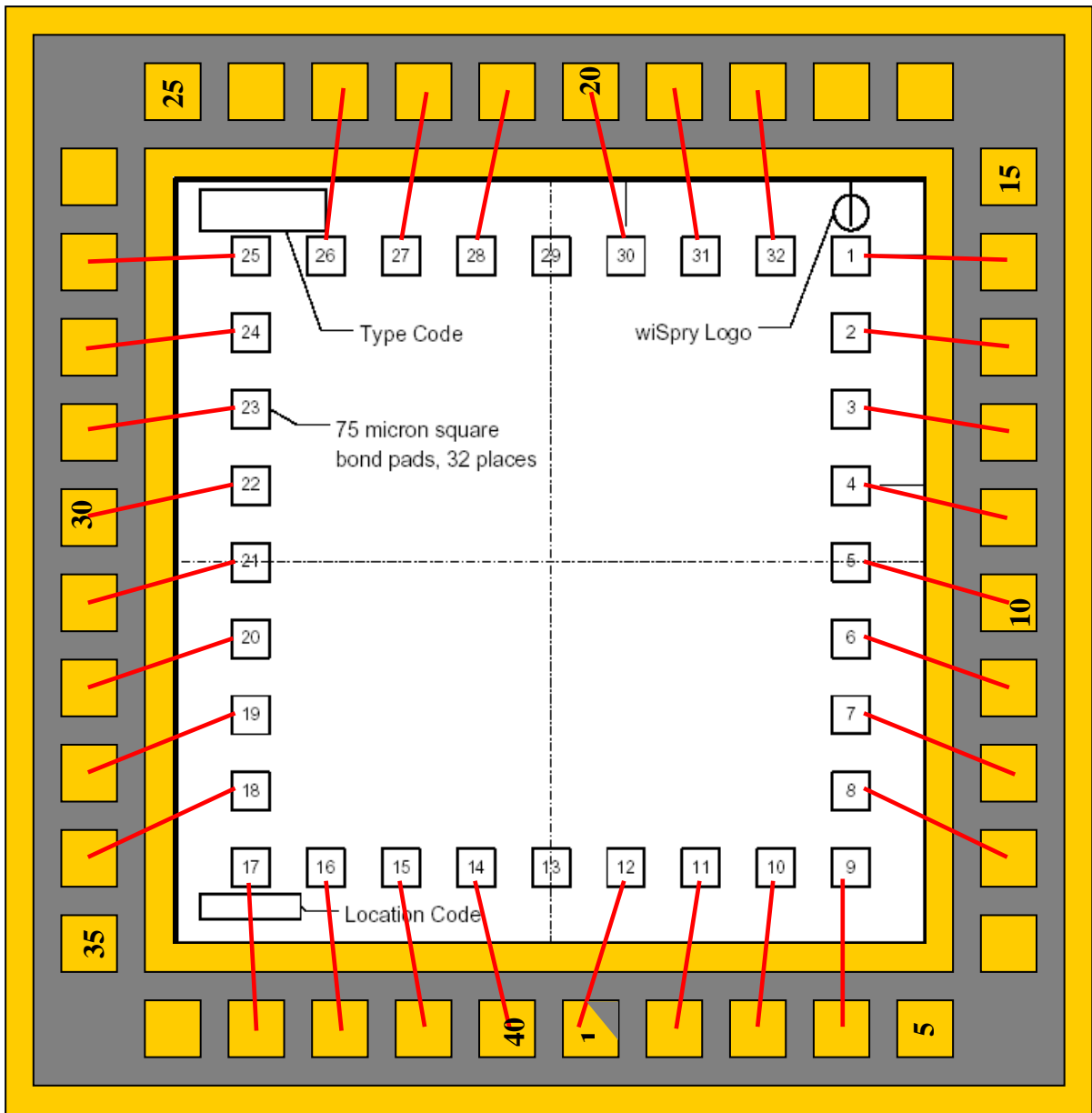


Figure A.1 – Wirebonding diagram for wiSpry RF MEMS switch to 40 pin ceramic package.

A.3 References

¹ Zavracky, P.M.; Majumder, S.; McGruer, N.E., "Micromechanical switches fabricated using nickel surface micromachining," *Microelectromechanical Systems, Journal of* , vol.6, no.1, pp.3-9, Mar 1997.

² Z. Yang, "Contact Material Optimization and Contact Physics in Metal-contact Microelectromechanical Systems (MEMS) Switches," Ph.D. dissertation, North Carolina State University, 2008.